Combined Electricity and Water Production Based on Solar Energy

Von der Fakultät für Energie-, Verfahrens- und Biotechnik der Universität Stuttgart

zur Erlangung der Würde eines Doktor-Ingenieurs (Dr.-Ing.)

genehmigte Abhandlung

Vorgelegt von

Dipl.-Ing. Massimo Moser

aus Mezzolombardo (Italien)

Hauptberichter: Prof. Dr. rer. nat. habil. André Thess

Mitberichter: Prof. Dr. Giorgio Micale

Tag der mündlichen Prüfung: 29.01.2015

Institut für Energiespeicherung

der Universität Stuttgart

2014

Content

Nomenclature

Acronyms

AC	Alternating Current
AP	Aromatic Polyamides
BaU	Business as Usual
bbl	Barrel
BOS	Balance of System
BW	Brackish Water
C	C programming language
$CIEMAT$	Centro de Investigaciones Energéticas, Medioambientales y Tecnológicas
$CIGS$	Copper Indium Gallium Diselenide
CIF	Cost, Insurance and Freight
CPV	Concentrating Photovoltaics
CR	Central Receiver
CSP	Concentrating Solar Power
$c-Si$	Crystalline Silicon
DAF	Dissolved Air Flotation
DC	Direct Current
$DEEP$	Desalination Economic Evaluation Program
DLR	German Aerospace Center (Deutsches Zentrum für Luft- und Raumfahrt e.V.)
DMF	Dual Media Filters
DoY	Day of the Year
DSG	Direct Steam Generation
ED	Electro Dialysis

EIA	Environmental Integrated Assessment
$EI\&C$	Electrical, Instrumentation and Controls
EPC	Engineering, Procurement and Construction
ERD	Energy Recovery Device
$ESNA$	Energy Saving Nanofiltration Membrane
$ESPA$	Energy Saving Polyamide Membrane
ET	Equation of Time
$FORTRAN$	Formula Translator programming language
GIS	Geographical Information System
$HFLCAL$	Heliostat Field Layout Calculator
HP	High Pressure
HTF	Heat Transfer Fluid
HX	Heat Exchanger
$INSEL$	Integrated Simulation Environment Language
$I\&C$	Instrumentation and Controls
LF	Linear Fresnel
LP	Low Pressure
$MATLAB$	Matrix Laboratory programming language
MCM	Million Cubic Meters
MD	Membrane Distillation
MED	Multi-Effect Distillation
$MED-MVC$	Multi-Effect Distillation - Mechanical Vapor Compression
$MED-TVC$	Multi-Effect Distillation - Thermal Vapor Compression
MEH	Multi-Effect Humidification
$MENA$	Middle East and North Africa

MF	Microfiltration
MPP	Maximum Power Point
MSF	Multi-Stage Flash
$MW_{(el\ /\ th)}$	Megawatt (electrical / thermal)
MW_p	Megawatt Peak
$M\&R$	Maintenance and Repair
NF	Nanofiltration
$NREL$	National Renewable Energy Laboratory
$O\&M$	Operation and Maintenance
PCM	Phase Change Material
ppm	Parts per Million
PT	Parabolic Trough
PV	Photovoltaic
PX	Pressure Exchange System
RE	Renewable Energy
$REMix-CEM$	Renewable Energy Mix – Capacity Expansion Model
RO	Reverse Osmosis
$ROSA$	Reverse Osmosis System Analysis
SAM	System Advisor Model
SF	Solar Field
$SKAL-ET\ 150$	Parabolic Trough Collector Type
$SOLEMI$	Solar Energy Mining
SW	Seawater
SWC	Seawater Composite
SWM	Spiral Wound Module

$SWRO$		Seawater Reverse Osmosis
TES		Thermal Energy Storage
$TIMES$		The Integrated MARKAL-EFOM System
$TRNSYS$		Transient Systems Simulation
UAE		Arab United Emirates
UF		Ultrafiltration
UTC		Universal Time Coordinate
$VP-1$		HTF Type
WHO		World Health Organization

Symbols

$a \dots f$	-	Relative mass flows of steam extractions
a_M	kg/s/m²/bar	Membrane constant
A	m^2	Area
AFS	ppm	Average feed salinity
Ap	m	Collector aperture
b_M	bar/%	Osmotic factor
c	€/unit	Specific cost
c_p	kJ/kg/K	Specific heat at constant pressure
$C(t)_{capital}$	Mio. €/y	Capital cost in the year t
$C(t)_{operation}$	Mio. €/y	Operating cost in the year t
C_M	-	Membrane-specific parameter
$CAPEX$	Mio. €	Capital expenditures
CF	-	Concentration factor
CPF	-	Concentration polarization factor
cr	-	Concentration ratio

CSI	-	Clear sky index
d	m	Distance
D	m	Diameter
DCA	K	Dry cooling approach
DHI	W/m²*	Diffuse horizontal irradiance (* kWh/m²/y)
DNI	W/m²*	Direct normal irradiance (* kWh/m²/y)
DoY	-	Day of the year
E_{el_y}	GWh_{el}/y	Annual electricity generation
$E_{el\_y\_des}$	GWh_{el}/y	Annual electricity consumption for desalination
ER	-	Entrainment ratio
ET	h	Equation of time
f_C	m	Focal length of the collector
FLH	h	Full load hours
g	m/s²	Gravity constant
GHI	W/m²*	Global horizontal irradiance (* kWh/m²/y)
GNI	W/m²*	Global normal irradiance (* kWh/m²/y)
GOR	-	Gain output ratio
GTI	W/m²*	Global tilted irradiance (* kWh/m²/y)
h	kJ/kg	Specific enthalpy
H	kJ	Enthalpy
I	A	Generated current
IAM	-	Incident angle modifier
ITD	K	Initial temperature difference
k	W/m²/K	Heat transfer coefficient
k_p	-	Membrane constant

k_s	-	Security factor
L	m	Length
LEC	€/kWh	Levelized electricity cost
$LMTD$	K	Logarithmic mean temperature difference
LWC	€/m³	Levelized water cost
$\dot{m}$	kg/s	Mass flow
M	kg	Mass
M_{w_y}	Mio. m³/y	Annual water production
MAF	-	Membrane ageing factor
n	-	Number of effects (MED) / Number of membranes (RO)
NTU	-	Nephelometric turbidity units
Nu	-	Nusselt number
$OPEX$	Mio. €	Operational expenditures
p	bar	Pressure
$P^*(t)$	GW	Worldwide installed capacity at the time t
P_{el}	MW	Electricity generation
PCF	-	Pressure correction factor
PR	-	Progress ratio
q	-	Specific humidity
Q	MWh	Thermal energy
$\dot{Q}$	MW	Thermal heat flow
R	-	Recovery rate
$\bar{R}$	J/kg/K	Universal gas constant

r_d	%/y	Discount rate
r_i	%/y	Interest rate
R_s	Ω	Series resistance parameter
R_p	Ω	Parallel resistance parameter
Re	-	Reynolds number
s	kJ/kg/K	Specific entropy
sA	m²/(kg/s)	Specific heat transfer area
SDI	-	Silt density index
SEC	kWh/m³	Specific electricity consumption
SM	-	Solar multiple
SPR	-	Split partial ratio
SR	-	Salt rejection
t	s	Time
t_{life}	y	Economic plant life
t_{debt}	y	Debt payback period
T	°C	Temperature
TCF	-	Temperature correction factor
TDS	ppm	Total dissolved solids
TOC	mg/l	Total organic carbon
TTD	K	Terminal temperature difference
U	V	Voltage
v	m/s	Velocity
V	m³	Volume
$\dot{W}_{turb}$	MW_{el}	Mechanical work of the steam turbine

x	m	Axial coordinate
x_s	-	Steam fraction
X	ppm	Salinity
z	m	Vertical distance

Greek

α	-	Absorptance
α_s	°	Sun elevation angle (positive if the sun is above the horizon)
α_{S_i}	-	Component-specific size scaling factor
β	°	Tracking angle
β_c	°	Collector axis tilt
γ	-	Relaxation factor
γ_c	°	Collector azimuth
γ_s	°	Solar azimuth angle
δ	°	Sun declination (positive in spring and summer)
ΔT	K	Temperature difference
ΔT_{BPE}	K	Boiling point elevation
$\Delta\pi$	bar	Osmotic pressure difference
$\Delta\Phi$	%/y	Relative mass flux change
ε	-	Emissivity
η	-	Efficiency
η_{irr}	-	Efficiency of the steam turbine stage
θ	°	Incident angle
$\theta_\perp$	°	Transversal incidence angle
θ_z	°	Zenith angle
λ	kJ/kg	Latent heat of evaporation

λ_{fr}	-	Darcy-Weisbach friction factor
ν	m^3/kg	Specific volume
ξ	-	Pressure loss factor
ρ	kg/m^3	Density
ρ_{refl}	-	Mirror average reflectivity
ρ_{ground}	-	Ground reflectivity
ρ_t	°	Tracking angle
σ	$W/m^2/K^4$	Stefan-Boltzmann constant
τ	-	Transmittance
φ	°	Geographic longitude (positive eastern from ref. meridian)
ϕ	°	Geographic latitude (positive in the northern hemisphere)
ω	°	Hour angle (negative in the morning)

Subscripts

0	Initial
abs	Absorber
amb	Ambient
avg	Average
b	Brine
BP	Booster pump
c	Concentrate
$chem$	Chemical
$coll$	Collector
$cond$	Condensation
$conv$	Convection
CT	Cold tank

cw	Cooling water
d	Distillate
d_{Flash}	Distillate produced by flashing
DES	Desalination plant
e	External
el	Electrical
eq	Equilibrium
ev	Evaporation / Evaporator
e_v	Entrained vapor
f	Feed water
fl	Fluid
gen	Generator
geo	Geometrical
$glass$	Glass envelope
HC	High concentration
ht	Heat transfer
HT	Hot tank
i	Internal / component counter
in	Inlet
inc	Incident
LC	Low concentration
m	Motive steam
M	Membrane
opt	Optical
out	Outlet
p	Permeate

PP	Power plant
$pers$	Personnel
ph	Pre-heating
rad	Radiative
rec	Receiver
RH	Re-heating
s	Steam
sf	Solar field
SG	Steam generator
$shad$	Shading
sw	Seawater
th	Thermal
$turb$	Turbine
v	Vapor
w	Water

Abstract

Several studies carried out at DLR such as [AQUA-CSP 2007], [MED-CSD 2010] and [MENAWATER 2011] have shown that the current water supply of several countries of the Middle East and North Africa (MENA) relies to a large extent on fossil groundwater extractions. Such extractions are characterized by continuously increasing energetic and economic efforts, which causes depletion of precious water resources and negative impact on the environment. The gap between water resources and water demand is likely to be sharpened by global changes such as population and economic growth and climate change. However, a series of technical approaches exist in order to mitigate water scarcity. Amongst others, water supply can be increased by means of unconventional solutions such as seawater desalination. Thereby, eventual negative impacts of such plants on local marine life can be minimized by means of targeted measures, while large part of the greenhouse gases emissions can be avoided by the introduction of renewable energy technologies such as concentrating solar power (CSP), photovoltaic (PV) and wind power.

The main objective of this dissertation is the development of a flexible model for the integrated techno-economic assessment of seawater desalination plants using renewable energy. A number of simulation models have already been implemented for the design and the simulation of renewable plants or desalination units. However, so far no established tool exists for the simulation of such integrated systems. The simulation tool INSEL has been selected for the analysis. This commercially available tool combines a modular structure with simple handling and low computational effort. The core of the present doctoral thesis consists in the extension of the currently available INSEL library with new models for a number of desalination technologies, i.e. multi-effect distillation (MED) and reverse osmosis (RO) as well as CSP components such as solar field, thermal energy storage and power block.

One of the focuses of this work has been the techno-economic evaluation and comparison of MED and RO plants. In the last few years RO has gained a dominant position in the global desalination market. This success is due to low capital cost, significant improvements in membranes (salt rejection rate, life time) and reduction of specific energy consumption. The optimal recovery ratio of RO plants, i.e. the ratio between produced drinking water and feed water, results from a compromise between minimization of investment cost, energy consumption and risk of membrane fouling. Feed water pre-treatment represents a challenging issue for RO plants. MED is characterized by relatively high investment cost, which also depends to a large extent on metal price, higher water consumption than RO but less demanding feed water pre-treatment. Heat cost for MED is a function of power supply technology, fossil fuel price and heating steam pressure. The optimal number of stages in a MED plant results from a trade-off between minimization of thermal energy requirements and maximization of plant efficiency. Due to the high temperature of the heating steam, thermal vapor compression (MED-TVC) is attractive only in the case low-cost heat is available (e.g. waste heat, low fuel cost).

The INSEL library has been further extended by a number of CSP components, which include parabolic trough, linear Fresnel and central receiver. The solar field models base on a steady-state thermal energy balance between incoming radiation, geometrical and optical losses, heat gains of the heat transfer fluid (HTF) and heat losses to the environment. The model takes into account layout and losses of the HTF system. In addition, transient effects are considered by means of a simplified approach. This is an important improvement which is not considered by the majority of the existing system analysis simulation tools. A two-tank molten salt storage has been selected as reference thermal energy storage, while the power block consists of a detailed thermodynamic model of a conventional Rankine cycle. Inlet steam quality, number and pressure level of steam extractions, and type of cooling (once-through, evaporative, dry) can be flexibly adapted. The INSEL CSP models have been developed with information from the DLR groups of the Institute of Solar Research and of the Department of Thermal Process Technology.

A potential application of the implemented INSEL models is shown in a final case study, which assesses the feasibility of combined power and water production plants. The analysis has been carried out for Marsa Alam, a remote touristic location in the South-East of Egypt. The governorate of Marsa Alam is not connected to the national networks, which makes it attractive for the development of renewable desalination plants. Under these assumptions RO provides slightly lower water production cost than MED; however, due to its robustness and simplicity of operation, MED could still be a competitive option wherever feed water pre-treatment is particularly challenging and RO plants would be prone to frequent fouling problems (e.g. Arabian Gulf). The molten-salt-based central receiver with a 14-16 hours thermal storage performs lowest levelized electricity cost among the analyzed CSP configurations.

Analysis of multi-purpose plants has been performed as a function of local requirements (electricity, water), available resources (solar irradiation, wind speed, air temperature, water quality) and techno-economic parameters (plant configuration, investment and operation cost, back-up fuel cost etc.) by means of annual yield simulations with hourly time steps. Different plant configurations need to be compared based on common boundary conditions. This implies e.g. that the same demand curves (i.e. electricity and water) have to be covered by all analyzed configurations, which allows also considering external costs such as the impact of fluctuating renewable power on fossil power plants´ performance. One of the main findings is that moving in due time towards an electricity supply system based on a mix of renewable and conventional technologies is not only convenient in the case of high fossil fuel price, but it also includes strategic advantages such as the reduction of the dependence on scarce resources and the stability of the supply cost. A cost-optimal power park consists of a mix of all available renewable technologies and fossil backup. Thereby, electricity generation by relatively cheap but variable renewable power plants is balanced by slightly more expensive power generation on-demand, which is provided by CSP.

Kurzfassung

Verschiedene Studien des DLR wie [AQUA-CSP 2007], [MED-CSD 2010] und [MENAWATER 2011] haben gezeigt, dass die Wasserversorgung in einigen Ländern des Nahen Osten und Nordafrikas (MENA, Middle East and North Africa) weitgehend auf fossile Grundwasserreserven angewiesen ist. Der energetisch und wirtschaftlich zu erbringende Aufwand zur Nutzung dieser Ressource ist in den letzten Jahren stetig gestiegen und mit negativen Umweltfolgen und der Verringerung der Trinkwasserqualität verbunden. Darüber hinaus, wird das Problem der Wasserknappheit voraussichtlich aufgrund von globalen Veränderungen wie z.B. dem Bevölkerungs- und Wirtschaftswachstum und dem Klimawandel zusätzlich verschärft. Diesen Entwicklungen stehen nicht-konventionelle Maßnahmen wie die Meerwasserentsalzung gegenüber, die eine wichtige zusätzliche Option für die Wasserversorgung darstellt. Hierbei kann der negative Einfluss von Entsalzungsanlagen auf die Umwelt mit gezielten Maßnahmen minimiert werden. Beispielweise ermöglicht der Einsatz von erneuerbaren Energien wie z.B. solarthermische Kraftwerke (CSP, concentrating solar power), Photovoltaik (PV) und Windkraft einen großen Teil der mit fossiler Energieerzeugung verbundenen Treibhausgasemissionen zu vermeiden.

Der Fokus der vorliegenden Arbeit liegt auf der Entwicklung eines flexiblen Modells für die integrierte technische und wirtschaftliche Bewertung von Meerwasserentsalzungsanlagen, deren Energieversorgung auf erneuerbaren Energien basiert. Für die Auslegung und Simulation von erneuerbaren Kraftwerken und Entsalzungsanlagen stehen bereits einige Modelle zur Verfügung, jedoch erlaubt keines dieser Modelle die integrierte Simulation solcher Systeme.

Die Simulationsumgebung INSEL wurde für die Analysen dieser Arbeit ausgewählt. Diese kommerziell verfügbare Simulationsumgebung kombiniert einen modularen Aufbau mit einer einfachen Bedienung sowie einem geringen Rechenaufwand. Im Rahmen der vorliegenden Doktorarbeit wurden neue technische Modelle für die CSP-Komponenten Solarfeld, thermischen Energiespeicher und Kraftwerksblock sowie für die Entsalzungs-technologien Umkehrosmose (RO, reverse osmosis,) und Mehreffekt-Verdampfung (MED, multi-effect distillation) entwickelt.

In der vorliegenden Arbeit liegt ein Schwerpunkt in der Untersuchung und dem Vergleich der Wirtschaftlichkeit der Technologien MED und RO. Während der letzten Jahre hat RO eine beherrschende Stellung auf dem Weltmarkt eingenommen. Niedrige Kapitalkosten, deutliche Verbesserung der Salzrückweisungsrate sowie der Lebensdauer der Membrane und Senkung des Energieverbrauchs zählen zu den wichtigsten Gründen dieses Erfolgs. Die optimale Rückgewinnungsrate, d.h. das Verhältnis zwischen gewonnenem Trinkwasser und verwendetem Meerwasser, ergibt sich aus einem Kompromiss zwischen Minimierung von Kapitalkosten, Energieverbrauch und „fouling“-Risiko der Membranen. Bei RO ist die Vorbehandlung des Meerwassers für den einwandfreien Betrieb der Anlage von großer Bedeutung. Im Gegensatz zu RO ist die Meerwasservorbehandlung bei MED weniger

anspruchsvoll, jedoch ist diese Technologie durch höhere Kapitalkosten, die weitgehend von den aktuellen Metallpreisen abhängen, und höheren Meerwasserverbrauch im Vergleich zu RO charakterisiert. Die Wärmekosten von MED hängen von der ausgewählten Technologie für die Energieversorgung, vom fossilen Brennstoffpreis sowie vom Druck des Heizdampfes ab. Die optimale Anzahl an Verdampfungsstufen ergibt sich aus einem Kompromiss zwischen Minimierung des thermischen Energiebedarfs und Maximierung der Effizienz der Anlage. Aufgrund der höheren Temperatur des Heizdampfes ist MED mit thermischer Dampfkompression (MED-TVC, thermal vapor compression) nur vorteilhaft, sofern kostengünstige Wärme zur Verfügung steht, z.B. Abwärme und niedrige Brennstoffkosten.

Die INSEL-Modellbibliothek wurde im Rahmen der vorliegenden Arbeit um verschiedene solarthermische Kraftwerktechnologien erweitert (Parabolrinne, Fresnel und Solarturm). Die Modelle des Solarfeldes basieren auf einer stationären Wärmebilanz zwischen eintreffender Solarstrahlung, geometrischen und optischen Verlusten, Wärmeeintrag in das Wärmeträgerfluid (HTF, heat transfer fluid) und Wärmeverlusten an die Umgebung. Das Layout sowie die Verluste des HTF-Leitungssystems und der Einfluss von transienten Effekten wurden berücksichtigt. Letztere werden lediglich rudimentär von den bisher existierenden systemanalytischen Simulationsmodellen berücksichtigt. Die Implementierung dieses Vorgangs in INSEL stellt daher einen wichtigen Beitrag zur Erweiterung von systemanalytischen Simulationsmodellen dar. Die ausgewählte Referenztechnologie für den thermischen Speicher ist ein zwei-Tank System, in dem flüssiges Salz gespeichert wird. Der Kraftwerksblock besteht aus einem konventionellen Rankine-Prozess. Ein detailliertes Modell der Dampfturbine erlaubt die flexible Anpassung wichtiger Parameter, wie z.B. Temperatur und Druck des Einlassdampfes, Anzahl und Druck der Dampfanzapfungen und Art der Kühlung, bei der zwischen Durchlauf-, Verdampfung- und Trockenkühlung unterschieden wird. Die CSP-Modelle sind in Zusammenarbeit mit dem Institut für Solarforschung und der Abteilung für thermische Prozesstechnik des DLR entwickelt worden.

Eine Fallstudie zeigt schließlich auf, welche Möglichkeiten sich aus der Entwicklung der neuen INSEL-Modelle ergeben. Der Fokus der Fallstudie liegt in der Untersuchung der Machbarkeit von kombinierten Anlagen für die Produktion von Strom und Wasser. Die Analyse wird für den ägyptischen Standort Marsa Alam durchgeführt. Der dortige Verwaltungsbezirk ist nicht mit den nationalen Versorgungsnetzen verbunden, so dass dieser Standort besonders attraktiv für die Entwicklung von erneuerbaren Entsalzungsanlagen ist. Unter diesen Annahmen liefert die Umkehrosmose leicht niedrigere Wassergestehungs-kosten als MED. Gleichwohl stellt MED aufgrund ihres einfachen und robusten Betriebs weiterhin eine wettbewerbsfähige Option dar, insbesondere bei niedriger Meerwasserqualität, die das „fouling“-Risiko in RO-Anlagen erhöht (z.B. Arabischer Golf). Aus den durchgeführten Vergleichsstudien von verschiedenen CSP-Technologien resultiert, dass der flüssigsalz-basierte Solarturm mit 14-16 Volllaststunden Speicherkapazität die niedrigsten Stromgestehungskosten liefert.

Die Analyse kombinierter Anlagen für die Produktion von Strom und Wasser wird als Funktion von lokalen Anforderungen (Strom- und Wasserbedarfsganglinien), verfügbaren Ressourcen (Sonneneinstrahlung, Windgeschwindigkeit, Lufttemperatur, Wasserqualität) und technisch-ökonomischen Parametern (Anlagenkonfiguration, Investitions- und Betriebskosten sowie Brennstoffkosten) durch Jahressimulationen auf stündlicher Basis durchgeführt. Unterschiedliche Anlagenkonfigurationen sollten unter gleichen Rahmenbedingungen (d.h. gleiche Nachfragekurven für Strom und Wasser) verglichen werden. Externe Kosten, wie z.B. der Einfluss von fluktuierenden erneuerbaren Kraftwerken auf bestehende fossile Kraftwerke, können dadurch berücksichtigt werden. Das Ergebnis der Arbeit zeigt, dass der rechtzeitige Wechsel zu einem Energiemix bestehend aus erneuerbaren und fossilen Energien nicht nur im Falle hoher fossiler Brennstoffkosten günstig ist. Eine solche Transformation führt zur Verringerung der Abhängigkeit von knappen Ressourcen und zu einer nachhaltigen Stabilisierung der Versorgungskosten. Der kostenoptimale Kraftwerkspark besteht aus einem Mix aus allen verfügbaren erneuerbaren Technologien. Dabei wird die Stromproduktion aus günstigen fluktuierenden erneuerbaren Kraftwerken von der bedarfsgerechten Stromversorgung aus CSP Kraftwerken ergänzt.

1 Introduction

1.1 Motivation

The countries of MENA are particularly affected by water scarcity. Climatic conditions are mainly characterized by modest rainfall, with few exceptions [FutureWater 2011]. Annual precipitation typically is around 50 mm/y, while large parts of Egypt and Libya practically do not have precipitation at all. As a result, 16 MENA countries out of a total of 21 countries already face water stress [AQUA-CSP 2007] [AQUASTAT], i.e. the per-capita available water resources are below 1,000 m³/y. The lowest water availability subsists in the countries of the Arabian Peninsula: Saudi Arabia, Qatar, UAE and Kuwait.

Although most of the MENA countries dispose over large fossil water reserves (i.e. aquifers with low or very low replenishment rates), their extraction is characterized by continuously increasing energetic and economic efforts, causing depletion of water quality and negative impact on the environment. A possible scenario for the water supply of MENA is presented in Figure 1 [MENAWATER 2011]. The considered time period is between 2000 and 2050.

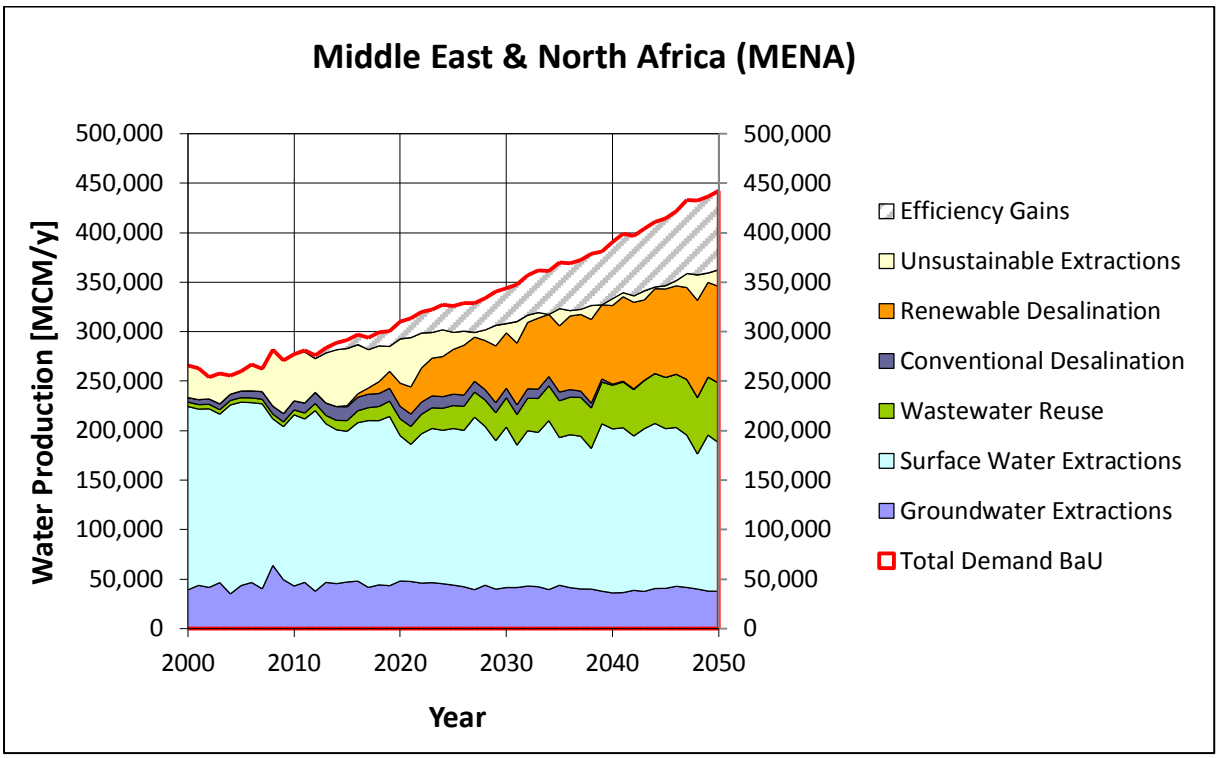

Figure 1: Water Supply Scenario for the MENA Region [MENAWATER 2011]; BaU = Business as Usual; MCM = Mio. m³

Water demand increments by a factor of almost 2 within the considered 50 years, while renewable water resources (rainfall, surface water and groundwater including inflows) reduce over time by approx. 20 % due to the impact of climate change [FutureWater 2011]. Such impact will be very region-dependent and cannot be fully appreciated on aggregated level; rainfall reduction in the considered time frame may locally rise up to 40 %.

The main outcome of the scenario is that a dramatically increasing gap opens between water demand and water supply. For the reasons explained above, the missing portion of the supply should not primarily rely on overexploitation of groundwater resources. Rather, a set of countermeasures should be taken into account as soon as possible. Such measures aim either at the reduction of demand or the increase of supply. The first group includes restoration of aged water distribution systems in order to reduce leakages, introduction of water saving technologies in irrigation such as drip systems and precision sprinklers, use of water non-intensive crops ("more crop per drop") and eventual replacement of irrigated areas by food imports. In addition, water supply can be increased by means of conventional and unconventional solutions. Among them count the realization of reservoir basins, waste water reuse and desalination plants. Each of these measures is taken into account in the scenario shown in Figure 1.

The mentioned solutions are characterized by a specific cost and eventually limited potentials. A mix of measures -rather than a single one- will be required to guarantee sustainable water supply. Thereby, desalination plants should be introduced as the option of last resort. The reason is that such plants are relatively expensive and cause a series of environmental impacts. The most important of them are greenhouse gas emissions due to rising energy consumption and local effects of water intake and discharge on local marine life [Lattemann 2008]. Such plants are regarded as proven and have already found large application in the MENA countries within the last decades. Currently, over 60% of the world desalination capacity is installed in this region. According to the presented scenario, desalination will gain a primary role in the water supply of several MENA countries. However, concerns exist about environmental impacts as well as about increasing energy cost due to limited fossil fuels resources.

This calls for the introduction of renewable energy technologies as a primary source for new desalination plants. The excellent solar potentials available in the MENA region can be deployed by means of solar technologies such as CSP and PV. Wind power is also available. Despite the large potentials, desalination powered by renewable energy is still not widely applied. Its development is limited to pilot plants and small units located in remote areas (Annex 10.1.6).

The feasibility of utility-scale renewable desalination plants needs to be analyzed by means of suited techno-economic models. A number of simulation models have already been implemented for the design and the simulation of renewable plants or desalination units. However, so far no established tool exists for the simulation of such integrated systems. Existing tools can be roughly divided in two groups, i.e. detailed thermodynamic programs and simplified system analysis tools. Detailed thermodynamic programs allow for flexible simulation of a large set of configurations, but are rather unsuitable for the quick realization of an elevated number of parametric studies. System analysis tools are well suited for simplified analysis due to their simplicity, but are inflexible.

These considerations lead to the conclusion that the right simulation program for the analysis of renewable desalination should be a compromise solution, which combines the advantages of both thermodynamic programs and system analysis tools. The development of such a model has been the main objective of this dissertation.

At the same time, the development of such a tool represents an important milestone for the DLR Department of System Analysis. The tool allows creating a bridge between the simplified optimization models used in this Department and the complex models of other DLR groups such as the Institute of Solar Research and the Department of Thermal Process Technology.

The utilization of this tool may be extended to a number of new applications: the integration between the implemented model and system optimization models like REMix (2.1), TIMES etc. will be beneficial for these tools in terms of reliability and quality of results. Finally, the implemented tool can be seen as the required preparatory step for more in-depth analysis of current and -in perspective- new research issues such as analysis of zero emission desalination plants, optimized dry cooling of CSP plants and concepts for the production of liquid synthetic solar fuels.

1.2 Structure of the Work

The main objective of this dissertation is the development of a flexible model for the integrated techno-economic assessment of desalination plants using renewable energy. The analyses consider local requirements (electricity, water), available resources (solar irradiation, wind speed, air temperature, seawater quality) as well as economic parameters (investment cost, back-up fuel cost, material cost etc.). The work is structured as follows (Figure 2):

1. The first chapter introduces the topic of water scarcity, with particular focus on the MENA region, and describes the motivation of this work. It is highlighted that the large potential of renewable energy sources in those countries should be used as a primary energy source for new desalination plants.
2. Renewable desalination still is a research topic: innovative solutions need to be analyzed by means of suited techno-economic models. After the screening of available simulation tools for the analysis of renewable desalination systems (2.1), it turned out that INSEL is the adapted software for such purposes. The key features of INSEL are exposed with focus on the own developments (blocks and systems).
3. The core of this work has been the setup of new technical models for several CSP components and desalination technologies in INSEL. The details of the implemented technical models are presented in the chapters 3 to 6. Desalination processes are described in chapter 3. Two desalination technologies, i.e. MED with and without thermal vapor compression and RO, have been identified as the most promising options for the coupling with renewable energies. The mathematical formulation of the technical performance models of MED and RO is reported in 3.1 and 3.2,

respectively. Desalination plants consist of more than the separation process itself. For each of the considered desalination technologies following plant components have been considered: water intake and feed water pre-treatment, product water post-treatment and brine discharge.

4. CSP is illustrated in chapter 4. This technology consists of three main components, i.e. solar collectors, thermal energy storage and power block. Solar collectors are divided into line focusing systems (parabolic trough and linear Fresnel) and point focusing systems (solar tower or central receiver). Each of these technologies is described in a dedicated section (4.2 - 4.4). In each case, insight is given into specific geometrical and optical efficiency, heat balances on receivers, plant layout and losses in the piping system. In addition, transient effects are considered by means of a simplified approach (4.2.4). Also, the impact of different heat transfer fluids (i.e. thermal oil, molten salt and water/steam) is considered in the models (4.2.5 and 4.2.6). The two-tank molten salt storage has been selected as the reference thermal energy storage technology (4.5). Finally, the power block model consists of a detailed thermodynamic model (4.6). Several cooling technologies such as evaporative cooling and dry cooling are considered.
5. Chapter 5 briefly describes the setup of the PV models. Such components are available in the commercial INSEL library. Therefore, no significant own implementation is required. PV modeling focuses on commercial crystalline silicon modules. Different tracking strategies (i.e. fixed mounted, 1-axis tracking and 2-axis tracking) are considered.
6. Chapter 6 describes the setup of the wind power model. The model is based on the commercial INSEL library; no significant own implementation is required, made exception for the consideration of the impact of height on the vertical wind speed profile and the effect of temperature and atmospheric pressure on air density.
7. Key results provided by the technical models are used as inputs in the economic model (chapter 7). This model mainly consists in the evaluation of the considered plants' investment cost and operation cost. The calculation of levelized electricity cost (LEC) and levelized water cost (LWC) are common means for the comparison of different power plants over their operation life. The calculation procedure for the assessment of such economic metrics is exposed in 7.1 and 7.2, respectively. In addition, the cost of the total supply (i.e. average annual cost for power and water supply) turned out to be a relevant objective function for the evaluation of multi-purpose systems (7.3).

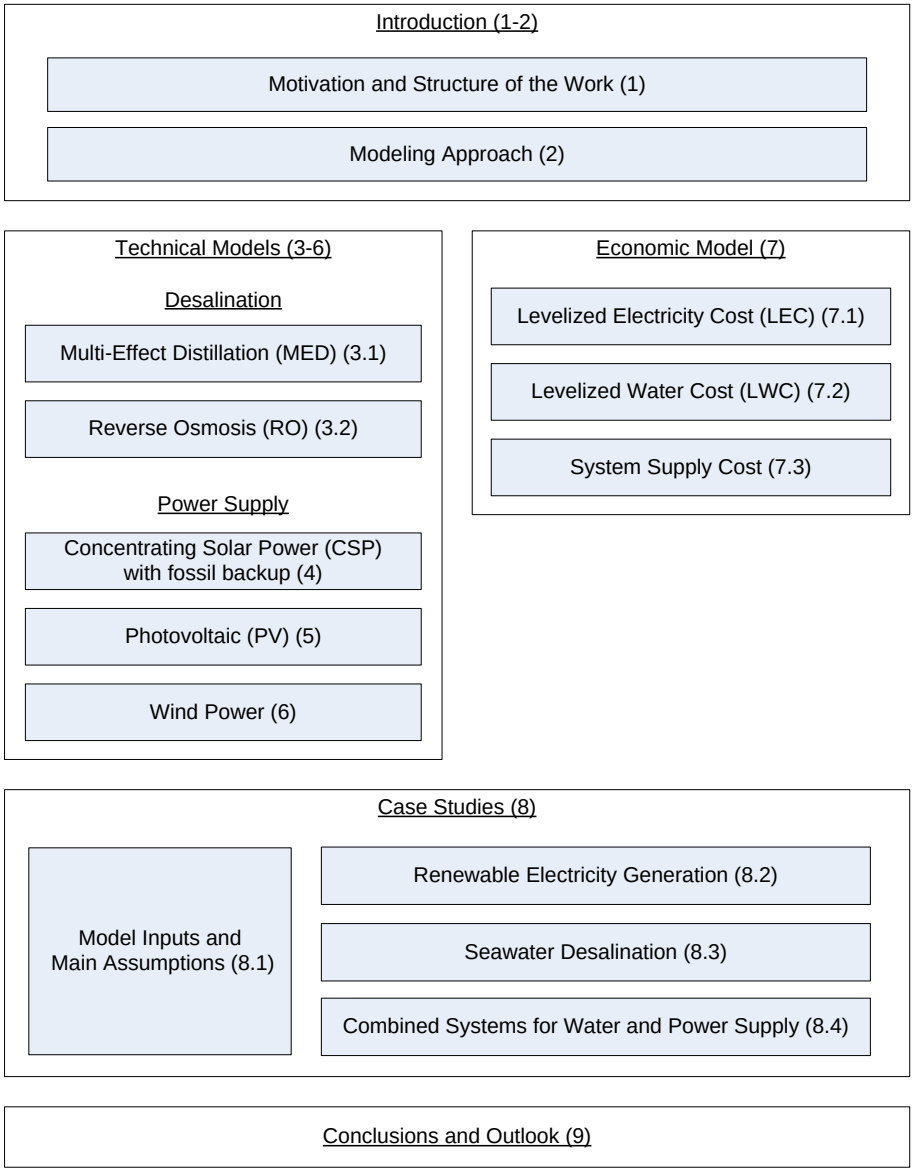

Figure 2: Schematic overview of the work structure

8. The potentiality of the implemented techno-economic model is exemplarily shown in a number of case studies (chapter 8). The case studies are structured in three parts: the first two analyze in detail the performance of each renewable technology and each desalination technology as standalone application, respectively. Where possible, a selection of best performing technologies has been carried out. Based on these findings, the third and last section analyzes combined systems for the supply of power and water. More precisely, the first part of the case study (8.2) gives insight into renewable power plants, with particular focus on CSP. Advantages and disadvantages of each CSP technology are discussed. Thus, the impact of geometrical and thermal efficiency as well as of plant layout on the results is highlighted. Concerning PV, different tracking systems are compared. Finally, the impact of year-by-year variations of solar and wind resources on plants´ annual yields is presented. A detailed characterization of desalination plants is performed within the second part of the case study (8.3). The flexibility of the developed models allows the analysis of a

large number of layouts. Concerning MED, parametric studies are carried out on the number of stages and on the pressure of the heating steam (including thermal vapor compression). The effect of economic parameters such as intake cost, material cost and heat cost on LWC is also assessed. It has been shown that the economics and the energy consumptions of RO are mainly affected by the type of pre-treatment, the temperature and the salinity of the feed water as well as by the design recovery ratio. Section 8.4 provides the analysis of combined electricity and water supply systems. Several scenarios take into account the impact of capital cost of renewable energy plants as well as the impact of the fossil fuel price. Optimal configurations have been identified as a function of the "renewable share" (i.e. the percentage of the annual load covered by renewable energy plants). Further, the total cost of supply (capital and operation cost for electricity and water supply) are calculated for selected configurations.

9. Finally, chapter 9 summarizes the main findings of the study and gives some indication on possible future research issues and further potential applications of INSEL.

2 Modeling Approach

2.1 Review of Existing Simulation Tools

The use of renewable energy technologies such as photovoltaic, concentrating solar power and wind power contributes producing clean power for desalination plants, thus reducing their environmental impact. The combination of renewable energy plants and desalination plants is perceived as very important by the scientific community as well as by local and international institutions. As a result, a large number of studies, projects and mainly small-scale demonstration plants have appeared in the last years. Several European research centers are involved in the development of such systems. Among them are CIEMAT-Plataforma Solar de Almería, Canary Islands Institute of Technology, Fraunhofer Institute for Solar Energy, DLR and many others. A comprehensive survey of the concepts proposed by these institutions can be found in [Cipollina 2009]. Several simulation tools have been developed for the design, simulation and optimization of renewable desalination systems. Such models can be roughly divided into three groups: special-purpose tools, system analysis tools and detailed design tools.

The first group consists of programs which have been specially created in order to analyze the performance of a particular process or a limited number of configurations. A large number of research papers and studies are based on this type of tools [Nafey 2010] [Palenzuela 2011]. Such programs generally are straightforward, while they exhibit different degrees of detail. A further common feature of such tools is their rigidity, i.e. the difficulty of adaptation of the model for purposes other than the original one. System analysis tools allow simulation and analysis of a wider range of renewable energy technologies. Some of

them are developed by research centers or universities and made available free of charge. Others are commercial tools; the price for a single academic license varies between approximately 1,000 € and 4,000 €. The best known system analysis tools are SAM, developed by NREL (National Renewable Energy Laboratory) [SAM], and Greenius, which is implemented by DLR and the Berlin University of Applied Sciences [Greenius]. Among the implemented options are a number of pre-defined configurations with focus on state-of-the-art renewable energy (RE) plants (e.g. parabolic trough CSP plants, fix-mounted crystalline PV modules, standard wind turbines) (Table 1).

Main Application	**System Analysis Simulation Tools**				**Thermodynamic Cycle Simulation Tools**	
Name	**SAM**	**INSEL**	**TRNSYS**	**Greenius**	**EBSILON Professional**	**IPSEpro**
Original Purpose	System analysis of RE systems	System analysis of RE systems	Evaluation of solar systems for heating and cooling	System analysis of CSP systems	Engineering of conventional power cycles	Engineering of conventional power cycles
Developed by	NREL (based on TRNSYS)	doppelintegral	University of Wisconsin	DLR	Steag/DLR	SimTech Simulation Technology
Annual Simulations (Time Resolution)	y (hourly)	y (variable)	y (variable)	y (hourly)	y (mainly for design, hourly)	y (mainly for design, hourly)
User-required Know-how	Low/medium	Low/medium	Medium	Low	High	High
Simulation Effort	Low	Low	Low	Low	Very high	Very high
User Programming Language	SamUL	FORTRAN, C, (MATLAB)	FORTRAN	Not implemented	EbsScript	Own developments possible
Models´ Documentation	Partial	Partial	Open source	Medium	Good	
Available Modules						
PV	y	y (various types)	y	y	n	n
Wind	y	y (various types)	y	n	n	n
CSP	y (various types)	(y) (various types)	y	y	y (various types)	y (various types)
Other RE Systems	Geothermal, Biomass	Solar collectors, Buildings	Solar collectors, Buildings	n	n	n
Energy Storage	Thermal	Thermal (molten salt, concrete), electrical	Thermal	Thermal	Thermal (molten salt)	Thermal (molten salt)
Desalination	n	(y) (MED/TVC /RO)	n	n	n	y - MED/TVC /RO/MSF
Economics	y	n	n	y	n	y

Table 1: Selection of available simulation tools [Arribas 2011], [Ho 2008], [Bognar 2012], [Mason 2011]; MSF = multi-stage flash; (y) = models under development

These features make such tools adapted for preliminary analysis and a quick generation of results. Simplified economic analysis is also available. The required user know-how is low and the time for a single run typically is a few seconds. However, only a limited number of

design parameters can be adapted by the user. Neither the setting up of models for tailor-made simulations nor the integration of self-programmed components is possible. In addition, desalination technologies are not included or are currently under development [Casimiro 2013]. In comparison to SAM and Greenius, TRNSYS [TRNSYS] and INSEL [INSEL] allow the user to program their own models and to integrate them into the user interface. Simulation of desalination processes typically has to be performed with separate tools such as DEEP [DEEP], implemented by the International Atomic Energy Agency or specific programs such as ROSA [ROSA], provided by the desalination company Dow Water. The system analysis tools also include models such as REMix and TIMES. In particular, REMix (Renewable Energy Mix) is an energy system model which has been developed since 2005 by the DLR department of System Analysis and Technology Assessment [Scholz 2012]. The main focus of the tool lies on the analysis of the introduction of renewable energy technologies in existing or future power supply systems. The objective function is the minimization of investment and operational expenditures of the power supply in a selected region and for a given time span (typically one year). In contrast to other system analysis tools such as INSEL or TRNSYS, which are mainly used for the relatively detailed technology assessment of integrated systems on plant level and of rather small power supply systems (e.g. a city), REMix is typically used for the optimization of power plant fleets on national as well as international level.

The last tool category is represented by design programs such as EBSILON Professional [EBSILON], IPSEpro [IPSEpro] and Thermoflow [Thermoflow]. They are commercial tools developed by specialized companies. These tools were originally developed for detailed analysis of heat balances in conventional power systems. In recent years, additional packages for the simulation of concentrating solar power and thermal desalination have been implemented. Other renewable technologies and reverse osmosis have not been considered so far. Such tools are very flexible and well-suited to simulate a wide range of specific problems. However, the utilization of these tools requires a high degree of know-how. The set-up of all required parameters is related to a high degree of effort and the time required for a single calculation is typically two orders of magnitude higher than in system analysis tools. The large degree of flexibility may also increase the risk of inconsistent calculations or software crashes.

This survey highlighted that no established tool exists for the integrated simulation of renewable desalination systems. Each of the previously described softwares is characterized by advantages and disadvantages: system analysis tools are well suited for simplified analysis due to their simplicity, but are inflexible. Detailed thermodynamic programs allow for flexible simulation of a large set of configurations, but are rather unsuitable for quick realization of an elevated number of parametric studies. In addition, their high complexity level is not necessarily required for the purpose of this dissertation. These considerations lead to the conclusion that the right tool for the analysis of renewable desalination is a “compromise tool”, which combines the advantages of both described software types. After

screening of a number of available programs, INSEL was selected as the best option for the analysis at hand. Further details on specific features of INSEL as well as an overview on the modeling approach are presented in the next section.

2.2 The INSEL Software

Technical analysis is performed with the tool INSEL (Integrated Simulation Environment Language). The tool has started being developed more than 20 years ago at the Oldenburg University and is currently being developed at the University of Applied Sciences in Stuttgart. The software is commercially distributed by the company doppelintegral GmbH, Stuttgart. INSEL is a graphical programming language to design, monitor and visualize renewable and conventional energy systems.

2.2.1 INSEL Blocks

INSEL is based on graphical symbols called "blocks". They may represent any type of mathematical functions (e.g. simple mathematical operations, the thermal energy storage of a CSP plant, or a complete multi-purpose plant…). Each block is characterized by one or more independent variables or "inputs", a number of constants called "block parameters" and one or several "outputs". Figure 3 shows a newly developed simple INSEL block, i.e. the sun position calculation block. The other newly implemented blocks have been set up according to the same principle. The sun position calculation block requires the definition of a number of block parameters by the user, i.e. geographic coordinates of the analyzed site (latitude and longitude) as well as time coordinates. The INSEL user can select different time steps for the calculation, the time coordinates system (either universal time coordinate (UTC) or local time) and the respective time zone. This last parameter is only relevant in the case local time has been selected.

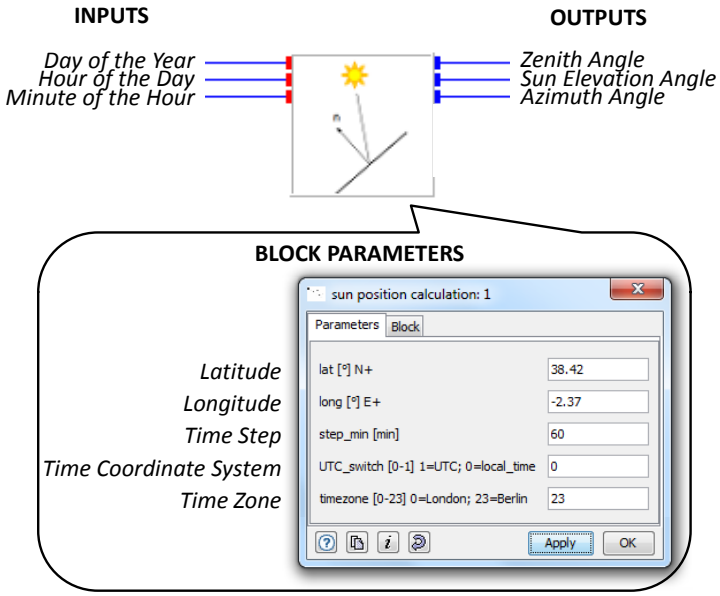

Figure 3: Screenshot and description of the sun position calculation INSEL block (Note: basic version only; extended version includes more output parameters)

The input values include information on the current time, i.e. the day of the year, the hour of the day and the minute of the hour. Such input values may be single values or a series of values. Due to the fact that renewable resources such as solar irradiance and wind speed are characterized by daily and seasonal variations, proper analysis of renewable technologies bases on annual yield simulations with hourly time steps. In principle, even higher time resolution could be used. However, such detailed meteorological data are not available in most cases. The models are fed with new inputs at each hour of the year, i.e. 8,760 steps per year are required. The key outputs of the sun position calculation block are the angles which allow the definition of the sun position at a certain time, i.e. sun elevation, azimuth and zenith angles.

2.2.2 INSEL Systems

Programming in INSEL basically consists of graphical symbols' interconnection. Single blocks are typically connected through simple mouse operations. A set of fundamental pre-defined blocks is provided within dynamic link libraries. Such libraries can be accessed by mouse click from the model palette on the left side of the user-interface (Figure 4).

Among these blocks are: time blocks (used for date and time handling), "read" and "write" functions from and to different types of file formats, as well as mathematical operations and statistics. Besides, a series of power equipment models are available in the current INSEL version: a large number of commercial PV modules and inverters, batteries, low-temperature solar thermal collectors, storage tanks and wind turbines. A simulation library for buildings is also under development [INSEL]. In addition, users have the possibility to implement own models and integrate them in INSEL. Different languages such as FORTRAN and C can be used for this purpose. The newly developed blocks can be seen in Figure 4 within the box below the commercial library. Figure 4 also shows exemplarily the setup of a typical CSP central receiver power plant in INSEL. The time block on the left part of the figure serves for time handling: herein the user can define the start and end time of the simulation. The site coordinates are defined in the sun calculation block. The hourly inputs such as meteorological data and demand data (electricity and water) are read from an input data file. Finally, the CSP power plant consists of three main blocks, i.e. heliostat field, thermal energy storage and steam turbine. A number of design parameters have to be defined such as steam turbine capacity, solar field size, storage capacity etc. A summary of the key inputs, block parameters and outputs of each developed INSEL system is presented at the end of the chapters describing the respective INSEL models:

- MED chapter 3.1.6 Figure 13
- RO chapter 3.2.6 Figure 20
- CSP chapter 4.7 Figure 37
- PV chapter 5.2 Figure 39
- Wind power chapter 6.2 Figure 41

During an annual simulation, a number of relevant output parameters for each INSEL block component is saved in an output file (a .txt file). The complete list of the output parameters is reported in Annex 10.5. The number of the outputs and their position in the output file is standardized, i.e. is independent of the analyzed configurations. This means that if a particular INSEL model do not consider all the possible options for electricity generation (CSP, PV, wind power and fossil backup power plant) and water production (MED and RO), the missing outputs are set to 0. This solution allows standardize also the Excel-tool used for economic analysis.

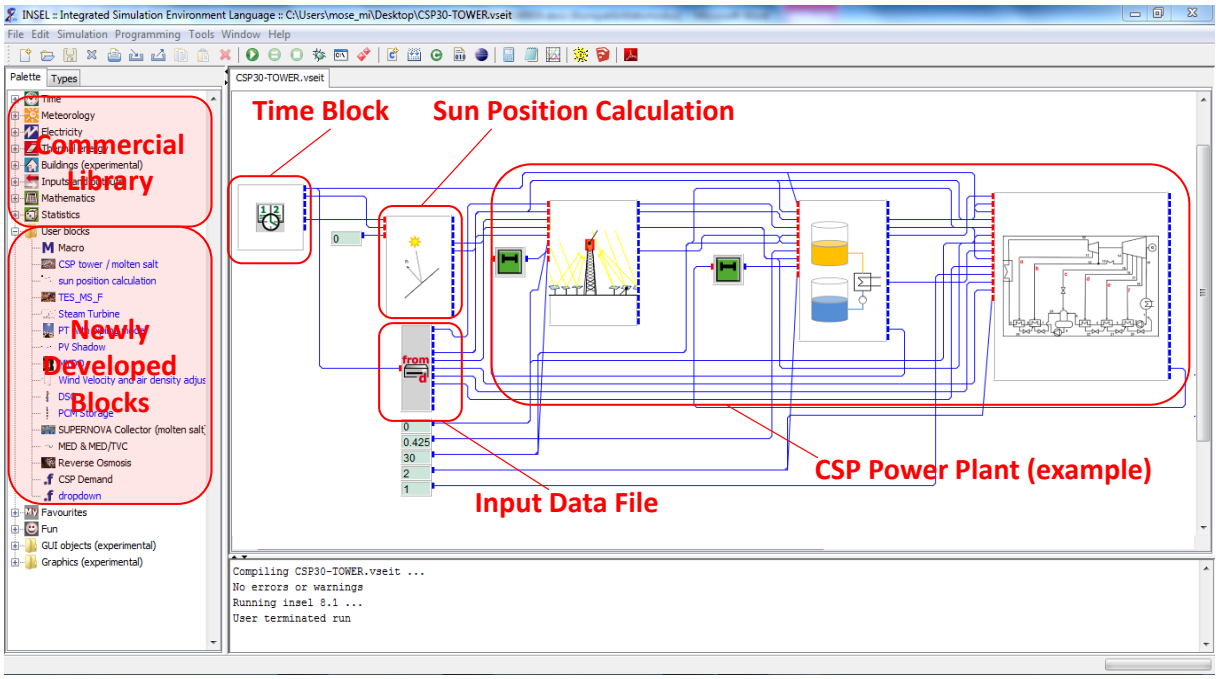

Figure 4: INSEL screenshot and general procedure of an annual yield simulation; in the sample diagram: CSP central receiver power plant

Finally, sensitivity analyses on technical parameters (e.g. solar field size, capacity of the thermal storage etc.) have been performed using batch scripts programmed in python instead of using the graphical user interface. Such scripts allow automatizing repetitive procedures which would be rather time-consuming if carried out manually.

2.3 Excel-Tool for Economic Analysis

Key results provided by the INSEL models are used as inputs in the economic model (chapter 7). This model mainly consists in the evaluation of the considered plants' investment cost and operation cost of each plant component and of the calculation of the specific power and water production cost (Figure 5). Such tool has been developed with the commercial tool Excel. The tool is divided in three parts:

- Evaluation of the INSEL results: key technical design parameters of each plant are summarized and statistical analysis is performed on the main performance indicators. For example, monthly and annual electricity generation, water production, peak and

average efficiency of each single plant component, fossil fuel consumption, auxiliary power requirements, eventual power dumping and land use have been assessed.

- CAPEX & OPEX database: extensive literature research has been carried out in order to provide capital expenditures (CAPEX) and operational expenditures (OPEX) of different technologies for power production and seawater desalination. The results of such researches are summarized in technology-specific and configuration-specific tables.
- Economic Assessment: the two previous steps allow carrying out the final economic evaluation which aims at the calculation of levelized electricity cost (LEC) and levelized water cost (LWC) for each technology. In addition, the average annual cost of supply for power and water has been assessed. Finally, a number of sensitivity analyses are performed automatically through a simple application programmed in Visual Basic.

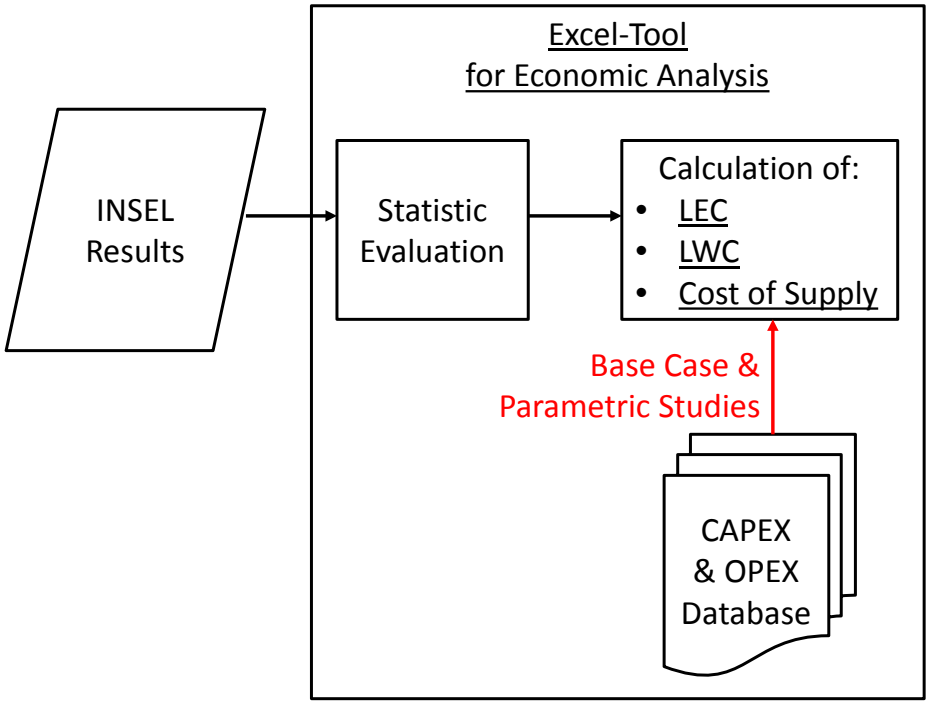

Figure 5: Scheme of the Excel-Tool for economic analysis

The tool also includes a number of diagrams in order to analyze daily and seasonal patterns of electricity generation as well as to compare the main technical and economic results of the analyzed configurations.

3 Desalination Models

Desalination refers to processes which aim to remove salts and other minerals from water. The main product is fresh water for drinking purposes and other human activities such as industrial applications, electricity generation and irrigation. Table 2 describes the working principle of some of the most important desalination technologies [Cipollina 2009].

Desal. Process	Description
MSF	Multi-stage flash (MSF) is based on flashing (i.e. water evaporation driven by sudden pressure reduction) in a number of serial-connected chambers with sequentially reducing pressure. The gain output ratio (GOR, i.e. the ratio between produced distillate flow and provided heating steam flow) of MSF plants is typically 8 - 10
MED	MED plants present a layout similar to MSF (series of evaporation chambers). However, in MED feed water is sprayed by nozzles -located on top of each chamber- to the external surface of a tube bundle. Evaporation occurs on the tubes, whereas heat is provided by condensation of steam flowing inside the tubes. The produced vapor is then used as motive steam in the successive stage. In the first effect, low pressure steam has to be externally supplied. MED plants can reach a gain output ratio of approx. 12
MED-TVC	Thermal vapor compression is based on the re-use of a portion of the produced distillate. Thereby, a part of the vapor produced in the last effect is compressed by a thermally driven steam ejector. The upgraded steam is used as motive steam in the first effect. MED-TVC processes are very efficient: the GOR can reach 16. However, the main disadvantage is that mid pressure steam is required to drive the ejector
MED-MVC	Mechanical vapor compression (MVC) systems have a design similar to TVC processes. The main difference is that in MVC all the steam produced in the last effect is mechanically compressed and used as motive steam in the first effect. MVC only make use of electrical energy
Multi-Effect Humidification	Multi-effect humidification (MEH) systems consist of chambers in which humid air circulates driven by natural convection. On one side of the chamber hot feed water is distributed on fleece surfaces. Water evaporates by convection and saturates the counter-current air flow. On the other side of the chamber, the vapor contained in the humid air condenses on the cold surface of a heat exchanger, providing at the same time some feed water pre-heating. MEH systems are typically coupled with solar collectors
Membrane Distillation	Membrane distillation (MD) couples thermal and membrane processes. Evaporation of water in MD systems occurs due to vapor partial pressure differences between a hot feed on one side and a condensate channel on the other side. The two parts are divided by hydrophobic membranes, i.e. membranes which enable the permeation of vapor only. The vapor generated in the feed side permeates through the membrane driven by pressure difference and condenses on the surface of an externally cooled channel
RO	The natural osmosis process can be inversed (thus RO, reverse osmosis) applying external pressure to a concentrated solution (e.g. seawater) and obtaining an elevated flow of almost salt-free water on the other side of a selective membrane. Water desalination by RO is based on this principle
Electro Dialysis	Electro dialysis (ED) is an electro-chemical process. Salt ions are forced to pass through a membrane, driven by electrical potential difference. Thus, ions can be separated from the source water. A similar technology is ionic exchange, where salts are captured by resins. These processes are solely used for brackish water
Solar Stills	Solar still desalination is an old concept which is based on the greenhouse effect. Thereby solar irradiation enters the system through the transparent surfaces at the top of the still and provides the heat of evaporation for a portion of the feed water. The vapor condenses on the colder still cover and finally flows into a collector

Table 2: Brief description of main desalination processes – based on [Cipollina 2009], [Müller-Holst 1999], [Koschikowski 2003]

Two types of thermal desalination technologies have found wide commercial application since the 70s of the last century: MSF and -to a lesser extent- MED. Two alternative MED systems are MED-TVC and MED-MVC. During the last years, the development of salt-rejecting membranes has led to the fast introduction of RO in the desalination market (Annex 10.1.5).

Due to a number of disadvantages in comparison to MED, namely higher electrical and thermal energy consumption (Annex 10.1.1), MSF is not considered in this work. The focus is on the techno-economic assessment of MED and RO plants, which are described in detail in 3.1 and 3.2, respectively. Table 3 briefly shows the key issues which are addressed for each of the two considered desalination technologies.

Unit	Description
Seawater intake and pre-treatment	Before feed water enters the desalination plant, a number of processes are required in order to minimize the content of foulants and other impurities (e.g. suspended matters) in the raw water source. These contaminants -if not adequately removed- would reduce the plant performance and irreversibly damage several plant components. These processes involve two main steps: water intake and water pretreatment. The pretreatment process includes the use of several chemical additives, which are partially discharged into the sea and cause local marine pollution
Desalination process	Desalination processes are the core of desalination plants and can be classified according to: modality of salt separation (water extraction, salt extraction), separation process (thermal, membrane) and used energy (mechanical, thermal, electrical)
Product water post-treatment	If desalinated water is used as drinking water, post-treatment is required in order to comply with local health regulations, preventing the risk of biological growth and reducing corrosion in the water distribution network [Cipollina 2009]. A number of drinking water regulations and guidelines define the concentration limits for several substances which are potentially hazardous for human health. The type of post-treatment mainly depends on the desalination process and the plant capacity. After post-treatment water is stored and distributed to consumers
Brine discharge	As the recovery ratio of desalination plants is limited by a series of technical and economic considerations, large volumes of brine (or retentate) have to be disposed. Brine from thermal and membrane desalination plants typically contains a number of potential contaminants such as increased salinity, high temperature (in the case of thermal desalination), various chemical residues from the pre-treatment process and cleaning solutions. Such potential contaminants have a negative impact on marine environment, while they also reduce public acceptance of desalination and potentially represent a hazard for local tourism and the fishing industry [Morillo 2014]

Table 3: Overview of key components of desalination plants

The implemented models allow the calculation of relevant performance parameters of MED and RO processes. A series of key design factors can be flexibly adapted to specific conditions or used to carry out parametric studies. Such technical models will be used to

deliver key inputs for economic analysis (7.2) and to perform a number of case studies (chapter 8).

3.1 Multi-Effect Distillation (MED)

3.1.1 Water Pretreatment

The intake water still contains contaminants (e.g. particulate, colloids, organic and mineral compounds, bacteria) that -if not removed with targeted measures- would reduce plant efficiency and increase the replacement cost of several plant components. These measures mainly include the use of several chemical additives, which are partially discharged into the sea and cause local marine pollution. The number and the complexity of the pretreatment steps depend on desalination technology and on seawater quality.

Without pretreatment, MED plants may suffer from corrosion and erosion problems due to free oxygen, bacteria and other suspended matters. In addition, if the maximal process temperature exceeds 70 °C, scaling problems may occur. These potential problems can be satisfactorily solved with a few standard actions.

The typical pretreatment steps of an MED are rather simple (Figure 6). After the source water passes a travelling screen, chlorine is added to kill microorganisms and to avoid growth of marine organisms such as shellfish and barnacles on the surfaces of pipes and other plant equipment. Chlorine oxidizes organic matter and breaks it into smaller particles. The disadvantage of this measure is that these particles represent a nutrient source for bacteria. Eventual bacterial after-growth in the downstream equipment of the plant would involve lower efficiency and higher maintenance cost. Shock chlorination (i.e. intermittent addition) leads to better performance than continuous chlorination [Lattemann 2003]. If the maximal process temperature exceeds 70 °C, the risk of scaling has to be prevented. The addition of sulfuric acid lowers the pH value and shifts the acidic reactions towards gaseous carbon dioxide [Gebel 2008].

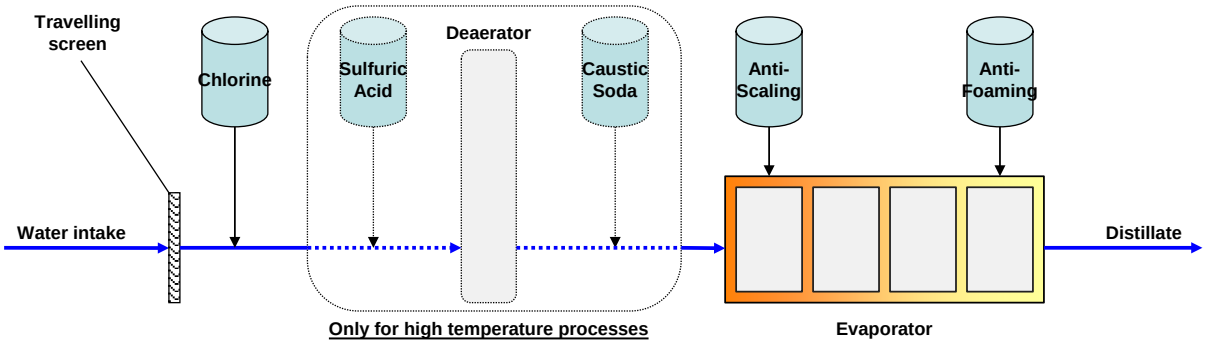

Figure 6: Conventional chemical treatment in thermal desalination plants. Adapted from [Gebel 2008] and [Wilf 2007]

After the deaerator, the pH is increased again by addition of caustic soda to avoid corrosion. If the maximum process temperature is lower than 70 °C, water de-carbonization is not

required. Finally, anti-scaling and anti-foaming agents are added to the feed water to avoid the precipitation of salts and foaming. Foam consists of thin liquid films which may grow in the evaporation chambers, even over the demisters (3.1.3). The problem of foaming consists in the fact that salt is still present in the liquid film, so that the distillate is contaminated by impurities and the demisters get blocked by scaling [Gebel 2008]. Typical concentrations and costs of chemicals in MED plants are presented in Annex 10.3.1.

3.1.2 Process Description

Similarly to MSF, MED belongs to the thermal desalination processes. These systems are typically constructed in cogeneration with thermal power plants in order to minimize energy requirements. Even if MSF has been the dominant seawater desalination technology in the Arabic Gulf region for many decades, MED presents a number of advantages such as lower operation temperatures and lower electricity requirements, which makes it attractive for desalination markets characterized by high energy cost and challenging seawater quality.

In MED processes, intake water passes through the tube side of the condenser (Figure 7 on the right), where it heats up (typically 8 K - 10 K), condensing excess heat (i.e. the vapor generated in the last stage). After that, intake water is divided into two streams: feed water and cooling water. Cooling water gets mixed with hot and highly saline brine coming from the MED stages and is finally released to the sea through the brine discharge. Brine blending with cooling water allows for the reduction of the environmental impact of brine on marine ecosystems (dilution of residual chemicals and brine salinity, temperature reduction).

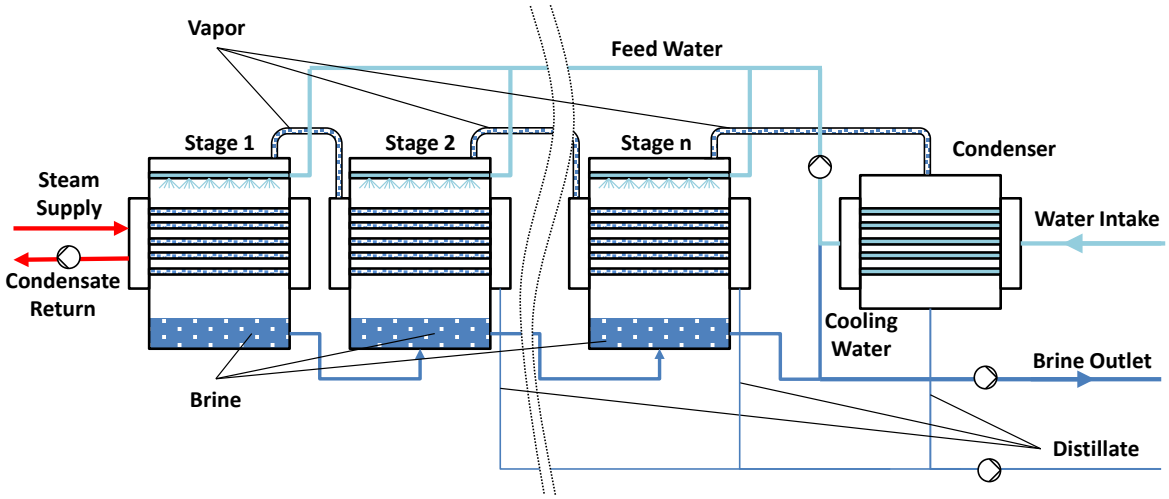

Figure 7: Simplified scheme of a MED process (parallel-cross configuration) – Adapted from [Gebel 2008]

In each of the chambers (also called effects or stages), pre-heated feed water is sprayed to the surface of the evaporators by nozzles (Figure 8). Horizontal tube bundles have established themselves against other evaporator layouts (e.g. submerged tubes, vertical tubes) due to lower scaling potential and a high overall heat transfer coefficient [Cipollina 2009]. However, the temperature of the feed water should not exceed approx. 70 °C in order to avoid scaling problems on the surface of the tube bundle.

The feed water forms a thin liquid film on the external surface of the heat exchangers, and a share of the feed evaporates. Heating steam is supplied along the tube side of the heat exchanger. The produced vapor passes through a demister and is conducted to the tube side of the successive stage. The non-evaporated share of the feedwater falls on subjacent tubes (Figure 8 on the right). The brine is collected at the bottom of the stage and is routed to the inferior part of the successive stage. In the new stage temperature and pressure are lower, which allows using the steam from the previous stage as heating steam and thus producing additional vapor. In addition, the pressure difference between the two effects also allows further generation of small steam amounts by distillate flashing (flashing boxes are not shown in Figure 7; more details are presented in 3.1.3).

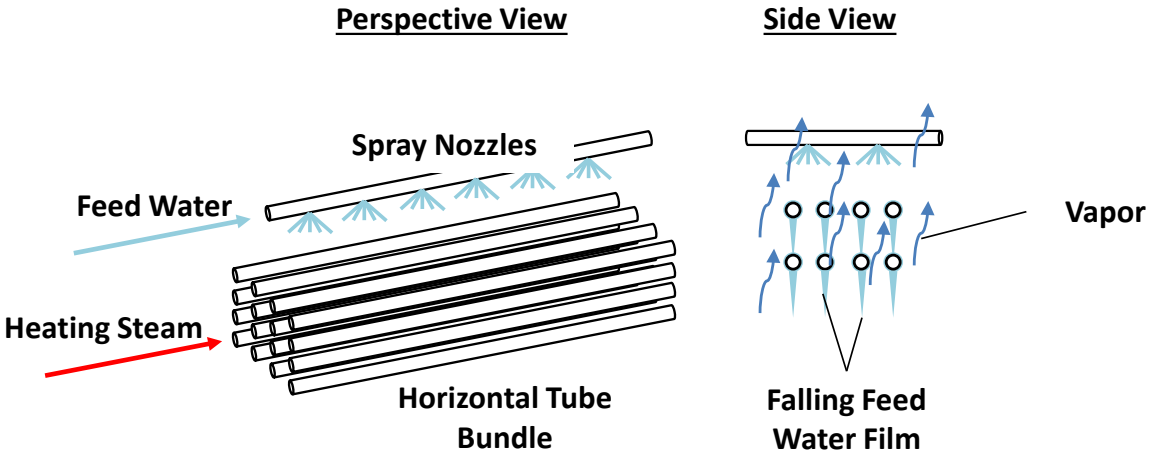

Figure 8: Perspective view of the heat exchanger inside each MED stage and side view of the feed water films - Adapted from [Cipollina 2009]

The process is repeated in each effect till the vapor generated in the last effect reaches the condenser. Finally, distillate is directed to the post-treatment section (3.2.4). Non-condensable gases need to be continuously vented through a steam jet ejector (Figure 10) to avoid the reduction of the effective heat transfer area and the decrease of the vapor partial pressure, which in turn diminish the driving temperature difference between condensing steam and feed water and thus the overall process efficiency. The sequence of evaporation and condensation processes in MED plants allows very efficient utilization of the supplied heating steam. Up to more than ten kilograms of distillate can be produced from one kilogram of heating steam. The process described in Figure 7 is known under the name of parallel-cross feed configuration. Other configurations such as forward feed, backward feed and simple parallel feed are possible (Annex 10.1.3, Table 37).

Due to its high efficiency, the parallel-cross feed layout has been selected as the reference MED process of this work. In addition, MED with thermal vapor compression is taken into account. MED-TVC processes are mainly used if medium quality motive steam is available (typically 2.5 bar - 5 bar) and if high desalination efficiency is required. The main disadvantage is that the electrical conversion efficiency of the power cycle is lower if steam is extracted at a relative high pressure. The particularity of MED-TVC systems is that a

portion of the vapor generated in the last stage is recycled by means of a thermo-compressor, which is fed with the motive steam from the power plant (Figure 9). The two vapor streams are mixed, whereas the quality of the sucked steam is increased, and used as heating steam in the first stage. After condensation, one part of the distillate returns to the power block, while the remaining part (which corresponds to the sucked vapor flow) is collected with the distillate of the other effects.

TVC is an open process, i.e. steam from the power block and from the desalination plant are mixed. Therefore, the water product may be contaminated with chemicals used in the steam turbine cycle. In this case, the polluted distillate stream should be rejected (dotted red line in Figure 9) [Gebel 2008]. Despite this eventual loss of polluted distillate, MED-TVC presents significantly higher efficiency (approx. 30 % - 35 % higher) in comparison to MED without TVC.

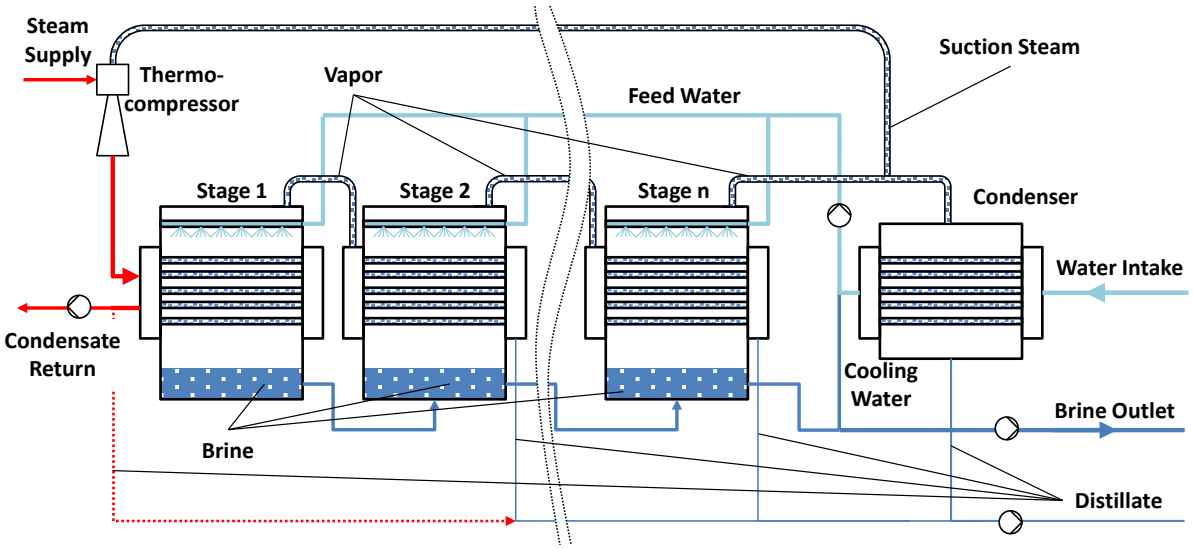

Figure 9: Simplified scheme of a MED-TVC process – Adapted from [Gebel 2008]

3.1.3 MED Model

The MED model consists of a set of equations and a number of empirical correlations for the estimation of physical properties, thermodynamic losses and heat transfer coefficients. Due to the non-linearity of the correlations, an iterative solution procedure is required. The model has been programmed in FORTRAN based on [El-Dessouky 2002] and [Gebel 2008] and successively integrated in INSEL.

The focus of this chapter is the description of the thermal balances, which allow the determination of temperatures, mass flows and salt concentration in the different stages of the plant. In addition, the heat transfer area of the evaporators and key performance parameters are assessed.

One of the most relevant parameters is the gain output ratio (GOR), which is defined as the ratio between distillate production and heating steam mass flow:

$$GOR = \frac{\dot{m}_d}{\dot{m}_s} \qquad \text{Eq. 3.1}$$

$\dot{m}_d$	[kg/s]	total distillate mass flow
$\dot{m}_s$	[kg/s]	heating steam mass flow

The GOR is often used to describe the efficiency of thermal desalination plants; however, it is not well suited for comparison of different thermal desalination configurations, as it does not specify the energy content and quality of the used steam (temperature and pressure) [Gebel 2008]. Rather, a final comparison of desalination technologies should be carried out by economic analysis considering all investment and operation costs over the complete plant life time (7.2 and Annex 10.3.1).

The model assumes:

- steady-state conditions: the impact of transients is not taken into account, as thermal desalination plants are typically operated round-the-clock. Start-up procedures are considered by means of simplified thermal balances.
- salt-free distillate: in real plants almost pure water is evaporated. Minimal salt content in distillate amounts to approx. 20 ppm, which is negligible if compared to the salt concentration in seawater (typically 30,000 ppm up to 45,000 ppm).
- equal heat transfer area in all effects: this is a common practice in commercial desalination plants. This assumption is also used as a condition for the iterative solution procedure (as explained later).

In each plant stage i, the material balances of water and salt are:

$$\dot{m}_{f(i)} = \dot{m}_{d(i)} + \dot{m}_{b(i)} \qquad \text{Eq. 3.2}$$

$$\dot{m}_{f(i)} \cdot X_{sw} = \dot{m}_{b(i)} \cdot X_{b(i)} \qquad \text{Eq. 3.3}$$

The salt concentration of the brine $X_{b(i)}$ is limited to approx. 65,000 ppm in order to avoid scaling problems. The concentration factor CF is defined as the ratio between feed and brine mass flow:

$$CF = \frac{\dot{m}_f}{\dot{m}_b} = \frac{X_b}{X_f} \qquad \text{Eq. 3.4}$$

$\dot{m}_f$	[kg/s]	total feed water mass flow
$\dot{m}_b$	[kg/s]	total brine mass flow

The higher the salinity of the source water, the lower the concentration factor. Thus, a low CF implies that more intake water is required. In this case, pumping and chemical costs are higher.

Typical concentration factors in MED plants are between 1.7 (e.g. Mediterranean Sea, X_{sw}= 35,000 ppm) and 1.4 (e.g. Arabian Gulf, X_{sw}= 45,000 ppm). The energy balance of the first stage is:

$$\begin{cases} \dot{Q}_s = \dot{Q}_{ph} + \dot{Q}_{ev} \\ \dot{m}_s \cdot \lambda_s = \dot{m}_{f(1)} \cdot c_p \cdot \left(T_1 - T_{f(1)}\right) + \dot{m}_{d(1)} \cdot \lambda_{v(1)} \end{cases} \quad \text{Eq. 3.5}$$

$\dot{Q}_s$	[kW]	thermal load of heating steam
$\dot{Q}_{ph}$	[kW]	thermal load used for feed water pre-heating
$\dot{Q}_{ev}$	[kW]	thermal load used for evaporation
λ_s	[kJ/kg]	latent heat of condensation of heating steam
c_p	[kJ/kg/K]	specific heat capacity at constant pressure of feed water
$\lambda_{v(1)}$	[kJ/kg]	latent heat of evaporation of distillate

$\dot{Q}_s$ is used to increase the temperature of the feed water from $T_{f(1)}$ to the boiling temperature T_1 as well as to evaporate the water amount $\dot{m}_{d(1)}$. The higher the portion of $\dot{Q}_s$ used for feed water pre-heating, the lower are distillate production and GOR. A series of measures have been implemented in MED plants in order to minimize pre-heating losses. These measures are based on recovery of the energy content of distillate and brine, i.e. feed water pre-heating with distillate and brine flashing. The first measure refers to the utilization of a portion of the produced distillate for feed water pre-heating. This process is exemplified in Figure 10 (at top, between last stage and condenser). The amount of vapor used for pre-heating is not available for further vapor generation in the successive stage; however, in the previous step evaporation is maximized.

The vapor amount used for feed water preheating $\dot{m}_{D\_ph}$ is:

$$\dot{m}_{d\_ph(i)} = \frac{\sum_{j=1}^{i} \dot{m}_{f(j)} \cdot c_p \cdot \left(T_{f(i)} - T_{f(i-1)}\right)}{\lambda_{v(i)}} \quad \text{Eq. 3.6}$$

The heat exchanger area for the preheaters $A_{ph(i)}$ can be calculated as:

$$A_{ph(i)} = \frac{\dot{m}_{d\_ph(i)} \cdot \lambda_{v(i)}}{k_{ph}(T_i) \cdot LMTD_{ph(i)}} \quad \text{Eq. 3.7}$$

k_{ph}	[kW/m²/K]	overall heat transfer coefficient of preheater
$LMTD_{ph(i)}$	[K]	logarithmic mean temp. difference of preheater i

k_{ph} is calculated according to [El-Dessouky 2002]. Preheaters typically account for approx. 10 % of the total heat exchanger area of MED plants [Gebel 2008], while the major share is represented by the evaporator tube bundles (Eq. 3.12).

The second measure relates to the generation of additional distillate outside the stages. In each stage the produced distillate is driven by a pressure difference to the successive effect, where it condenses. After that, condensate leaves the heat exchanger as boiling water. The distillate enters a flashing box (bottom of Figure 10), where pressure and boiling temperature are lower. The sudden pressure change enables the flashing (i.e. evaporation) of a portion of the distillate stream. The amount of distillate generated by flashing is relatively low in the initial stages. However, due to the fact that flashing boxes are fed with the cumulated mass flow of distillate, vapor production by flashing increases in each new box along the path toward the condenser.

Similarly, the energy content of the brine can be recovered by means of brine flashing boxes. The amount of distillate produced by flashing is [Gebel 2008]:

$$\dot{m}_{d_{Flash}'(i)} = \frac{\left(\sum_{j=1}^{i-1} \dot{m}_{d(i)}\right) \cdot c_{p,d} \cdot \left(T_{v(i)} - T_{v(i-1)}\right)}{\lambda_{v(i)}} \qquad \text{Eq. 3.8}$$

$$\dot{m}_{d_{Flash}''(i)} = \frac{\left(\sum_{j=1}^{i-1} \dot{m}_{b(i)}\right) \cdot c_{p,b} \cdot \left(T_{v(i)} - T_{v(i-1)}\right)}{\lambda_{v(i)}} \qquad \text{Eq. 3.9}$$

$\dot{m}_{d_{Flash}'(i)}$	[kg/s]	flashing mass flow from distillate box
$\dot{m}_{d_{Flash}''(i)}$	[kg/s]	flashing mass flow from brine box

Summing up, the vapor mass flow which enters the successive stage ($\dot{m}'_{d(i-1)}$ according to Figure 10) is diminished by the portion used for feed water pre-heating $\dot{m}_{d\_ph(i-1)}$ and increased by the flashing of distillate and brine:

$$\dot{m}'_{d(i-1)} = \dot{m}_{d(i-1)} - \dot{m}_{d\_ph(i-1)} + \dot{m}_{d_{Flash}'(i-1)} + \dot{m}_{d_{Flash}''(i-1)} \qquad \text{Eq. 3.10}$$

Figure 11 shows the temperature profiles of feed water and distillate in the MED plant. Intake water flows through the condenser and increases its temperature from T_{sw} to T_{cw}. Successively, the feed water temperature is increased by the pre-heaters, so that the temperature difference between feed water $T_{f(i)}$ and stage T_i is constant at each stage. As explained previously, feed water pre-heating allows a significant increase of the efficiency of the initial stages, where the brine temperature is higher.

The temperature difference between vapor condensing along the tube side of the heat exchanger $T_{c(i-1)}$ and the boiling water film on the external tube surface $T_{(i)}$ goes under the name of heat transfer temperature difference ($\Delta T_{ht(i)}$) or driving temperature difference:

$$\Delta T_{ht(i)} = T_{c(i-1)} - T_{(i)} \qquad \text{Eq. 3.11}$$

$T_{c(i-1)}$ [°C] vapor condensation temperature

The higher $\Delta T_{ht(i)}$, the lower the area required for heat transfer and the lower the investment costs:

$$A_i = \frac{\dot{m}_{d(i)} \cdot \lambda_{v(i)} + \dot{m}_f \cdot c_p \cdot \left(T_i - T_{f(i)}\right)}{k_{ev}(T_i) \cdot \Delta T_{ht(i)}} \qquad \text{Eq. 3.12}$$

Depending on the plant configuration, the heat exchanger tubes represent a significant share of investment cost (Annex 10.3.1). The driving temperature difference primarily depends on the total number of stages. The higher is the number of stages, the lower the available temperature difference for the heat transfer.

In addition, two loss mechanisms reduce $\Delta T_{ht(i)}$ (Figure 11):

- Boiling point elevation ($\Delta T_{BPE(i)}$): saline water boils at a higher temperature than pure water. The difference between the boiling temperature of pure and saline water is called BPE, which is calculated according to [Gebel 2008]. For typical MED applications, the $\Delta T_{BPE(i)}$ ranges between 0.35 K and 0.7 K.
- Other losses ($\Delta T_{Loss(i)}$): a number of other losses further reduce the driving temperature difference. These losses are caused by a pressure drop in the demister and in the tubes as well as by partial condensation of the vapor within the tubes. The evaluation of these losses is rather complex and based on semi-empirical correlations such as those proposed by [El-Dessouky 2002].

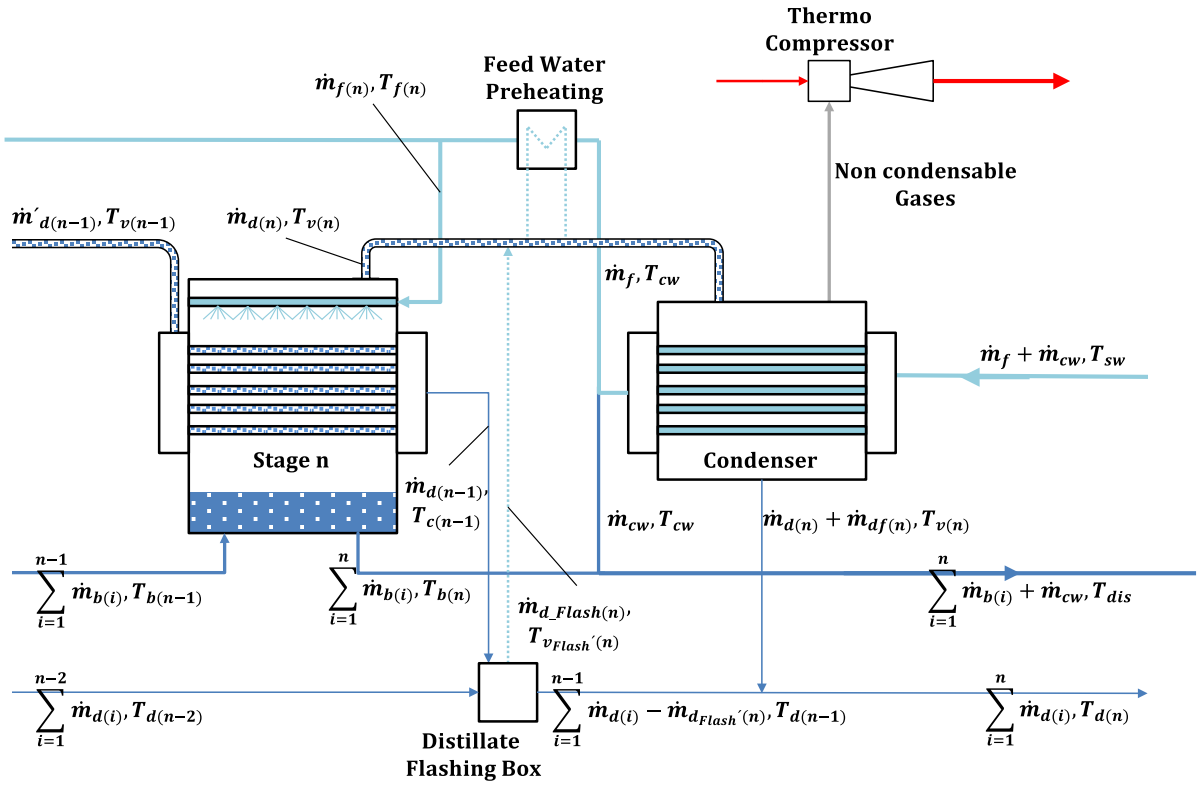

Figure 10: Detailed scheme of last MED stage and condenser – Adapted from [Cipollina 2009]

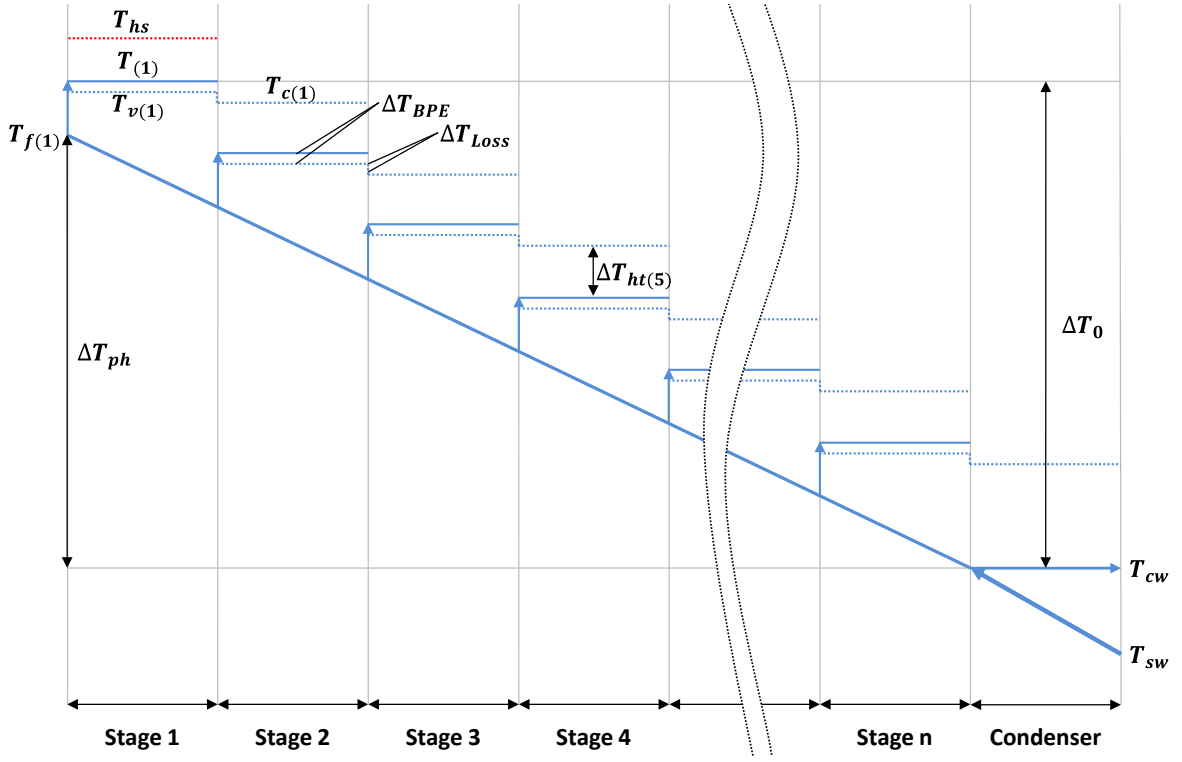

Figure 11: Simplified temperature profile of a parallel feed MED process – Adapted from [Gebel 2008]

According to the definitions of Figure 11:

$$T_{v(i)} = T_i - \Delta T_{BPE(i)} \quad \text{Eq. 3.13}$$

$$T_{c(i)} = T_{v(i)} - \Delta T_{Loss(i)} \quad \text{Eq. 3.14}$$

Finally, the cooling water mass flow $\dot{m}_{cw}$ and the condenser heat transfer area A_{cond} are calculated with the following thermal balances:

$$\dot{m}'_{d(n)} \cdot \lambda_{c(n)} = \left(\dot{m}_f + \dot{m}_{cw}\right) \cdot c_p \cdot (T_{cw} - T_{sw}) \quad \text{Eq. 3.15}$$

$\lambda_{c(n)}$ [kJ/kg] heat of condensation calculated at $T_{c(n)}$

$$\dot{m}'_{d(n)} \cdot \lambda_{c(n)} = A_{cond} \cdot k_{cond} \cdot LMTD_{cond} \quad \text{Eq. 3.16}$$

The higher the number of stages, the lower the amount of distillate produced in each stage. In this case, the requirements for the condenser (i.e. $\dot{m}_{cw}$ and A_{cond}) are also lower.

Iterative Solution Procedure

A number of input parameters such as the heating steam mass flow, seawater temperature, seawater salinity, the number of stages and other design parameters have to be specified in order to solve the equations. An overview of key input parameters and results of the MED model is given in Table 4.

The most relevant results are distillate production, GOR, intake water, feed water and brine mass flows, temperature profiles within the plant as well as the heat transfer area of evaporators, pre-heaters and condenser. The solution procedure is based on an iterative calculation which is summarized in Table 5. The iterative procedure is required due to the non-linearity of the used correlations (material properties and loss mechanisms).

The first step consists of a first estimation of distillate production, feed water distribution and temperature profile along the MED stages. With this the feed water is equally distributed among the effects. The temperature profile is assumed to be linear. A rule of thumb is used for a rough assessment of the total distillate production (Eq. 3-17) [Glade 2009]. The calculation proceeds with the calculation of the main thermal balances. As explained previously, it is a common practice in commercial MED plants that heat transfer areas A_i are equal in all stages. This condition is achieved by means of an iterative calculation, whereas the temperature profile within the stages is adjusted at each new iteration step.

Also, the feed water supply $\dot{m}_{f(i)}$ is eventually adapted in order to control salt concentration in the brine. The temperature adjustment depends on the ratio between A_i and the average area A_{avg} (Eq. 3-22) [El-Dessouky 2002]. In addition, the introduction of a relaxation factor

(γ) has proven to improve numerical stability and to reduce calculation time of the model [Moser 2009]. The iteration stops as soon as the maximal difference of the HX area of two consecutive stages drops below a given tolerance.

Input Parameter	Unit	Typical Range	Description
n	-	2 - 12	number of stages
$\dot{m}_s$	kg/s	-	heating steam mass flow
T_s	°C	60 - 73	heating steam temperature
T_{sw}	°C	15 - 35	seawater temperature
X_{sw}	ppm	35,000 – 45,000	seawater salinity
ΔT_{cond}	K	8 - 10	condenser temperature difference (intake water)
ΔT_{TTD_cond}	K	3 - 5	condenser terminal temperature difference (TTD)
ΔT_{TTD_ph}	K	< 5	terminal temperature difference of pre-heaters
Result	**Unit**	**Typical Range**	**Description**
T_i	°C	40 - 70	temperature of stage i
$\dot{m}_{f(i)}$	kg/s	-	feed water flow at the inlet of stage i
$\dot{m}_{d(i)}$	kg/s	-	distillate flow of stage i
$\dot{m}_{b(i)}$	kg/s	-	brine flow of stage i
$X_{b(i)}$	ppm	65,000	brine salt concentration of stage i
sA	m²/(kg/s)	100 - 500	specific heat transfer area of evaporators
$\dot{m}_{cw}$	kg/s	-	cooling water flow
$\dot{m}_f$	kg/s	-	total feed water flow
GOR	-	3 - 10	gain output ratio

Table 4: Overview of key input and output parameters of the MED model (without TVC) [Cipollina 2009]

Step	Description	Used Equations	
First Estimations			
1	Distillate production	$\dot{m}_d = \dot{m}_s \cdot n^{0.9}$	Eq. 3-17
2	Feed water mass flow distribution	$\dot{m}_{f(i)} = \frac{\dot{m}_d}{n} \cdot \frac{CF}{CF-1}$	Eq. 3-18
3	Temperature distribution	$\Delta T_i = \Delta T_0 / n$	Eq. 3-19
4	BPE and other losses	Eq. 3.13 and Eq. 3.14	
Iterative Calculations			
1	Distillate production in the stages	Eq. 3.5	
2	Brine production and brine salinity	Eq. 3.2 and Eq. 3.3	
3	Distillate production in flashing boxes	Eq. 3.8 and Eq. 3.9	
4	Distillate used for pre-heating	Eq. 3.6	
5	Heat exchangers area: - Tube bundle - Pre-heating - Condenser	 Eq. 3.12 Eq. 3.7 Eq. 3.16	
6	Maximal heat transfer area difference	$\Delta A = \lvert\max(A_i - A_{i-1})\rvert$	Eq. 3-20
Convergence Criterion and Setup of New Iteration			
1	New iteration required, if condition Eq. 3-21 is not verified. Otherwise, temperatures are recalculated and a new iteration starts	$\Delta A \leq tolerance$	Eq. 3-21
2	Recalculation of temperatures	$\Delta T_{new(i)} = \Delta T_{(i)} \left(\frac{A_i}{A_{avg}}\right)^{\gamma}$	Eq. 3-22

Table 5: Solution procedure of MED model

MED-TVC Model

The presented MED model has been extended in order to consider the impact of thermal vapor compression on the performance of the MED plant. Just a small number of adaptations needs to be considered. With respect to Figure 9, the following steam mass flows are defined:

$\dot{m}_m$	[kg/s]	motive steam supplied from the turbine
$\dot{m}_{e\_v}$	[kg/s]	entrained vapour extracted from MED last stage
$\dot{m}_s$	[kg/s]	heating steam of the first MED stage

The amount of entrained vapor is:

$$\dot{m}_{e\_v} = \dot{m}_s - \dot{m}_m \qquad \text{Eq. 3.23}$$

Similarly to the previous model, the steam flow supplied by the turbine is assumed to be known. The heating steam mass flow is calculated according to the steam jet ejector model proposed by [El-Dessouky 2002], whereas ER is the entrainment ratio of the ejector:

$$\dot{m}_s = \dot{m}_m \cdot \left(1 + \frac{1}{ER}\right) \qquad \text{Eq. 3.24}$$

$$ER = \frac{\dot{m}_m}{\dot{m}_{e\_v}} = 0.296 \cdot \frac{p_s^{1.19}}{p_{e\_v}^{1.04}} \cdot \left(\frac{p_m}{p_{e\_v}}\right)^{0.015} \cdot \frac{PCF}{TCF} \qquad \text{Eq. 3.25}$$

p_s	[bar]	heating steam pressure
p_{e_v}	[bar]	entrained vapor pressure
p_m	[bar]	motive steam pressure
PCF	[-]	pressure correction factor
TCF	[-]	temperature correction factor

The entrainment ratio is calculated by means of a semi-empirical correlation, which mainly depends on the pressure level of entrained, motive and heating steam. Finally, the calculation of the gain output ratio can be generalized as:

$$GOR = \frac{\dot{m}_d}{\dot{m}_s - \dot{m}_{e\_v}} \qquad \text{Eq. 3.26}$$

3.1.4 Drinking Water Post-Treatment

If desalinated water is used as drinking water, post-treatment is required in order to comply with local health regulations, preventing the risk of biological growth and reducing corrosion in the water distribution network [Cipollina 2009]. A number of drinking water regulations and guidelines define the concentration limits for several substances which are potentially hazardous for human health. The world health organization (WHO) reports the concentration limits of harmful substances according to up-to-date scientific information [WHO 2014]. A selection of these values is presented in [Fritzmann 2007]. The type of post-treatment mainly depends on the desalination process and the plant capacity. MED plants produce almost pure distillate (salinity lower than 20 ppm) which needs to be re-mineralized before it can be used for civil purposes. In particular, water hardness (i.e. the concentration of multi-valent ions such as Ca^{2+} and Mg^{2+}) has to be increased. The post-treatment process of large-scale thermal desalination plants typically consists of a number of steps, as shown in Figure 12.

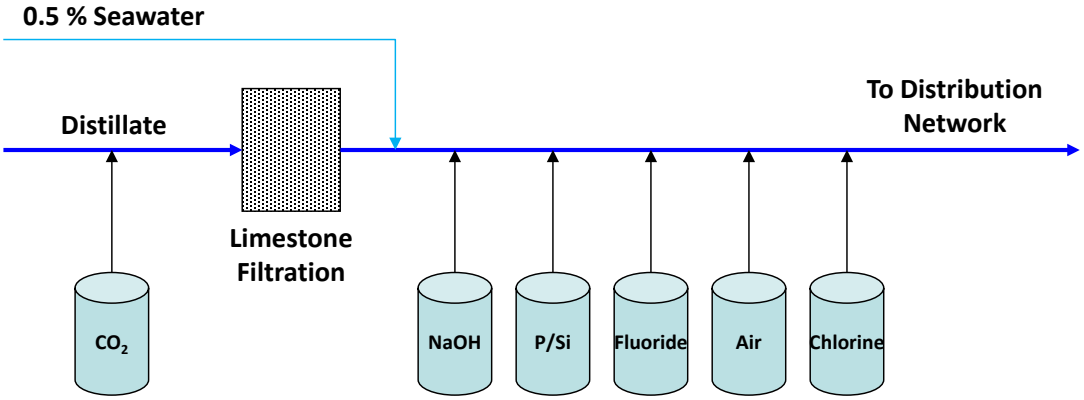

Figure 12: Post-treatment process in a typical large-scale MED plant [Gebel 2008]

After CO_2 is added by means of a gas-liquid contactor, the distillate flows through a limestone filter, which serves to increase the calcium and carbonate content of water. Some disinfected seawater is added to increase salt content of the distillate. The final salinity of post-treated water typically is between 200 ppm and 400 ppm [Cipollina 2009]. Sodium hydroxide ($NaOH$) is added to increase pH, whose final value should range between 8 and 9 in order to provide sufficient corrosion protection. In addition, phosphates and silicates are added. These substances tend to form thin layers on the surfaces of water piping structures and thus help preventing corrosion. Small concentrations of fluoride are also used to avoid tooth decay. Due to the high temperature of thermal desalination processes, the oxygen content of distillate has to be restored (e.g. by air injection). Finally, the water is disinfected using chlorine gas or sodium hypochlorite ($NaClO$) to avoid eventual bacterial contaminations along the water distribution system. Typical concentrations and costs of chemicals used for the post-treatment of MED plants are presented in Annex 10.3.1.

3.1.5 Brine Discharge

As the recovery ratio of desalination plants is limited by a series of technical and economic considerations (3.1.3 and 3.2.3), large volumes of brine have to be disposed. Many solutions have been proposed, which can be classified according to their purpose (e.g. zero liquid discharge, commercial salt recovery, brine discharge in water bodies) [Morillo 2014]. Most emerging technologies such as zero brine discharge, forward osmosis and electro-dialysis are characterized by an early development status, technical drawbacks and high cost. Even if these figures may change in the future, the applicability of these solutions on an industrial scale still has to be fully demonstrated. The current state-of-the-art brine disposal of commercial desalination plants is open sea discharge (Annex 10.1.4).

Brine from thermal desalination plants such as MED typically contains a number of potential contaminants such as increased salinity, high temperature, various chemical residues from the pre-treatment process and cleaning solutions [Lattemann 2008]. Such potential contaminants do not only have a negative impact on marine environment, but also reduce public acceptance of desalination and potentially represent a hazard for local tourism and the fishing industry [Morillo 2014].

3.1.6 MED INSEL Block

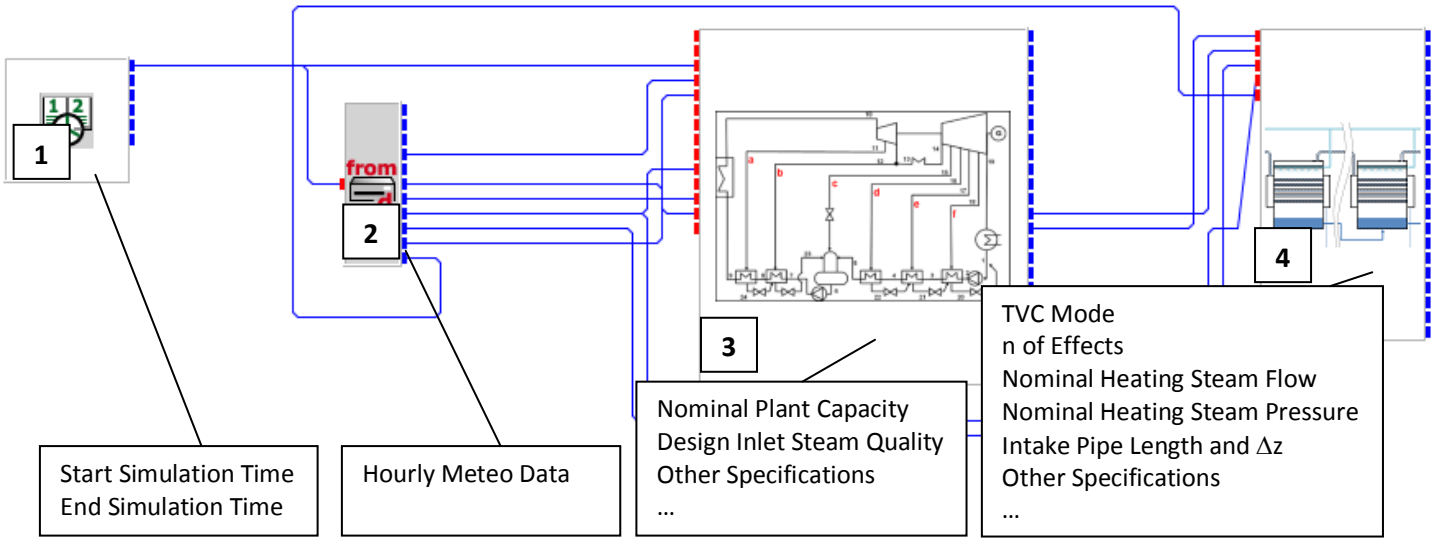

1 - Time Block		2 - Read Block		3 - Steam Turbine		4 - MED	
Input	**Output**	**Input**	**Output**	**Input**	**Output**	**Input**	**Output**
-	Time	Time	T_{sw} X_{sw} H_2O Demand $\dot{Q}_{turb}$ T_{steam_in} T_{amb} P_{el_demand}	$\dot{Q}_{turb}$ T_{steam_in} T_{amb} P_{el_demand}	P_{el_gross} η_{turb_gross} Part Load p_{cond} $\dot{m}_{s\_cond}$ T_{cond}	$\dot{m}_{s\_cond}$ p_{cond} T_{sw} X_{sw} H_2O Demand	$\dot{m}_d$ GOR $\dot{m}_{sw}$ $\dot{m}_f$ $\dot{m}_{discharge}$ $T_{discharge}$ $X_{discharge}$ sA $\dot{q}_{th\_consumption}$ $P_{parasitic\_MED}$

Figure 13: Screenshot of the developed MED INSEL model with specification of main design parameters (in the boxes), input and output values (in the table) for each INSEL block; Note: only relevant parameters for this particular simulation are listed in the table; the complete list of the parameters of the newly developed INSEL blocks is reported in Annex 10.5; for commercial INSEL blocks refer to [INSEL]

3.2 Reverse Osmosis (RO)

3.2.1 Water Pretreatment

RO plants require more complex pretreatment than MED. This is due to the high susceptibility of membranes on fouling. Fouling consists of the formation of a thick layer of organic or suspended matter on the membrane surface, which reduces plant efficiency and increase the replacement cost of membranes. The most relevant seawater quality parameters with regard to the RO pretreatment are:

- Turbidity: is caused by the presence of suspended (i.e. non-dissolved) and colloidal matter in water. It can be measured by means of light scattering or transmissivity methods. Its value is expressed in nephelometric turbidity units (NTU). The NTU of seawater is typically between 0.5 and 2.0, while the NTU of feed water for RO plants should be preferably below 0.1 in order to reduce fouling risk.
- SDI (silt density index): its value gives an estimation of the fouling potential of the water source which can be induced by undissolved solid matters. This measurement is particularly important for RO plants, as it is an indicator of the tendency of a membrane to get blocked. The SDI value should be consistently lower than 4.0 in order to guarantee stable and long-term membrane operation [Wilf 2007].
- TOC (total organic carbon): is the amount of carbon bound in organic matters, which typically originates from the decomposition of algae and humic substances. A portion of the TOC is biodegradable, i.e. these organic matters serve as feed for microorganisms and enhance their growth rate. Unless countermeasures are taken, microorganisms easily plug RO membrane pores (so-called biofouling), so that the performance of the RO plant is permanently reduced. On the contrary, biofouling does not represent a severe problem in thermal desalination plants. TOC levels above 0.1 mg/l indicate elevated fouling potential. Typical TOC values for seawater are approx. 0.2 mg/l or lower; however, during algal bloom events (red tides), the TOC value may increase up to 8 mg/l [Voutchkov 2010].
- Salt Solubility: the knowledge of the solubility value of salts (e.g. calcium carbonate, calcium sulfate and magnesium hydroxide) also plays an important role for the pretreatment, as their crystallization and the consequent formation of scaling layers would reduce the performance of the desalination plant. A number of equilibrium reactions (dissolution of carbon dioxide, acidic reaction, alkaline reaction, water dissociation and salt formation) are involved in the precipitation process [Gebel 2008]. Salt solubility issues may represent a problem for thermal as well as for membrane desalination plants; RO plants are limited by the maximal yield (3.2.3), while MED plants are limited by the maximum temperature (3.1.3).
- Dissolved gases: the determination of the amount of dissolved gases (mainly nitrogen, oxygen, argon and carbon dioxide) is important, as they reduce heat transfer in thermal desalination plants and may cause corrosion.

- Salinity (or total dissolved solids, TDS): is the concentration of dissolved ions in water and is typically expressed in parts per million (ppm) [Wilf 2007]. Reduction of salinity in intake water is not foreseen in conventional pretreatment systems.

Although each RO project is unique, experience gained from existing plants allows the formulation of some general recommendations for pretreatment selection as the function of seawater quality. Two cases are taken into account by the developed models:

- Conventional Pretreatment: in such a configuration, firstly intake water is screened and disinfected with chlorine (Figure 14). Secondly, remaining contaminants such as colloids, algae, suspended organic particles and silt are retained by granular filters (dual media filters (DMF)). Ferric chloride ($FeCl_2$) is added prior to the DMF, which promotes the conglomeration of small colloidal compound and of a fraction of dissolved organics to larger particles (coagulation and flocculation). The relatively large flocs are effectively retained by the media filters. Coagulation-flocculation processes are very effective and allow the filtration of particles with a diameter down to 0.2 μm. Without coagulants, only particles larger than 50 μm could be retained. However, optimal coagulant dosage is a very critical issue: a too low addition leads to lower filter efficiency, while overdosing causes coagulant accumulation (i.e. fouling) on downstream equipment (cartridge filters and RO membranes). In order to restore full retention volume, DMF are backwashed every 24-48 hours using filtered seawater or RO concentrate [Voutchkov 2010]. Cartridge filters are installed downstream of the DMF. Residual chlorine has to be removed upstream of the RO equipment to avoid membrane damages. This is done by the addition of scavengers such as sodium bisulfite ($NaHSO_3$). In addition, pH conditioning may be required in order to avoid scaling.
- Demanding Pretreatment: Lower quality seawater may need additional pretreatment upstream of the filtration step. The following alternatives may be considered: sand removal, sedimentation and dissolved air flotation (DAF). Sedimentation basins are installed prior to DMF to pretreat high-turbidity intake water and to reduce the turbidity value down to approx. 2 NTU. The particle settlement process is enhanced by the addition of coagulant and flocculant agents. DAF makes use of small air bubbles in order to separate floating compounds such as algae, oil and grease from seawater. DAF is well suited for the pretreatment of source water with turbidity spikes below 50 NTU. The typical turbidity of the treated water lies between 0.5 NTU and 1.5 NTU.

Additional information about chemical dosing and cost is presented in Annex 10.3.1. Alternative membrane pretreatment processes also exist. Over the last ten years significant improvement of microfiltration (MF) and ultrafiltration (UF) technologies has been reached, not only for waste water applications but also for desalination. In addition, nanofiltration (NF) membranes are typically used for softening (i.e. reduction of bivalent ions) or treatment

of low salinity water. Currently, more than 20 desalination plants make use of MF/UF pretreatment systems [Voutchkov 2010 b] (Annex 10.1.2).

In addition to pre-treatment, RO membrane cleaning is required to prolong the operational lifetime of the modules. Cleaning is considered whenever relevant performance parameters such as membrane pressure differential, water flux and salt flux drop by 10 % - 15 %, which is an index for gradual fouling. Most used chemicals are acids, alkaline and anti-precipitating agents, biocides and detergents.

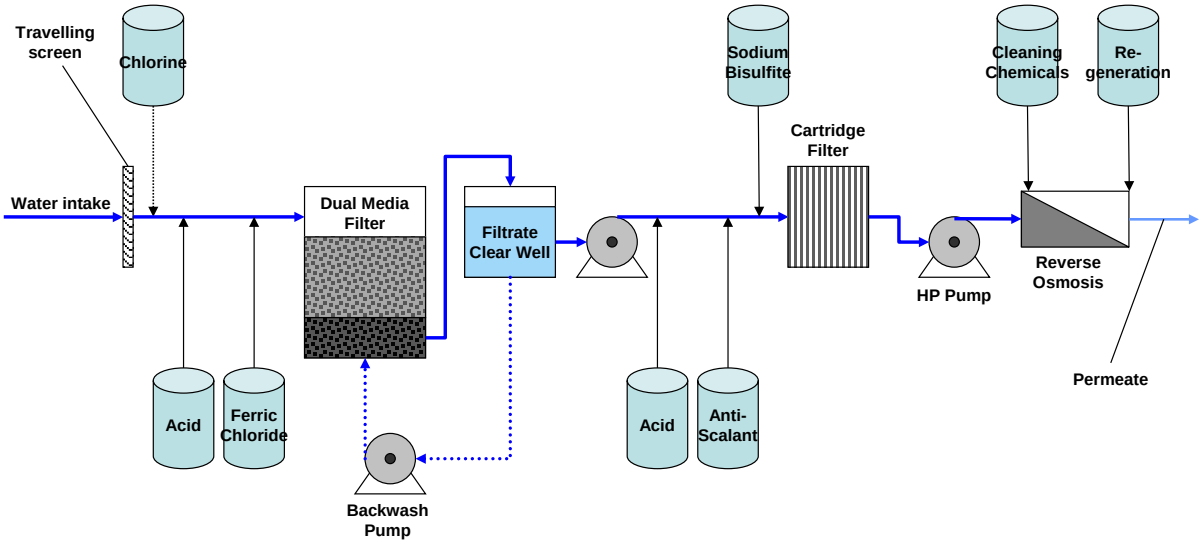

Figure 14: Conventional chemical treatment in seawater reverse osmosis (SWRO) plants. Adapted from [Wilf 2007] and [Gebel 2008]

3.2.2 Process Description

Osmosis and Reverse Osmosis

In reverse osmosis plants water/salt separation occurs by means of selective membranes, whereas "selective" means that water molecules cross the membrane at a higher flow rate than salt ions do. The selectivity is due to specific physical and chemical membrane characteristics such as pore size and surface charge [Cipollina 2009]. As a result, if saline water is fed on one membrane side, water crosses the membrane and is separated from the salt, which mainly remains on the feed side. Similarly to all desalination processes, RO is not spontaneous, i.e. energy has to be supplied to the desalination system. The driving force of RO processes is the pressure difference between the two membrane sides (i.e. feed water side and product water side). In the absence of externally applied pressure and of temperature differences, the spontaneous movement of solvent across the membrane would tend towards the region of higher solute concentration, as shown in Figure 15.

This process goes under the name of (direct) osmosis. The net flow of solvent continues until an equilibrium is reached, i.e. when the hydrostatic pressure difference Δp equals the osmotic pressure difference $\Delta\pi$ (Eq. 3.27) between the two solutions.

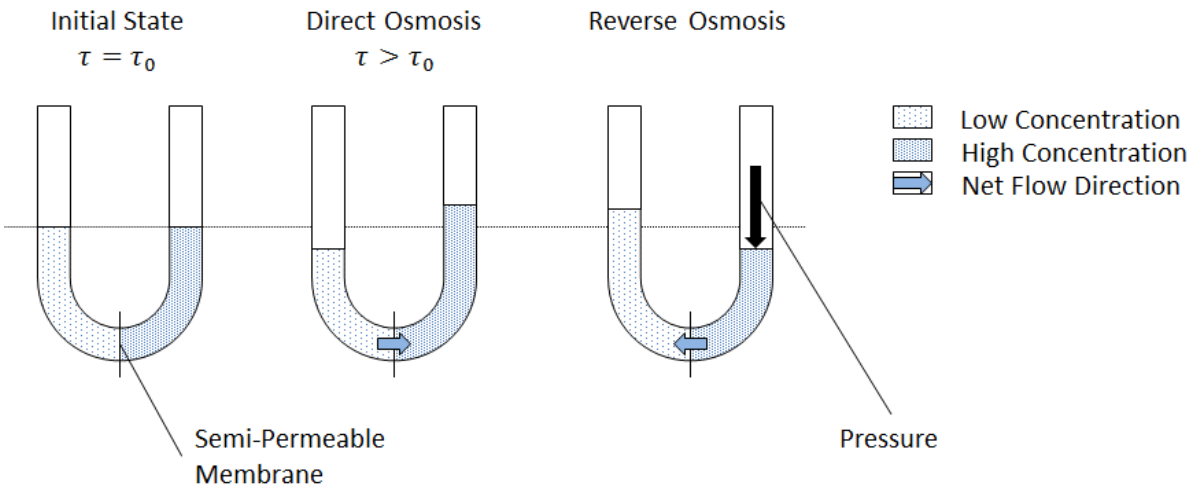

Figure 15: Principle of direct and reverse osmosis – Adapted from [Wilf 2007]

The osmotic pressure difference is directly proportional to the concentration difference of the solutions [Wilf 2007]:

$$\Delta\pi \cong 0.77 \cdot (X_{HC} - X_{LC}) \qquad \text{Eq. 3.27}$$

$\Delta\pi$	[bar]	osmotic pressure difference
0.77	[bar/10^3 ppm]	conversion factor
X_{LC}	[g/l]	salinity of low-concentrated solution
X_{HC}	[g/l]	salinity of high-concentrated solution

Eq. 3.27 is an approximated formulation which only holds under the assumption of dilute salt solutions and water temperature of around 25 °C. Under these conditions it can be assumed that a salt concentration of 1,000 ppm corresponds to 0.77 bar osmotic pressure.

The osmotic pressure of seawater typically ranges between 23 bar (X_{sw} = 33,000 ppm) and 35 bar (X_{sw} = 45,000 ppm). By the application of external hydrostatic pressure to the side of the most concentrated solution (Figure 15 on the right) the osmosis process can be reversed, which means that a net water flow occurs from the more concentrated solutions (e.g. seawater) to the less concentrated one. This is the case if $\Delta p > \Delta\pi$. The net specific water flow across the membrane is [Gebel 2008]:

$$\dot{m}_{H_2O\_spec} = a_M \cdot (\Delta p - \Delta\pi) \qquad \text{Eq. 3.28}$$

$\dot{m}_{H_2O\_spec}$	[kg/s/m²]	net specific water flow across the membrane
a_M	[kg/s/m²/bar]	membrane constant
Δp	[bar]	applied hydrostatic pressure difference

The salt flow (or salt passage) does not depend on the applied pressure, but only on the osmotic pressure difference:

$$\dot{m}_{salt} = b_M \cdot (X_{HC} - X_{LC}) \qquad \text{Eq. 3.29}$$

b_M [bar/%] osmotic factor

RO Membranes

Membranes are the core of RO systems. The commercial application of RO membranes for seawater desalination started during the early 1980s due to the development of composite aromatic polyamides (AP) membranes, whereas "composite" means that salt rejection layer and supporting layer consist of different materials. This made the separate optimization of the two layers possible. As a result, the salt rejection could be significantly improved (approx. 99.5 %) in comparison to cellulose acetate membranes without reducing water permeability. In addition, chemical cleaning can be applied, as these membranes also withstand extreme pH values. These advantages made AP membranes the preferred technology for seawater RO applications. The main disadvantages of AP membranes are degradation in the presence of chlorine and a relatively high tendency to fouling.

A number of membrane modules such as plate-and-frame, spiral wound, tubular, capillary and hollow-fibre have been used for desalination purposes. These configurations are characterized by different packing density, fouling tendency, cleaning procedure and investment cost. The higher the packing density (i.e. the ratio between membrane surface area and module volume), the lower the cost but the higher the fouling tendency and the effort for cleaning.

Spiral wound modules (SWM) are commonly used for desalination processes (Figure 16). Two flat-sheet membranes are placed back-to-back and successively glued on three sides, so that they form an envelope. The free side is attached to a perforated tube, which serves as a permeate collector. The two membranes are successively wound around the permeate tube. The feed enters the module along the front-to-front side between the two membranes. A feed spacer is introduced on the feed side in order to guarantee a minimal distance between membranes and to enhance mixing. Part of the feed crosses the membranes, flows along a permeate carrier and is collected in the central tube. The remaining brine (also called retentate) is collected at the end of the module. Commercial SWM consist of 20 to 40 wound membranes (diameter approx. 20 cm, module length ca. 1 m). Accordingly, the typical thickness of the feed channel amounts to approx. 0.7 mm. The possible presence of suspended solids in the channels should be avoided as it may lead to obstructions.

NF membranes are typically used for softening (i.e. reduction of bivalent ions) or treatment of low salinity water. They are characterized by high water permeability but low salt

rejection (SR). On the contrary, seawater (SW) membranes and brackish water (BW) membranes have a very high salt rejection.

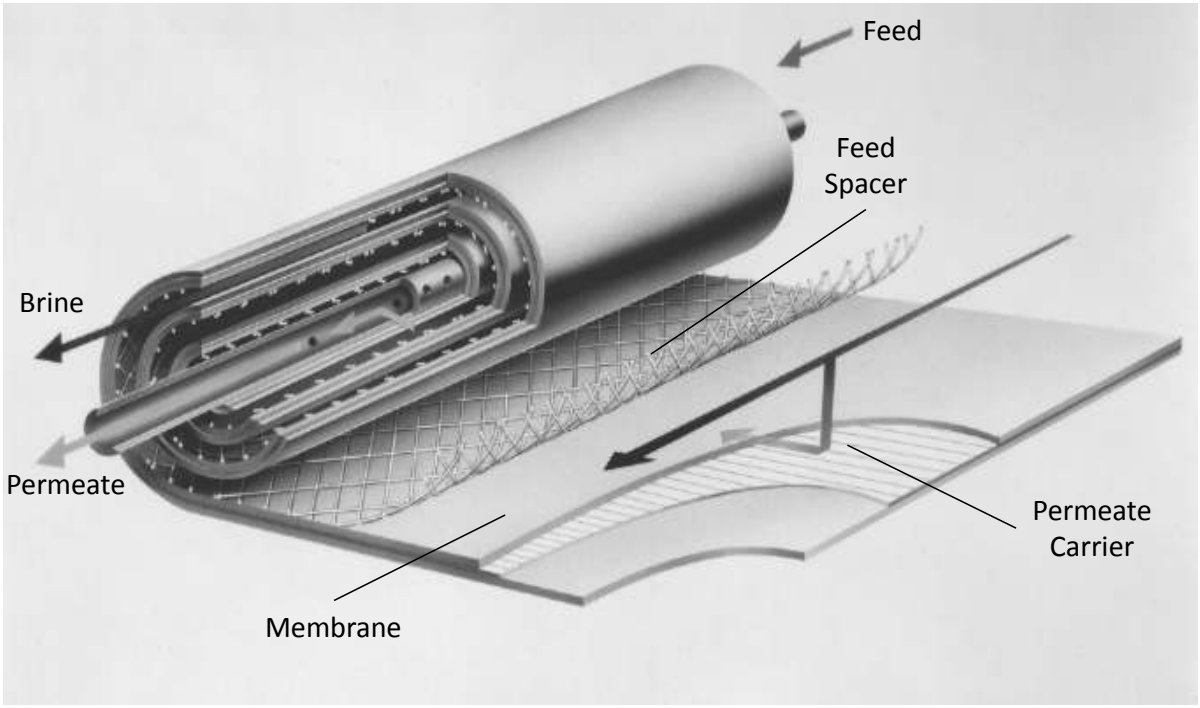

Figure 16: Scheme of a spiral wound RO module [Wilf 2007]

A selection of commercial membranes for SW, BW and NF applications with key performance data is presented in Table 6.

		SWRO		BWRO		NF	
	Unit	**SWC4+**	**SWC5**	**ESPA2+**	**ESPA4+**	**Hydracore**	**ESNA-LF**
Membrane Area	m^2	37.1	37.1	40.0	40.0	37.1	37.1
Permeate Flow	m^3/d	24.6	34.1	41.6	49.2	31.0	29.5
Salt Rejection (SR)	%	99.8	99.8	99.6	99.6	50.0	80.0
Test Flux Rate	$l/m^2/h$	27.6	38.2	43.5	51.3	34.8	33.2
Permeability	$l/m^2/h/bar$	1.0	1.5	5.0	8.2	7.7	7.2

Table 6: Key data of commercial membranes [Cipollina 2009]; BWRO = Brackish water reverse osmosis; SWC = Seawater composite membrane; ESPA = Energy saving polyamide membrane; ESNA = Energy saving nanofiltration membrane

In SWRO systems, a number of membrane elements (typically 6-8) are connected in series, whereas the retentate of the previous element serves as feed for the successive one. The elements are contained in a pressure vessel. As in each element a portion of water crosses the membrane, the salinity of the retentate gradually increases along the elements of the vessel. As a result, the osmotic pressure increases and the net water flow decreases, while the absolute salt passage is higher.

The reduction of net driving pressure along the stage, i.e. the difference between feed pressure and osmotic pressure, is shown in Figure 17.

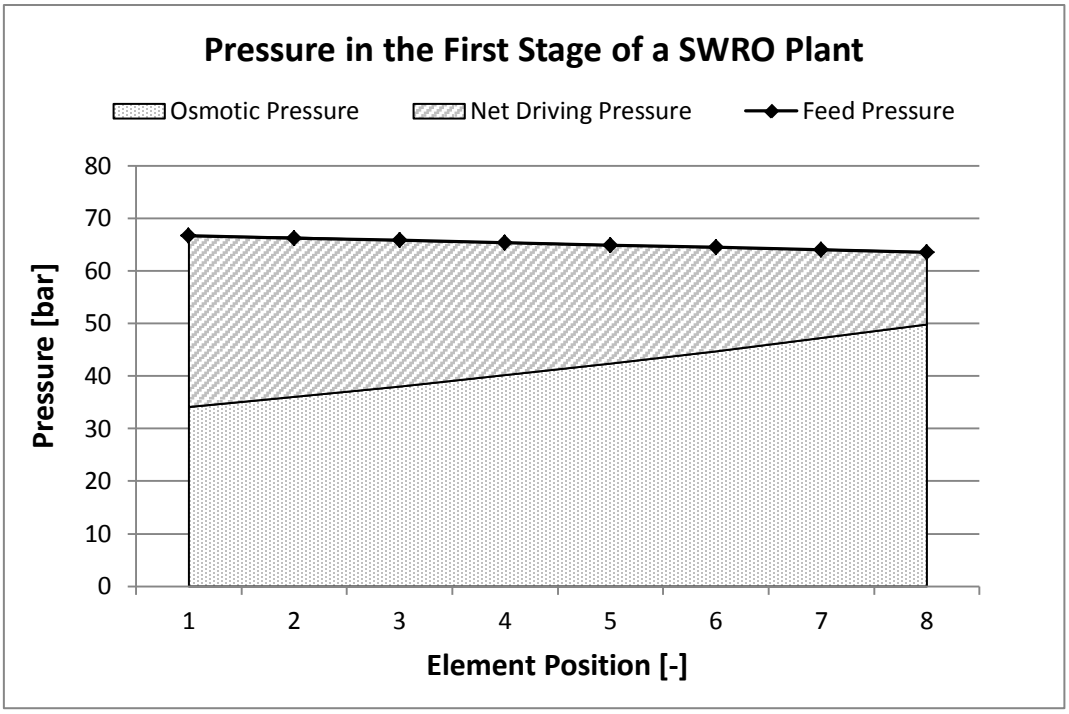

Figure 17: Pressure distribution in the first stage of a SWRO plant (8 elements)

Operating Parameters

The two most important design parameters of RO plants are the recovery rate (or yield) and the applied pressure. These two parameters are extremely important for the economics of the plant. The recovery rate R is defined as the ratio between permeate and feed mass flow:

$$R = \frac{\dot{m}_p}{\dot{m}_f} \qquad \text{Eq. 3.30}$$

$\dot{m}_p$	[kg/s]	permeate mass flow
$\dot{m}_f$	[kg/s]	feed water mass flow

Optimal R in SWRO applications is a compromise between opposing considerations. According to Eq. 3.30, the higher the recovery rate is, the lower the disposal mass flow (in the absence of environmental restrictions) and the investment cost for pretreatment equipment. However, high R also means elevate osmotic pressure on the retentate side and higher energy cost. The typical recovery rate in SWRO desalination plants is between 40 % and 55 %. In BWRO plants R ranges between 75 % and 90 %.

The choice of the recovery rate is also related to two other phenomena such as concentration polarization and scaling. Due to the membrane selectivity and to the laminar flow conditions near the membrane surface, salt and other rejected matters tend to accumulate into the boundary layer. Under steady state conditions, the salt accumulation equals the back-diffusion towards the bulk of the solution. The concentration polarization is a function of a number of parameters such as recovery rate, water flux across the membrane

and Reynolds number. Concentration polarization results in increased osmotic pressure, reduced water mass flow, higher permeate salinity and the risk of scaling due to the exceeding of solubility limits of certain suspended matters (e.g. silica, sulfate, magnesium and calcium ions). The concentration polarization factor CPF can be expressed as [Wilf 2007]:

$$CPF = k_p \cdot e^{\left(\frac{2 \cdot R_i}{2 - R_i}\right)} \quad \text{Eq. 3.31}$$

k_p	[-]	membrane constant
R_i	[K]	recovery ratio of the element i

The higher the recovery rate of a single element, the higher the polarization ratio. Membrane manufacturers recommend avoiding CPF higher than 1.2, which corresponds to R_i of approx. 18 %. In addition, it has been observed that the salt and water transport rate through membranes depends on temperature. Water and salt passage increases approx. 3 %/K within the typical RO temperature operation range (10 °C – 35 °C). Accordingly, the higher the temperature of seawater, the lower the required pressure. This behavior can be explained with the decreasing viscosity of water by increasing temperature [Wilf 2007]. The impact of varying temperature on plant performance is taken into account by means of a temperature correction factor TCF for water and salt passage [Wilf 2007]:

$$TCF = \left[e^{C_M \cdot \left(\frac{1}{T_{sw\_K}} - \frac{1}{T_{sw\_K0}} \right)} \right]^{-1} \quad \text{Eq. 3.32}$$

C_M	[-]	membrane-specific parameter (2,500 – 3,000)
T_{sw_K0}	[K]	reference seawater temperature expressed in Kelvin

However, the positive impact of temperature increase on energy consumption tends to level off above 30 °C, due to the increase of osmotic pressure in the downstream elements of the vessel (8.3.3). Finally, membrane performance declines over time. The reduction of the water flux and the consequent increase of salt passage are due to the formation of fouling layers and to mechanical damages on the membrane's surfaces (e.g. abrasion by particles, use of aggressive chemicals). The decrease of water flux is expressed as a function of the average operation time of the membranes and is therefore related to the membrane replacement rate [Wilf 2007]:

$$MAF_{H_2O} = \left(1 - \Delta\Phi_{H_2O}\right)^t \quad \text{Eq. 3.33}$$

MAF_{H_2O}	[-]	membrane ageing factor with regard to water passage
$\Delta\Phi_{H_2O}$	[%/y]	relative water passage loss (assumed: 7 %/y)

t	[y]	average membrane operation time in years

The salt passage increase over time is assumed to be linear:

$$MAF_{salt} = 1 + \Delta\Phi_{salt} \cdot t \qquad \text{Eq. 3.34}$$

MAF_{salt}	[-]	membrane ageing factor with regard to salt passage
$\Delta\Phi_{salt}$	[%/y]	relative salt passage increase (assumed: 10 %/y)

RO Plant Configuration

The membrane assembly unit (also called "RO train") consists of pressure vessels, piping and manifolds. Each pressure vessel typically contains up to 8 membrane elements. A number of vessels connected in parallel is referred to as a "stage". The configuration of RO stages mainly depends on the available feed water salinity and the required permeate quality. The ratio between the number of vessels in the first and in the second stage is typically 2:1 [Wilf 2007], so that the flow rates of feed and retentate remains almost constant along the entire RO train. Therefore, the risk of elevated pressure drops (e.g. due to very high feed flow) or high CPF (e.g. insufficient feed flow) is avoided.

3.2.3 RO Model

Design and operation of RO plants depend on several parameters such as plant capacity, seawater quality (temperature, salinity and their seasonal variations) and required permeate composition (salinity, boron concentration etc.) [Ludwig 2010]. The implemented model simulates a typical large-scale SWRO plant. The reference configuration is shown in Figure 18. Other common configurations are shown in Annex 10.1.3. The pre-treated feed water enters the high pressure pump, where it reaches operating pressure. The required pressure has to be higher than the sum of osmotic pressure at the end of the first stage and several pressure losses (frictional, piping and other equipment) (Eq. 3.39).

The pressurized water enters the first RO stage, which consists of 6-8 membrane elements. The permeate is separately collected at both ends of the stage. The low-salinity permeate from the first three elements is blended with the permeate of the second stage. The remaining permeate from the first stage passes through a booster pump and enters the second stage. Due to the lower salinity of the feed, the pressure applied by the booster pump is much lower than the pressure applied by the HP (high pressure) pump.

Other particularities of the selected layout are recycling of the second stage's brine, which has very low-salinity (typically few thousands ppm). The brine is mixed with pre-treated feed water, thus allowing for a slight reduction of the overall HP pump requirements. A much larger reduction of the power consumption is provided by the reuse of the pressure of the first-stage brine. Different energy recovery devices (ERD) exist, which will be described in a

dedicated section within this chapter. Finally, an additional by-pass is foreseen upstream of the booster pump.

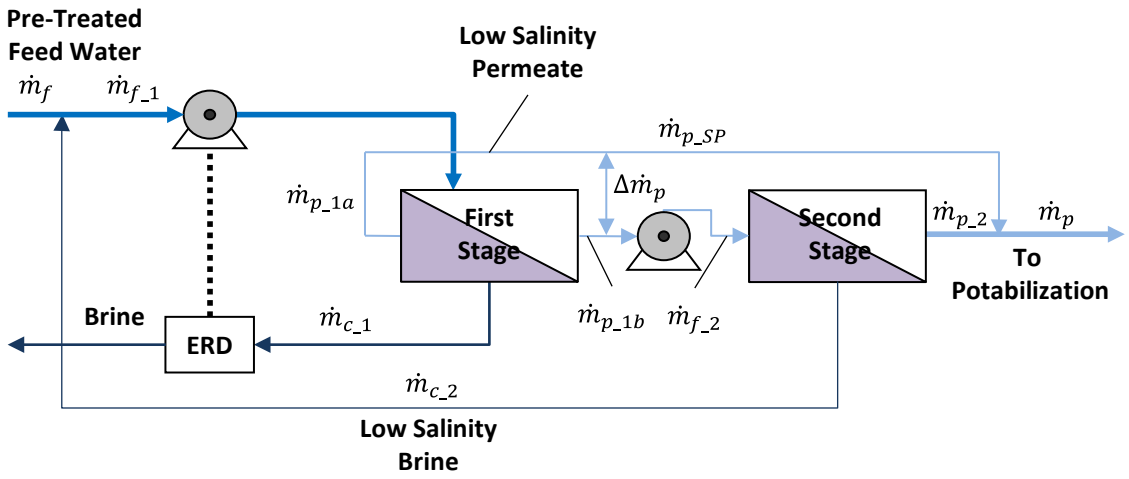

Figure 18: Scheme of the simulated SWRO plant – Adapted from [Wilf 2007], [Ludwig 2010]

This layout allows adjusting flow rates to variations of seawater temperature and salinity as well as minimizing investment and operating cost of the SWRO plant (e.g. smaller second stage, lower energy consumption) [Ludwig 2010]. The first step of the modeling procedure is the estimation of the required feed water flow. A number of assumptions have to be made with regard to:

- membrane type (membrane area, salt, rejection)
- recovery rate of first and second stage
- stage layout (i.e. number of elements per vessel and number of parallel vessels in each stage).

For this scope, Table 7 may be used as a guideline. For seawater applications, SW5 membranes or similar are commonly used in the first stage, while the second stage is typically equipped with brackish water membranes such as ESPA4+ or similar (Table 6).

Parameter	Unit	1st Stage	2nd Stage
Membrane Type	-	SW5 or similar	ESPA4+ or similar
Recovery Rate	%	35 - 55	85 - 90
Permeate Flux	l/m²/h	11 - 15	25 - 32
Elements per Vessel	-	6 - 8	6 - 8
Split Partial Ratio (SPR)	%	20 - 60	-

Table 7: Guideline for the selection of two-stages SWRO plants – [Wilf 2007], [Ludwig 2010]

The split partial ratio SPR is defined as:

$$SPR = \frac{\dot{m}_{p\_SP}}{\dot{m}_p} \qquad \text{Eq. 3.35}$$

$\dot{m}_{p\_SP}$ [kg/s] split partial mass flow

$\dot{m}_p$	[kg/s]	final permeate mass flow

The higher SPR is, the smaller is the required capacity of the second stage, but the higher is the salt content of the final permeate. With regard to Figure 18, the following mass balances can be written:

$$\begin{cases} \dot{m}_p = \dot{m}_{p\_2} + \dot{m}_{p\_SP} \\ \dot{m}_p = \dot{m}_{f\_2} \cdot R_2 + SPR \cdot \dot{m}_p \end{cases} \quad \text{Eq. 3.36}$$

$\dot{m}_{p\_2}$	[kg/s]	permeate production of the second stage
$\dot{m}_{f\_2}$	[kg/s]	feed water at the inlet of the second stage
R_2	[-]	recovery rate of the second stage

The feed water mass flow at the entrance of the second stage $\dot{m}_{f\_2}$ is expressed as function of $\dot{m}_{f\_1}$:

$$\begin{cases} \dot{m}_{f\_2} = \dot{m}_{p\_1} - \dot{m}_{p\_SP} \\ \dot{m}_{f\_2} = \dot{m}_{f\_1} \cdot R_1 - SPR \cdot \dot{m}_p \end{cases} \quad \text{Eq. 3.37}$$

$\dot{m}_{f\_1}$	[kg/s]	feed water at the inlet of the first stage
R_1	[-]	recovery rate of the first stage

Finally, the substitution of $\dot{m}_{f\_2}$ in Eq. 3.36 allows estimating the required feed water flow $\dot{m}_{f\_1}$:

$$\dot{m}_{f\_1} = \frac{\dot{m}_p \cdot [1 + SPR \cdot (R_2 - 1)]}{R_1 \cdot R_2} \quad \text{Eq. 3.38}$$

The following step consists of the calculation of the required pressure to be applied by the HP pump:

$$\Delta p_{HP} = \Delta \pi_{end} \cdot k_s + \sum_{i=1}^{i_{final}} p_{loss\_i} \quad \text{Eq. 3.39}$$

Δp_{HP}	[bar]	pressure difference applied by the high pressure pump
$\Delta \pi_{end}$	[bar]	osmotic pressure at the end of the vessel
k_s	[-]	security factor (start value: 1.1 – 1.15)
p_{loss}	[bar]	pressure losses in the element i

The applied pressure has to overcome pressure losses and increasing osmotic pressure along the vessel. In order to avoid negative values of net pressure difference, a security factor k_s is considered. This procedure is required to define the first guess value of the feed pressure. The final value of Δp_{HP} is found through an iterative process as described later. The value of the osmotic pressure at the end of the stage is calculated using Eq. 3.27, whereas the salinity of the brine X_{c_1} is:

$$X_{c\_1} = \left(1 + \frac{R_1 \cdot SR_1}{1 - R_1}\right) \cdot X_f \qquad \text{Eq. 3.40}$$

SR_1	[%]	salt rejection of the membranes in the first stage

Recovery rate and salt rejection are model inputs. The calculation proceeds with the detailed calculation of permeate production in each element of the vessel. The pressurized feed water enters the first element of the stage. The average osmotic pressures within each element are calculated as a logarithmic mean in order to consider the salinity increase of the feed along the element:

$$AFS_i = \frac{X_{f\_i}}{R_i} \cdot ln\left(\frac{1}{1 - R_i}\right) \cdot CPF_i \qquad \text{Eq. 3.41}$$

AFS_i	[ppm]	average feed salinity of element i

The recovery rate of the elements R_i is not known a priori; therefore a guess is needed to start the iterative process. The water flow through the membrane is (Eq. 3.28):

$$\dot{m}_{H_2O} \cong \dot{m}_p = a_M \cdot \left(\bar{p}_{f\_i} - \bar{\pi}_{osm\_i}\right) \cdot A_M \qquad \text{Eq. 3.42}$$

$\bar{p}_{f\_i}$	[kg/s]	average feed pressure of element i
$\bar{\pi}_{osm\_i}$	[kg/s]	average osmotic pressure of element i

The water flow is assumed to be equivalent to the total permeate flow (water and salt), as the salt passage is negligible (approx. three orders of magnitude smaller). The membrane constant a_M is calculated using testing conditions provided by the membrane manufacturer:

$$a_M = \left[\frac{\dot{m}_{p\_0}}{A_M \cdot \left(\bar{p}_{f\_0} - \bar{\pi}_{osm\_0}\right)}\right] \cdot TCF \cdot MAF_{H_2O} \qquad \text{Eq. 3.43}$$

The expression within the square brackets represents the nominal conditions, i.e. 25 °C and a new membrane. In addition, the impact of temperature and membrane ageing are considered by the factors TCF and MAF_{H_2O}, respectively.

The permeate salinity is the ratio between salt and water passage:

$$X_{p\_i} = \frac{\dot{m}_{salt}}{\dot{m}_{H_2O}} \qquad \text{Eq. 3.44}$$

The salt passage is calculated according to Eq. 3.29. The osmotic factor b_M is:

$$b_M = \frac{1 - SR}{SR} \cdot \dot{m}_{H_2O\_spec\_0} \qquad \text{Eq. 3.45}$$

$\dot{m}_{H_2O\_spec\_0}$ [kg/s/m²] specific water flow under membrane testing conditions

Finally, the salinity of the concentrate is:

$$X_{c\_i} = \frac{X_{f\_i} - R_i \cdot X_{p\_i}}{1 - R_i} \qquad \text{Eq. 3.46}$$

The procedure continues with the calculation of the successive elements. The feed of each new element corresponds to the concentrate of the previous element. At the end of the first iteration, the permeate salinity as well as the recovery rate do not match exactly the given specifications. Therefore, an iterative calculation is necessary. The entire procedure is repeated adjusting the initial feed pressure and the split partial ratio.

Energy Consumption

The energy consumption of an RO plant consists of the sum of the consumption of each process, i.e. high pressure pump, the booster pump, pre-treatment, potabilization and waste water treatment:

$$P_{RO} = P'_{HP} - P_{ERD} + P_{BP} + P_{PreT} + P_{Pot} + P_{WWT} \qquad \text{Eq. 3.47}$$

P_{RO}	[MW]	RO electrical power demand
P'_{HP}	[MW]	high pressure pump power without energy recovery
P_{ERD}	[MW]	power savings by energy recovery device
P_{BP}	[MW]	booster pump power
P_{PreT}	[MW]	power for feed water pre-treatment
P_{Pot}	[MW]	power for potabilization
P_{WWT}	[MW]	power for waste water treatment

The total energy consumption is dominated by the HP pump demand. A portion of the brine's energy content of the first stage can be recycled by means of energy recovery devices

such as energy recovery turbines or pressure exchange systems (PX). In the first case, the pressurized brine impinges on the blades of a Pelton turbine, whose shaft is connected with the HP pump. Such systems allow for approx. 30 % energy savings in comparison to a RO plant without ERD. The net power requirements of the HP pump is:

$$P_{HP} = P'_{HP} - P_{ERD} = \frac{\dot{m}_{p\_1} \cdot \Delta p_{HP}}{\rho_p \cdot \eta_{HP}} \qquad \text{Eq. 3.48}$$

P_{HP}	[MW]	high pressure pump net power
η_{HP}	[-]	efficiency of high pressure pump

Due to their high efficiency (approx. 98 %), PX systems have gained wide acceptance in the last years. The energy consumption of the booster pump P_{BP} is calculated as:

$$P_{BP} = \frac{\dot{m}_{f\_2} \cdot \Delta p_{BP}}{\rho_p \cdot \eta_{BP}} \qquad \text{Eq. 3.49}$$

As the second stage is not equipped with any ERD, the entire feed mass flow $\dot{m}_{f\_2}$ has to be brought to operation pressure. On the contrary, in Eq. 3.48 the used mass flow is $\dot{m}_{p\_1}$, due to the fact that the energy content of the brine is almost totally recovered by the PX system. The power consumption of the remaining processes are assumed to be a function of the type of pre-treatment and feed water salinity according to [Ludwig 2010].

3.2.4 Drinking Water Post-Treatment

The post-treatment in SWRO plants is less demanding, as salinity in permeate is usually sufficiently high (Figure 19). Limestone filtration is not needed. However, calcium hydroxide ($Ca(OH)_2$) is added to increase calcium content and to prevent corrosion. Air addition is also not required due to the lower RO process temperature in comparison to thermal desalination. Specific additional post-treatment may be required in SWRO plants to remove excess silica and boron [Fritzmann 2007].

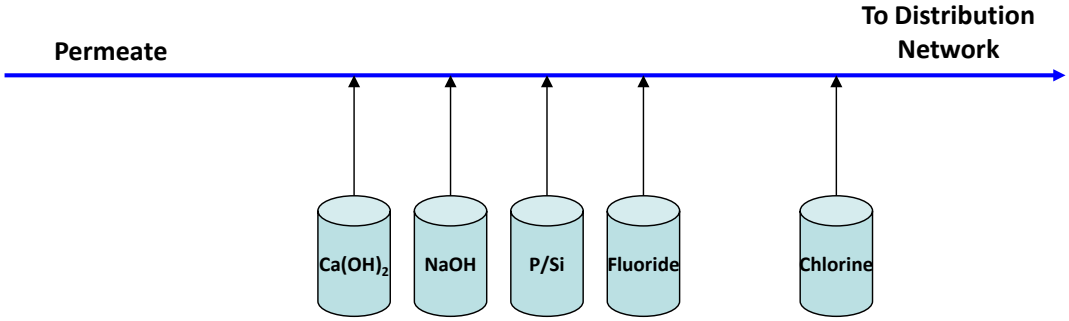

Figure 19: Post-treatment process in a typical large-scale SWRO plant [Gebel 2008]

3.2.5 Brine Discharge

In reverse osmosis processes, brine salinity may reach up to 85,000 ppm. The brine density is higher than the density of seawater and the brine plume is characterized by negative buoyancy, i.e. the brine mainly flows along the sea bottom. In addition, brine from RO plants typically contains a number of potential contaminants such as various chemical residues from the pre-treatment process and cleaning solutions [Lattemann 2008]. Such potential contaminants do not only have a negative impact on marine environment, but also reduce public acceptance of desalination and potentially represent a hazard for local tourism and the fishing industry [Morillo 2014].

3.2.6 RO INSEL Block

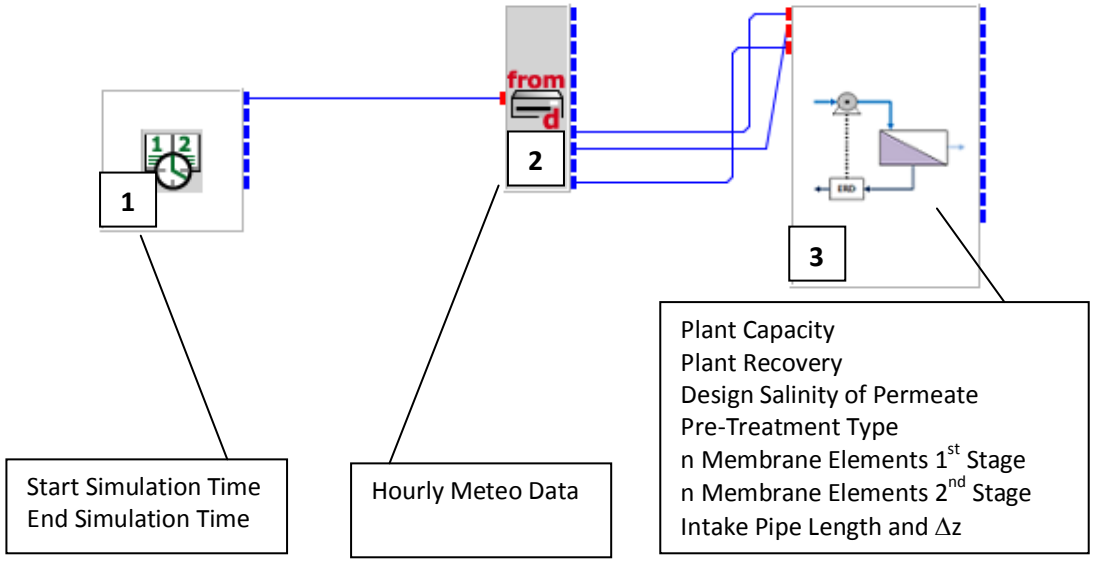

1 - Time Block		2 - Read Block		3 - RO	
Input	**Output**	**Input**	**Output**	**Input**	**Output**
-	Time	Time	T_{sw} X_{sw} H_2O Demand	T_{sw} X_{sw} H_2O Demand	$\dot{m}_p$ X_p R Part Load $\dot{m}_f$ $\dot{m}_c$ X_c A_M SEC_{intake} $SEC_{RO\ Plant}$

Figure 20: Screenshot of the developed RO INSEL model with specification of main design parameters (in the boxes), input and output values (in the table) for each INSEL block; Note: only relevant parameters for this particular simulation are listed in the table; the complete list of the parameters of the newly developed INSEL blocks is reported in Annex 10.5; for commercial INSEL blocks refer to [INSEL]

4 Concentrating Solar Power (CSP) Models

Concentrating solar power allows the conversion of solar irradiation into high temperature heat, which is then transformed into mechanical energy and finally into electricity (Figure 21). Concentration of the solar radiation is a requirement for the achievement of high temperatures (8.2.1 and Annex 10.2.1). The generation of electricity typically occurs using a conventional steam cycle (Rankine cycle). In principle, a gas turbine could also be used [Schwarzbözl 2006]. The key component of this technology is the solar field, which consists of a series of mirrors (collectors) that reflect direct normal irradiance (DNI) to a focus line or point (receiver). Temperatures up to over 1,000 °C can be achieved, depending on the selected technology [Buck 2008]. Contrary to other renewable energy technologies such as PV or wind power, these plants are able to deliver power capacity on demand (dispatchable power), thanks to the utilization of the thermal energy storage (TES). The optimal utilization of the TES is reached by over-sizing the solar field (with respect to the turbine requirements) and storing the share of the heat which exceeds the turbine capacity into the TES [Trieb 2009]. The surplus energy can be used whenever required for later power generation, for short-term compensation of cloud transients or for anti-freezing purposes in the solar field during stand-by periods.

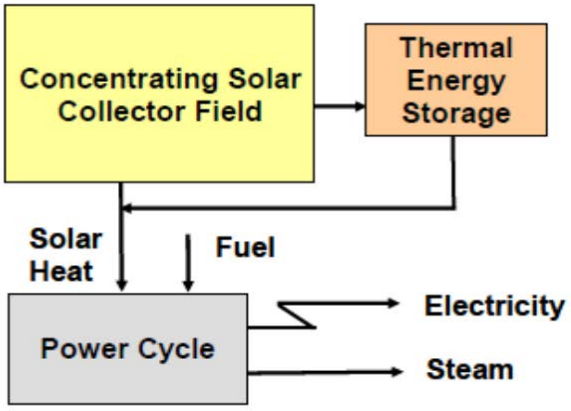

Figure 21: Basic scheme of a CSP plant [AQUA-CSP 2007]

Base load operation is possible and has already been demonstrated in the Gemasolar plant [Gemasolar 2013]. The plant dispatchability is guaranteed also at times with no DNI and completely discharged TES, since CSP makes use of conventional steam cycles, in which hybrid operation with fossil fuel is possible. In this sense, solar energy can be seen as an effective and flexible fuel saver within a conventional power plant. From the point of view of a grid operator, CSP with TES and auxiliary heater behave like any other fossil-fired power plant. For this reason CSP also represents an important factor for grid stability in future electricity supply systems with high shares of renewable energy. This feature will be particularly important in the Middle East and North Africa, where the potential of other balancing and flexible renewable resources such as biomass and hydropower is limited. CSP

plants for electricity production can be designed from 5 MW to several 100 MW of capacity. Smaller capacities would not be economically attractive, at least in the short term, while the upper capacity limitation is typically given by a techno-economic optimization of the solar field size. The design of CSP plants can be adapted to the demand and to the load segments (base-, intermediate- or peak load), as required by grid operators [Trieb 2012]. In addition, CSP offers a wide spectrum of potential applications: electricity can be used not only for local purposes, but -due to the high power quality and to the huge potentials- also for export e.g. from MENA to Europe [Trieb 2009 b]. Other options are the combined production of electricity and heat, which in turn can be used to run thermal and reverse osmosis desalination plants [AQUA-CSP 2007], [Moser 2013]. The collected heat could also be used for industrial heating processes and cooling applications. Finally, CSP also holds potential for the generation of other energy carriers such as hydrogen and other solar hydrocarbon fuels [Buck 2008], [Pregger 2009]. The worldwide CSP installed capacity currently is approximately 2.5 GW [CSP Today 2013], which is a factor more than 100 times smaller than the worldwide installed wind power capacity. This means that substantial scale effects, technological improvements and investment cost reduction can still be expected.

Collectors

CSP can be classified in line focusing and point focusing systems. Line focusing systems comprehend parabolic trough (PT) and linear Fresnel reflectors (LF). Point focusing systems include central receiver (CR, or solar tower) and parabolic dishes. Each technology has different characteristics and presents a different degree of technological maturity. The parabolic trough technology has been commercially available for almost 30 years and can be considered as a proven technology also with the relatively recent combination with the two-tank indirect molten salt storage. In contrast, Fresnel reflectors and Solar Tower only recently became commercially available. Finally, Dish Stirling shows serious disadvantages despite its high efficiency; these include the lack of a suitable thermal storage and the direct competition with the cheap PV technology.

Thermal Energy Storage

Unlike PV and wind power, which directly convert available resources into electrical power, CSP first transforms the absorbed radiation into thermal power. Thus, a part of the collected heat can be cost-effectively stored in the thermal energy storage. Thermal storage in CSP applications is typically used to provide backup during periods with low or no irradiation (e.g. avoiding partial load operation during cloud transients) and to prolong electricity generation to evening and night hours [Sioshansi 2010]. In addition, a storage allows for adapting electricity generation to the demand. Even if thermal storage is essential for making CSP dispatchable, it is also one of the less developed components [Gil 2010]. There are three types of TES, i.e. sensible, latent, and thermochemical. In sensible heat storage systems the energy is stored in the temperature increase of the storage medium. This kind of storage is the most used in commercial CSP applications. Thermal energy can alternatively be stored

almost isothermally in latent heat energy storages. In this case the energy is stored in the phase change of a so-called phase change material (PCM). Latent heat storage systems present higher energy density than sensible storage systems. However, optimal heat transfer design, media selection and material degradation are still challenging issues [Steinmann 2010]. The third storage option is based on reversible endothermic chemical reactions. During storage charge procedures, heat has to be provided to the storage system. Despite of several technical advantages, the development of this kind of storage is still at a very early stage.

Power Block

The power block consists of the equipment required to convert thermal energy into mechanical and finally electrical energy. In large-scale CSP applications, the power block typically is a conventional steam Rankine cycle. The essential components of this system are a steam generator, a steam turbine, a condenser and a feed-water pump [Strauß 2007].

4.1 Sun Position Calculation

The accurate assessment of the angle between the sun and the normal vector to the collector surface is of essential importance for the calculation of the performance of solar systems, and in particular of concentrating systems. This angle is referred to as the incidence angle θ (Figure 22). Aim of this module is the calculation of the position of the sun at each time step of the simulation, which is the first step in order to calculate the incidence angle. The final assessment of θ will not be part of this module. This is because the position of the collector is technology-specific, as tracking of the collectors may be involved (CSP, tracking PV). According to Figure 22, the position of the sun is described by two angles, i.e. the sun elevation angle α_s and the solar azimuth γ_s [Duffie 1991]:

$$\alpha_s = arcsin(\sin\phi \cdot \sin\delta + \cos\phi \cdot \cos\delta \cdot \cos\omega) \qquad \text{Eq. 4.1}$$

$$\gamma_s = \begin{cases} 360° + arcsin\dfrac{-\cos\delta \cdot \sin\omega}{\cos\alpha_s}; & if \quad \cos\omega < \dfrac{\tan\delta}{\tan\phi} \\ 180° - arcsin\dfrac{-\cos\delta \cdot \sin\omega}{\cos\alpha_s}; & if \quad \cos\omega \geq \dfrac{\tan\delta}{\tan\phi} \end{cases} \qquad \text{Eq. 4.2}$$

α_s	[°]	sun elevation angle; positive if the sun is above the horizon
ϕ	[°]	geographic latitude; positive in the northern hemisphere
δ	[°]	declination; positive in spring and summer (Eq. 4.3)
ω	[°]	hour angle; positive after noon (Eq. 4.4)
γ_s	[°]	solar azimuth angle (positive, as defined in Figure 22)

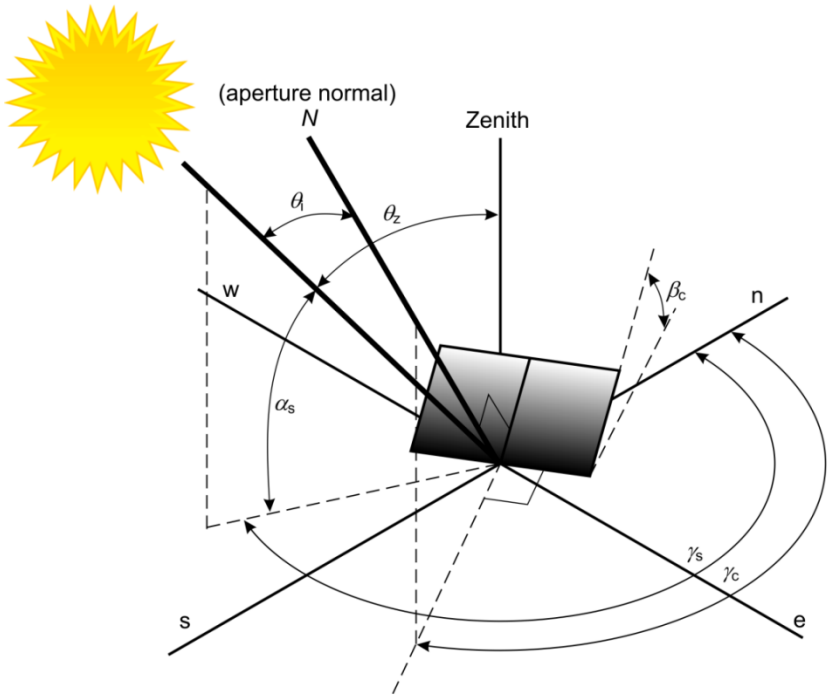

Figure 22: Definition of sun-collector angles [EnerMENA 2012]

The declination angle δ is the angle between the sun elevation at noon and the earth equator plane. This angle changes over time due to rotation of the earth around the sun [Sokrates 2004]:

$$\delta = 23.27 \cdot sin\left(360 \cdot \frac{DoY - 80}{365.25}\right) \qquad \text{Eq. 4.3}$$

DoY	[-]	day of the year

The value of the declination varies along the year between $-23.27° \leq \delta \leq +23.27°$. The hour angle ω corresponds to the local time in degrees:

$$\omega = \frac{360}{24} \cdot t_{local} \qquad \text{Eq. 4.4}$$

The local time is calculated starting with the standard time. The standard time has been introduced for practical reasons in order to synchronize clocks in different geographical locations within a time zone. In contrast, the local time uses the local meridian (i.e. geographical latitude) as reference. The local time is calculated as:

$$t_{local} = t_{UTC} - 12 + \frac{24}{360} \cdot \varphi + ET \qquad \text{Eq. 4.5}$$

t_{UTC}	[-]	UTC time
φ	[°]	geographic longitude; positive eastern from reference meridian
ET	[h]	equation of time

In Eq. 4.5 the equation of time also appears. This term considers the fact that -due to the elliptical rotation of the earth around the sun- the local time advances non-uniformly. In other words, depending on the current earth position relative to the sun, the duration of one day is slightly shorter or longer than 24 hours. The formulation of ET proposed by Spencer, cited by [Duffie 1991] has been used.

4.2 Parabolic Trough

PT systems use parabolic mirrors to concentrate direct-beam radiation onto a receiver located on the focal line of the parabola (Figure 23). Currently available collectors have an aperture width between 4.4 meters [Kearney 2007] and 6.8 meters [Kötter 2010]. The typical optical concentration ratio is ca. 80. The solar collectors are supported by a metal structure and -at both ends- by pylons. Line focusing technologies are equipped with one-axis tracking systems. For this purpose, one of the pylons is furnished with hydraulic drive units. The steel supporting structures must be designed in order to prevent deviations of the collector from nominal incidence also in case of wind loads [Barlev 2011].

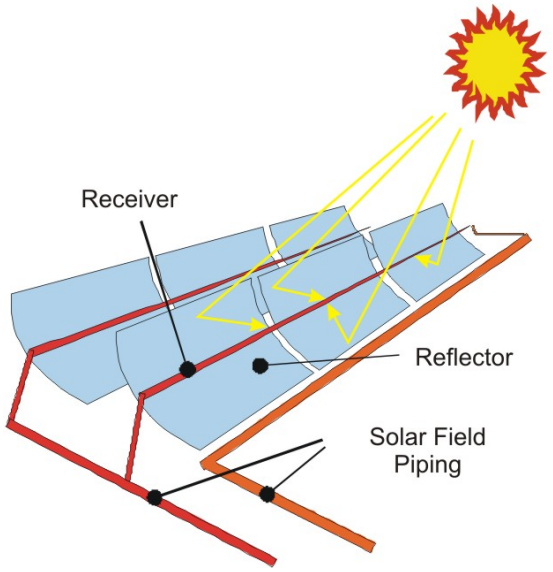

Figure 23: Scheme of a parabolic trough solar field [EnerMENA 2012]

The receivers are constituted by special coated steel tubes and evacuated glass envelopes in order to minimize heat losses by convection. So-called ball joints connect the receivers of two consecutive collectors and allow for independent tracking of each collector. Parabolic trough solar fields are typically designed in parallel rows, each row being ca. 600 meter long. Groups of collectors are organized in two or more subfields (4.2.3). The heat collected in the solar field is either transferred through the piping system to the water/steam loop of the Rankine cycle to directly generate electricity or stored in the TES. The majority of the current parabolic trough solar fields run on thermo-oil as HTF; however, molten salt or water/steam can alternatively be used.

This chapter describes in detail the parabolic trough model which has been implemented in INSEL. The parabolic trough model is structured in several sections, i.e. geometrical efficiency, receiver, piping, transient effects and model adaptations for different HTFs.

4.2.1 Geometrical Efficiency

Several loss mechanisms reduce the available incoming solar radiation. Some of these losses are due to non-ideal material properties and geometrical imperfections in the collector manufacturing, while other losses are caused by the single-axis tracking and depend on the position of the sun.

Optical Losses

A series of losses is caused by manufacturing and assembling errors such as tracking errors and mirror alignment errors. Other loss mechanisms are due to non-ideal material properties (e.g. mirror reflectance and absorptivity). Finally, dirt presence on collector and absorber further reduce the performance of the collectors [Forristall 2003]. These losses are independent of the sun position. The design optical efficiency η_{opt_peak} is:

$$\eta_{opt\_peak} = \frac{\dot{Q}_{abs\_design}}{DNI_{design} \cdot A_{sf}} \qquad \text{Eq. 4.6}$$

$\dot{Q}_{abs\_design}$	[MW_{th}]	solar energy absorbed by the receiver under design conditions
A_{sf}	[m^2]	mirror area of the solar field

whereas perpendicular irradiation (i.e. incidence angle equal to zero) is assumed. More details are reported in [Sokrates 2004].

Cosine Losses

According to Figure 22, the position of the collector is characterized by the collector azimuth γ_c and by the collector axis tilt β_c. As parabolic trough collectors are commonly oriented in the North-South direction and track the sun in the East-West direction, the formula for the calculation of the incidence angle can be simplified [EnerMENA 2012] [Duffie 1991]:

$$\cos\theta = \sqrt{1 - \cos^2\alpha_s \cdot \cos^2\gamma_s} \qquad \text{Eq. 4.7}$$

The cosine of the incidence angle θ describes the portion of the collector which is effectively "seen" by the sun at different times (i.e. the projection of the collector surface on the plane perpendicular to the sun beams). This loss mechanism is independent of the selected collector and goes under the name of cosine losses. The lower the incidence angle, the lower the cosine losses. For collector orientations other than North-South, Eq. 4.7 is not valid anymore and the general formula should be used (Annex 10.2.2) [Duffie 1991].

Incidence Angle Modifier (IAM)

Before a simulation is started, the INSEL user has the possibility to select specific collectors and receivers in the block parameters window of the solar field module (Annex 10.5, Table 71). Different types of commercial parabolic trough collectors and receivers are implemented. An overview on the available options and on their geometrical characteristics is given in Annex 10.2.3 (Table 41) [Cordes 2011]. SKAL-ET 150 collectors and PTR-70 receivers are used in the standard case. Once the geometry of the collectors is defined, the model can proceed with the calculation of a further loss mechanism, i.e. the incidence angle modifier.

The IAM is caused by the fact that sun beams are not perfectly parallel, as the sun is seen from the earth as a disk with a finite solid angle (16´). This means that the direct solar radiation, which is reflected from a point on the receiver, comes from a cone of beams. This cone is then reflected with the same angle onto the receiver. Therefore IAM losses depend on the collector geometry as well as on the actual incidence angle. IAM losses are typically described by polynomial equations as a function of the incidence angle and are determined with measurements or ray-tracing simulations [Dudley 1994], [EnerMENA 2012].

Shading

During morning and evening hours -due to the low sun elevation angle- a part of the collector aperture is shaded by the neighbor collector. The shading effect is [Sokrates 2004]:

$$\eta_{shad} = 1 - min\left(0; \frac{n_{row} - 1}{n_{row}} \cdot \frac{Ap - d_{row} \cdot \cos\rho_t}{Ap}\right) \qquad \text{Eq. 4.8}$$

n_{row}	[-]	number of parallel rows in a sub-field
Ap	[m]	collector aperture
d_{row}	[-]	distance between parallel rows
ρ_t	[°]	tracking angle

For North-South oriented collectors, the tracking angle is expressed as:

$$\rho_t = arctan\left(\frac{\cos\gamma_s}{\tan\alpha_s}\right) \qquad \text{Eq. 4.9}$$

End Effects

Due to the distance between two collectors put in series, a part of the radiation reflected by the final part of a collector does not meet the receiver (if the incidence angle is larger than zero) and is lost:

$$\eta_{end} = 1 - \frac{f_C \cdot \tan\theta}{L_{coll}} + \eta_{end\_gain} \qquad \text{Eq. 4.10}$$

f_C	[m]	focal length of the collector
L_{coll}	[m]	length of a collector module
η_{end_gain}	[-]	end-gain efficiency

The end-gain efficiency takes into account that -typically- a part of the lost radiation in the previous collector meets the receiver of the following module:

$$\eta_{end\_gain} = \frac{n_{coll\_\Sigma} - 1}{n_{coll\_\Sigma}} \cdot \frac{max(0; f_C \cdot \tan\theta - d_{coll})}{L_{coll}} \qquad \text{Eq. 4.11}$$

n_{coll_Σ}	[-]	number of aligned serial collectors
d_{coll}	[-]	distance between serial collectors

Finally, the geometrical efficiency η_{geo} is given by the multiplication of the efficiencies of the four loss mechanisms:

$$\eta_{geo} = \cos\theta \cdot IAM \cdot \eta_{shad} \cdot \eta_{end} \qquad \text{Eq. 4.12}$$

4.2.2 Receiver Model

The receiver model is based on the energy balance of the absorber tube, which includes the impact of DNI and of geometrical, optical and thermal losses and the effective heat gain into the HTF. The collector configuration has been set according to the current typical layout of parabolic trough solar fields. In the base case (SKAL-ET 150 collectors), each loop consists of four collectors, arranged in two parallel rows with two collectors for each row. The total length of one loop is approximately 600 m. The parabolic trough receiver model is based on a series of nested iterative calculation loops, which are repeated at each time step of the simulation. This chapter focuses on the description of the model structure and the iteration procedure, as exemplified in Figure 24. At each time step, the geometrical collector efficiency is calculated. In order to calculate the net heat absorbed by the receiver $\dot{Q}_{abs}$ and heat losses between HTF and ambient $\dot{Q}_{loss}$, a radial steady-state energy balance between HTF, absorber, glass envelope and ambient is applied.

Because physical properties of materials (absorber emissivity, HTF heat capacity and density etc.) depend on temperature, the entire length of the collector loop is divided into a series of short steps (Δx).

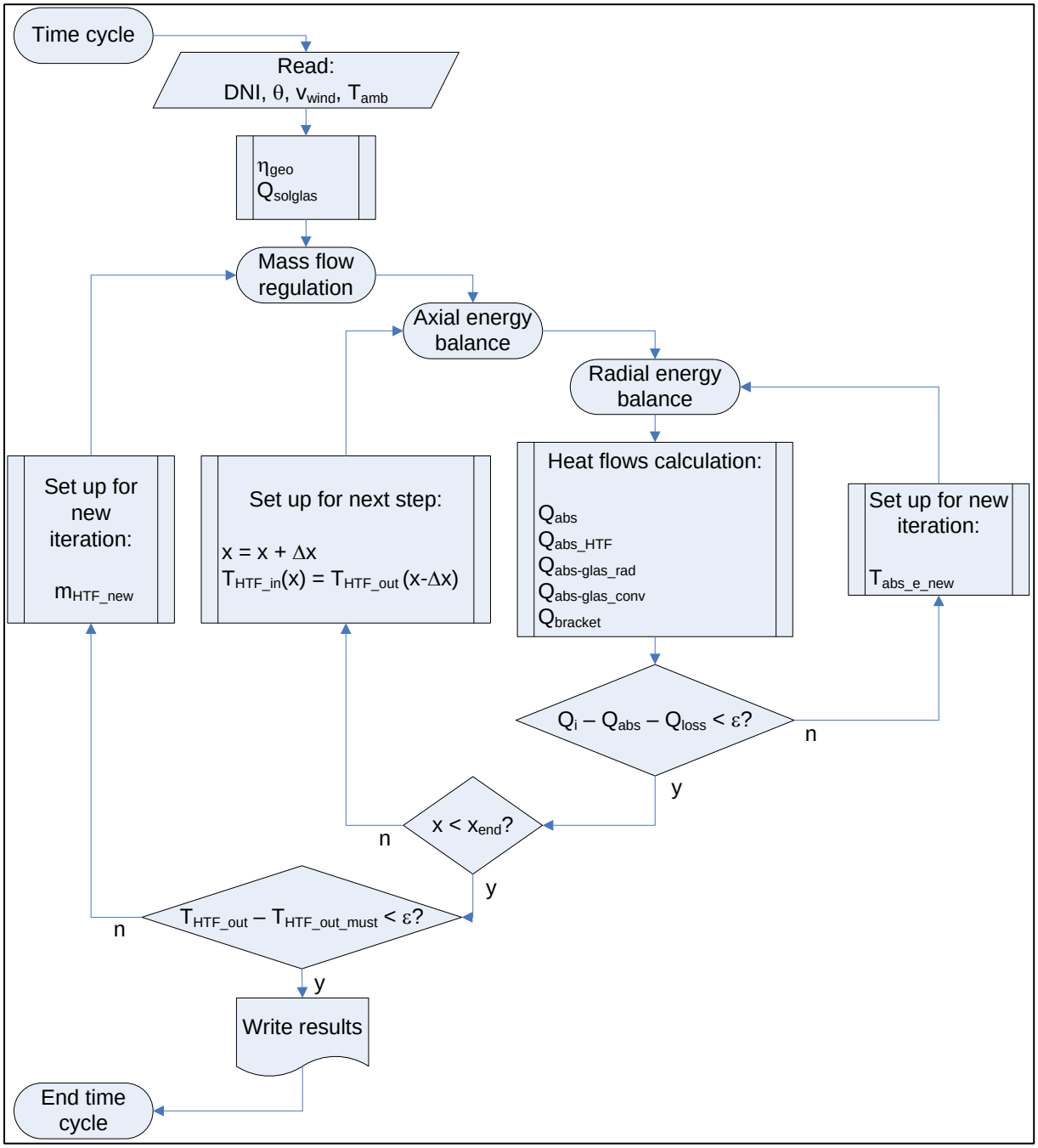

Figure 24: Flow diagram of the implemented absorber model; ε = tolerance

Figure 25 shows schematically the heat transfer mechanisms for a single axial step.

Figure 26 presents the heat flows of an absorber cross-section. The radiation reflected by the collector is focused on the receiver. A share of this heat flow is absorbed by the glass envelope ($\dot{Q}_{inc\_glass}$), while another share impinges on the external surface of the absorber ($\dot{Q}_{inc\_abs}$). In turn, $\dot{Q}_{inc\_abs}$ is split into two components. The first part is absorbed by the

steel absorber ($\dot{Q}_{abs}$) and passed by convection to the HTF ($\dot{Q}_{abs\_HTF}$). The second part is lost by the absorber through radiation ($\dot{Q}_{abs\_glass\_rad}$) and convection ($\dot{Q}_{abs\_glass\_conv}$) to the inner surface of the glass envelope. The vacuum (typically 10^{-4} torr) existing in the annulus between absorber and glass contributes to significantly damping convection losses.

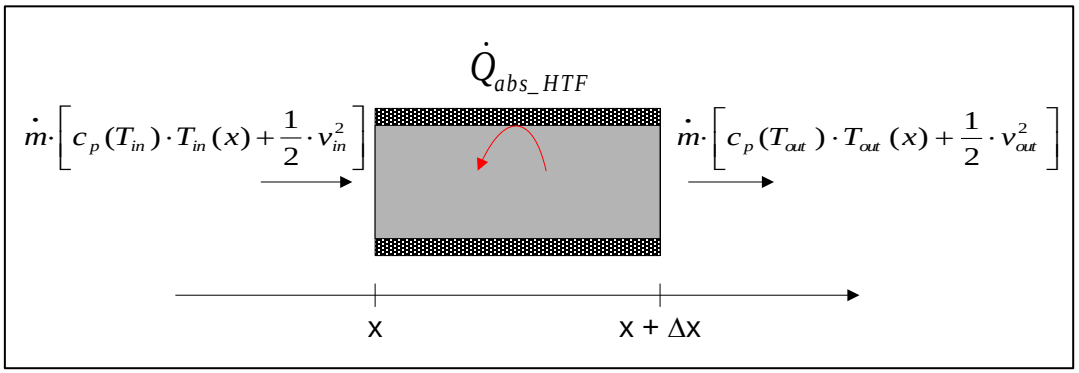

Figure 25: Schematic of the energy balance for an axial step [Forristall 2003, modified]

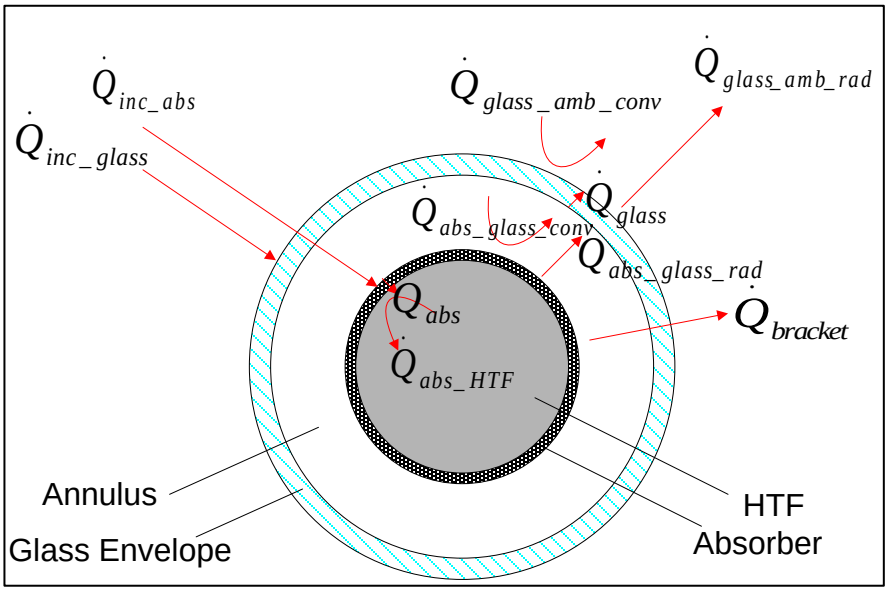

Figure 26: Schematic of the radial heat flows between HTF, steel absorber, glass envelope and ambient [Forristall 2003, modified]

The heat lost through the annulus is finally dissipated to the ambient by radiation ($\dot{Q}_{glass\_amb\_rad}$) and convection ($\dot{Q}_{glass\_amb\_conv}$). Further losses occur due to the support brackets ($\dot{Q}_{bracket}$) which connect the absorber and the rest of the collector structure. The total heat losses ($\dot{Q}_{loss}$) are the sum of the heat losses through the glass envelope and through the brackets:

$$\dot{Q}_{loss} = \dot{Q}_{glass\_amb\_rad} + \dot{Q}_{glass\_amb\_conv} + \dot{Q}_{bracket} \qquad \text{Eq. 4.13}$$

The energy balance described in Figure 26 can be formulated as follows. For the absorber:

$$\begin{cases} \dot{Q}_{inc\_abs} = \dot{Q}_{abs} + \dot{Q}_{abs\_glass} + \dot{Q}_{bracket} \\ \dot{Q}_{abs} = \dot{Q}_{abs\_HTF} \\ \dot{Q}_{abs\_glass} = \dot{Q}_{abs\_glass\_rad} + \dot{Q}_{abs\_glass\_conv} \end{cases} \quad \text{Eq. 4.14}$$

The heat incident to the absorber $\dot{Q}_{inc\_abs}$ is explicitly calculated as:

$$\dot{Q}_{inc\_abs} = DNI \cdot Ap \cdot \eta_{geo} \cdot \eta_{glass} \cdot \tau_{glass} \cdot \alpha_{abs} \quad \text{Eq. 4.15}$$

η_{glass}	[-]	effective optical efficiency of reflector and glass envelope
τ_{glass}	[-]	transmittance of the glass envelope
α_{abs}	[-]	absorptance of the absorber

The effective optical efficiency at the glass envelope η_{glass} is given by the product of several factors (shadowing, tracking errors, mirror alignment errors, mirror reflectance, dirt presence on collector and absorber) [Forristall 2003].

The energy balance for the glass envelope leads to:

$$\begin{cases} \dot{Q}_{inc\_glass} + \dot{Q}_{abs\_glass} = \dot{Q}_{glass\_amb} \\ \dot{Q}_{abs\_glass} = \dot{Q}_{glass\_cond} \\ \dot{Q}_{glass\_amb} = \dot{Q}_{glass\_amb\_rad} + \dot{Q}_{glass\_amb\_conv} \end{cases} \quad \text{Eq. 4.16}$$

Similarly to Eq. 4.15, $\dot{Q}_{inc\_glass}$ is calculated explicitly:

$$\dot{Q}_{inc\_glass} = DNI \cdot Ap \cdot \eta_{geo} \cdot \eta_{glass} \cdot \alpha_{glass} \quad \text{Eq. 4.17}$$

Solution of the Energy Balance

An iterative procedure is necessary for the calculation of the heat losses of each Δx, because the temperature is not known a-priori in different radial positions (e.g. internal and external surface of absorber and glass envelope). However, the knowledge of the temperature in the different parts of the HCE is important to correctly determine all relevant heat flows and to exactly fulfil the energy balance. In order to simultaneously solve Eq. 3.14 and Eq. 4.16, initial values of the temperature profile of each radial position and of each Δx have to be assumed. The first Eq. 4.15 can be reshaped as:

$$\dot{Q}_{inc\_abs} = A_{abs\_e} \cdot \left[\begin{array}{c} k_{in} \cdot \left(T_{abs\_e} - T_{HTF} \right) + k_{out} \cdot \\ \cdot \left(T_{abs\_e} - T_{glass\_e} \right) + k_{bracket} \cdot \left(T_{bracket} - T_{amb} \right) \end{array} \right] \quad \text{Eq. 4.18}$$

A_{abs_e}	[m²]	surface of the external area of the absorber

k_{in}	[W/m²/K]	heat transfer coeff. between external absorber surface and HTF
k_{out}	[W/m²/K]	heat transfer coeff. between external abs. surface and glass
$k_{bracket}$	[W/m²/K]	heat transfer coefficient between bracket and ambient

All heat transfer coefficients are related to the external surface of the steel absorber tube. The radial heat flows can also be thought as a system of thermal resistances, as represented in Figure 27. The heat flows are divided in serial and parallel ones.

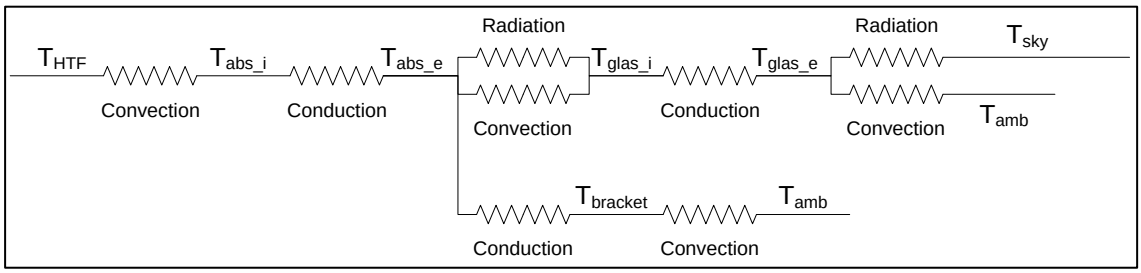

Figure 27: Thermal resistance model for an absorber cross-section [Forristall 2003, modified]

According to Figure 27, the external heat transfer coefficient k_{out} is:

$$k_{out} = \frac{1}{\left(\frac{1}{k_{abs\_glass}} + \frac{1}{k_{glass}}\right)} \qquad \text{Eq. 4.19}$$

k_{out} describes the losses through the different layers of the absorber, respectively in the vacuum between steel tube and glass (k_{abs_glass}) and through the glass (k_{glass}). k_{in} is defined similarly. The detailed description of the calculation of the heat transfer coefficients is given in [Forristall 2003].

The absorber temperature is recalculated [Duffie 1991]:

$$T_{abs\_e\_new} = \frac{\dot{Q}_{inc\_abs} + A_{abs\_e} \cdot \left(k_{in} \cdot T_{HTF} + k_{out} \cdot T_{glass} + k_{br} \cdot T_{br}\right)}{A_{abs\_e} \cdot \left(k_{in} + k_{out} + k_{br}\right)} \qquad \text{Eq. 4.20}$$

For the calculation of T_{glass_new} a similar procedure applies. The heat flows are recalculated with the new temperatures. The iteration is repeated until both equations Eq. 4.14 and Eq. 4.16 are satisfied.

Once the radial energy balance of a section Δx is fulfilled, the same procedure applies through the entire axial length of the collector loop. At the end of this calculation the model checks if the difference between the current HTF temperature and the design value is lower than the given tolerance (Figure 24). If this is not the case, the HTF mass flow is adjusted iteratively till the design value is reached. The $\Delta\dot{m}$ for the new iteration is proportional to the error ($T_{HTF\_out} - T_{HTF\_out\_design}$) through a constant.

The total heat collected by a loop is then the sum of the heat in each Δx:

$$\dot{Q}_{loop} = \sum_{x=0}^{x_{end}} \dot{Q}_{abs\_HTF}(x) \qquad \text{Eq. 4.21}$$

Finally, the heat effectively collected by the solar field is:

$$\dot{Q}_{sf} = \dot{Q}_{loop} \cdot n_{loop} - \dot{Q}_{loss\_piping} \qquad \text{Eq. 4.22}$$

whereas the heat of one loop is multiplied by the total number of loops. This value is slightly reduced by the heat losses which occur along the piping system.

4.2.3 Piping Model and Auxiliary Power Consumption

The minimization of the internal power consumption is very important for both the calculation of net power generation as well as for the economics of a CSP plant. In the solar field, power is required in order to circulate the HTF between collectors and heat exchanger and to compensate pressure losses along the flow path. CSP plants (in the case synthetic oil or molten salt are used as HTF) typically have a layout with 4 subfields, whereas the power block is located at the center of the plant in order to minimize pressure and heat losses in the piping (Figure 28). A different layout has to be taken into account for DSG configurations (Annex 10.2.4, Figure 86 and Figure 87).

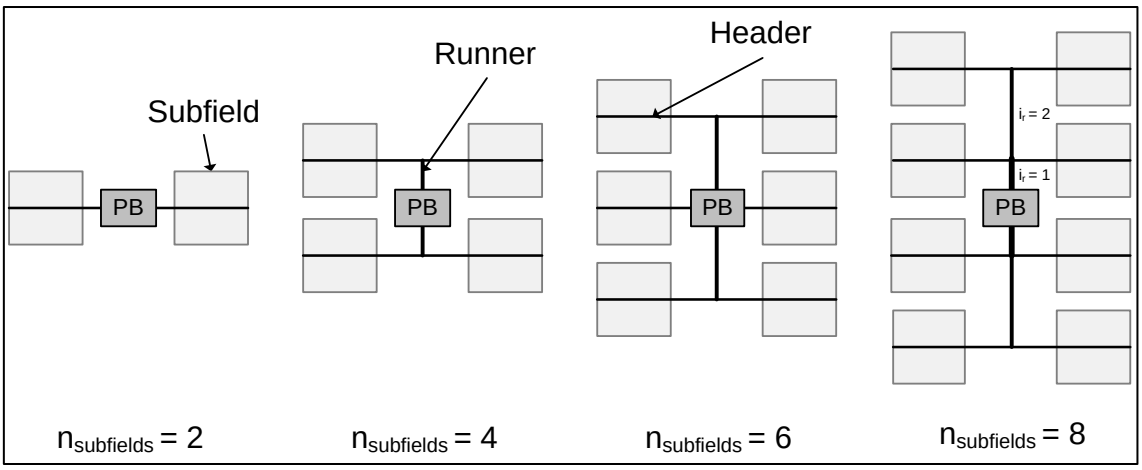

Figure 28: Possible subfield layouts for a parabolic trough CSP plant [Cordes 2011, adapted]

The internal power consumption in the HTF loop can be calculated in general with the following relation:

$$P_{parasitic\_sf} = \frac{\Delta p_{HTF} \cdot \dot{m}_{HTF}}{\rho_{HTF} \cdot \eta_{pump}} \qquad \text{Eq. 4.23}$$

Δp_{HTF} [bar] total HTF pressure losses

$\dot{m}_{HTF}$	[kg/s]	total HTF mass flow
ρ_{HTF}	[kg/m³]	HTF density
η_{pump}	[-]	pump efficiency at nominal conditions

The required pump power is proportional to the total pressure losses and to the total HTF mass flow. Δp_{HTF} consists of the sum of distributed (e.g. pipes) and concentrated (e.g. devices) pressure drops:

- Runners (main tubing between power block and subfield piping)
- Headers (subfield tubing between runner and solar field collectors)
- Collector loop (receiver tubes, ball joints, elbows and valves)

In addition, it has to be considered that the HTF pressure at the end of each loop is different. In fact, the loops placed nearby the runner are characterized by lower pressure losses than loops at the end of the header. Thus, the calculation of the representative Δp_{HTF} is made for the loop at the end of the header (i.e. largest pressure drop). The HTF density ρ_{HTF} has to be evaluated at the inlet temperature to the collectors, as pumps are located along the "cold" side of the piping.

For the calculation of the total pressure loss it is necessary to know pipe length, diameter and corresponding design velocity for each pipe segment, while for devices specific loss factors ξ_k are required:

$$\Delta p_{HTF} = \sum_{i=1}^{n} \frac{1}{2} \cdot \rho_{HTF} \cdot v_{HTF\_i}^2 \cdot \left(\lambda_{fr} \frac{L_i}{D_i} + \sum_{k=1}^{m} \xi_k \right) \qquad \text{Eq. 4.24}$$

i	[-]	pipe counter
v_{HTF}	[m/s]	HTF velocity
λ_{fr}	[-]	Darcy-Weisbach friction factor
L_i	[m]	tube length
D_i	[m]	Internal tube diameter
ξ_k	[-]	pressure loss factor for the device k

According to Figure 28, the solar field is characterized by four $\dot{m}_{HTF}$:

- $\dot{m}_{HTF\_tot}$ the total mass flow
- $\dot{m}_{HTF\_runner}$ the flow rate in the runner
- $\dot{m}_{HTF\_subfield}$ the flow rate at the beginning of the subfield header
- $\dot{m}_{HTF\_loop}$ the mass flow in a single collector loop

Independently of the selected transfer fluid, $\dot{m}_{HTF}$ at design conditions for a given solar field size is:

$$\dot{m}_{HTF} = \frac{A_{sf} \cdot DNI \cdot \eta_{sf}}{h_{HTF\_out} - h_{HTF\_in}} \qquad \text{Eq. 4.25}$$

DNI	[W/m²]	design direct normal irradiance
η_{sf}	[-]	design solar field efficiency (according to Eq. 10.7)
$h_{HTF\_(out/in)}$	[kJ/kg]	design specific HTF enthalpy at collector outlet and inlet, respectively

Note that both η_{sf} as well as $h_{HTF\_(out/in)}$ depend on the selected HTF and on the selected inlet and outlet HTF temperature and pressure. The calculation of the pressure losses has been implemented by [Cordes 2011] based on [Wagner 2011]. The details of the piping model are presented in Annex 10.2.4.

4.2.4 Transient Model

Steady-state models usually do not take into account the impact of transient effects due to thermal inertia of different solar field components (HTF, receivers, piping system, etc.). These effects play an important role and their disregard leads to overestimation of the solar field yield. This over-estimation may reach up to 15 % of the solar field heat output in oil-based parabolic trough plants in a single day [Hirsch 2010] and ca. 10 % on an annual basis [Feldhoff 2011].

The consideration of transient effects is particularly important for the following conditions:

- start-up of the solar field, which occurs each morning as soon as sufficient irradiation is available
- broken clouds conditions, which are characterized by short-term DNI fluctuations (in the minute-range).

These effects can be taken into account by detailed transient models such as Dymola/Modelica [Hirsch 2010]. These tools are able to accurately describe the short-term dynamic behavior of the plant. However, they are more complex than steady-state models and the computation time is significantly higher. A second aspect is that transient models work best if high-time-resolution DNI data are available. The feed of hourly data into a transient model would lead to higher inaccuracy, as in this case the HTF temperature rise would be time-delayed, and the heat yield would be consequently underestimated [Rheinländer 2010]. In addition, high-time resolution data can only be gathered by ground measurement stations and may not be available for the majority of the sites, especially in the early stages of project development.

For these reasons, a simplified approach for transient calculation is developed in INSEL. In principle, the existing steady-state model is extended to a quasi-static model. The used DNI data resolution is still of one hour; this way it is possible to perform a model run in a short time (2 - 5 minutes). The solar field cool-down and start-up are considered by simplified energy balances which take into account the HTF and steel mass in the system.

Solar Field cool-down and start-up

After sunset or if the DNI drops below threshold conditions, the HTF is slowly recirculated while the solar field cools down. During offline-times of the solar field, the HTF temperature is calculated with a modification of the lumped capacitance method described by [Mittelman 2010], [Cordes 2011].This simplified approach neglects the spatial HTF temperature distribution along the loop and piping system, i.e. the entire HTF system is approximated by a single average temperature:

$$T_{HTF,t+1} = T_{amb} + \Delta T_t \cdot e^{-\frac{1}{c_p \cdot m} \cdot \frac{\dot{Q}_{loss,t}}{\Delta T_t} \cdot \Delta t} + \frac{\dot{Q}_{abs,t}}{\dot{Q}_{loss,t}} \cdot \Delta T_t \cdot \cdot \left(1 + e^{-\frac{1}{c_p \cdot m} \cdot \frac{\dot{Q}_{loss,t}}{\Delta T_t} \cdot \Delta t}\right) \quad \text{Eq. 4.26}$$

T_{amb}	[°C]	ambient temperature
ΔT_t	[°C]	temperature difference between T_{HTF} and T_{amb}
Δt	[s]	time step
$\dot{Q}_{loss,t}$	[MW]	solar field heat losses as function of ΔT_t
$\dot{Q}_{abs,t}$	[MW]	solar field absorbed heat
$c_p \cdot m \cdot \Delta T_t$	[kJ]	sum of HTF and steel heat capacities

The cool-down behavior of the solar field is described by an exponential function which mainly depends on the heat losses of the solar field and the piping system and the heat capacity of HTF and steel masses. Further details of the transient model can be found in Annex 10.2.4.

The heat losses of the piping system $\dot{Q}_{loss\_piping}$ are assumed to be 10 W/m² [Dersch 2009] under nominal operation conditions. At off-line times this value is reduced by a factor proportional to $\Delta T_t / \Delta T_{t\_design}$ [Cordes 2011].

4.2.5 Molten Salt Collector Model

The model described in 4.2.1 to 4.2.4 applies for different heat transfer fluid types (synthetic oil, molten salt, water/steam). However, HTFs have different physical properties, so that an

extension of the model is required. This involves a differentiation of typical HTF parameters (temperature and pressure) at the inlet and at the outlet of the collectors as well as an eventual adaptation of the solar field layout. The plant operation of a CSP molten salt plant presents some particularities in comparison to a state-of-the-art VP-1 (synthetic oil) plant. Freeze protection of the HTF at night is guaranteed by recirculation of the molten salt in the solar field as soon as the HTF temperature falls below 270 °C, which results from the salt freezing temperature (240 °C) plus a security buffer. During night operation the HTF enters the solar field with a temperature of 280 °C, whereas the heat required for the compensation of thermal energy losses in the receivers and in the piping system is given by the cold tank of the thermal energy storage [Wittmann 2012]. If the temperature of the cold tank falls below 280 °C, the auxiliary heater is switched on. In addition, receiver loops designed for molten salt operation are typically longer than standard ones. In general, one loop should be designed as long as possible in order to reduce the number of required components (valves at the inlet and at the outlet of the loop, cross-over pipes etc.). On the other hand, long pipes would increase the pressure drops and the required power for pumping [Riffelmann 2012]. While loops for synthetic oil operation typically are 600 m long, molten salt loops can be longer (e.g. 800 m) due to lower required HTF velocities and consequently lower pressure losses. A further advantage of this layout is that the velocity of the HTF in the receivers is higher even at low DNI, which increases the heat exchange and reduces the risk of thermal stress on the tubes [Wittmann 2012], [Falchetta 2012].

4.2.6 Direct Steam Generation

Direct steam generation (DSG) systems use water/steam as HTF. This means that the steam required by the turbine is directly produced in the solar field. Therefore, the heat exchanger between solar field and power block is no longer necessary, while the receivers only need to be adapted in order to withstand higher pressures (i.e. larger tube wall thickness). In addition, steam temperatures up to 550 °C can be reached. These features lead to higher thermodynamic efficiency and potentially to lower investment and operating cost [Feldhoff 2010]. The environmental risk in case of leakages is also minimized [Zarza 2002].

So far, the most severe drawback for a wide-scale introduction of this technology is the lack of commercially available thermal energy storage adapted for DSG. Possible solutions -as the use of phase change materials (PCM)- are currently under research [Laing 2011]. Several DSG concepts have been investigated in the past years [Eck 2001], [Zarza 2002], [Valenzuela 2005] such as once-through, recirculation and injection. The recirculation mode has been selected as the current reference scheme for DSG plants and has been modeled accordingly in INSEL.

DSG Model Structure

This chapter describes the DSG model implemented in INSEL, which integrates and partially substitutes the solar field model previously described. The existing solar field model had to

be extended in order to properly describe the behavior of a DSG solar field. Main reasons for this requirement are:

- the two-phase flow in the receiver and the impact on heat transfer and pressure drop
- the separation of the solar field in two sections: the pre-heating/evaporation segment, which is run in recirculation mode, and the superheating unit

Figure 29 presents the schematic layout of a DSG solar field which works with a modified recirculation mode. In order to obtain better controllability of the steam parameters at the outlet of the solar field an injection cooler was included in the design.

Beside other user parameters which are common with the one-phase model, user specific inputs for this module are the number of collectors in the pre-heating/evaporation segment and in the superheating sections, the pressure at the outlet of the solar field and the design steam fraction at the end of the evaporator segment x_{design}.

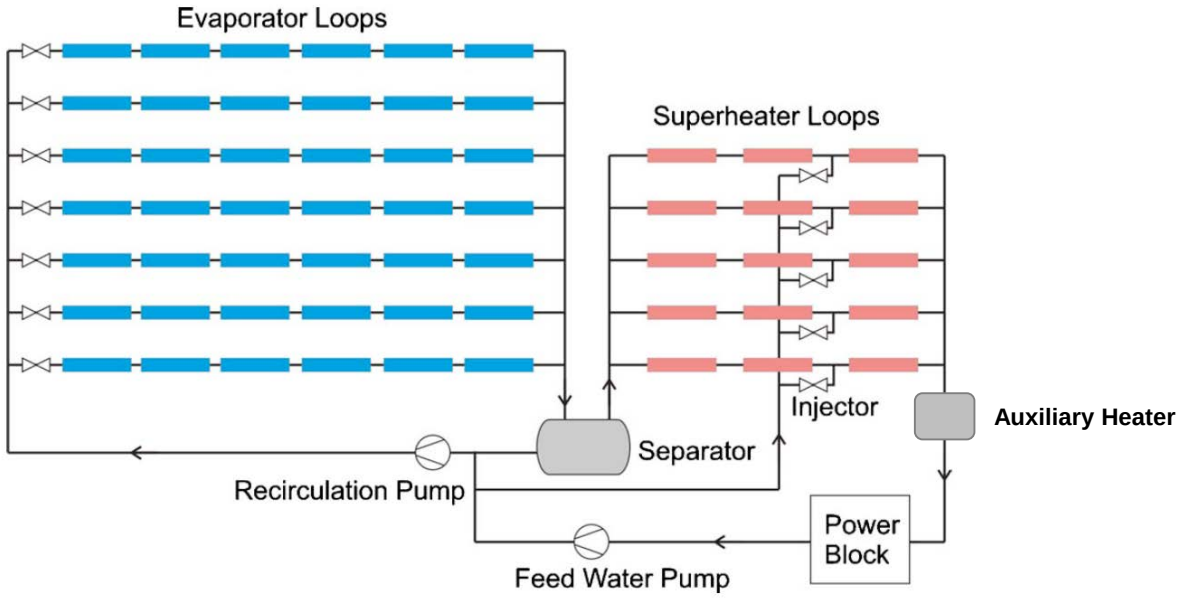

Figure 29: Scheme of a DSG solar field with recirculation layout and injection cooler in the superheating section [Feldhoff 2010]

The steam fraction is defined according to the homogeneous flow assumption as [Eck 2007]:

$$x_s = \frac{\dot{m}_s}{\dot{m}_w + \dot{m}_s} = \frac{h - h'}{h'' - h'} \qquad \text{Eq. 4.27}$$

with

$\dot{m}_s$	[kg/s]	steam mass flow
$\dot{m}_w$	[kg/s]	water mass flow
h	[kJ/kg]	specific enthalpy of the water/steam mix

h'	[kJ/kg]	specific water enthalpy at boiling conditions
$h"$	[kJ/kg]	specific enthalpy of saturated steam

The model firstly calculates the required water mass flow at the inlet of the solar field. The calculation is carried out by means of an iterative call of the "Energy Balance" subroutine, until the condition $x_s = x_{s\_design}$ at the end of the evaporation section is met. According to [Hirsch 2011], the typical design value for x_{s_design} is 0.75. Other results are the collected heat and the water/steam parameters (temperature, pressure and enthalpy) at the end of the evaporation section. In the successive step the water is separated from the produced steam and recirculated towards the collector inlet, where it is mixed with the pre-heated feed water coming from the power block. The steam enters the superheating section. The steam temperature at the outlet of the collector T_{s_out} generally differs from the design temperature $T_{s\_out\_design}$. As the steam parameters at the turbine inlet must be kept constant, the operation strategies are as follows:

- $T_{s\_out} > T_{s\_out\_design}$: in this case the injector cooler is switched on and the water injection mass flow is iterated in the "Energy Balance" subroutine until the design steam temperature is reached
- $T_{s\_out} \leq T_{s\_out\_design}$: the steam temperature gap is filled by a fossil-fired auxiliary heater

The key results of this module are the collected thermal power $\dot{Q}_{loop}$, the steam mass flow $\dot{m}_s$, the steam temperature T_s, and -eventually- the thermal power required from the auxiliary heater $\dot{Q}_{cofiring}$.

Heat Transfer and Pressure Losses of Two-phase Flow

The most relevant adaptations of the one-phase receiver model (included in the "Energy Balance" subroutine) to a two-phase model concern the heat transfer between absorber's inner surface and the water/steam mix. According to [Forristall 2003] this is:

$$\dot{Q}_{abs\_HTF} = k_{conv} \cdot D_{abs,i} \cdot \pi \cdot \left(T_{abs,i} - T_{HTF}\right) \qquad \text{Eq. 4.28}$$

where the heat transfer coefficient k_{conv} is calculated according to the available literature [Gnielinski 1976], [VDI 2010]. The decision as to which correlation should be used in which particular receiver segment is based on the enthalpy. An overview of the calculation procedure is given in Annex 10.2.4 (Table 43). For one-phase flows the calculation of the Nusselt number Nu_D is required as the first step. For turbulent liquid flows the Gnielinski correlation is used. The one-phase gas flow is taken into account with a similar procedure; only the correlation of the Nusselt number needs to be slightly adapted [VDI 2010]. The water/steam properties are calculated according to the IAPWS standards [Wagner 1998]. As dynamic viscosity and heat conductivity are not available in this reference, their assessment

is based on [Haar 1984]. The calculation of the two-phase flow is carried out according to [Feldhoff 2007], which assumes the convective boiling as the dominant boiling mechanism.

4.3 Linear Fresnel

Linear Fresnel systems have been developed with the aim to simplify the collector layout of the parabolic trough and thereby reducing investment cost. In a Fresnel system, the parabolic shape of PT is split into several slightly curved, long and narrow segments called primary mirrors (Figure 30, on the left). This arrangement makes it possible to increase the land use factor (i.e. the ratio between collector area and land area of a solar field) in comparison to the parabolic trough technology. In addition, wind loads are strongly reduced and therefore the required steel supporting structure is less expensive [Mertins 2009]. Also, the light construction allows smaller tracking motors than in PT. The primary reflectors are supported by rod bars which allow individual tracking of the mirrors during the day. The absorber tube is located some meters above the mirrors at the center line of each collector loop. Contrary to PT, the absorber tube is fixed, so that receivers tracking as well as ball joints are no longer required [Feldhoff 2012]. The higher focal line in comparison to the parabolic trough layout and the smaller mirrors´ curvature cause higher optical losses, particularly at sun positions which do not coincide with design conditions. In order to reduce optical losses, most of the implemented collectors are equipped with a secondary concentrator, which is mounted above the receiver (Figure 30, on the right).

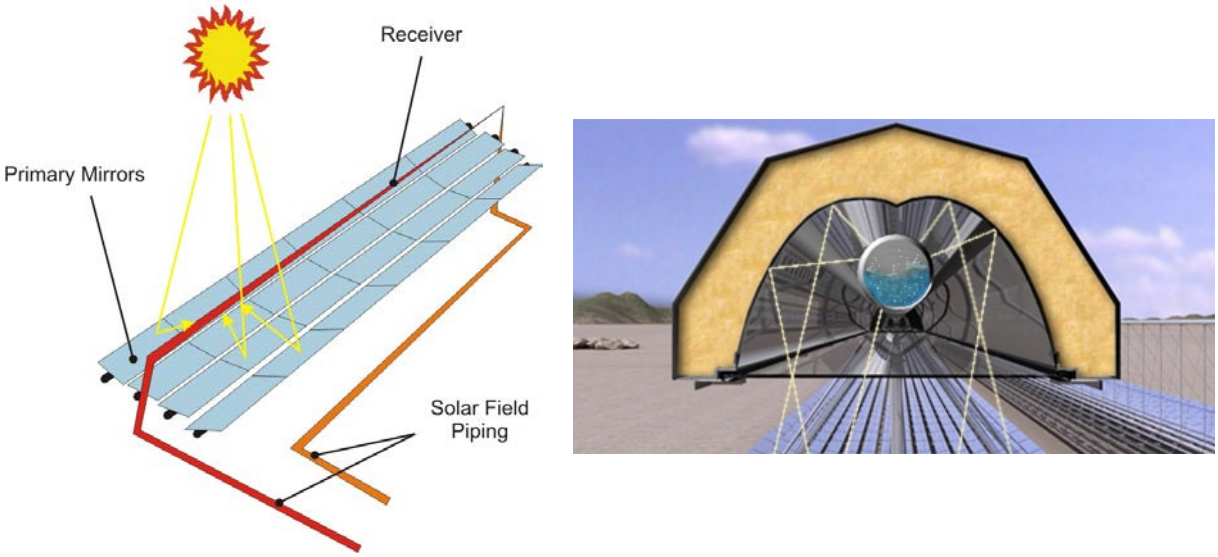

Figure 30: Scheme of a linear Fresnel collector (on the left) [EnerMENA 2012] and of a secondary reflector (on the right) [Novatec Solar 2013]

Due to the high land use factor, linear Fresnel collectors can be integrated to industrial or agricultural uses. The shadow provided by Fresnel collectors can be used for building covers, parking decks or for reducing irrigation requirements of crops [Kögler 2009]. Linear Fresnel collectors historically focused on direct steam generation, even if in principle other choices are possible. In the past LF collectors were designed for lower temperature applications. However, recent developments show that PT as well as LF collector systems can be used to

generate similar steam parameters. First LF plants were constructed in Spain by the company Novatec Solar [Novatec Solar 2013]. These plants work with a saturated steam process at 270 °C and 55 bar [Schenk 2012]. Other companies are Areva Solar, which follows a different receiver concept (multiple tube receivers), MAN/Solar Power Group, Industrial Solar, Fera and CNIM [Morin 2011].

The linear Fresnel model is analogous to the parabolic trough model presented in 4.2. The receiver heat losses can be described in principle by the same correlations. However, a series of adaptations has to be taken into account. They mainly concern the calculation of the geometrical efficiency (IAM losses) and of the solar field pressure losses (e.g. amount of flexible connections).

4.3.1 Geometrical Efficiency

Similarly to the parabolic trough technology, geometrical and optical efficiencies of linear Fresnel reflectors are reduced by several loss mechanisms (4.2.1). Linear Fresnel modules are characterized by lower design optical efficiency than parabolic trough collectors. This is caused by higher spillage, additional reflection losses due to the secondary reflector and collector shading by the receiver structure.

An additional loss mechanism is blocking, which occurs if the beams reflected by a primary mirror are blocked by the back of neighbor mirrors (Figure 31). These effects are particularly significant at low sun elevation angles.

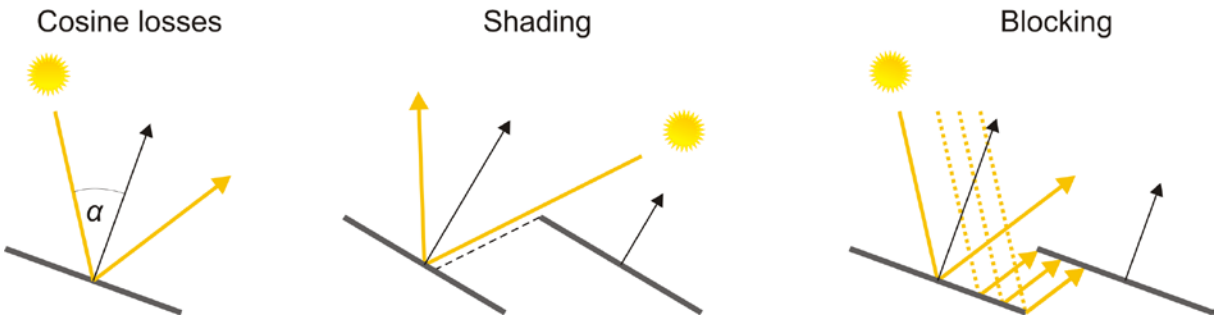

Figure 31: Overview of optical loss mechanisms in linear Fresnel collectors [EnerMENA 2012]

Different from PT, the IAM losses are not a function of the incident angle only. For this reason, the IAM should be measured for all possible sun positions. However, a simplified approach is commonly used in order to reduce the computing time of raytracing simulations, which consists of considering just the longitudinal plane and the transversal plane (Figure 32).

The IAM is expressed as [EnerMENA 2012]:

$$IAM = IAM_{trans}(\theta_{\perp}) \cdot IAM_{long}(\theta_i) \qquad \text{Eq. 4.29}$$

$\theta_{\perp}$ [°] transversal incidence angle

For North-South oriented collectors, the transversal incidence angle is:

$$\theta_{\perp} = arctan(|\sin \gamma_s| \cdot \tan \theta_z) \qquad \text{Eq. 4.30}$$

The zenith angle θ_z is the complementary angle of α_s, as described in Figure 22. In the case of Fresnel reflectors, the IAM function typically also includes cosine losses and shading, while the end loss efficiency is calculated separately according to Eq. 4.10. A comparison of the time profile of geometrical and thermal efficiencies of the parabolic trough and of the Fresnel collectors is presented in the case study (chapter 8).

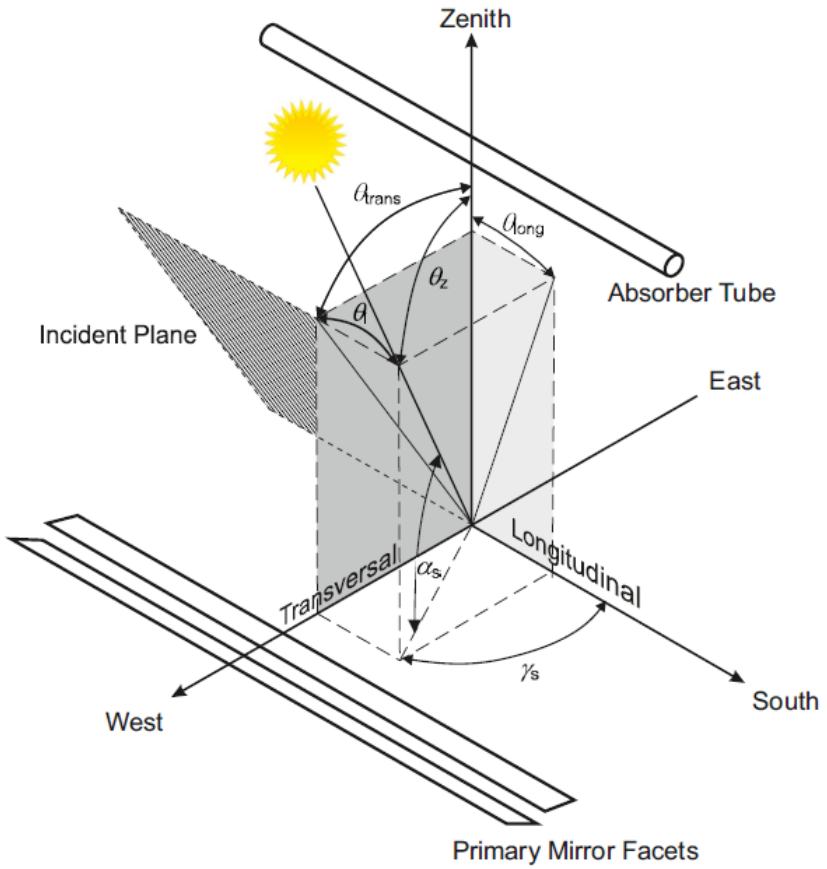

Figure 32: Definition of angles for North-South oriented linear Fresnel reflectors [Mertins 2009]; $\theta_i = \theta_{(PT)}$

The INSEL user has the possibility to specify collector and receiver geometry in the block parameters window of the solar field module. An overview on commercially available Fresnel collectors is given in [Morin 2011].

4.3.2 Receiver Model

Fresnel receivers are modeled according to the same approach presented in 4.2.2, whereas single vacuum tube receivers are assumed. Multiple tube receivers and receivers without vacuum are not included in the current version of the model. However, receivers without glass cover could be relatively easily modeled by an adaptation of the energy balances Eq. 4.14 and Eq. 4.16. Linear Fresnel collectors are characterized by approximately 50 % lower specific thermal losses than parabolic troughs [Schenk 2012]. Flexible pipe connections are no longer required and the consequent elevate thermal losses can be avoided.

In addition, the ratio between net mirror area and receiver diameter (concentration ratio) is higher than for parabolic trough. Fresnel reflectors typically use water/steam as HTF. The introduction of alternative heat transfer media such as molten salt currently is in the demonstration phase [Novatec Solar 2013].

4.3.3 Piping and Auxiliary Power Consumption

The structure of the piping model is the same as described in 4.2.3. As flexible pipe connections (e.g. elbows) are not required in Fresnel reflectors, the pressure losses and the specific auxiliary power requirements are lower than in parabolic troughs.

4.4 Central Receiver

Central receiver systems consist of a large number of slightly curved mirrors called heliostats, which reflect direct solar radiation onto a receiver located at the top of a tower (Figure 33). Each heliostat tracks the sun on both axes and is therefore equipped with a drive unit. The drive unit also permits the heliostat to reach the guarding safe position in a few minutes in case of strong wind loads [Lata 2010] or hail. The typical optical concentration factor ranges from 500 to 1,000 [Buck 2008]. With such concentration ratios it is possible to achieve high HTF temperatures (in principle also over 1,000 °C), higher thermodynamic efficiencies (Annex 10.2.1) and potentially lower electricity generation cost. Air, water/steam or molten salts can be used as HTF in the receiver. Oil is excluded due to its thermal instability at temperatures higher than 400 °C. The utilization of small particles as HTF is also an option which is currently under research [Wu 2011].

The first CSP tower pilot-project (Solar One, converted later in Solar Two) was constructed in the Mojave Desert in 1982 [Stine 2001] and decommissioned in 1999. The first worldwide commercial project was realized by Abengoa in 2007. This plant called Planta Solar 10 (PS10) is an 11 MW_{el} plant equipped with a saturated steam receiver working at 55 bar [TroughNet 2013]. A further relevant commercial project is Gemasolar, a 20 MW_{el} plant constructed by Torresol Energy in southern Spain. The plant works with molten salt as HTF and is equipped with a 15-hours thermal energy storage, which allows for base-load electricity generation in summer [Gemasolar 2013].

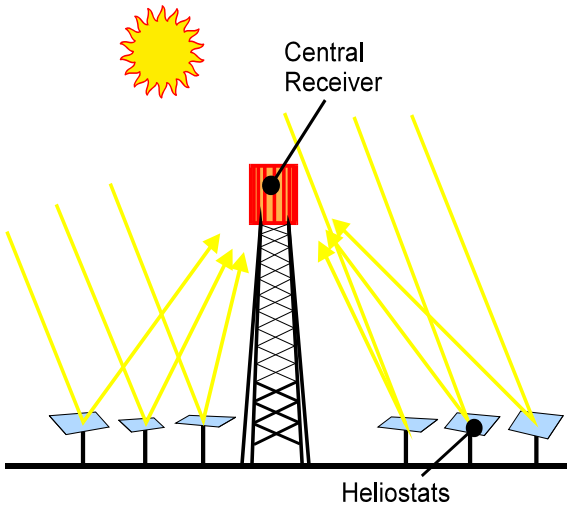

Figure 33: Scheme of a central receiver [EnerMENA 2012]

The modeling of solar tower systems is more complex than the modeling of linear focusing collectors. In parabolic trough or linear Fresnel the required thermal output is reached -independently of local factors- by adding up standardized collector rows. In central receiver systems, the layout of the heliostat field, i.e. the optimal position of each heliostat relative to the receiver, is strongly dependent on site-specific parameters such as latitude and local atmospheric conditions. For this reason, the calculation of optimized heliostat fields typically requires time-demanding calculations with tailor-made tools such as HFLCAL, DELSOL, SolTRACE or others [Garcia 2008]. In order to reduce the computation time, a simplified approach was chosen for the modeling of solar tower plants in INSEL. The selected methodology is based on the work of [Dersch 2010]. This approach is also currently used in the simulation tools EBSILON Professional and Greenius.

4.4.1 Geometrical Efficiency

The tracking system continuously adjusts the inclination angle of each heliostat in the transversal plane as well as in the longitudinal plane, so that the normal vector of the mirror surface bisects the angle between the direction of the sun rays and the receiver (Figure 34). As a consequence, each heliostat has an individual efficiency. As it is the case in Fresnel reflectors, mirrors opposite to the sun perform best.

In addition to cosine losses, shading and blocking -which have already been discussed previously in 4.2.1 and 4.3.1-, further loss mechanisms are particularly relevant in CSP tower plants, i.e. heliostat errors and atmospheric extinction.

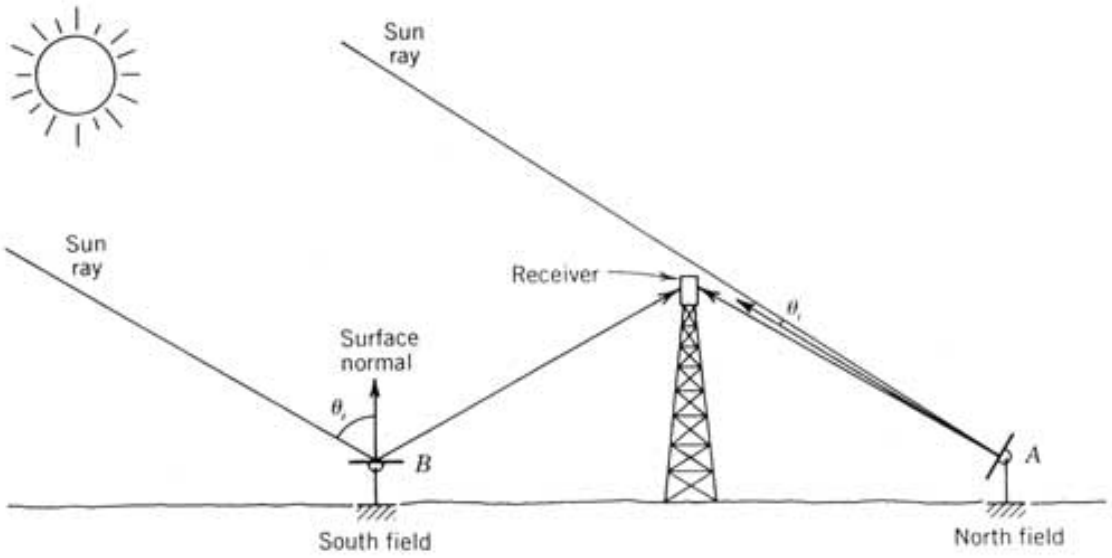

Figure 34: Tracking angles of single heliostats in different field positions [Stine 2001]

Heliostat Errors

Each heliostat typically consists of a series of mirror elements, whereas each mirror is individually canted to the receiver. In addition, each mirror is slightly concaved. Ideal heliostats would have the center of the receiver as focal point. However, a series of factors increases the image size of the mirrors on the receiver and -consequently- the spillage. The spillage typically amounts from 2 % to 6 % of the incident power. These errors include mirror surface waviness, gross curvature error, positioning errors and structural deflections due to gravity and wind loads [Stine 2001].

The optimal size of the heliostats is a trade-off between heliostat errors -which are lower for smaller heliostats- and investment cost for mirrors, supporting structure and tracking gears -which are lower for large heliostats [Buck 2008].

Atmospheric Extinction

Absorption and scattering by aerosols, dust and water vapor are responsible for the attenuation of incident light on its path between heliostats and the receiver. This effect may reduce the optical efficiency by 10 %/km (clear days) to 25 %/km (hazy days) [Hanrieder 2012]. Aerosol distributions near to the ground level are very location-specific parameters. However, usually no detailed information about local meteorological conditions is available, so that the assessment of the impact of atmospheric extinction is rather difficult. Other loss effects are wind-induced tower oscillations, which increase the spillage, and decrease of mirror reflectivity at high incidence angles [Kleemann 1993].

Finally, high incidence angles also imply higher astigmatism losses [Schwarzbözl 2009]. Table 8 gives an overview on the typical impact of different loss mechanisms on solar tower plants on annual average.

Error Category	Efficiency Factor
Blocking and Shading	0.98 – 0.99
Cosine	0.70 – 0.95
Mirrors and Tracking	0.90 – 0.99
Wind impact on heliostats and tower	0.93 – 0.97
Reflection	0.80 – 0.95
Heliostats´ availability	0.98 – 1.00

Table 8: Typical range of several loss mechanisms in solar towers (annual average values) [Kleemann 1993]

Geometrical Efficiency Tables

The overall geometrical efficiency of the heliostat field is a function of several parameters such as design incident power at the receiver, latitude, design date, heliostat size and shape, heliostat layout, tower height, aiming point strategy and current sun position [Dersch 2010]. The optimization of the heliostat field layout requires high computing effort. For this reason, INSEL uses a modular approach to separately assess the impact of the mentioned parameters on efficiency. The calculation of the impact of each parameter is performed with the help of an external tool called HFLCAL. HFLCAL is a software developed by DLR for layout and optimization of heliostat fields [Schwarzbözl 2009]. In order to reduce the number of the HFLCAL calculations, only three design parameters are taken into account, i.e. latitude, design incidence power and relative tower height (Eq. 4.31). The efficiency of -in each case- optimized heliostat fields has been calculated for a wide range of design parameters and sun positions. The covered range of values is summarized in Table 9.

Design Parameters	**Unit**	**Values in the Lookup Tables**
Latitude	°	20 / 30 / 40
Design Incidence Power	MW_{th}	11.5 / 45.7 / 182.5 / 731.7
Relative Tower Height	-	0.7 / 1.0 / 1.3
Sun Position Parameters	**Unit**	**Values in the Lookup Tables**
Elevation Angle	°	1.2 / 5.2 / 15 / 24.9 / 44.6 / 59.4 / 75.2 / 90
Azimuth Angle	°	0 - 360, step 30

Table 9: Overview of the values used in the lookup tables for interpolation; 1.0 relative tower height corresponds to Eq. 4.31

Finally, the calculation of the actual heliostat field efficiency of a specific CSP tower plant occurs in INSEL by multi-dimensional interpolation between the generated lookup tables. According to [Dersch 2010 b], the tower height z_{tower} is a function of the design thermal power at the receiver:

$$z_{tower} = 36.7 \cdot \dot{Q}_{rec}^{0.288} \qquad \text{Eq. 4.31}$$

z_{tower} [m] tower height

$\dot{Q}_{rec}$ [MW_{th}] design thermal power at the receiver

The generated lookup tables also include values for different tower heights in the range of ± 30 %.

4.4.2 Receiver Model

The used HTF has a significant impact on the receiver design. Thereby, two options are currently implemented in commercial projects (direct steam generation, molten salt), while two other concepts are under research (air receiver, particle receiver) [Buck 2008]. The implemented model applies to molten salt receivers and takes the Gemasolar plant as reference [Gemasolar 2013].

The incident power $\dot{Q}_{inc}$ at the receiver is:

$$\dot{Q}_{inc} = DNI \cdot A_{sf} \cdot \rho_{refl} \cdot \eta_{sf}\left(\phi; \dot{Q}_{inc\_design}; z_{tower}; \alpha_s;\ \gamma_s\right) \cdot \eta_{wind} \cdot \eta_{focus} \qquad \text{Eq. 4.32}$$

$\dot{Q}_{inc}$	[MW_{th}]	incident power
A_{sf}	[m²]	heliostat field aperture area
ρ_{refl}	[-]	mirror average reflectivity
η_{sf}	[-]	solar field average optical efficiency
η_{wind}	[-]	wind correction factor
η_{focus}	[-]	focus factor

The mirror reflectivity ρ_{refl} (0.893) has to be understood as the annual average of reflectiveness, cleanliness factor and field availability [Giuliano 2013]. The heliostat field aperture area is simply calculated by multiplication of the number of heliostats and the surface of a single mirror. The solar field optical efficiency η_{sf} is calculated from the HFLCAL lookup tables as previously explained. The wind correction factor takes into account the reduction of tracking accuracy of the heliostats at high wind velocity. This parameter can be set equal to one for simplified calculations. In addition, a focus status is considered. The focus factor η_{focus} reflects the actual state of charge of the storage (and eventually the actual electricity demand). For example, if the thermal storage is completely charged, the maximum amount of heat which can be collected by the receiver cannot exceed the heat needed by the turbine. If this is the case, a share of the heliostats has to be defocussed. Defocussing is also required if a maximum value of $\dot{Q}_{inc}$ is exceeded, in order to avoid overheating of the receiver surface and consequent damages to receiver components.

The heat effectively absorbed by the receiver is lower than the incident power due to the impact of a series of losses:

$$\begin{aligned} \dot{Q}_{rec} &= \dot{Q}_{inc} - \dot{Q}_{loss} \\ &= \dot{m}_{HTF} \cdot \left(h_{rec\_out} - h_{rec\_in}\right) \end{aligned} \qquad \text{Eq. 4.33}$$

$\dot{Q}_{rec}$	[MW_{th}]	effective receiver heat

$\dot{Q}_{loss}$	[MW_{th}]	sum of receiver thermal losses
h_{rec_out}	[kJ/kg]	specific HTF enthalpy at the receiver outlet
h_{rec_in}	[kJ/kg]	specific HTF enthalpy at the receiver inlet

The thermal losses consist of optical, convective, radiative and piping losses [Pawellek 2011]:

$$\dot{Q}_{loss} = \dot{Q}_{loss\_opt} + \dot{Q}_{loss\_conv} + \dot{Q}_{loss\_rad} + \dot{Q}_{loss\_piping} \quad \text{Eq. 4.34}$$

The optical losses are calculated as:

$$\dot{Q}_{loss\_opt} = \dot{Q}_{inc} \cdot \left(1 - \eta_{opt}\right) \quad \text{Eq. 4.35}$$

η_{opt}	[-]	receiver optical efficiency

The value of the optical efficiency has been estimated at 0.90 by [Giuliano 2013]. The convective losses are a function of the average receiver temperature T_{rec} and the convective heat transfer coefficient k:

$$\dot{Q}_{loss\_conv} = k \cdot (T_{rec} - T_{amb}) \cdot A_{rec} \quad \text{Eq. 4.36}$$

k	[W/m²/K]	convective heat transfer coefficient
T_{rec}	[°C]	average receiver temperature
A_{rec}	[m²]	aperture area of the receiver

The heat transfer coefficient k is estimated at 13 W/m²/K by [Giuliano 2013]. The receiver temperature is a function of the average temperature of the HTF flowing along the receiver and of the over-temperature of the receiver wall ΔT_{wall}:

$$T_{rec} = \frac{T_{HTF\_in} + T_{HTF\_out}}{2} + \Delta T_{wall\_design} \cdot \frac{\dot{Q}_{inc}}{\dot{Q}_{inc\_design}} \quad \text{Eq. 4.37}$$

ΔT_{wall_design}	[K]	design receiver wall over-temperature

The value of the over-temperature of the receiver wall is assumed to be proportional to the ratio between current incidence heat and design incidence heat. The design value of ΔT_{wall_design} has been set to 25 K [Giuliano 2013]. The HTF temperatures at the inlet and at the outlet of the receiver (T_{HTF_in} and T_{HTF_out}, respectively) are fixed parameters.

The aperture area of the receiver is defined in accordance with the design incident energy flux:

$$\dot{q}_{rec_{design}} = \frac{\dot{Q}_{inc\_design}}{A_{rec}} \qquad \text{Eq. 4.38}$$

$\dot{q}_{rec\_design}$ [kW/m²] design specific receiver flux

The design energy flux is set to 575 [kW/m²] for molten salt receivers [Giuliano 2013]. The maximal incidence heat at the receiver is equal to $\dot{Q}_{inc\_design}$. The radiative losses are expressed with the Stefan-Boltzmann law:

$$\dot{Q}_{loss\_rad} = \varepsilon \cdot \sigma \cdot \left(T^4_{rec\_K} - T^4_{amb\_K}\right) \cdot A_{rec} \qquad \text{Eq. 4.39}$$

ε [-] receiver emissivity

The value of the emissivity is 0.83 [Zavoico 2001]. In Eq. 4.39, the temperatures have to be given in Kelvin. Finally, the heat losses in the piping system are approximately 250 W/m piping line.

4.4.3 Piping and Auxiliary Power Consumption

A certain amount of electrical power is required for the pumping of the HTF along the path between heat exchanger, receiver and thermal storage (parasitic losses). The calculation of the parasitics is made according to Eq. 4.23. The pressure losses in the receiver (and in the heat exchanger) can be approximated as:

$$\Delta p_{rec} = \Delta p_{rec\_design} \cdot \left(\frac{\dot{m}_{HTF}}{\dot{m}_{HTF\_design}}\right)^2 \qquad \text{Eq. 4.40}$$

A similar correlation applies for the molten salt/water-steam heat exchanger.

4.5 Molten Salt Tanks Storage

This chapter describes the thermal energy storage model (2-tank molten salt storage) developed in INSEL. The concrete storage model is described in Annex 10.2.6.

The 2-tank molten salt storage concept is implemented in a large number of commercial parabolic trough CSP plants in Spain (e.g. Andasol). The typically used storage medium is a non-eutectic salt mixture consisting of 40 % potassium nitrate (KNO_3) and 60 % sodium nitrate ($NaNO_3$) [Bauer 2011]. During storage charge procedures, a share of the HTF (synthetic oil) coming from the solar field is diverted to the oil-to-salt heat exchanger, where it cools down from approximately 391 °C to 298 °C. On the storage side, the molten salt, coming from the cold tank (291 °C), flows through the heat exchanger, where it heats up to

384 °C and finally enters the hot tank [Gil 2010]. During the discharge the flow directions in the heat exchanger are reversed. Each of the two storage tanks of the Andasol plant has a diameter of almost 40 m and a height of 14 m. This corresponds to a thermal capacity of approx. 1,000 MWh_{th} [Gathmann 2011]. The temperature difference in the heat exchanger is limited on the upper side by the maximal operation temperature of the HTF (max. 400 °C in the case VP-1 is used as HTF), and on the lower side by the freezing temperature of the molten salt (approx. 240 °C). The main advantages of this storage concept are the high storage capacity at acceptable cost, the constant temperature during discharge and the gained experience in industrial applications. In addition, the molten salt only flows within the storage system and not in the solar field, so the risk of freezing is reduced. On the other hand, heat exchangers are expensive and the temperature decrease in the heat exchanger leads to exergy losses and lower power block efficiency during the storage discharge. Finally, a number of crucial issues have to be considered during the planning phase of a molten salt storage, e.g. material choice, corrosion risk, thermal stresses and thermal losses [Pacheco 2002].

An improvement of the previous system is provided by the two-tank direct storage. Within this concept the molten salt is used as HTF in the solar field as well as in the storage tanks. This allows increasing the maximal operation temperature in the solar field up to approx. 565 °C and raising the turbine efficiency over 40 %. Due to the higher temperature difference between cold and hot tank (approx. 275 °C instead of 100 °C), the specific storage investment costs are lower. In addition, the costs of the heat exchangers are avoided. The main disadvantages are the need for expensive heating along the receivers (particularly disadvantageous in parabolic trough systems) and the increased heat losses due to the higher temperatures. This storage concept is in operation in the Gemasolar tower plant. The development of direct molten salt storage in linear focusing systems is still under research [Wittmann 2012].

Molten Salt Tanks Storage Model

The storage capacity is selected by the INSEL user as a number of equivalent full load hours h_{TES}. The storage capacity is also expressed as:

$$Q_{TES\_design} = M_{salt} \cdot c_{p\_salt} \cdot \Delta T \qquad \text{Eq. 4.41}$$

M_{salt}	[ton]	molten salt mass
c_{p_salt}	[kJ/kg/K]	specific heat of the molten salt (constant pressure)
ΔT	[K]	temperature range of operation

Thus, the required molten salt mass can be calculated. The decision, whether the storage is charged or discharged mainly depends on the comparison between heat required by the turbine and heat provided by the solar field.

Additional constraints are set by the minimal and maximal state of charge of the storage. The heat required by the turbine is:

$$Q_{turb\_target} = \frac{P_{el\_demand} + \sum P_{parasitic}}{\eta_{turb}} \quad \text{Eq. 4.42}$$

Q_{turb_target}	[MWh_{th}]	turbine heat requirements
P_{el_demand}	[MWh_{el}]	net electricity demand
$P_{parasitic}$	[MWh_{el}]	auxiliary electrical consumption of plant components
η_{turb}	[-]	gross turbine efficiency

The net electricity demand is a time-variable input (i.e. one value per time step). The auxiliary electricity consumption is calculated as the sum of the consumptions of each plant component (solar field, storage, turbine, power block cooling). The turbine efficiency depends on the type of cooling, actual electricity demand and meteorological conditions (4.6.1). Q_{sf} has been calculated in the solar field block.

According to Table 10, four storage operation cases are distinguished.

Condition	Additional Constraint	Storage Operation
$Q_{sf} \geq Q_{turb\_target}$	$Q_{TES(t-1)} + \lvert Q_{HX}\rvert \leq Q_{TES\_design}$	Storage charge
	$Q_{TES(t-1)} + \lvert Q_{HX}\rvert > Q_{TES\_design}$	Limited storage charge; → Partial solar field defocusing
$Q_{sf} < Q_{turb\_target}$	$Q_{TES(t-1)} - \lvert Q_{HX}\rvert \geq 0$	Storage discharge
	$Q_{TES(t-1)} - \lvert Q_{HX}\rvert < 0$	Limited storage discharge; → Eventual fossil backup required

Table 10: Overview of storage operation cases; HX = heat exchanger

An imperfect heat exchanger is assumed:

$$\lvert Q_{HX}\rvert = \left|Q_{sf} - Q_{turb\_target}\right| \cdot \eta_{HX} \quad \text{Eq. 4.43}$$

Heat losses in the heat exchanger are expressed with the efficiency η_{HX} [EnerMENA 2012]. Case two is managed by setting an additional condition in the solar field model:

$$Q_{sf\_max} = Q_{turb\_target} + \left(Q_{TES\_design} - Q_{TES(t-1)}\right) \quad \text{Eq. 4.44}$$

This back-coupling is also important to determine the correct value of the auxiliary power in the solar field. The actual storage state of charge is calculated as:

$$Q_{TES(t)} = Q_{TES(t-1)} - Q_{TES\_loss} + Q_{HX} \quad \text{Eq. 4.45}$$

Thermal losses of the storage are taken into account by the actual temperature of the molten salt in the storage tanks. For the cold tank [Bonacina 1992]:

$$T_{CT\_(t)} = T_{amb} - \left(T_{amb} - T_{CT\_(t-1)}\right) \cdot e^{-\frac{\Delta t}{\Delta t_0}} \qquad \text{Eq. 4.46}$$

$T_{CT\_(t)}$	[°C]	actual cold tank temperature
$T_{CT\_(t-1)}$	[°C]	cold tank temperature in the previous time step
T_{amb}	[°C]	ambient temperature
Δt	[s]	time step (typically one hour)
Δt_0	[s]	time constant of the cool-down process

The used equation represents only an approximated solution of the problem. The salt is assumed to have a negligible internal thermal resistance, i.e. the salt temperature is constant in each point of the tank. The time constant of the cooling process is a function of the storage size and of the molten salt volume:

$$\Delta t_0 = \frac{c_{p\_salt} \cdot \rho_{salt} \cdot V_{salt}}{k \cdot A_{tank\_e}} \qquad \text{Eq. 4.47}$$

ρ_{salt}	[kg/m³]	molten salt density
V_{salt}	[m³]	molten salt volume
k	[W/m²/K]	heat transmission coefficient of the ext. tank surface
A_{tank_e}	[m²]	tank external surface

The process time constant Δt_0 can be interpreted as the ratio between the internal heat capacity and the superficial thermal resistance. The larger Δt_0, the lower the thermal losses and the longer the cool down process. The heat losses of the cold tank are:

$$Q_{TES\_loss\_CT} = M_{salt\_CT} \cdot c_{p\_salt} \cdot \left(T_{CT\_(t-1)} - T_{CT\_(t)}\right) \qquad \text{Eq. 4.48}$$

A similar correlation applies for the hot tank. The freezing process in an Andasol-like storage is assumed to start after 85 days of continuous cooling [Flagsol 2005]. The heat transmission coefficient α has been empirically set considering this condition.

The diameter of the storage tanks has been calculated assuming a fixed tank height of 14 m. A maximal molten salt mass of 28,500 tons has been assumed for two-tank systems [Gathmann 2011]. This limitation is motivated by constructional reasons. If the maximal salt mass is exceeded, the basic two-tank system is replicated until the required capacity is achieved.

The electrical power required for the salt pumps is calculated as:

$$P_{parasitic\_TES} = P_{parasitic\_TES_0} \cdot \frac{\dot{m}_{salt}}{\dot{m}_{salt\_0}} \qquad \text{Eq. 4.49}$$

$P_{parasitic\_TES_0}$ [MW_{el}] power consumption of reference plant at design

$\dot{m}_{salt\_0}$ [ton/h] salt mass flow of reference plant at design

$\dot{m}_{salt}$ [ton/h] actual salt mass flow

The Andasol plant has been assumed as a reference plant for the definition of reference power consumption (1.5 MW_{el}) [Wittmann 2009] and reference salt mass flow (953 kg/s) [Doenitz 2009]. The actual salt mass flow is:

$$\dot{m}_{salt} = \frac{\dot{Q}_{HX}}{c_{p\_salt} \cdot (T_{HT} - T_{CT})} \qquad \text{Eq. 4.50}$$

4.6 Power Block

The power block model aims at the characterization of design and off-design performances of steam Rankine cycles for CSP applications. The implemented model can be applied for a wide range of power block configurations.

The main user inputs of the INSEL model are several design parameters such as turbine capacity, steam pressure at the inlet of the turbine (the temperature has been previously defined in the solar field model), the number of steam extractions and the cooling system type. The used steam physical properties are based on the industry standard IAPWS-IF97 [Wagner 1998].

4.6.1 Steam Turbine

Design Conditions

The basic layout of the modeled Rankine cycle is shown in Figure 35. This configuration is assumed to be the standard configuration for 50 MW_{el} parabolic trough power plants [Montes 2009]. According to this cycle size, six steam extractions are required. The steam extractions are essential for the improvement of the turbine efficiency as they allow increasing the average temperature of the heat supply [Strauß 2007]. The optimal number of steam extractions depends on the gross turbine capacity and is the result of a techno-economic trade-off. Each extraction is connected to a feed-water pre-heater.

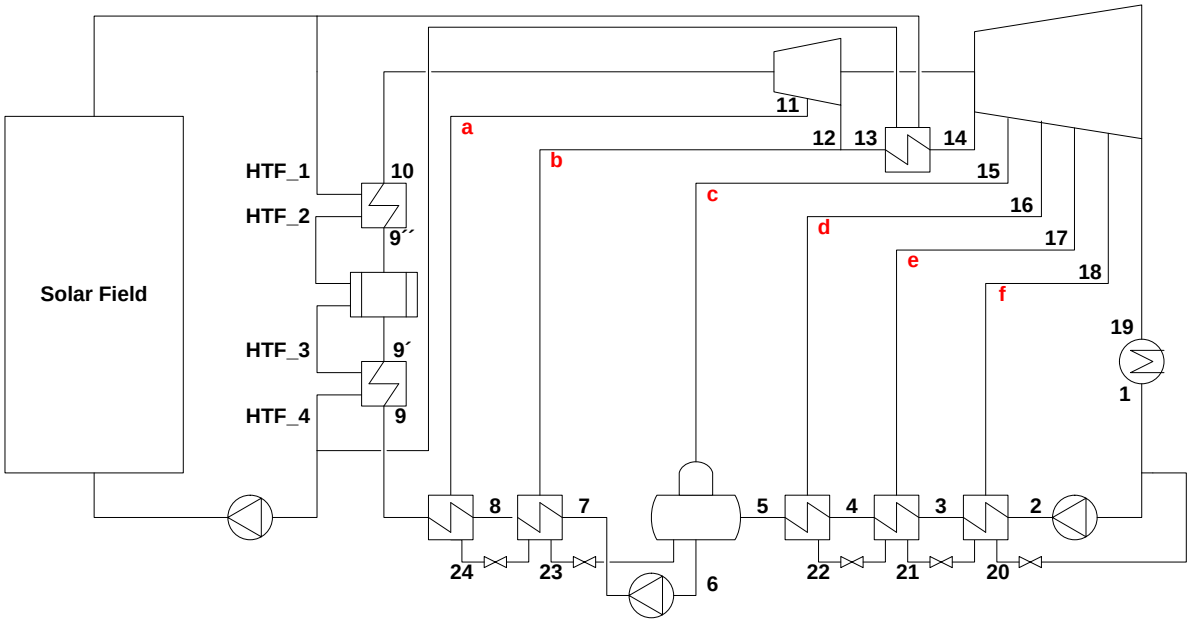

Figure 35: Schematic view of the implemented Rankine cycle [Montes 2009, adapted]

The fourth pre-heater (5-6 in Figure 35) also acts as deaerator. The pressure levels of the reference plant's steam extractions (100 bar at the turbine inlet) have been set according to [Montes 2009] in order to achieve the best cycle efficiency (equal specific enthalpy drop between two consecutive extractions). Alternatively, the user can define the pressure values in the user interface of INSEL. Figure 36 presents the temperature-entropy diagram corresponding to the reference power cycle.

The reheating section (12-13) fulfils two important functions. First, it permits a further increase in the turbine efficiency (the average temperature of heat supply is further raised). Second, it reduces the steam end moisture in the condenser, which has to be kept below approx. 12 % in order to avoid damage to the turbine components.

One of the most important tasks of the power block model is the calculation of the thermal efficiency of the turbine [Strauß 2007]:

$$\eta_{th} = \frac{\left|\dot{W}_{turb}\right|}{\dot{Q}_{in}} = \frac{\Delta H_{turb} - \Delta H_{pump}}{\Delta H_{SG} + \Delta H_{RH}} \qquad \text{Eq. 4.51}$$

$\dot{W}_{turb}$	[MW_{el}]	mechanical work of the steam turbine
$\dot{Q}_{in}$	[MW_{th}]	total supplied heat
ΔH_{turb}	[kJ]	enthalpy drop in the turbine stages: (10-12) and (14-19)
ΔH_{pump}	[kJ]	enthalpy increase in the feed water pump (1-2)
ΔH_{SG}	[kJ]	enthalpy increase in the steam generation (8-10)
ΔH_{RH}	[kJ]	enthalpy increase in the re-heating section (13-14)

Inlet steam parameters as well as steam condensation pressure have a relevant impact of the thermal efficiency of the steam turbine (Annex Figure 112).

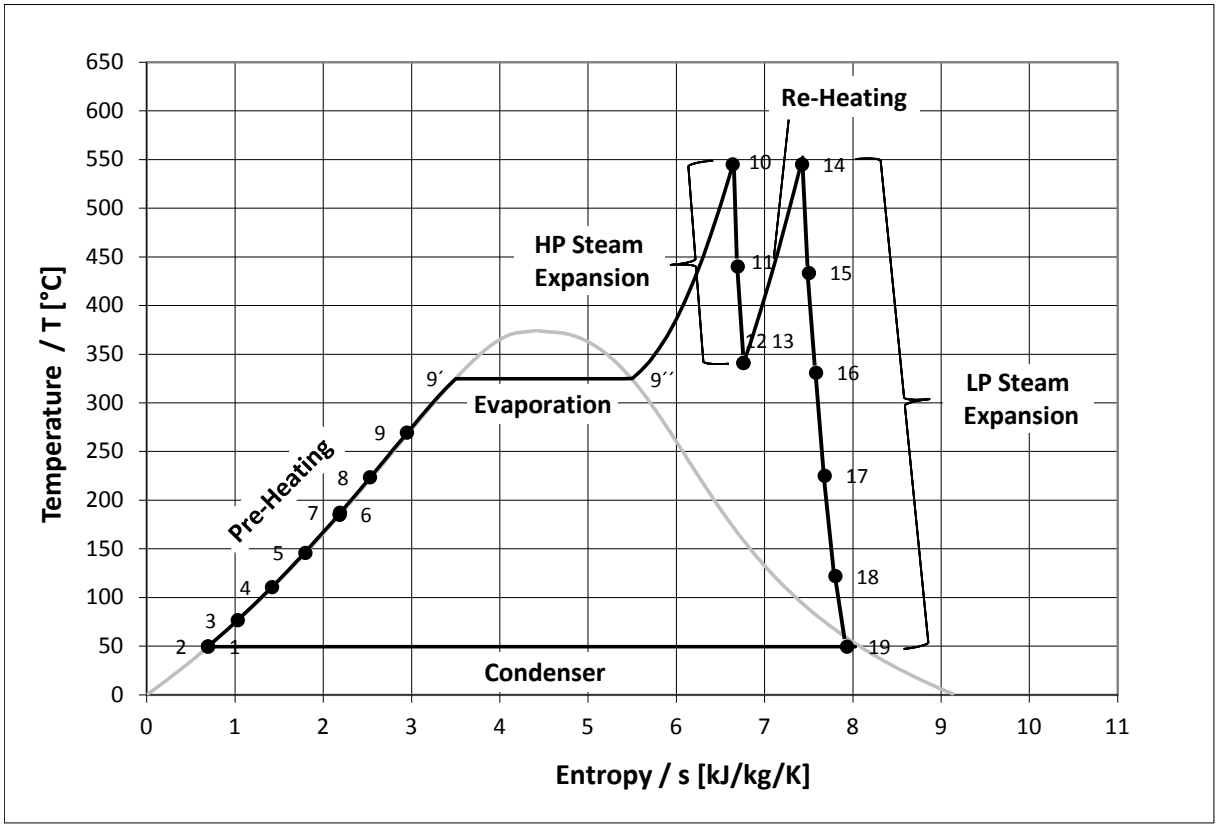

Figure 36: T-s diagram of a CSP Rankine cycle (Gemasolar-like CSP plant, molten salt receiver)

The calculation of the enthalpy values is made difficult by the presence of a relatively elevated number of steam extractions. Therefore, the solution procedure is divided into two steps. First, the specific enthalpy differences [kJ/kg] in the different cycle stages are calculated. Second, the water and steam mass flows are determined. Finally, Eq. 4.51 can be solved. The specific enthalpy supply of the two feed water pumps is:

$$\Delta h_P = \nu_1 \cdot \frac{(p_2 - p_1)}{\eta_{pump}} + \nu_6 \cdot \frac{(p_7 - p_6)}{\eta_{pump}} \qquad \text{Eq. 4.52}$$

ν_1	[m³/kg]	spec. feed water volume in 1
η_{pump}	[-]	pump efficiency
p_2	[bar]	feed water pressure in 2

The pressure values after the two pumps, i.e. p_2 and p_7, are calculated taking into account the constraints given by the downstream components of the power block. These constraints are the pressure at the deaerator p_6 and the pressure at the inlet of the turbine p_{10}, respectively. In turn, p_6 is defined by the pressure of the correspondent steam extraction p_{15}, whose design value is an input. In addition, pressure losses along the water

and steam piping system are taken into account (expressed as the percentage of the pressure of the previous stage) [Schüller 1999].

The enthalpy drop during steam expansion (Δh_{turb}) is the sum of the enthalpy drop of each turbine stage:

$$\Delta h_{turb} = \sum_{i=1}^{2} \Delta h_{HP\_i} + \sum_{i=1}^{5} \Delta h_{LP\_i} \qquad \text{Eq. 4.53}$$

Δh_{HP}	[kJ/kg]	enthalpy drop in the high pressure (HP) turbine section
Δh_{LP}	[kJ/kg]	enthalpy drop in the low pressure (LP) turbine section

The enthalpy drop of each turbine stage is calculated taking into account the enthalpy losses due to irreversibility:

$$\Delta h_{turb\_i} = \eta_{irr} \cdot \left(h_{i-1} - h_{i\_ideal}\right) \qquad \text{Eq. 4.54}$$

η_{irr}	[-]	efficiency of the turbine stage
h_{i_ideal}	[kJ/kg]	spec. enthalpy of the ideal process in i

The specific enthalpy of the ideal process is calculated assuming the same entropy of the previous stage. In the final stages of the turbine it has to be checked if the steam content x_{s_i} is within a safe range:

$$h_i = h_i^{'} + x_{s\_i} \cdot \left(h_i^{''} - h_i^{'}\right) \qquad \text{Eq. 4.55}$$

$$x_{s\_i} = \frac{s_i - s_i^{'}}{s_i^{''} - s_i^{'}} \qquad \text{Eq. 4.56}$$

$h_i^{'}$	[kJ/kg]	spec. enthalpy of saturated liquid water
$h_i^{''}$	[kJ/kg]	spec. enthalpy of saturated vapor
s	[kJ/kg/K]	specific entropy

The steam content has to be higher than 88 % [Strauß 2007]. The heat supply $\dot{Q}_{in}$ is given by the sum of heat required for steam generation and for re-heating. For the steam generator (pre-heating, evaporation and superheating) the enthalpy increase is:

$$\Delta h_{SG} = h_{10} - h_9 \qquad \text{Eq. 4.57}$$

The enthalpy difference between the points 2 and 9 is provided through steam extractions from the turbine (internal feed water pre-heating) and therefore it is not included in the calculation of Δh_{SG}.

The enthalpy at the inlet of the turbine h_{10} is easily assessed, because steam temperature and pressure are model inputs. The feed water temperature after the last pre-heater T_9 is calculated taking into account the temperature at the first steam extraction (Figure 35):

$$T_9 = T_{11} - TTD \qquad \text{Eq. 4.58}$$

TTD	[K]	terminal temperature difference of the feed water HX

TTD is defined as the temperature difference between the saturation pressure of the steam from the extraction and the feed water temperature at the outlet of the heat exchanger. Its value has been set to 1.5 K according to [Montes 2009].

The second step of the calculation procedure consists of the determination of the water and steam mass flows in each of the cycle stages. This is done by solving the thermal energy balance in each pre-heater. The total steam mass flow $\dot{m}_s$ is calculated taking into account the heat supply $\dot{Q}_{in}$, which is a known value:

$$\dot{m}_s = \frac{\dot{Q}_{in}}{\Delta h_{SG} + \Delta h_{RH} \cdot (1 - a - b)} \qquad \text{Eq. 4.59}$$

$\dot{m}_s$	[kg/s]	total steam mass flow
a	[-]	relative mass flow of the first steam extraction
b	[-]	relative mass flow of the second steam extraction

The mass flows a and b are relative mass flows, i.e. the mass flows are expressed as a relative fraction of the total mass flow $\dot{m}_s$ (which has the value of 1.00). The equations for the first and for the last heat exchanger are presented as two representative examples (Figure 35):

$$a = \frac{h_9 - h_8}{h_{11} - h_{24}} \qquad \text{Eq. 4.60}$$

$$f = \frac{(h_3 - h_2) \cdot (1 - a - b - c) - (h_{21} - h_{20}) \cdot (d + e)}{h_{18} - h_{20}} \qquad \text{Eq. 4.61}$$

The temperature of the condensed steam at the exit of the pre-heater is e.g. (Figure 35):

$$T_{22} = T_4 - DCA \qquad \text{Eq. 4.62}$$

DCA	[K]	dry cooling approach

The dry cooling approach is defined as the difference between the feed water at the inlet of the HX and the sub-cooled steam at the exit of the pre-heater. Its value has been set to 5 K according to [Montes 2009].

Finally, gross and net turbine efficiencies can be calculated [EnerMENA 2012]:

$$\eta_{gross} = \frac{P_{el\_gross}}{\dot{Q}_{in}} = \eta_{th} \cdot \eta_{gen} \qquad \text{Eq. 4.63}$$

$$\eta_{net} = \frac{P_{el\_gross} - P_{parasitic}}{\dot{Q}_{in}} \qquad \text{Eq. 4.64}$$

η_{gen}	[-]	generator efficiency
$P_{parasitic}$	[MW_{el}]	parasitic electrical consumption of plant components

The parasitic electrical consumption of the power block includes the power requirements of feed water pumps and cooling system.

Off-Design Conditions

A number of model adaptations have to be considered in order to describe the turbine performance under part load conditions. The actual load is defined as the ratio between actual steam mass flow and design steam mass flow:

$$Load = \frac{\dot{m}_s}{\dot{m}_{s\_design}} \qquad \text{Eq. 4.65}$$

The efficiency of the feed water pump and the generator are [Lippke 1995]:

$$\eta_{pump} = \eta_{pump\_design} \cdot (2 \cdot Load - Load^2) \qquad \text{Eq. 4.66}$$

The efficiency of the turbine stages is [Patnode 2006]:

$$\eta_{turb} = \eta_{turb\_design} \cdot [1 - (0.191 - 0.409 \cdot Load + 0.218 \cdot Load^2)] \qquad \text{Eq. 4.67}$$

The pressure losses along the feed water and steam lines are assumed to be proportional to the square of the load [Patnode 2006].

Another important model adaptation concerns the part load pressure in the different stages of the turbine. They are calculated according to the Stodola´s theory [Sigloch 1993]:

$$p_{i-1} = \sqrt{p_i^2 + \left(p_{i-1\_design}^2 - p_{i\_design}^2\right) \cdot Load^2} \qquad \text{Eq. 4.68}$$

Start-up Procedure

The power block -similarly to the solar field- has to be heated up before electricity generation is started. Once thermal resource becomes available, a certain amount of heat from the solar field or from the thermal energy storage has to be provided for the start-up process. The required heat is calculated with a simplified approach [EnerMENA 2012]:

$$Q_{turb_{start-up}} = Q_{in\_design} \cdot k_{turb\_start-up} \qquad \text{Eq. 4.69}$$

$k_{turb\_start-up}$ [-] power block start-up factor

The start-up factor $k_{turb\_start-up}$ takes into account the thermal inertia of the power block components under the assumption that they are a homogeneous thermal mass. Typical values of $k_{turb\_start-up}$ are between 0.10 and 0.50 [Wagner 2011] [Schenk 2012 b].

4.6.2 Cooling System

A key step of the power generation in Rankine processes is the condensation of the exhaust steam. The steam is condensed and returned to the steam generator. The lower the condensation temperature, the higher the conversion efficiency of the power block. The choice of the cooling system has a large impact on capital expenditures, operational expenditures, auxiliary loads and possibly water requirements. Main cooling configurations are once-through cooling, evaporative cooling and dry cooling [Moser 2013 b].

Cooling System Models

The models of the three described cooling systems are based on a simplified approach as presented in [Strauß 2007] and [Sokrates 2004]. The models mainly aim at the calculation of the condenser temperature and of the auxiliary power requirements for components such as pumps and ventilators. In the case of once-through cooling, the steam condensation temperature is calculated as the sum of the temperature of the cooling water (T_{cw}) and of the initial temperature difference (ITD) of the heat exchanger. The ITD is the temperature difference between the cooling fluid at the inlet of the condenser and the condensing steam. In turn, the ITD consists of the sum of temperature difference in the HX (ΔT_{cond}) and terminal temperature difference (TTD). The values of ΔT_{cond} and TTD as well as the calculation procedure are summarized in Table 11.

The required cooling water mass flow is calculated by solving the energy balance of the condenser. Finally, the electricity required by the cooling water pump is estimated with the Bernoulli equation, taking into account elevation difference between intake and cooling system, initial water velocity in the tubes and pressure losses by friction and plant devices. The steam condensation temperature in the case of evaporative cooling relies on the wet bulb air temperature. The temperature of the cooled water at the outlet of the evaporative

tower is assessed taking into account the equilibrium temperature difference ΔT_{eq}, which is the difference of the air saturation temperatures before and after the cooling process. Similarly to once-through cooling, the ITD of the water/steam heat exchanger has to be added as well. The water pump parasitic consumption is assessed similarly to the previous case. The power consumption of the tower fans also has to be considered. In the case of dry cooling, T_{cond} is equal to the dry bulb temperature plus the ITD of the condenser. Due to the poor heat capacity of air, higher ITD is typically selected in comparison to once-through and evaporative cooling. Optimal ITD is mainly a trade-off between investment and operation cost on the one hand and cooling efficiency on the other hand [Moser 2013 b].

		Once-Through	**Evaporative Cooling**	**Dry Cooling**
Calculation of condensation temperature				
T_{cond}	°C	$T_{cw} + ITD$	$T_{wet\_bulb} + \Delta T_{eq} + ITD$	$T_{dry\_bulb} + ITD$
ITD	K	$\Delta T_{cond} + TTD$	$\Delta T_{cond} + TTD$	$\Delta T_{cond} + TTD$ (15 - 25 K)
ΔT_{cond}	K	6 - 10	11	-
TTD	K	3 - 5	3 - 4	-
ΔT_{eq}	K	-	= f(T_{wet_bulb}; h_{air})	-
Calculation of parasitic consumption				
P_{par_cool}	MW_{el}	P_{par_pump}	$P_{par\_pump} + P_{par\_vent}$	P_{par_vent}
$\dot{m}_w$	kg/s	$\dot{m}_s \cdot \frac{\Delta h_{cond}}{c_{p\_w} \cdot \Delta T_{cond}}$	$\dot{m}_s \cdot \frac{\Delta h_{cond}}{c_{p\_w} \cdot \Delta T_{cond}}$	-
v	m/s	2.5 @ design	2.5 @ design	-
P_{par_vent}	MW_{el}	-	$\dot{m}_a^3 \cdot \frac{k_{vent}}{\eta_{vent}}$	$\dot{m}_a^3 \cdot \frac{k_{vent}}{\eta_{vent}}$
$\dot{m}_a$	kg/s	-	$\frac{\dot{m}_{W\_evap}}{\Delta x_a}$	$\dot{m}_s \cdot \frac{\Delta h_{cond}}{c_{p\_W} \cdot \Delta T_{cond}}$
k_{vent}	m^2/kg^2	-	[Sokrates 2004]	[Sokrates 2004]

Table 11: Summary of the cooling system models [Sokrates 2004], [enolcon 2010]

For CSP plants, optimal ITD is a function of several parameters such as solar field size and specific investment cost of different plant components. The power consumption of the ventilators is calculated with the same methodology as used for the evaporative cooling. However, in this case a much higher air mass flow is required, because the cooling process only involves sensible heat. Consequently, the total parasitic load of dry cooled units (assumption: forced convection) is higher than for once-through and evaporative cooling.

4.7 CSP INSEL Blocks

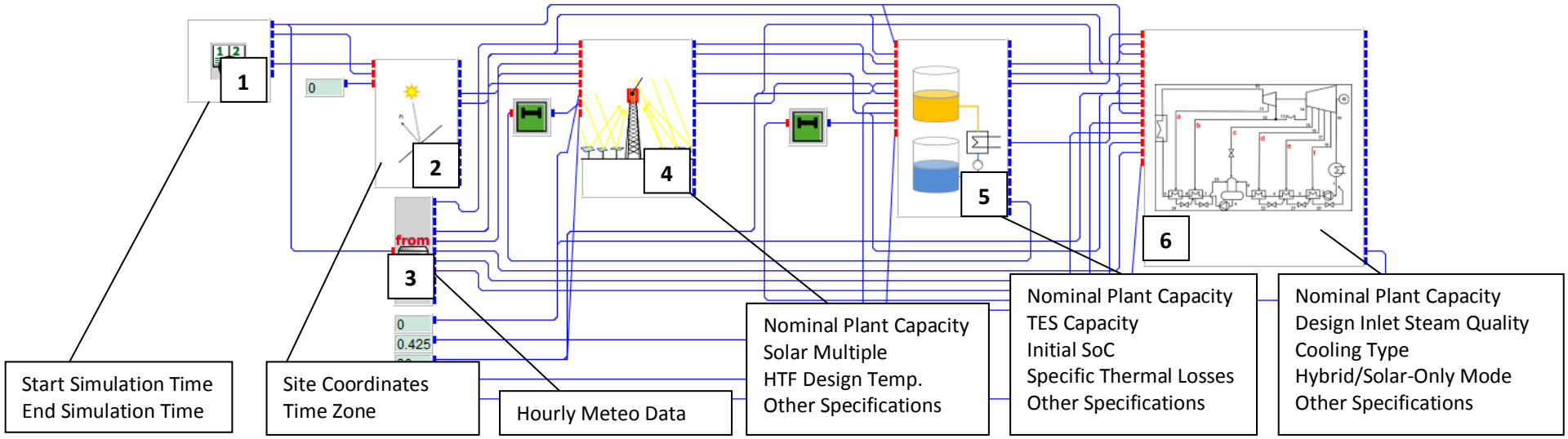

1 - Time Block		2 - Sun Position		3 - Read Block		4 - Heliostat Field and Central Receiver		5 - Thermal Storage (Molten Salt)		6 - Steam Turbine	
Input	**Output**	**Input**	**Output**	**Input**	**Output**	**Input**	**Output**	**Input**	**Output**	**Input**	**Output**
-	Time	Time	α_s γ_s	Time	DNI T_{amb} v_{wind} P_{atm} Q_{TES_rest} P_{el_demand}	Time α_s γ_s DNI T_{amb} v_{wind} Q_{TES_rest} P_{el_demand}	$\dot{Q}_{inc}$ $\dot{Q}_{rec}$ T_{HTF_sf} η_{sf} $\dot{Q}_{dump}$ $P_{parasitic\_sf}$ $Q_{startup}$ $\dot{Q}_{loss}$ Rec. Flux	Time T_{amb} T_{HTF_sf} $\dot{Q}_{sf}$ $P_{parasitic\_sf}$ $\dot{Q}_{rest\_turb}$ HTF Type P_{el_demand}	$\dot{Q}_{turb}$ T_{TES_out} Q_{TES} $\dot{Q}_{cofir}$ $d\dot{m}_{salt}$ $P_{parasitic\_TES}$ M_{hot_tank} M_{cold_tank} T_{hot_tank} T_{cold_tank} $\dot{Q}_{dump}$ Q_{TES_rest}	$\dot{Q}_{turb}$ T_{steam_in} T_{amb} P_{el_demand} $P_{parasitic\_sf}$ $P_{parasitic\_TES}$ Q_{TES} T_{cool_water} Cofir. Switch Rel. Hum. P_{atm} HTF Type	P_{el_gross} η_{turb_gross} η_{turb_net} Part Load p_{cond} $\dot{m}_{s\_cond}$ T_{cond} $P_{parasitic\_plant}$ P_{el_net} P_{el_solar} Q_{cofir}

Figure 37: Screenshot of the developed CSP INSEL models (central receiver) with specification of main design parameters (in the boxes), input and output values (in the table) for each INSEL block; only relevant parameters for this particular simulation are listed in the table; the complete list of the block parameters is reported in Annex 10.5

5 Photovoltaic Model

Photovoltaics (PV) are electronic devices which directly convert solar irradiation into electricity [IRENA 2013]. Other than CSP, PV makes use of both the direct and the diffuse radiation share. This is the reason why PV is able to generate electricity on cloudy or even rainy days, though with reduced production and conversion efficiency. The worldwide cumulated installed capacity reached 102 GW at the end of 2012, whereas approx. 30 GW of additional capacity had been installed in each of the two years before [EPIA 2013]. One of the key advantages of PV is its modularity. In fact, PV systems are used in a variety of plant capacities which ranges from a few Watts to hundreds of MW. Despite the very large potentials, the future development of PV will be affected by the additional costs for a number of measures such as optimized grids and energy storage, which will be required in order to manage increasing shares of variable electricity generation in the respective national electricity supply systems [IRENA 2013].

As the technology name indicates, the conversion of irradiation to electricity occurs due to the photovoltaic effect, i.e. two differently doped semiconductor layers are superposed and exposed to irradiation. In this way, electrons move across the junction between the two layers and generate a direct current (DC) [Quaschning 2007].

The basic element of a crystalline silicon (c-Si) PV plant is the solar cell. Cells are electrically connected and assembled in modules. A c-Si module typically consists of 60 up to 72 cells and has a capacity of between 120 and 300 W_p. Depending on the cell efficiency, this corresponds to a module area between 1.5 m² and 2.5 m² [IRENA 2013]. Modules are then connected in series to increase the voltage and in parallel to increase the current. In addition, a number of components other than the PV modules are necessary. They go under the name of balance of system (BOS) and include an inverter -which is needed in order to convert the generated DC into alternating current (AC)-, power control, cabling and racking. Even if the BOS consists of proven technologies, its price has been significantly reduced in the last few years. The balance of system may also include the backup system, e.g. batteries, which -however- have not yet reached commercial prices.

Technologies

Several PV technologies exist which have achieved commercial maturity or still are under development. They can be divided into three groups (also called generations), i.e. wafer-based crystalline silicon, thin film and emerging and novel concepts. The largest market share is currently taken by crystalline silicon (c-Si) technologies with roughly 90 % (the other 10 % is represented by thin film technologies). c-Si have been selected as the reference PV technology within this work.

5.1 PV Model

Tracking

PV plants can be classified in three groups according to their sun tracking strategy: fix-mounted, one-axis tracking and two-axis tracking (Figure 38).

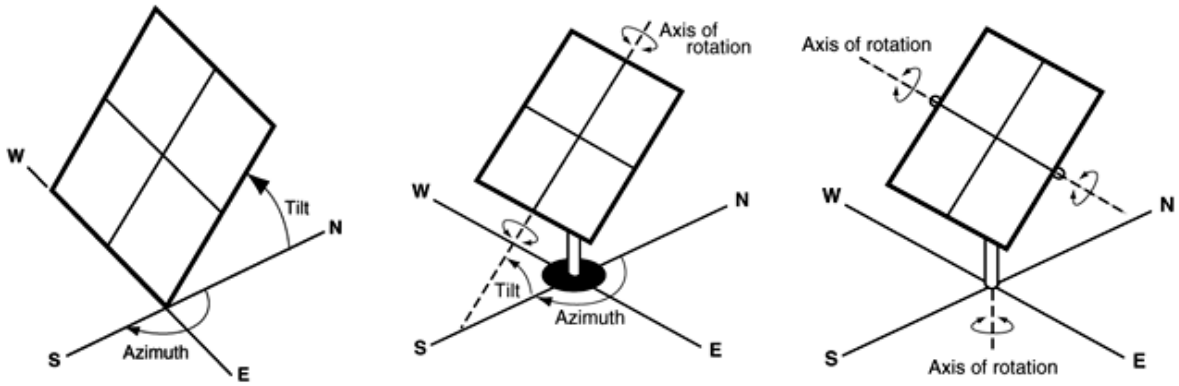

Figure 38: Sun tracking options of PV modules [PV WATTS 2013]

In fix-mounted systems, both tilt angle and azimuth angle do not change over time. The collectors are typically oriented to the south (in the northern hemisphere), while the optimal tilt angle mainly is a function of latitude. In one-axis tracking systems, the axis of rotation typically is perpendicular to the tilt axis. The calculation of the optimal effective tracking angle is performed in INSEL by means of the PHIOPT block [INSEL]. The required inputs are sun elevation angle and sun azimuth. In addition, collector azimuth and tilt angle also have to be specified. Finally, in the case of two-axis PV tracking systems, both azimuth angle and tilt angle change over time. These angles are set equal to γ_s and to the complementary angle to α_s (i.e. the zenith angle), respectively.

PV Modules

The modeling of PV plants in INSEL is easily performed, as the software includes a wide library of commercial PV modules and inverters [INSEL]. The PV system model includes a number of components which are PV modules, a maximum power point (MPP) tracker and an inverter. The performance of a c-Si PV module is carried out using the PVI block. This block is divided into two parts, i.e. electrical model and thermal model. The thermal model is based on a simplified thermal balance of the modules [INSEL]. The electrical model calculates the output current as a function of incident irradiance, module orientation, ambient temperature and wind velocity. The model bases on the two-diode model [Quaschning 2007] [INSEL]. The electricity generation is the product of current I and voltage U:

$$P = I \cdot U \qquad \text{Eq. 5.1}$$

P [W] electricity generation of a single PV cell

The maximal power output is iteratively calculated at each time step of the simulation by the MPP-tracker. Typical PV modules consist of a number of cells connected in parallel and in series. In this way, current and voltage can be increased:

$$\begin{cases} I_p = I \cdot n_p \\ U_s = U \cdot n_s \end{cases} \qquad \text{Eq. 5.2}$$

n_p [-] number of cells connected in parallel

n_s [-] number of cells connected in series

The inverter losses are assessed in INSEL with the IVP block. This block is based on the model proposed by [Schmidt 1996]. A constant share of the produced power is used by the inverter for self-consumption. In addition, it is assumed that voltage losses are linearly proportional to the generated power, while ohm losses are proportional to the second power of P. The inverter efficiency is close to the nominal value for a large range of irradiance.

A number of other losses which reduce the overall PV plant efficiency have to be taken into account. These losses include nameplate DC rating, mismatch, wiring, soiling and system availability (Table 12).

Component Loss Factor	Typical Value	Description
PV module nameplate DC rating	0.95	There is typically a difference between the nominal capacity given by the manufacturer (nameplate) and the actual power generation under STC
Mismatch	0.98	Each cell has a slightly different current-voltage curve (within a tolerance). As a number of cells is connected in series and in parallel, they are not exactly operated at their MPP
DC wiring	0.98	Resistive losses exist in the wiring between modules and along the connection between the PV array and the inverter
AC wiring	0.99	Resistive losses exist in the wiring between the inverter and the electricity grid connection
Soiling	0.95	Dirt and other foreign matters reduce the amount of radiation which actually reaches the cell. This parameter depends on meteorological conditions and proximity of the plant to high-traffic roads and high-pollution areas
System availability	0.98	Takes into account for off-line times due to maintenance and unforeseen outages (e.g. inverter)

Table 12: Loss factors of PV systems [PV WATTS 2013]

5.2 INSEL PV Blocks

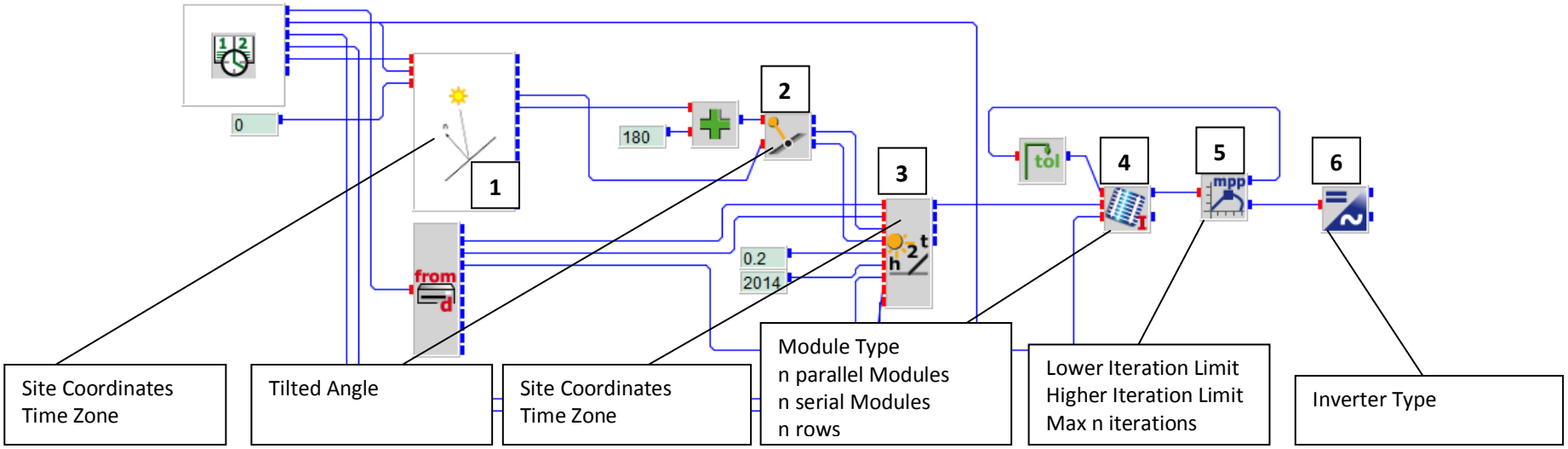

1 - Sun Position		2 - Optimum Tracking (1-axis)		3 - Horizontal to Tilted Irradiance		4 - PV Modules		5 - MPP Tracker		6 - Inverter	
Input	**Output**	**Input**	**Output**	**Input**	**Output**	**Input**	**Output**	**Input**	**Output**	**Input**	**Output**
Time	α_s γ_s	α_s γ_s	β γ_c	GHI DHI β γ_c ρ_{ground} Time	GTI	U GTI T_{amb}	I	I	U P_{el_DC}	P_{el_DC}	P_{el_AC} $\eta_{inverter}$

Figure 39: Screenshot of the developed PV INSEL model with specification of main design parameters (in the boxes), input and output values (in the table) for each INSEL block; Note: only relevant parameters for this particular simulation are listed in the table; the complete list of the parameters of the newly developed INSEL blocks is reported in Annex 10.5; for commercial INSEL blocks refer to [INSEL]; GHI = global horizontal irradiance; DHI = diffuse horizontal irradiance; GTI = global tilted irradiance;β= tracking angle; ρ_{ground}= ground reflectivity

6 Wind Power Model

Wind power is currently the second largest contributor to the renewable electricity generation -after hydropower. The worldwide installed capacity at the end of 2013 amounted to ca. 320 GW [GWEC 2014]. The large installation rate in the last years has driven the cost down and wind actually is currently among the cheapest options for renewable electricity generation. The typical capacity of new installed turbines is around 2 MW; however turbines up to 7 MW are being developed, mainly for offshore applications [Vestas 2012].

6.1 Wind Model

Figure 40 shows a typical characteristic power generation curve of a wind turbine (as provided by the wind power producer [Gamesa 2014]).

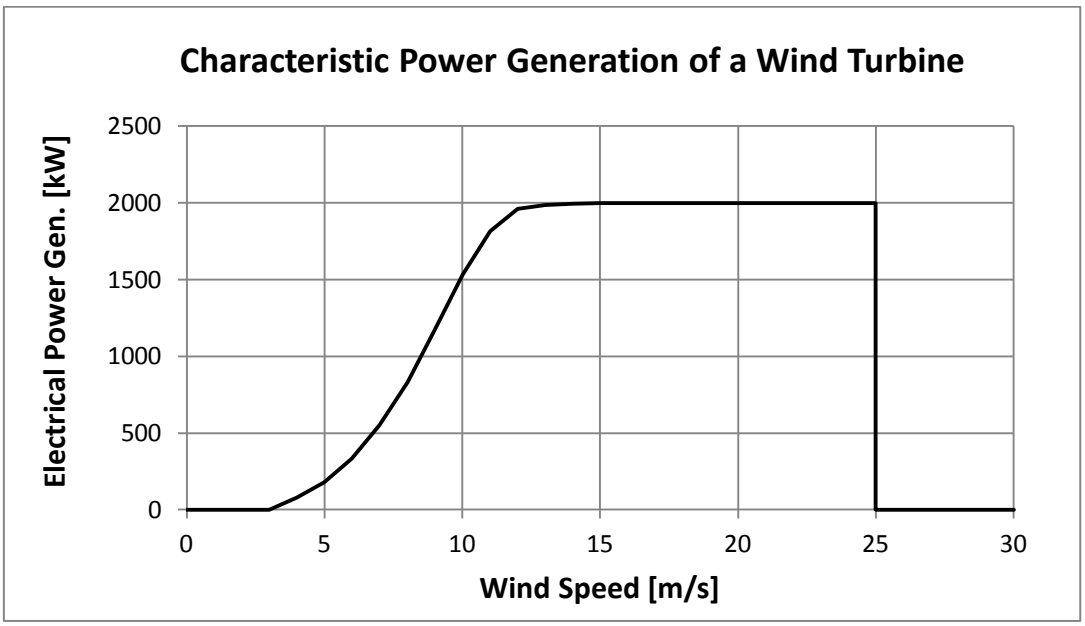

Figure 40: Characteristic power generation curve of a 2 MW wind turbine [Gamesa 2014]

The turbine starts operation if the wind speed $\bar{v}_{Wind}$ exceeds a threshold called cut-in wind speed (typically 2.5 m/s to 5.0 m/s). This speed corresponds to the velocity at which the power generation overcomes friction losses in the shaft and in the gearbox. If wind speed ranges between ca. 4 m/s and 12 m/s the generated power increases proportionally to the third power of $\bar{v}_{Wind}$ [Emeis 2013]. Above 12 m/s, wind power production is maintained almost constant in order to guarantee stable operation of the machine. Finally, turbine operation has to be interrupted due to safety reasons in the case wind speed exceeds cut-off velocity (typically ca. 25 m/s).

The characteristic power generation curves refer to the wind velocity at hub height. Wind speed measurements are typically carried out at a height of 20 meters above the ground.

Modeling of vertical wind velocity profiles is a rather vast topic [Emeis 2013] [Jensen 2007]. One of the most simple wind profile formulations is represented by the logarithmic law:

$$v_{Wind}(z_{hub}) = v_{Wind}(z_{hub}) \frac{ln\left({}^{z_{hub}}/_{z_0}\right)}{ln\left({}^{z_{meas}}/_{z_0}\right)} \qquad \text{Eq. 6.1}$$

z_{hub}	[m]	hub height
z_{meas}	[m]	measurement height
z_0	[m]	surface roughness length

which assumes flat uniform terrain and neutral buoyancy conditions. The surface roughness length z_0 depends on terrain surface characteristics: it typically varies between 0.0001 m in vast water surfaces to approx. 1.0 m in tall forests.

The combined impact of air temperature, humidity and site elevation on air density also have to be taken into account [Ackermann 2000]:

$$\rho_{air}(z) = \frac{p_{meas}}{\bar{R} \cdot \bar{T}_{virt}} \cdot exp^{\left[\frac{-g \cdot (z - z_{meas})}{\bar{R} \cdot \bar{T}_{virt}}\right]} \qquad \text{Eq. 6.2}$$

$\rho_{air}(z)$	[kg/m³]	air density at hub elevation
p_{meas}	[hPa]	atmospheric pressure at measurement elevation
$\bar{R}$	[J/kg/K]	universal gas constant
$\bar{T}_{virt}$	[K]	average virtual temp. between measurement and hub elevation

The impact of humidity on air density is considered by the virtual temperature. $\bar{T}_{virt}$ is defined as the temperature of a virtual dry air mass which has the same density of the considered humid air at the current temperature T. The virtual temperature is defined as [Emeis 2013]:

$$T_{virt} = T \cdot (1 + 0.609 \cdot q) \qquad \text{Eq. 6.3}$$

q	[-]	specific humidity

A series of losses (i.e. wiring, wake losses, time lag in the adjustment of the turbine direction) reduces power generation. A constant all-inclusive loss factor $k_{loss} = 15\ \%$ has been assumed as a first approximation [Sader 2012].

Finally, the power generation of the wind park is expressed as:

$$P_{Wind} = n_{turb} \cdot P(v_{Wind}(z_{hub})) \cdot \frac{\rho_{air}(z)}{\rho_{air\_0}} \cdot (1 - k_{loss}) \qquad \text{Eq. 6.4}$$

n_{turb}	[-]	number of wind turbines
ρ_{air_0}	[kg/m³]	reference air density (= 1.225 [kg/m³])
k_{loss}	[-]	all-inclusive loss factor

6.2 INSEL Wind Blocks

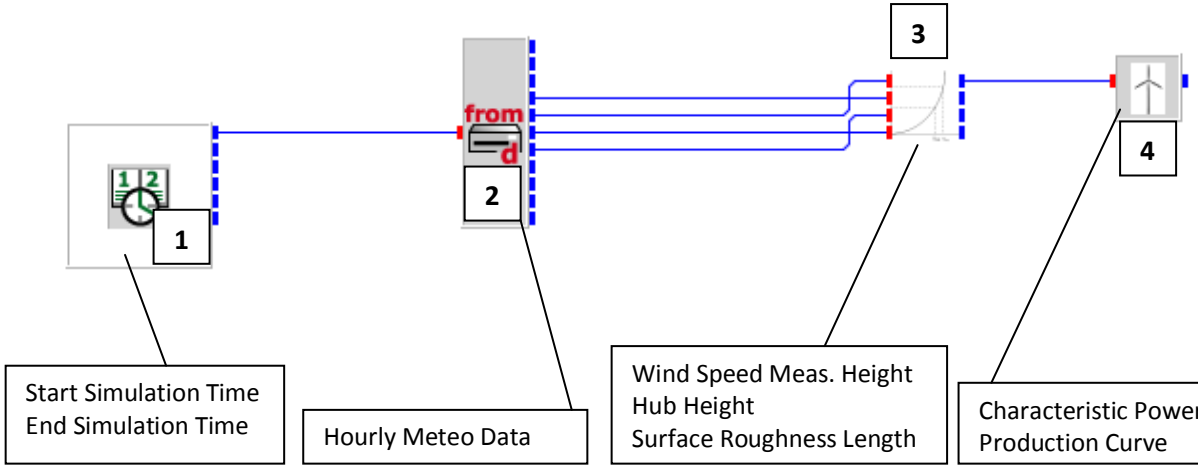

1 - Time Block		2 - Read Block		3 - Wind Speed Height Adjustment		4 - Wind Turbine	
Input	**Output**	**Input**	**Output**	**Input**	**Output**	**Input**	**Output**
-	Time	Time	T_{amb} $v_{wind@meas}$ P_{atm} Rel. Hum.	T_{amb} $v_{wind@meas}$ P_{atm} Rel. Hum.	$v_{wind@hub}$	$v_{wind@hub}$	P_{el}

Figure 41: Screenshot of the developed wind power INSEL model with specification of main design parameters (in the boxes), input and output values (in the table) for each INSEL block; Note: only relevant parameters for this particular simulation are listed in the table; the complete list of the parameters of the newly developed INSEL blocks is reported in Annex 10.5; for commercial INSEL blocks refer to [INSEL]

7 Economic Analysis

This chapter presents the methodology used for economic evaluation of renewable desalination plants. The analysis is limited to power generation technologies and desalination technologies which have been described in the previous chapters. The main result of the economic analysis is the levelized water cost (LWC) of the analyzed desalination plant. The LWC calculation involves a number of steps. First, the cost of power supply (electricity and -eventually- heat) is estimated. The heat cost is assessed according to a simplified reference cycle method. Secondly, the water cost is calculated, whereas the power requirements of the desalination plant are considered as operating costs.

The values provided in this dissertation are mainly qualified for rough estimation and the detection of general trends. The calculated investment cost and operating cost are not suitable for project development, as the uncertainty of the cost estimation is high, even for direct costs. Depending on the analyzed technology, the uncertainty may reach ± 35 %. The high uncertainty is due to local factors as well as to the lack of data availability for technologies or configurations which are still in an early development stage.

7.1 Levelized Electricity Cost (LEC)

The calculation of the levelized electricity cost is a common mean for the comparison of different power plants over their operational life. The term “levelized” means average product cost over the complete life time of the plant. Despite its broad utilization, the LEC calculation is based on some assumptions which should be critically discussed:

- LEC does not provide any information about the quality (i.e. availability over time, dispatchability) of the generated electricity in a power supply system [ISE 2012]. Rather, LEC represents only the electricity generation cost at plant-level without consideration of any system externality.
- In addition, LEC is mainly an indicator of investor costs under the assumptions of certainty of production and stability of revenues. This means that specific market or technological risks are not taken into account in the calculation [IEA 2010]. For this reason, LEC is closer to the specific electricity generation cost in a regulated electricity market with guaranteed loans and secured tariffs (e.g. power purchase agreements) than in a completely liberalized electricity market.
- Finally, LEC has not to be confused with the feed-in tariff. In fact, the latter can only be calculated by taking into account additional parameters such as the taxation law [ISE 2012].

The LEC is calculated as the equivalence between the present value of the sum of annual discounted cost and annual discounted revenues over the whole plant life. The costs and the revenues occurring at different times cannot be simply added, because cash flows at

different times also have different values of money. So, before the cash flows can be added, they have to be harmonized (i.e. discounted) to a common reference time, which is assumed to be the year of the plant operation start:

$$Cash\ Value_0 = \frac{Cash\ Value_n}{(1+r_d)^n} \qquad \text{Eq. 7.1}$$

r_d	[%/y]	discount rate

The assumed loss in the value of money over time may be caused by different reasons such as inflation, existence of risk over the value of a certain amount in the future and the need for a return for investors [EDF 2010]. In fact, the idea of discounting is also related to the concept of opportunity cost: the money which is invested at a certain time in a project is not available anymore for alternative investments. According to Eq. 7.1, the further away the cash flow in the future, the lower the corresponding present value. Moreover, the higher the discount rate, the higher the project risk. The levelized electricity cost is:

$$LEC = \frac{\sum_{t=1}^{t_{life}} \frac{C(t)_{capital} + C(t)_{operation}}{(1+r_d)^t}}{\sum_{t=1}^{t_{life}} \frac{E_{el\_y}}{(1+r_d)^t}} \qquad \text{Eq. 7.2}$$

$C(t)_{capital}$	[Mio. €/y]	capital cost in the year t
$C(t)_{operation}$	[Mio. €/y]	operating cost in the year t
E_{el_y}	[GWh_{el}/y]	yearly net electricity generation
t_{life}	[y]	economic plant life

Some discussion exists about the appropriateness of also discounting the electric annual yield, which is at the denominator of the LEC calculation (Eq. 7.2). As physical parameters do not change their value over time, at a first glance it seems inappropriate to discount them. However, even if it seems that the electricity yield is discounted, in reality the discount is related to the cash flow which is generated by selling that amount of electricity [IEA 2010]. This issue can be better understood by reshaping Eq. 7.2 as equivalence between discounted revenues and discounted costs:

$$\sum_{t=1}^{t_{life}} \frac{E_{el\_y} \cdot LEC}{(1+r_d)^t} = \sum_{t=1}^{t_{life}} \frac{C(t)_{capital} + C(t)_{operation}}{(1+r_d)^t} \qquad \text{Eq. 7.3}$$

Therefore, the applied calculation appears justified. The net electricity generation is assumed to be constant over the whole plant life. Neither the deterioration of plant components nor the year-to-year variability of renewable resources is considered. The

economic life of the plant is a technology-specific parameter, which will be discussed more in detail in chapter 8.

The capital costs are calculated by means of the annuity method:

$$C(t)_{capital} = CAPEX \cdot \frac{r_i \cdot (1 + r_i)^{t_{debt}}}{(1 + r_i)^{t_{debt}} - 1} \qquad \text{Eq. 7.4}$$

$CAPEX$	[Mio. €]	capital expenditures at plant operation start
r_i	[%/y]	interest rate
t_{debt}	[y]	debt payback period

As the debt payback period is lower than the economic plant life, $C(t)_{capital}$ is equal to zero in Eq. 7.2 for $t_{debt} < t \leq t_{life}$. The CAPEX also considers the interests on capital during construction. Figure 42 shows an exemplary cash flow for a CSP plant. The assumed plant construction time is two years; inflation is neglected. After the plant starts operation, the revenues obtained by electricity selling allow paying back the debt in constant rates. During the first years of operation, the debt share represents more than half of the annual capital cost. After the debt has been paid back, operating costs are the only remaining cost factor.

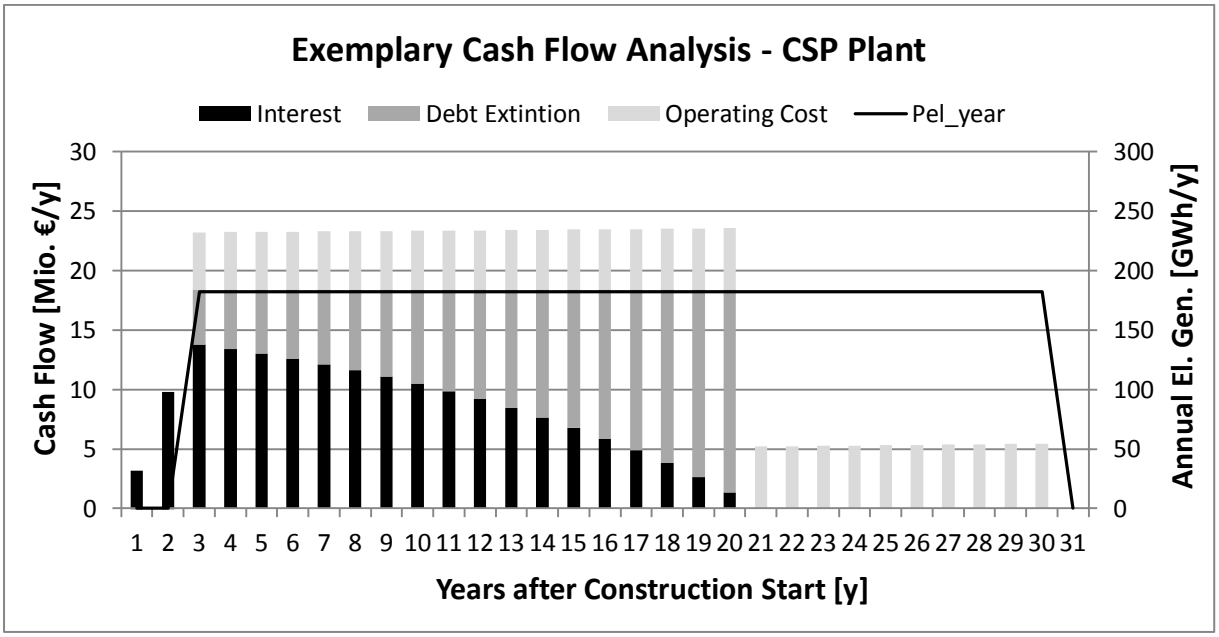

Figure 42: Exemplary cash-flow analysis of an CSP plant (assumptions: 50 MW, SM 2.5, 2 years construction time, 20 years debt payback period, 30 years economic plant life, interest rate = 8.0 %/y, discount rate = 5.0 %/y)

Capital cost includes the expenditures for all relevant plant components which are land cost and site improvements, main plant components, civil and electrical works as well as contingencies. The detailed breakdown of CAPEX for each of the considered technologies (CSP, PV and wind power) is reported in Annex 10.3.2. Operating cost includes operation and maintenance (O&M), insurance and eventually fuel cost.

Scale Effects

The size of components of a particular technology impacts the specific investment cost [Turchi 2010], [Turchi 2013], [MENAWATER 2011]. Due to effects of scale, the larger the size of a component, the lower the capacity-specific unit cost. The estimation of specific investment cost is performed according to [Singer 2013]:

$$c_i = c_{i\_0} \cdot \left(\frac{Size_i}{Size_{i\_0}} \right)^{\alpha_{S\_i}-1} \qquad \text{Eq. 7.5}$$

c_i	[€/unit]	specific investment cost of component i
c_{i_0}	[€/unit]	specific investment cost of component i (reference size)
α_{S_i}	[-]	component-specific size scaling factor

Learning Curves

A last consideration should be made about the price development of specific components of a technology over time. For each of the plant components a learning curve was assumed, which is the function of the worldwide installed capacity over time and of the progress ratio, as defined in Eq. 7.6 [Trieb 2009]:

$$c_i(t) = c_i(t_0) \cdot \left(\frac{P^*(t)}{P^*(t_0)} \right)^{\frac{log(PR_i)}{log(2)}} \qquad \text{Eq. 7.6}$$

$c_i(t)$	[€/unit]	specific cost of the component i at the time t
$c_i(t_0)$	[€/unit]	specific cost of the component i at the reference time t_0
$P^*(t)$	[GW]	worldwide installed capacity at the time t
PR_i	[-]	progress ratio of the component i

The progress ratio quantifies the percentage reduction of the investment cost of a specific plant component which occurs by doubling the worldwide installed capacity of the considered technology.

7.2 Levelized Water Cost (LWC)

The calculation of the levelized water cost is based on the evaluation of investment cost and operating cost of desalination plants. In most cases such data are not in the public domain [Gebel 2008] and are generally available only to the general contractor [Desportes 2013]. Nevertheless, thanks to data found in the literature and other data made available from

different project partners [SIDEM 2010], [MENAWATER 2011], it was possible to develop a water cost model for MED and RO plants.

The simplest approach for the determination of the investment cost of a desalination plant is to use the specific capital cost (e.g. [€/(m³/day)]). Such data are available in the literature. However, the interpretation of these data is complicated by the fact that often the system limits of the plant are not clearly indicated (e.g. if the intake cost and the pipeline cost to and from the plant are included in the evaluation). In addition, the specific capital cost refers to a specific plant capacity and configuration, given metal and material prices, and site-specific conditions. Due to the high number of the involved design parameters, a pre-set specific investment cost cannot be used. The calculation of LWC is similar to Eq. 7.2, which has been used for the assessment of LEC:

$$LWC = \frac{\sum_{t=1}^{t_{life}} \frac{C(t)_{capital} + C(t)_{operation}}{(1+r_d)^t}}{\sum_{t=1}^{t_{life}} \frac{M_{w\_y}}{(1+r_d)^t}} \qquad \text{Eq. 7.7}$$

whereas M_{w_y} is the annual water production [Mio. m³/y].

Annual capital cost is calculated by means of the annuity method, using the same procedure shown in Eq. 7.4. Capital cost includes the expenditures for all relevant plant components which are seawater intake, feed water pre-treatment, desalination process, potabilization, brine discharge, civil and electrical works as well as contingencies. The detailed breakdown of CAPEX for MED and RO is reported in Annex 10.3.1.

Operation costs include, personnel, maintenance, energy cost (electricity and heat), chemicals and replacement of components (e.g. membranes in RO plants). While the calculation of most of the operation cost items is rather straight-forward, the calculation of heat cost in MED plants needs some explanation.

Heat Cost

Energy costs (electricity and eventually heat) are the most important positions in the assessment of variable costs of desalination plants. Different approaches have been proposed for the calculation of this cost item [El-Nashar 1999], [Wade 1999].

In this dissertation a quite straight-forward methodology has been applied, which is based on the reference-cycle method described in [Sommariva 2010]. This approach mainly consists of the comparison between the performances of a defined reference power cycle (electricity generation only) and the dual-purpose power cycle, under the assumption that the power outputs of both power plants are the same. It is assumed that the thermal desalination unit uses the waste steam of the power cycle as heat source. The reference

cycle is defined as a cycle with the same steam parameters at the inlet of the turbine as in the dual-purpose case, but with conventional cooling.

Dependent on site-specific conditions such as seawater temperature, air temperature and relative humidity, the conventional cooling may be once-through or evaporative cooling. The steam condensation temperature and the electrical efficiency of the steam turbine are higher in the reference case than in the dual-purpose configuration. Figure 43 shows that the higher the pressure (and hence the temperature) of steam extraction, the higher the specific electricity losses in comparison to the reference case (steam condensation pressure of approx. 0.1 bar).

The heat cost is the cost which is needed to compensate for the missing incomes of the power plant due to the electricity losses:

$$C_{heat} = P_{el\_y\_loss} \cdot LEC_{ref} \qquad \text{Eq. 7.8}$$

C_{heat}	[Mio. €/y]	annual cost for heat supply
$P_{el\_y\_loss}$	[kWh/y]	annual electricity losses
LEC_{ref}	[€/kWh]	LEC of the reference power plant

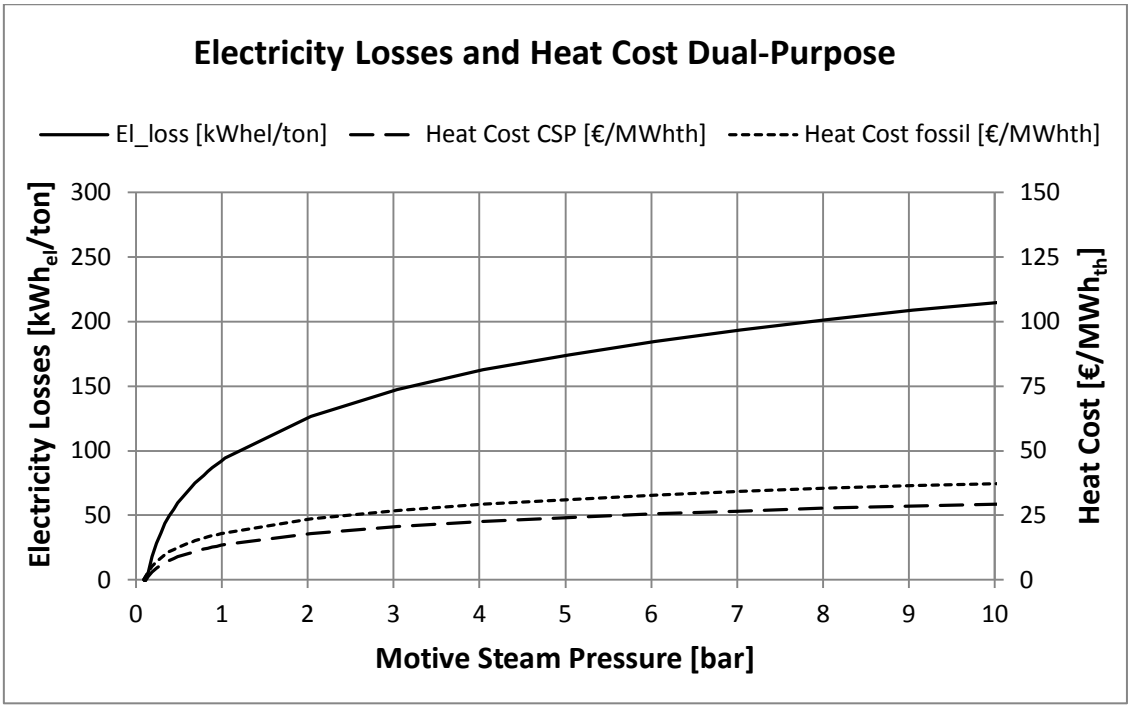

Figure 43: Specific electricity losses (in kWh_{el} per ton of feed steam) and heat costs for a CSP plant and a fossil power plant; Assumptions: state-of-the-art CSP investment costs; fossil fuel price: 100 $/bbl

Scale Effects

The data which have been used as a reference for the development of this cost model apply for utility scale desalination plants, with a capacity of approximately 100,000 m³/day. In order to calculate the investment cost of plants of the same type, but with different capacities, the exponential method can be used as a rough assumption [Gebel 2008].

According to this method, the CAPEX of a MED plant are:

$$C_{CAPEX\_MED} = c_{CAPEX\_MED\_0} \cdot \dot{m}_d^{2/3} \qquad \text{Eq. 7.9}$$

C_{CAPEX_MED}	[Mio. €]	MED plant CAPEX
c_{CAPEX_MED}	[€/(m³/day)]	MED specific CAPEX
$\dot{m}_d$	[m³/day]	design plant capacity

For RO plants a similar approach can be used. In this case the factor at the exponent should be 0.83 instead of 2/3.

7.3 System Supply Cost

When analyzing electricity supply systems, the weighted LEC of the power park is used as a mean for final comparison among different plant configurations. The same approach has been used with regard to desalination plants, which are compared by means of the LWC.

The question as to which objective function should be used for the final economic assessment of combined power and water supply systems remains to be answered. A possibility is the calculation of the annual average cost of supply for electricity and desalinated water. Such a function can be used as a final means of comparison, due to the fact that each of the analyzed cases has to cover the same power and water demand profiles. The annual average cost consists of the sum of the OPEX of each of the power plants and of the desalination plant:

$$Supply\ Cost = \sum_{PP=1}^{n} OPEX_{PP} + \sum_{DES=1}^{k} OPEX_{DES} - ENEX_{DES} \qquad \text{Eq. 7.10}$$

The energy cost of the desalination plants ($ENEX_{DES}$) has to be subtracted from the operation cost due to the fact that the costs of the energy supply (i.e. also the energy supply of the desalination plants) have been already considered within the operation cost of the power plants ($OPEX_{PP}$). This is to avoid the energy cost of the desalination plant being taken into account twice. The annual average supply cost is expressed in [Mio. €/y], whereas the term “average” means that such a cost is calculated as an average over the lifetime of each plant.

8 Case Studies

The final part of this dissertation shows potentiality and flexibility of the developed model within a case study. A summary of the used input data (i.e. meteorological inputs and selected technologies) is represented in 8.1. The actual case study is structured in three main parts. The first two sections analyze in detail the performance of each renewable technology (8.2) and each desalination technology (8.3) as standalone application, respectively. The main objective of these two tasks is the identification of key parameters which impact the performance of the plants and their optimal configuration. For each considered technology a pre-selection of best performing configurations has been carried out, if possible. Based on these findings, the third and last section (8.4) analyzes combined systems for the supply of power and water.

The modeling of renewable desalination plants depends on a wide range of parameters. Renewable energy sources are characterized by time intermittency, and even if electricity generation patterns of renewable power plants present some regularity, a secure prediction is not possible. Location-specific meteorological inputs with sufficient time resolution are of foremost importance for the design and the correct yield assessment of renewable technologies such as CSP, PV and wind power. Except for remote, mainly small-scale units, which are not object of this analysis, renewable power plants are integrated into power supply systems. Such systems aim at satisfying the power demand of a defined region or municipality without any interruption. As the intermittent nature of renewable resources does not generally match power demand fluctuations, additional components have to be considered in order to guarantee power supply. Accumulators such as thermal storages in CSP plants allow buffering eventual power generation surpluses, while conventional back-up systems (e.g. diesel generators and gas turbines) are used whenever the power delivered by RE plants and storages is insufficient to cover the demand. Thus, the impact of power dumping (i.e. eventual curtailments due to excessive renewable generation at certain times) and efficiency losses due to part-load behavior and start-up procedures of conventional power generation plants and steam turbines have an important impact on technical and economic performances of the overall system.

Utility scale desalination plants typically are operated round the clock, as the water demand does not experience significant daily fluctuations. Water demand fluctuations as well as eventual plant outages are bridged by one-day-capacity storages. Depending on the location, the water demand may present seasonal variations, which are -however- less accentuated than power demand fluctuations [Ludwig 2004]. The water demand in the selected site (Marsa Alam, Egypt) experiences minimal seasonal variations only and can be assumed as constant [MENAWATER 2011].

8.1 Model Inputs and Main Assumptions

The main model inputs are summarized in this section, which starts with a brief characterization of the two analyzed locations at the Marsa Alam Governorate. Information is given about local electricity and water demand, renewable resources as well as technical and economic assumptions.

Site Information and Demands

Marsa Alam has been selected as the main site for the case study. This city is a remote touristic location in the South-East of Egypt, along the coast of the Red Sea. The governorate of Marsa Alam is not connected to the main national networks (i.e. water, electricity and natural gas) [Abou Rayan 2003], which makes it attractive for the development of renewable desalination plants. A geographical information system (GIS)-based analysis has been performed in order to select two potentially suitable areas for the development of such projects. This analysis has been partially carried out within the MENA Regional Water Outlook project [MENAWATER 2011]. The investigation mainly consists of exclusion of unsuitable areas such as high terrain slope, shifting sands, protected areas, urban areas and infrastructures [Moser 2013]. The first site (from now on also: site 1) is an area located not far from the shore, which could in principle be adapted for the realization of a combined CSP-MED plant. Other plant configurations will be also analyzed. The second site (from now on also: site 2) is a desert inland location, approx. 60 km away from Marsa Alam. This site was selected in order to assess the impact of dry cooling on CSP and the combination with SWRO.

A water demand of 30,000 m³/d has been assumed as the base case. Two other plant capacities (i.e. 20,000 m³/d and 100,000 m³/d) have been additionally considered (Annex 10.4.4). The water demand is assumed to be covered by new desalination plants. The power demand is characterized by daily and seasonal fluctuations: typically two peaks per day exist, i.e. at noon and during evening hours. Further, demand in summer is significantly higher than in winter due to a high consumption for cooling (Figure 74 and Figure 75). The power demand is in the range between approx. 50 MW and 150 MW. The electricity demand of desalination plants depends on specific plant configurations, and is therefore considered as an additional demand case-by-case. Table 13 summarizes site geographical information as well as main water and electricity demand data.

	Unit	Site 1 – Marsa Alam Coast	Site 2 – Marsa Alam Desert
Latitude	°N	25.51	25.09
Longitude	°E	34.63	34.12
Elevation a.s.l.[1]	m	10	590
Power Demand[2]	MW	151.6/99.3/51.7	
Water Demand	m³/d	30,000 (additional cases: 20,000, 100,000)	

Table 13: Geographical site information and local demand; [1]a.s.l. = above sea level; [2]max/avg/min

Meteorological Data

Hourly meteorological data have been gathered for the two selected sites (Table 14). Solar resources data over a time span of 20 years have been generated through the SOLEMI database [SOLEMI]. Wind speed data of site 1 originate from [MERRA]. Such data have been used for the impact assessment of year-by-year resource variations on the annual power yields of renewable plants. In addition, a reference year in line with the long-term average has been selected for further analysis. Air temperature and relative humidity from the Meteonorm software have been used [Meteonorm]. Such data are available for a typical meteorological year. Finally, monthly seawater temperature and salinity values come from NOAA [NOAA]. Both sites are characterized by excellent solar and wind resources. DNI exceeds 2,500 kWh/m²/y in Marsa Alam, while site 2 disposes of more than 2,600 kWh/m²/y. Wind speed in Marsa Alam has an annual average value of 7.0 m/s (hub height).

Parameter	Unit	Marsa Alam Coast	Marsa Alam Desert
Direct normal irradiance (DNI)	kWh/m²/y	2,530	2,614
Global horizontal irradiance (GHI)	kWh/m²/y	2,386	2,429
Diffuse Horizontal Irradiance (DHI)	kWh/m²/y	722	708
Dry bulb temperature[1]	°C	36.6/24.9/12.6	37.4/23.4/7.4
Wind speed (hub height)[1]	m/s	15.6/7.0/0.1	n.s.
Seawater temperature (at intake)[1]	°C	27.8/24.9/21.9	
Seawater salinity	ppm	40,150 ± 500	

Table 14: Overview of meteorological inputs; [1]max/avg/min; n.s. = not specified

The average temperature lies between 23 °C and 25 °C, whereas site 2 is characterized by slightly higher day-night temperature differences. Seawater temperature seasonally oscillates between ca. 22 °C and 28 °C (Figure 44).

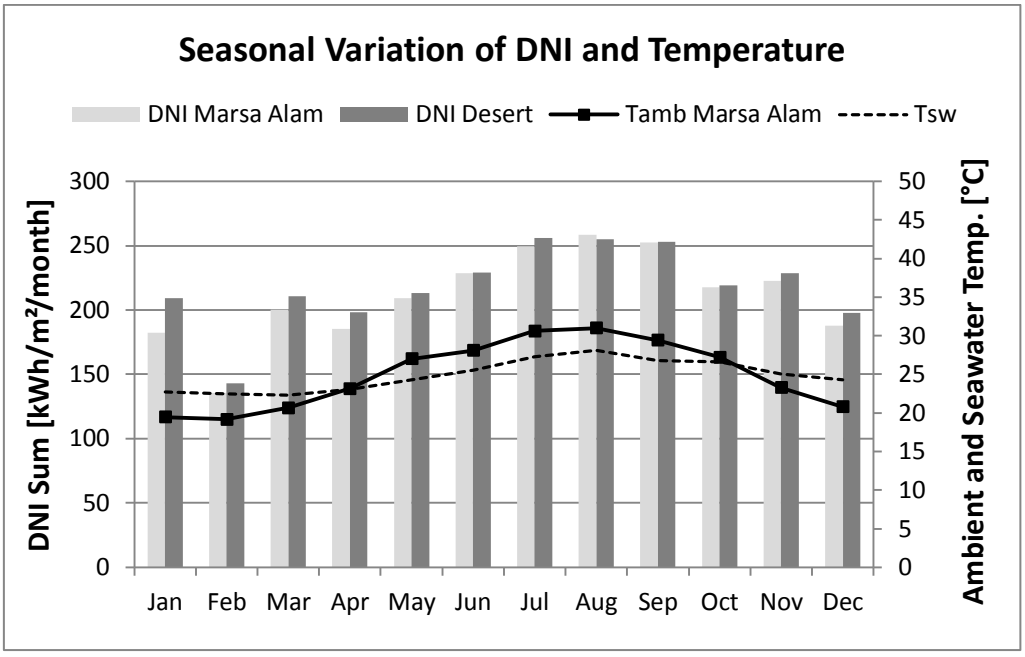

Figure 44: Monthly sum of DNI and average air and seawater temperature

The salinity is approx. 40,000 ppm and presents minor variations along the year. Isopleth and isotach diagrams (i.e. isoline diagrams for irradiance and wind speed, respectively) are shown in Annex 10.4.1 (Figure 106, Figure 107 and Figure 108). Figure 44 also shows the monthly distribution of DNI at both sites. During the summer months very similar DNI sums can be observed; in contrast, during the winter months DNI tends to be higher at the inland site.

Technical Parameters

The three main CSP technologies have been analyzed, i.e. parabolic trough (PT, 4.1), linear Fresnel (LF, 4.3) and central receiver (CR, 4.4). Reference collectors have been selected for each technology, as summarized in Annex 10.4.2 (Table 61). Different heat transfer fluids have also been compared (thermo-oil VP-1, solar salt and water/steam). The 2-tank molten salt storage has been selected as the reference thermal energy storage for VP-1 and solar salt calculations. Such a layout is not adopted for direct steam generation configurations, as it is not particularly attractive from both a technical and economic point of view (Annex 10.2.6, Figure 100). Phase change material storage has still not reached economic maturity and is not considered. DSG is thus considered without TES.

The power block consists of a conventional Rankine cycle. A fixed pressure of 100 bar at the inlet of the turbine has been used for all calculations, while the maximal steam temperature is dependent on the collector type (precisely on the concentration ratio) and -eventually- on issues related to the physical stability of the HTF. A single steam re-heating and a few number of steam extractions are assumed in order to maximize conversion efficiency. Different cooling types have been assumed, i.e. evaporative cooling or MED for CSP plants located in Marsa Alam, and dry cooling for plants located in the desert.

Concerning PV, the plant layout used in [MENAWATER 2012] has been taken as a reference. Such a plant consists of typical polycrystalline modules and standard inverters. The base configuration reported in Annex Table 62 (1 MW_p) has been scaled case-by-case according to the requirements. The slope of the fix-mounted collectors is adjusted in order to maximize the annual power yield. In addition, 1-axis and 2-axis sun-tracking layouts have been considered.

Standard 2 MW wind turbines have been selected [Gamesa 2014]. The hub height of such wind turbines is 90 m above ground level. The adaptation of wind speed between the measurement height and the hub height has been carried out according to Eq. 6.1. Finally, the backup system consists of a conventional steam turbine using a mixture of light and heavy fuel oil.

Two desalination technologies have been analyzed, i.e. MED (3.1) and RO (3.2). Common assumptions have been taken for nominal capacity, annual average availability and intake (Annex Table 63).

Economic Parameters

Data used for economic analysis are affected by a certain degree of uncertainty because they are commonly not in the public domain. The main financial and economic inputs are summarized in Annex 10.3 (Table 61 to Table 64). A common interest rate of 8.0 %/y has been selected. The debt period and operational plant life are assumed to be technology-dependent. These choices -which impact LEC and LWC- are in line with track records of existing plants.

Main Assumptions

A number of additional assumptions have been considered:

- Equal power quality: a fair technology comparison takes into account options with an equal power quality. This implies that the same demand curve is covered by all analyzed configurations, which allows considering the external supply cost caused by the intermittent electricity generation of RE plants.
- The entire electricity and water systems are assumed to be constructed at once ("greenfield-status"), which may seem an oversimplification of the problem. However, this assumption permits assessing the full cost of supply, which represents a key parameter for the comparison of different supply systems.
- Marsa Alam is considered to be an island electricity network. According to the available information [MENAWATER 2012], the national grid will not be extended south of Safaga.
- In contrast to detailed power plant commitment models such as REMix [Fichter 2014], the INSEL model assumes a simplified dispatch. Renewables have feed-in priority as long as their cumulated power generation is lower than the load. Such a choice is supported by the fact that renewable energy technologies provide lower LEC than the backup power plant as long as world market fossil fuel prices are assumed. The backup power plants are used to satisfy the demand at times of insufficient renewable electricity generation. If the sum of renewable electricity generation is higher than the load, a differentiation is made between configurations with or without MED. In the first case, the CSP plant is constantly operated at full load in order to guarantee continuous heat supply to the thermal desalination unit. In contrast, if the desalination plant is an RO, CSP can be flexibly operated between full load and minimal load (i.e. 20 % of the full load). In both cases, PV and wind power are curtailed as soon as their cumulated electricity generation exceeds the residual load (i.e. the difference between load and CSP electricity production). For PV results:

$$P_{PV_{dump}} = P_{Dump} \cdot \frac{P_{PV}}{P_{PV} + P_{Wind}} \qquad \text{Eq. 8.1}$$

P_{PV_dump}	[MW_{el}]	PV power curtailments
P_{PV}	[MW_{el}]	PV power production without curtailments
P_{Wind}	[MW_{el}]	Wind power production without curtailments
P_{Dump}	[MW_{el}]	Total curtailments

$$P_{Dump} = \begin{cases} P_{CSP} + P_{PV} + P_{Wind} - Load; & P_{CSP} + P_{PV} + P_{Wind} > Load \\ 0 & ; \quad else \end{cases} \qquad \text{Eq. 8.2}$$

The wind power curtailments are calculated according to the same method.

- An empirical requirement has been introduced, which involves the minimum amount of secondary control reserve [UTCE 2009]. This condition implies that at least one turbine (either a backup plant or the CSP plant) has to be operated at least at minimum load conditions in order to control any short-term variations of electricity generation or of demand.

Definitions

Finally, the concepts of "solar multiple" and of "equivalent full load storage hours" are introduced, which are two commonly used parameters in order to express the basic design of CSP plants. The solar multiple (SM) is defined as the ratio between the yield of the solar field at design conditions and the nominal turbine capacity:

$$SM = \frac{\dot{Q}_{SF\_design}}{\dot{Q}_{turb\_in}} = \frac{\dot{Q}_{SF\_design}}{\left(P_{el\_0} / \eta_{gross\_0} \right)} \qquad \text{Eq. 8.3}$$

$\dot{Q}_{SF\_design}$	[MW_{th}]	design yield of the solar field
$\dot{Q}_{turb\_in}$	[MW_{th}]	design yield at the inlet of the turbine
P_{el_0}	[MW_{el}]	nominal gross power
η_{gross_0}	[%]	nominal gross turbine efficiency

The definition of $\dot{Q}_{SF\_design}$ is arbitrary, as the position of the sun and the intensity of the radiation continuously change. The exact value of $\dot{Q}_{SF\_design}$ is the result of a project-specific techno-economic optimization. However, 800 W/m² DNI and the sun position corresponding to the 21th of June at 12:00 are common choices for design of PT and LF plants [Hirsch 2011].

The equivalent full load storage hours (FLH_{TES}) is the ratio between design storage capacity and nominal turbine capacity:

$$FLH_{TES} = \frac{Q_{TES\_design}}{\dot{Q}_{turb\_in}} \quad \text{Eq. 8.4}$$

Q_{TES_design} [MWh_{th}] design capacity of the thermal energy storage

8.2 Renewable Electricity Generation

Within this section advantages and disadvantages of each CSP technology (and each HTF) are discussed (Table 15). Thus, the impact of geometrical and thermal efficiency as well as of plant layout on the results is highlighted. Concerning PV, different tracking systems are compared. Finally, the impact of year-by-year variations of solar and wind resources on plants´ annual yields is presented.

Technology	Description	Objective
CSP (8.2.1)		
a) Geometrical efficiency of the solar field	Analysis of daily and seasonal patterns of geometrical efficiency; different collector types considered (PT, LF, CR)	Basic understanding of the performance differences among CSP collectors
b) HTF temperature	Impact of concentration ratio, steam temperature and DNI on system efficiency	Selection of best HTF temperature as function of solar collector
c) Cooling type and land cost	Techno-economic evaluation and comparison of cooling options for CSP: wet cooling (coast site) and dry cooling (desert site); impact of dry cooling design and land cost on LEC	Selection of best cooling type and site for CSP plant
d) CSP technologies and optimal layout	Analysis of solar collectors(PT, LF, CR) and solar field sizes, HTF (oil, solar salt, DSG) and TES capacity; techno-economic evaluation	Selection of Min. LEC (mainly: collector and HTF type, solar multiple and TES capacity) (to be used in 8.4)
e) Long-term resource availability	Evaluation long-term variability of solar resources (20 years)	Understanding the impact of resource availability on multi-year basis
PV (8.2.2)		
a) Tracking systems	Daily and seasonal impact of tracking systems (fixed, 1-axis, 2-axis) on electricity generation profiles	Performance differences among PV tracking systems; selection of Min. LEC (to be used in 8.4)
b) Long-term resource availability	Evaluation of long-term variability of solar resources (20 years)	Understanding the impact of resource availability on multi-year basis
Wind Power (8.2.3)		
a) Long-term resource availability	Evaluation of long-term variability of wind resources (20 years)	Understanding the impact of resource availability on multi-year basis

Table 15: Overview of the first section of the case study (8.2): analysis and pre-selection of renewable power plants

8.2.1 CSP

a) Geometrical Efficiency of the Solar Field

The analysis starts with the comparison of the geometrical efficiency η_{geo} (i.e. the ratio between the incident heat flow on the receiver and DNI) of PT, LF and CR. The mathematical

formulation of several geometrical loss mechanisms has been previously discussed (4.2.1, 4.3.1 and 4.4.1, respectively).

The values of η_{geo} are mainly affected by the relative position of reflectors and receiver as well as by the position of the sun. Figure 45 and Figure 46 show the geometrical efficiency profiles of PT, LF and CR on a typical winter day and a typical summer day, respectively. In line focusing collectors η_{geo} is independent of the solar multiple. In winter, PT reaches its maximal geometrical efficiency during morning and evening hours, while it experiences a local minimum at noon. This is due to the north-south orientation of the collectors and to the east-west tracking. Even if the solar elevation α_s has a maximum at noon, its value is significantly lower than 90°. As a consequence, the incidence angle θ is large and only a portion of the mirror surface is effectively "seen" by the sun (cosine losses). In summer, η_{geo} is close to 1.0 for the majority of the day, due to the fact that the sun rays are almost perpendicular to the collectors. At sunrise and sunset α_s is close to 0, which causes high geometrical losses due to shading between parallel collectors.

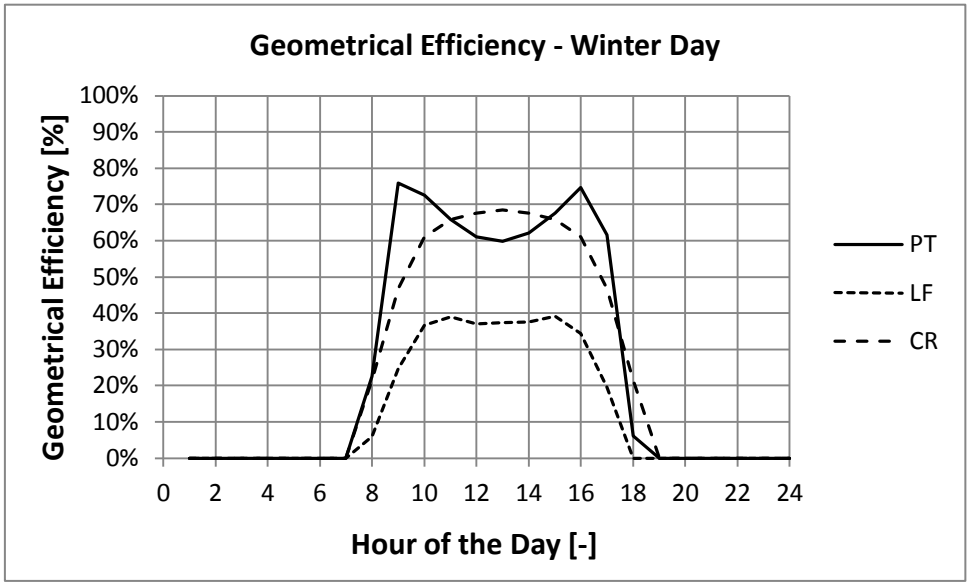

Figure 45: Comparison of geometrical efficiency of CSP technologies on a winter day (Marsa Alam); Note: the impact of heat losses is not part of this analysis

Shading losses may be minimized increasing the distance between collectors (which is typically 3 times the collector aperture). However, a trade-off between geometrical efficiency and land cost exists. Linear Fresnel collectors are characterized by much lower geometrical efficiency than PT (20 % to 60 % lower). In addition, the operation time of LF is shorter. Such differences can be explained by the different collector geometry. First, LF consists of a number of parallel mirrors arranged horizontally, which causes high shading during morning and evening hours (high transversal incident angle $\theta_\perp$). Second, the mirrors are almost flat, and each of them has a different focal length. In addition, in contrast to PT, the receiver of LF reflectors is fixed. For values of $\theta_\perp$ other than the design value, a portion of the reflected irradiance does not impinge the receiver as the curvature of the reflectors is not optimal. Also in summer, η_{geo} of LF is lower than η_{geo} of PT. This has to be compensated

by a larger collector area. Further differences between PT and LF (e.g. thermal losses, land use, costs) will be discussed later.

The geometrical efficiency of central receiver plants significantly differs from η_{geo} of linear focusing systems. The main reason is the 2-axis tracking of each heliostat. The geometrical efficiency is a function of the heliostats´ layout and of the receiver capacity. In addition, the solar field is designed in order to minimize heat supply cost on annual basis. Therefore a common assumption is to consider March 21, solar noon as a reference time for the design. This allows obtaining a profile of η_{geo} almost independent of the season. In fact, the peak geometrical efficiency is approx. 70 % in winter as well as in summer and presents a maximum at noon. Nevertheless, a common feature of all considered CSP technologies is that the energy yield is lower in winter than in summer, due to the shorter duration of the day and to the different declination angle of the earth δ, which in turn influences α_s and $\theta_\perp$.

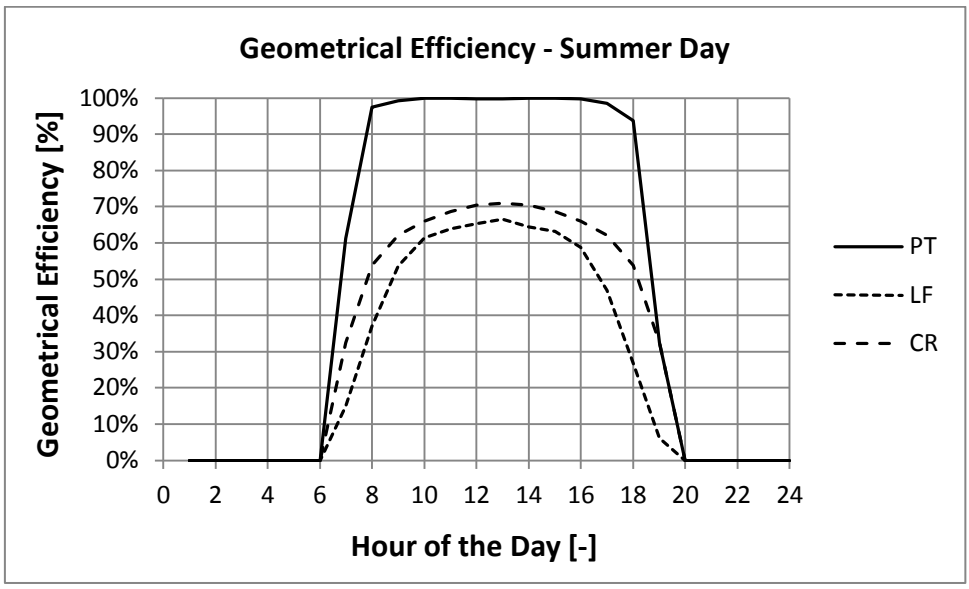

Figure 46: Comparison of geometrical efficiency of CSP technologies on a summer day (Marsa Alam)

A last remark concerns the non-perfectly symmetric form of the geometrical efficiency curves with respect to the solar noon. The main reasons behind this are the hourly time step of the calculation and the difference between local time and solar time. The curves would be smoother if a higher time resolution was used (or if the solar time would be taken as the time reference).

The seasonal profiles of electricity generation clearly reflect the differences in geometrical efficiency. Figure 47 shows the monthly cumulated electricity production for the three analyzed CSP technologies. A common plant layout has been selected for all technologies in order to achieve better comparability (i.e. solar multiple 3.0, 14 equivalent full load hours TES capacity, molten salt as HTF). The design has been carried out taking into account the peak thermal efficiency of the respective solar fields.

As a result, for the given layout LF presents an approx. 7 % higher mirror area than PT and CR. The maximal monthly electricity generation has been used as a reference value for normalization (i.e. 100 % case, achieved by CR in July). All other values are expressed as a percentage of this reference. The first consideration is that in each month the electricity yield of the central receiver is higher than that of PT and LF. In addition, the gap between CR and PT is more accentuated during the winter months. These figures can be explained with the combined effect of geometrical efficiency, solar field thermal efficiency and turbine conversion efficiency. As previously explained, the geometrical efficiency of CR is characterized by a more even distribution over the year than PT and LF.

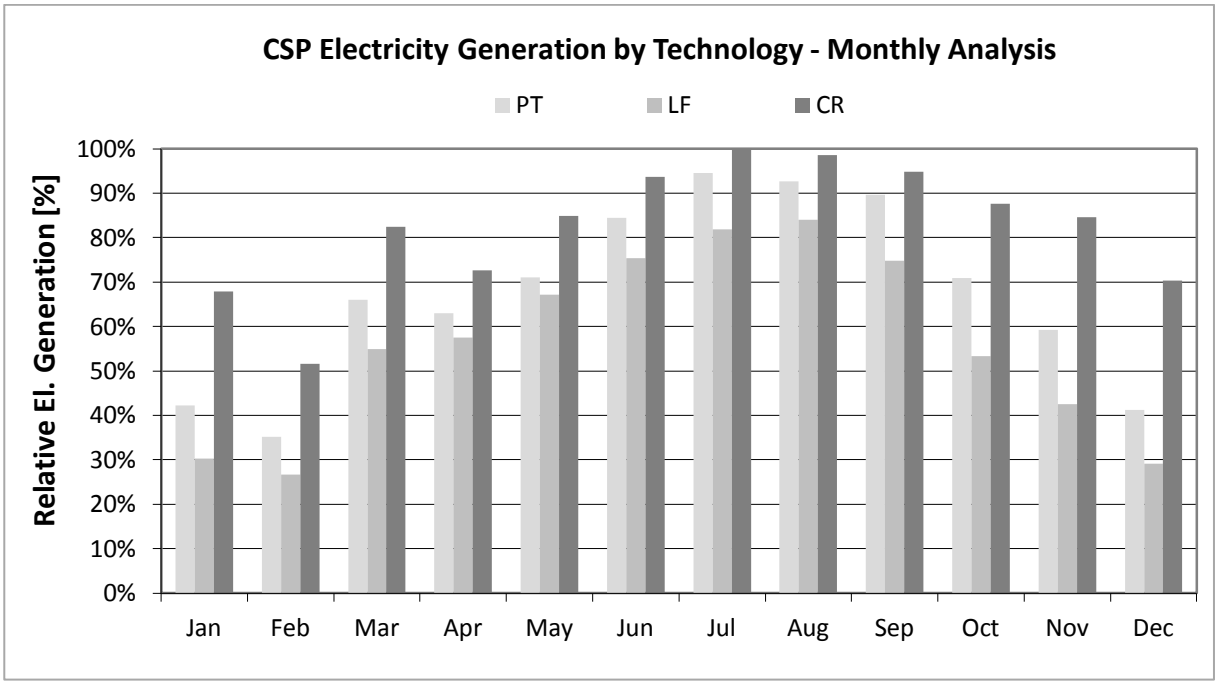

Figure 47: Comparison of the monthly sum of electricity generation by CSP technology; Assumptions: SM 3.0, 14 h TES, HTF molten salt, wet cooling

In addition, the higher concentration ratio of CR allows minimizing thermal losses during plant operation (Eq. 10.6), while further thermal losses related to HTF cool-down during stand-by can be minimized. In contrast, in line focusing systems (in particular PT) thermal losses during night hours and consequent start-up procedures are responsible for a lower electricity yield. Another minor contribution to such differences is given by the different maximal HTF temperature. Even if all three considered systems use the same heat transfer fluid, the optimal design temperature is technology-dependent. Again, the different concentration ratio is the source of such differences.

b) HTF Temperature

According to Carnot´s theorem, the higher the steam temperature at the inlet of a Rankine cycle, the higher the conversion efficiency of the turbine. However, in CSP plants a number of techno-economical limitations exist which reduce the optimal top HTF temperature (i.e. the temperature at the outlet of the solar field) and so the steam temperature. In fact, the

optimal top HTF temperature mainly depends on the used heat transfer fluid and on the geometry of the CSP collector. The maximal operating temperature of the VP-1 thermal oil is limited to 400 °C, while the upper temperature limit of solar salt is 565 °C. In both cases, the exceeding of such limitations would lead to chemical instability of the HTF. The concentration ratio is also limited by the non-ideal apparent size of the sun (32´ as seen from the Earth). If the diameter of the receiver is lower than $32´ \cdot Ap$, the share of the radiation reflected by the mirrors on the receiver (intercept factor) is reduced and the spillage is higher [Riffelmann 2012].

In addition, for each concentration ratio (as described in Annex Eq. 10.4) an optimal top HTF temperature exists. The higher the concentration ratio, the lower the receiver area per square meter of collector. This allows reducing thermal losses, while the top HTF temperature and the turbine efficiency can be increased. However, this trend levels off at very high receiver temperatures, mainly because irradiance thermal losses increase with the fourth power of the temperature (Stefan-Boltzmann law). The impacts of such mechanisms on the efficiency of a CSP system can be appreciated in Figure 48, whereas "system efficiency" is defined as the multiplication between solar field efficiency and power block efficiency under nominal conditions. Three concentration ratios are analyzed: the first case represents a low-concentration system ($cr = 10$), while the second and third cases show typical concentration ratios for parabolic trough ($cr = 80$) and central receiver ($cr = 1000$), respectively. The results clearly show that the higher the concentration ratio, the higher the optimal top HTF temperature and the correspondent system efficiency.

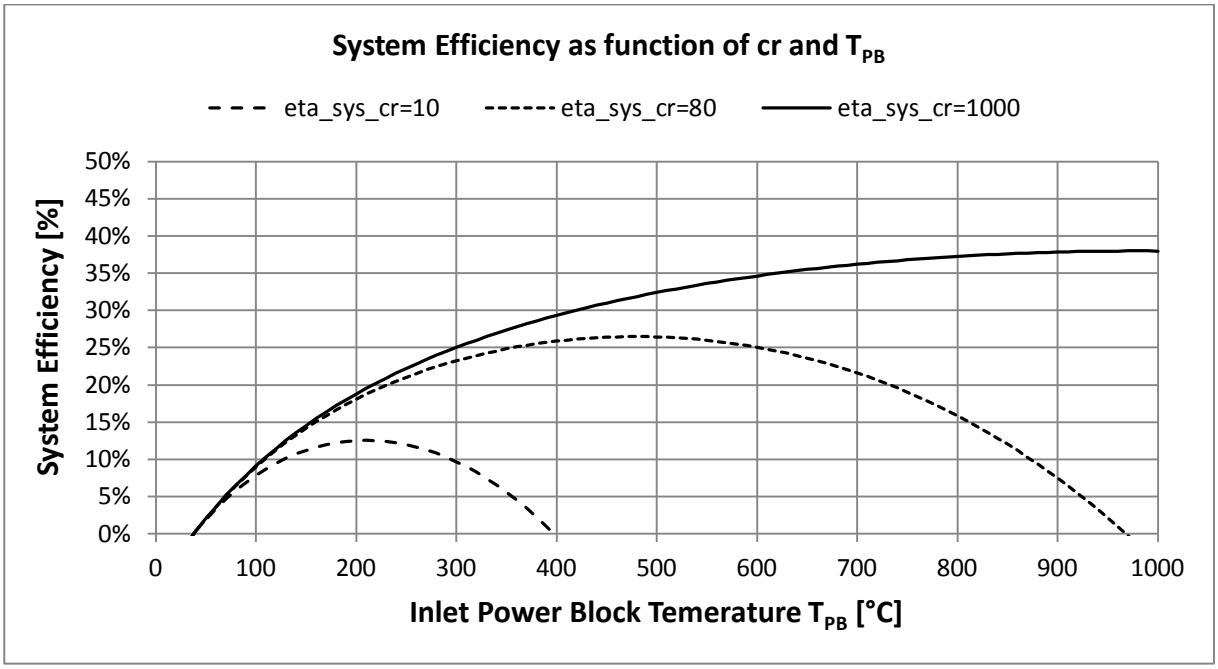

Figure 48: Dependence on the efficiency and the optimum working temperature on the solar radiation concentration factor; system efficiency = $\eta_{sf} \cdot \eta_{turb}$ (nominal conditions)

The curves plotted in Figure 48 are obtained assuming a DNI of 800 W/m², which is a commonly used value for the design of CSP collectors. However, such a DNI condition is

exactly achieved only for a few hours during the year. In contrast, in the morning and evening hours the radiation typically has to cover a longer path through the atmosphere, so that the DNI is lower than 800 W/m² even under clear-sky conditions. Other losses such as cosine losses, blocking and shading, further reduce the effectively available DNI. At low DNI the relative weight of thermal losses is more relevant than under design conditions (Figure 49). This effect leads not only to a reduction in the system efficiency, but also to a decrease in the optimal top HTF temperature.

The optimal top HTF temperature can be assessed by means of annual simulations, which allow considering the complete DNI distribution over a typical meteorological year. Taking into account the results of the simplified model presented in Figure 48, the optimization of parabolic trough systems using molten salt as HTF seems to be particularly interesting because the optimal system efficiency under nominal conditions (approx. 500 °C) lies below the upper operation limit of molten salt applications (565 °C). The results of such an optimization are shown in Figure 50. The diagram shows the impact of the HTF temperature on both levelized electricity cost and annual solar-to-electricity efficiency. The two curves present a specular behavior, i.e. the higher the solar-to-electricity efficiency, the lower the LEC and vice versa. The minimum of LEC corresponds to a top HTF temperature of approx. 490 °C. As a final remark, other parameters such as the plant configuration (i.e. solar multiple and TES capacity) and the annual DNI resources are expected to have a minor impact on the optimal HTF temperature. Such aspects have not been considered in detail and could be the subject of future analysis. However, according to the consideration exposed above, one would expect that the higher the frequency of part load conditions (e.g. low solar multiple, low annual DNI sum), the lower the optimal HTF temperature.

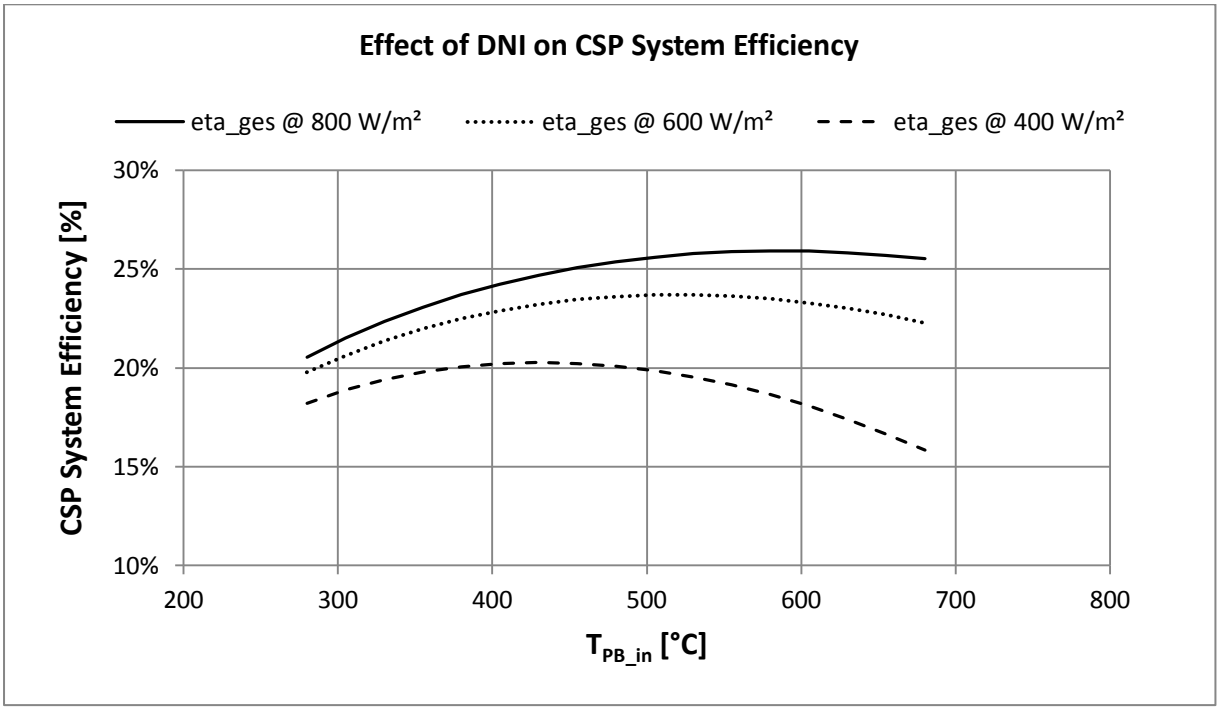

Figure 49: Impact of DNI on optimal steam temperature at power block inlet and CSP system efficiency

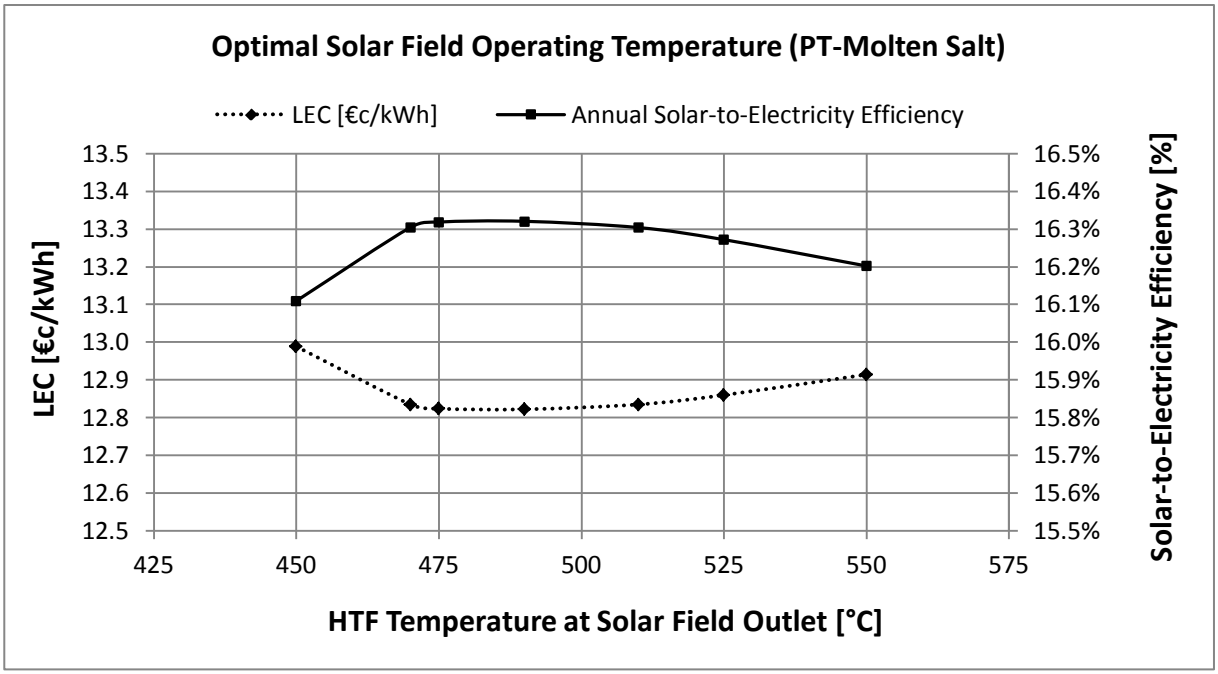

Figure 50: Exemplary molten salt design temperature optimization (parabolic trough: SM 2.8, 13 h TES)

c) Cooling Type and Land Cost

Recirculating (i.e. evaporative) cooling systems are often designed for the highest wet-bulb temperature of the year (99 % occurrence) [Maulbetsch 2004]. In contrast, the design temperature of dry cooling units is typically significantly lower than the maximal dry bulb temperature. As a consequence, dry cooling is not able to maintain the design plant output as soon as the temperature exceeds design conditions (i.e. hottest hours of the year). This disadvantage is intensified by the fact that such periods are often characterized by peak demand [O´Hagan 2003]. Due to these considerations, particular attention should be given to the proper design of dry cooling units.

The steam condensation temperature T_{cond} is calculated as the sum of the dry bulb temperature and the initial temperature difference (ITD) of the condenser. While the dry bulb temperature is a meteorological input, ITD is the main design parameter of the dry cooling unit. Due to the poor heat capacity of air, a higher ITD is typically selected in comparison to once-through and evaporative cooling. Optimal ITD is mainly a trade-off between investment and operation cost on the one hand and cooling efficiency on the other [Moser 2013 b]. For CSP plants, optimal ITD is a function of several parameters such as solar multiple and specific investment cost of different plant components.

Figure 51 shows the impact of the CSP plant configuration on the LEC and on the optimal ITD. The analysis has been carried out for a desert region in the inland of the Marsa Alam governorate (site 2, Table 14). This site presents just marginally higher DNI resources (2,614 kWh/m²/y) than the coastal site (2,530 kWh/m²/y). Molten salt-based linear Fresnel collectors have been selected for this analysis. In particular, three CSP layouts have been considered: SM 1.5, SM 2.5 and SM 3.5. These systems are equipped with 2, 8 and 14 full

load hours TES capacity, respectively. Solar-only operation has been assumed. ITD values between 10 K and 40 K have been analyzed. The results highlight the strong impact of the CSP layout on LEC and optimal ITD. The LEC difference between the SM 1.5 case and the SM 3.5 case amounts to roughly 3.5 €c/kWh$_{el}$. For a given CSP configuration, the ITD also impacts on the LEC. In addition, the optimal ITD depends on the CSP configuration. In the first case (SM 1.5) the optimal ITD amounts to around 30 K, which is higher than in the other two configurations. In this case, overall investment costs are relatively low in comparison to the other two cases. The CSP plant operates at full load only 2,350 equivalent hours per year. Due to these two factors, additional high investments for an efficient cooling (i.e. lower ITD) do not seem to be economically favorable. However, the situation changes for the other two configurations. In particular, the SM 3.5 case is characterized by a high investment cost for the solar field and the thermal storage. The plant reaches almost 5,700 equivalent full operation hours per year. In this case the resulting optimal ITD lies between 22 K and 23 K. The SM 3.5 layout can be also regarded as the economically optimal configuration (in LF plants). As regards the comparison between conventional and CSP plants, typical ITD values of conventional power plants constructed in the last years vary between 20 and 40 K [GEA 2013]. This reflects the fact that high investment in efficient cooling are only justified in the case of high heat production cost (e.g. high investment cost and high fuel cost).

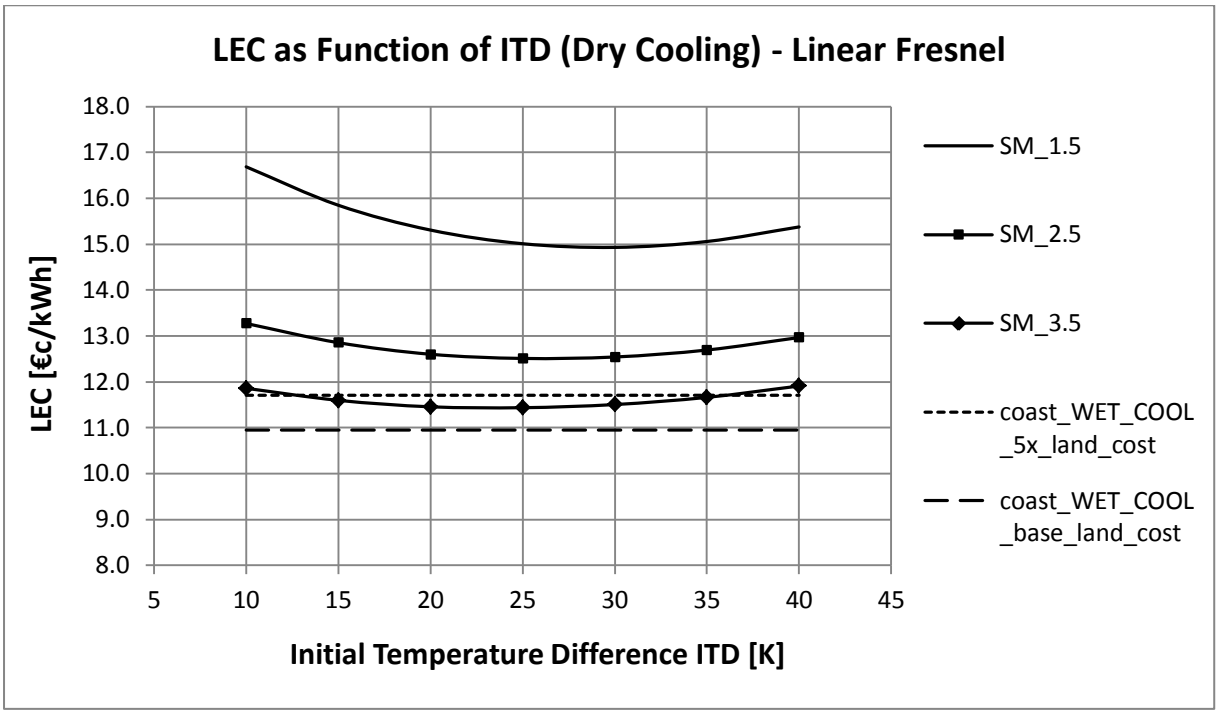

Figure 51: Impact of different CSP layouts on the optimal dry cooling design (linear Fresnel collectors); analyzed sites: Marsa Alam desert for dry cooling; Marsa Alam coastal region for wet cooling

Finally, the dry cooled plants have been compared with a reference wet cooled linear Fresnel plant (located in the Marsa Alam coastal region). Similar results could have been obtained using PT or CR. An electricity network between the dry cooled power plant and Marsa Alam is assumed to be in place. No additional costs have been considered for water transport (mirror cleaning etc.) and fossil fuel transport (anti-freezing) to the inland power

plant, which is a very optimistic assumption. The comparison focuses rather on the impact of land cost on the overall project economics. Unfortunately, it was not possible to gather real land cost data for the two selected locations. It has been decided to analyze two different land costs: the land costs are 1.8 €/m² and 9.0 €/m² for the "coast_base" and the "coast_5x_land_cost", respectively. In the base case the LEC of the wet cooled CSP plant is approx. 4.5 % lower than the dry cooled plant, which is in line with the results reported by similar studies (2 % to 10 % LEC differences according to [DOE 2001]). In contrast, assuming 5-times higher land cost in the coast site results in an eventual economic advantage for the dry cooled inland CSP plant.

These boundaries should be considered case-by-case in a detailed case study. Within the following analysis "base land cost" has been assumed. Accordingly, wet cooling (at Marsa Alam) has been selected as the reference cooling option for CSP plants within the following case studies, as such a configuration performs lower LEC than dry cooling at the considered desert site.

d) CSP Technologies and Optimal Layout

In CSP plants LEC depends on a series of technical parameters such as collector and receiver type, used HTF, maximal HTF temperature as well as solar multiple and storage capacity. The first part of the economic analysis explains the procedure applied for the identification of the optimal plant configuration of a single CSP technology. In general, CSP configuration also depends on the plant commitment. For example, a mid-merit CSP plant will have a lower solar multiple and a smaller TES capacity than a base-load plant. The analysis in Figure 52 exemplarily shows the results of the optimization of a reference PT plant (VP-1 as HTF and molten salt TES). Similar results could have been obtained using LF or CR (Annex 10.4.3 Figure 110). Annual yield calculations have been carried out for a wide range of configurations. For each of these configurations the LEC has been calculated. The plant is assumed to operate without any load constraints and in solar-only mode, i.e. no fossil fuel is directly used for electricity generation. The results show that a quite broad minimum exists, which includes low as well as high SM and TES capacities. As one would expect, a low SM (e.g. 1.5) corresponds to a relatively small optimal TES capacity and vice versa. A solar multiple of 3.0 and a 14-hour TES provides lowest LEC under the given economic assumptions. Lower CAPEX would correspond -beside to lower LEC- to higher optimal SM. Non-optimal layouts include either TES over-sizing (i.e. also SM under-sizing) or vice versa. In the first case (left part of Figure 52) high investment costs are required for the installation of a large TES, which is used inefficiently as it mostly remains almost completely discharged. In contrast, an ideal TES utilization would imply a full charge-discharge cycle per day. The other extreme case is shown in the right part of Figure 52. In this case an over-sized solar field is combined with a relatively small TES. As a result the storage is mostly fully charged, while a considerable amount of potentially available heat from the solar field has to be dumped, i.e. the collectors would often be defocused and the solar field investment would be not used efficiently.

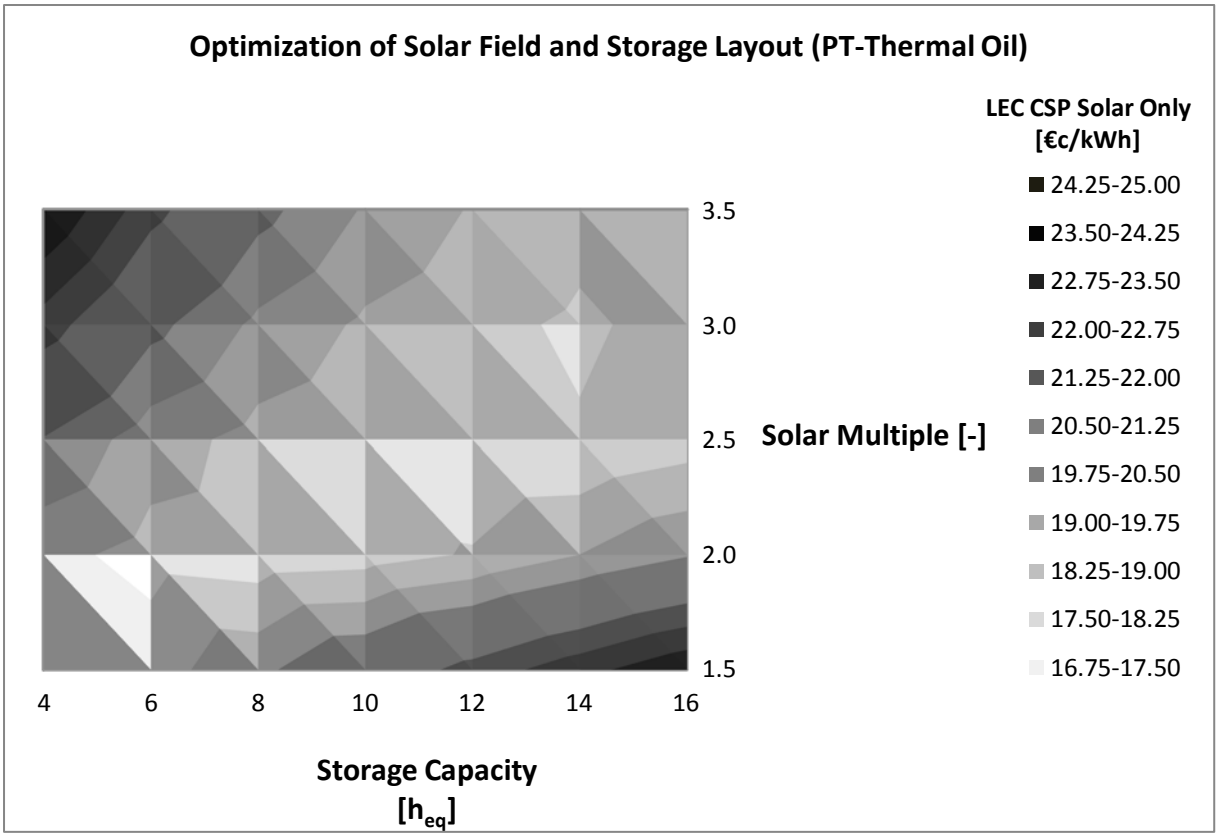

Figure 52: CSP layout optimization (parabolic trough, VP-1 HTF, solar-only operation); Optimization raster: SM 0.5 steps, TES 2 h steps

A fair economic comparison of different CSP technologies and HTFs should be carried out taking into account optimized systems instead of fixed configurations (i.e. same solar multiple or same mirror area). The results shown in Figure 53 present a summary of such an analysis, while technical and economic details are provided in Table 16 and in Annex Table 66, respectively. The considered cases include parabolic trough, linear Fresnel reflector and central receiver as well as different HTF types (i.e. case 1: thermal oil; case 2: molten salt; case 3: water/steam). The impact of all three mentioned HTFs has been assessed for linear focusing systems. In the case of central receiver, only molten salt has been considered as the most promising option.

All analyzed cases are assumed to operate in the solar-only mode (i.e. co-firing is allowed only for anti-freezing) and without any commitment restriction. The common power block capacity is 50 MW. Evaporative cooling is assumed; the impact of dry cooling is assessed in a separate case study. Table 16 summarizes the technical design data and the key results of the three analyzed PT plants. The nominal gross turbine efficiency ranges between 38.6 % in the case of oil-based PT to 42.6 % in the case of molten salt-based PT. Even if the temperature at the outlet of the solar field is similar in the second and in the third case (molten salt and DSG, respectively), the turbine efficiency in the DSG case is slightly lower due to plant specifications (Annex 10.2.5). In the PT-OIL case the maximal HTF temperature is limited to 393 °C due to the previously discussed constraints.

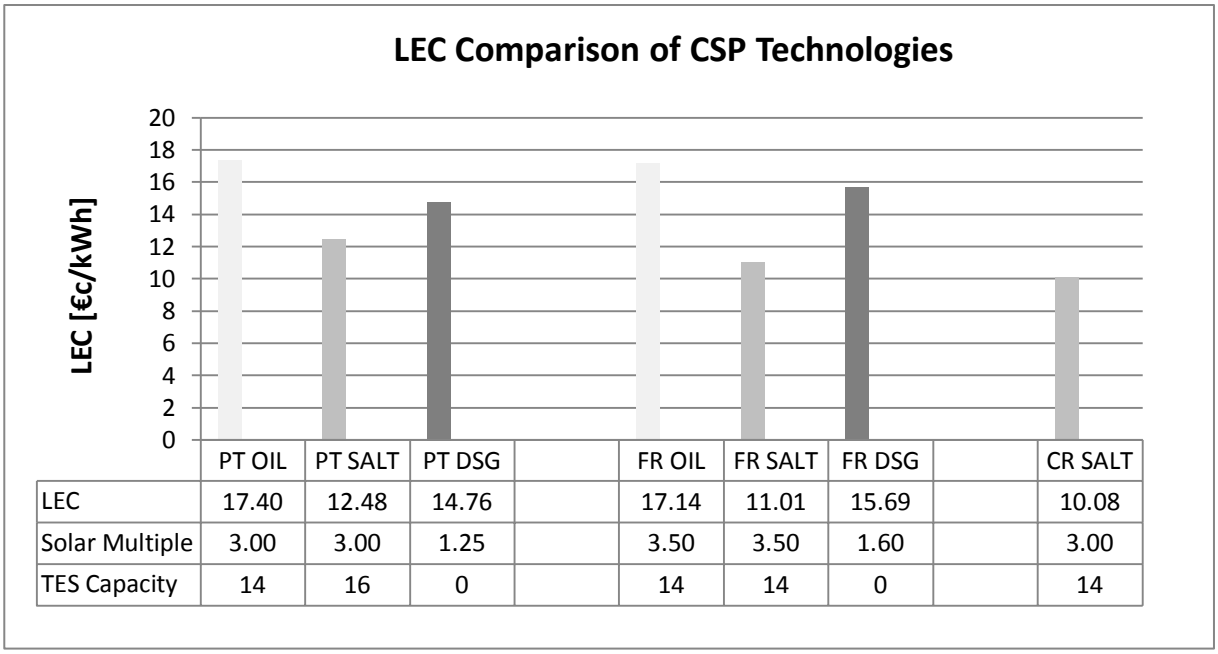

	PT OIL	PT SALT	PT DSG		FR OIL	FR SALT	FR DSG		CR SALT
LEC	17.40	12.48	14.76		17.14	11.01	15.69		10.08
Solar Multiple	3.00	3.00	1.25		3.50	3.50	1.60		3.00
TES Capacity	14	16	0		14	14	0		14

Figure 53: LEC comparison of different CSP technologies and heat transfer fluids

For the other two cases (i.e. PT SALT and PT DSG), the maximal HTF temperature is 500 °C. The auxiliary electricity consumption (i.e. parasitics) is much higher in the PT OIL case, due to the physical properties of the thermal oil and to the lower temperature gradient in the solar field. The economic analysis revealed that for both PT OIL and PT SALT the optimal solar multiple is 3.0, while the TES capacity varies between 14 and 16 full load hours (FLH). In contrast, the DSG case does not consider any TES, which leads to an optimal SM of approx. 1.25. Although cases one and two have the same solar multiple, the required collector area is lower in the PT SALT case due to the higher turbine efficiency. Looking at the annual performance, it is interesting to note that the highest net electricity generation occurs in case two, even if the heat supplied to the turbine is less than in case one (699.5 vs. 813.7 GWh_{th}/y). Solar heat dumping (i.e. mirror defocusing) is particularly high in the DSG case, as in this case no TES is used for buffering of surpluses. The defocusing is particularly high during summer days, due to the high geometrical efficiency (Figure 46).

The annual gross turbine efficiency is very similar to the nominal value of the two systems equipped with large TES, because transients and part load losses are minimized. In contrast, DSG systems (without thermal storage) are more prone to part load losses. The main disadvantage of molten salt-based linear focusing systems is the relatively large fossil fuel consumption for anti-freezing during stand-by. In fact, the temperature of the HTF in the solar field has to be kept higher than approx. 270 °C in order to avoid freezing along the piping system.

Finally, the comparison of optimized PT configurations shows that PT SALT systems seem to provide lowest LEC. The main advantages of such systems are the lower specific investment cost in comparison to PT OIL plants. In particular, this difference can be explained by the higher power block efficiency and by the lower molten salt mass requirements for the

storage. DSG systems are characterized by several advantages such as high process efficiency and a simple plant layout, due to the fact that heat exchangers between HTF and water/steam cycle are no longer required. However, no proven TES concept for DSG is commercially available so far, which currently limits potential LEC reduction and the attractiveness of such systems.

CSP Technology		PT OIL	PT SALT	PT DSG
Key Design Data				
Power Block				
Capacity	MW_{el}	50.0	50.0	50.0
Cooling type	-	Wet cooled	Wet cooled	Wet cooled
Nominal gross turbine efficiency	%	38.6	42.6	40.8
Design plant auxiliary cons.	MW_{el}	11.1	2.9	1.7
Solar Field				
Solar technology	-	Parabolic trough	Parabolic trough	Parabolic trough
Heat transfer fluid	-	VP-1	Solar Salt	Water/Steam
Solar multiple	-	3.0	3.0	1.25
HTF temperature SF inlet	°C	293	290	290
HTF temperature SF outlet	°C	393	500	500
Net aperture area	m^2	758,640	654,000	265,960
Design power of solar field	MW_{th}	451.5	433.1	184.1
Thermal Storage				
TES capacity	MWh_{th}	1,820	1,880	0
Equivalent full load hours	h	14.0	16.0	0.0
Annual Performance				
Solar heat to turbine	GWh_{th} /y	813.7	699.5	312.5
Solar heat dumping	GWh_{th}/y	109.8	46.5	184.3
Solar net electricity generation	GWh_{el}/y	275.5	283.7	117.1
Solar full load hours	h/y	5,503	5,674	2,342
Total full load hours	h/y	5,503	5,674	2,342
Annual gross turbine efficiency	%	38.4	42.3	38.7
Annual gross solar-to-el eff.	%	14.3	17.1	17.4
Heat for anti-freezing (SF + TES)	GWh_{th} /y	3.0	15.4	0.0

Table 16: Technical comparison of optimized PT systems; SF = solar field

The second part of the analysis focuses on the comparison of molten salt-based systems, as they turned out to be the most cost-competitive systems under the assumed economic conditions. Table 17 gives an overview of the most relevant technical design parameters. The first case (PT SALT) is exactly the same configuration which has been analyzed in the two previous tables. This configuration is then compared with an optimized linear Fresnel system (LF SALT) and a central receiver system (CR SALT). The nominal gross turbine efficiency is slightly higher in the CR case due to the higher HTF temperature at the outlet of the solar field. The optimal solar multiple in the LF case is larger than in the other two cases. This is mainly due to the lower geometrical efficiency of Fresnel collectors for conditions other than design (large transversal incident angle), which has to be compensated by a larger solar field

(approx. 23 % larger than PT and CR). The optimal TES capacity ranges between 14 and 16 FLH.

The lower part of Table 17 shows a summary of the annual plant performances. The highest electricity generation is achieved by the CR system (342.4 GWh/y), whereas the number of solar equivalent full load hours exceeds 6,800. This substantial difference in comparison to both linear focusing systems is due to the particular heliostats´ layout, which allows a relatively high solar heat collection also during winter months. At the same time, excessive heat dumping during summer months can be avoided (Figure 45 and Figure 46). In contrast to CR, PT and LF plants are based on standardized modules with a single tracking axis. As a consequence, such systems are more prone to geometrical losses whenever the incidence angle is not optimal. Accordingly, the CR plant presents the highest annual solar-to-electricity gross efficiency (21.2 %). PT and LF follow with 17.1 % and 13.2 %, respectively. Finally, fossil fuel consumption for anti-freezing purposes is particularly high for LF systems, due to the longer stand-by periods in comparison to PT.

CSP Technology		**PT SALT**	**LF SALT**	**CR SALT**
Key Design Data				
Power Block				
Capacity	MW_{el}	50.0	50.0	50.0
Cooling type	-	Wet cooled	Wet cooled	Wet cooled
Nominal gross turbine efficiency	%	42.6	42.6	43.2
Design plant auxiliary consumption	MW_{el}	3.0	3.4	3.5
Solar Field				
Solar technology	-	Parabolic Trough	Linear Fresnel	Central Receiver
Solar multiple	-	3.0	3.5	3.0
HTF temperature solar field inlet	°C	290	290	290
HTF temperature solar field outlet	°C	500	500	565
Net aperture area	m^2	654,000	804,460	639,490
Design power of solar field	MW_{th}	433.1	454.6	381.9
Thermal Storage				
TES capacity	MWh_{th}	1,880	1,650	1,620
Equivalent full load hours	h	16.0	14.0	14.0
Annual Performance				
Solar heat to turbine	GWh_{th} /y	699.5	666.8	834.8
Solar heat dumping	GWh_{th}/y	46.5	6.5	71.2
Solar net electricity generation	GWh_{el}/y	283.7	268.1	342.4
Solar full load hours	h/y	5,674	5,377	6,861
Total full load hours	h/y	5,674	5,377	6,861
Annual gross turbine efficiency	%	42.3	43.0	43.5
Annual gross solar-to-electricity eff.	%	17.1	13.2	21.2
Heat for anti-freezing (SF + TES)	GWh_{th} /y	15.4	33.3	1.7

Table 17: Technical comparison of optimized molten salt systems

The detailed breakdown of investment and operation costs for the three considered systems is presented in Annex Table 66. As a final result, the LEC of the three considered systems is in

a quite narrow range between 12.5 €c/kWh and 10.0 €c/kWh. Key advantages of CR systems are the high heat collection in summer as well as in winter time, the high turbine efficiency and the low anti-freezing requirements. LF plants offer a simple layout (e.g. avoiding flexible joints, easy drainage) and a high land use factor, which allows reducing investment costs. However, LF systems are characterized by low geometrical efficiency and consequently lower heat collection. Although molten salt-based CSP technologies contribute to a substantial efficiency increase and a considerable investment cost reduction, a number of hurdles still remain. The high heat losses during stand-by operation in line focusing system may increase the risk of freezing, which makes the development of a suitable anti-freeze infrastructure necessary. In addition, material questions are not fully solved.

e) Impact of long-term Resource Availability

The previous chapters highlighted that the electrical yield of renewable power plants depends on seasonal, daily and hourly availability of solar resources. Annual simulations with adequate accuracy and time resolution of input data are required to carry out such analyses. However, most current studies limit their assessments to one single year. Nevertheless, relevant year-by-year variations in resources availability exist. They mainly depend on the resource and on the selected site. The following analysis considers the impact of the long-term availability of renewable resources on CSP plants. Two different technologies have been analyzed (i.e. linear Fresnel reflector and central receiver). The used meteorological input data include 20 years of satellite-based irradiance data [SOLEMI] and of wind speed [MERRA]. Figure 54 shows the long-term power yield variation of a molten salt-based linear Fresnel power plant.

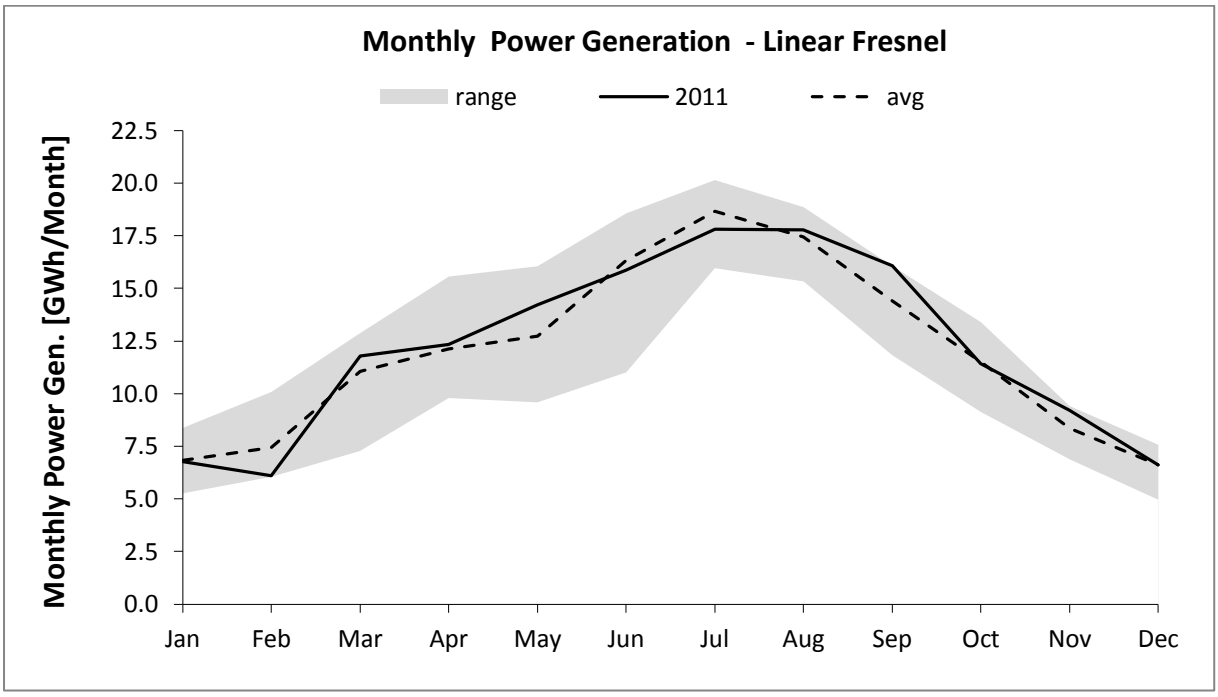

Figure 54: Monthly sum of power generation (linear Fresnel SM3, 14 h storage, long-term analysis)

The values present the monthly electricity generation and the range of variation in the period of analysis. The dashed line represents the average value over the considered time span.

Finally, the orange line shows the data of the year 2011, which has been selected as reference year in the case studies. This choice is justified by the fact that in this year both solar as well as wind resources are close to the respective annual average values. The relative seasonal variability of power output is particularly high during the spring months (March - June) and reaches 43.5 %. In contrast, the uncertainty is lower during the central summer months, i.e. July and August, which show a variability of ca. 20 %.

Central receiver systems are characterized by a relatively even power yield distribution over the year (Figure 55). Similarly to the previous case, the uncertainty of power output is highest in spring (up to 38.1 %). However, the variability of electricity generation in July and August is lower than for Fresnel reflectors (approx. 10 %). This is probably due to the chosen solar field configurations. In fact, in both cases a solar multiple of 3.0 has been selected. However, LF has lower geometrical efficiency than CR. As a consequence, the solar field of LF is slightly undersized, which leads to more accentuated power yield reduction during years with low DNI. The results of the previous analyses have shown that the optimal solar multiple for LF is approx. 3.5. In contrast, a solar multiple of 3.0 is the optimal choice for central receiver plants.

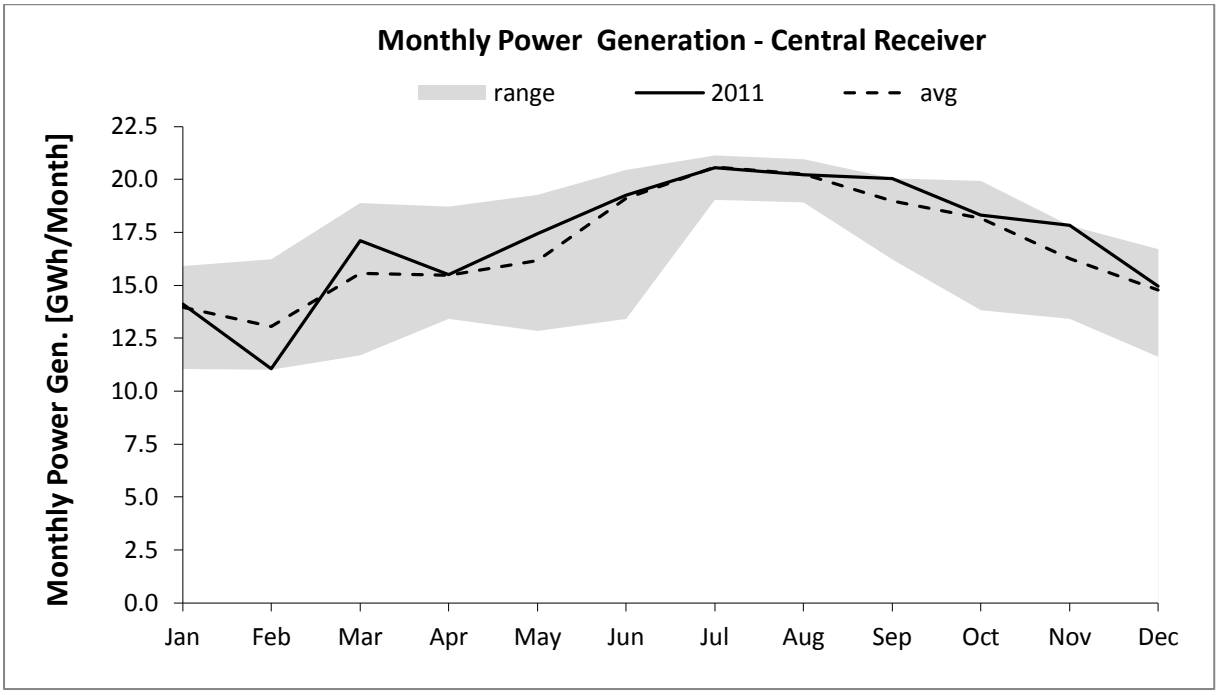

Figure 55: Monthly sum of power generation (central receiver SM3, 14 h storage, long-term analysis)

8.2.2 PV

a) Tracking Systems

The reference PV plant considered in the following discussion consists of a 10 MW_p plant using polycrystalline modules. Concentrating photovoltaics is not taken into account. Three types of mounting have been considered, i.e. fixed, 1-axis sun tracking and 2-axis sun tracking. The first step of the analysis focuses on the differences in these three PV systems with regard to technical performance on a daily and seasonal basis. In the second step, the economics of such plants is assessed.

Figure 56 compares the electricity generation of the three PV plants on a typical winter day. In fix-mounted systems, both tilt angle and azimuth angle do not change over time. As the modules are oriented towards the south, the maximal electricity yield is at noon, while in the morning and in the afternoon it decreases rapidly. In one-axis tracking systems, the axis of rotation is perpendicular to the tilt axis. This is the reason why the electricity generation at noon is the same as in the previous case. However, the tracking allows increasing the power yield during the remaining hours of the day. The daily yield difference between fixed and 1-axis tracking systems amounts to 23.8 %.

In the case of two-axis PV tracking systems, both azimuth angle and tilt angle change over time, which allows an ideal sun tracking. The electricity generation profile is similar to the 1-axis case: it is characterized by a relatively flat peak at noon and by sudden drops during early morning and late afternoon hours. Due to the ideal tracking, the power production of the 2-axis system is 9.0 % higher than in the 1-axis case (34.9 % more than in the case of fix mounted modules).

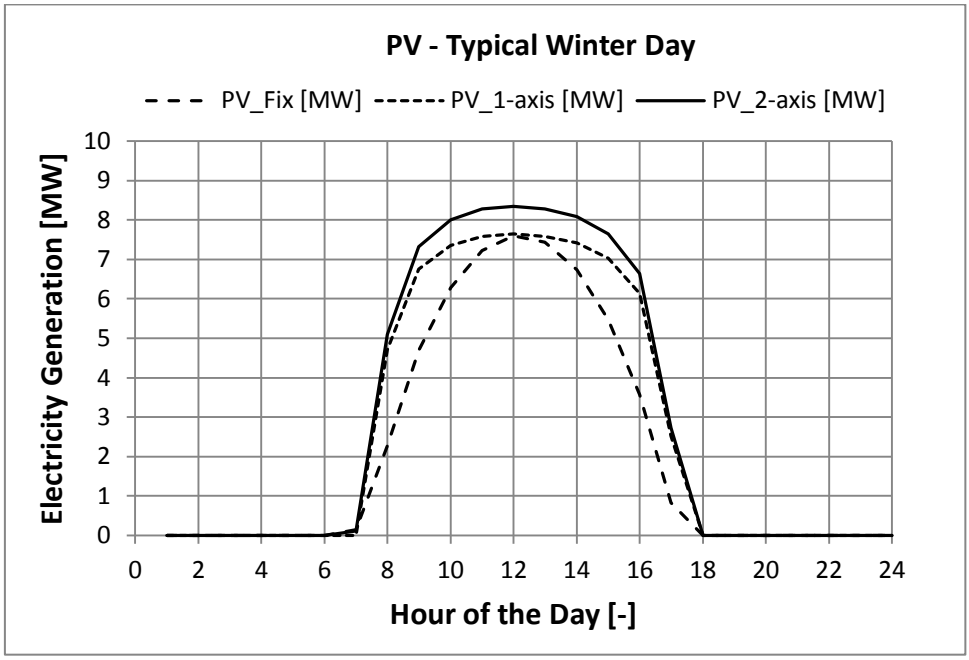

Figure 56: Comparison of daily electricity generation profiles of PV plants; typical winter day, Marsa Alam

Most of the exposed considerations remain true when analyzing a typical summer day (Figure 57). The main difference is the higher number of hours with irradiation, which allows increasing the daily electricity generation in all three considered PV systems. As the fix mounted PV plant is designed in order to maximize the annual plant performance (which is done through an optimization of the module slope), the peak power production of the three systems is within a narrower range than in winter. Independent of the tracking type, the absolute peak power production at noon is slightly lower in summer than in winter. This can be explained by the higher air temperature, which impacts negatively on the modules´ efficiency.

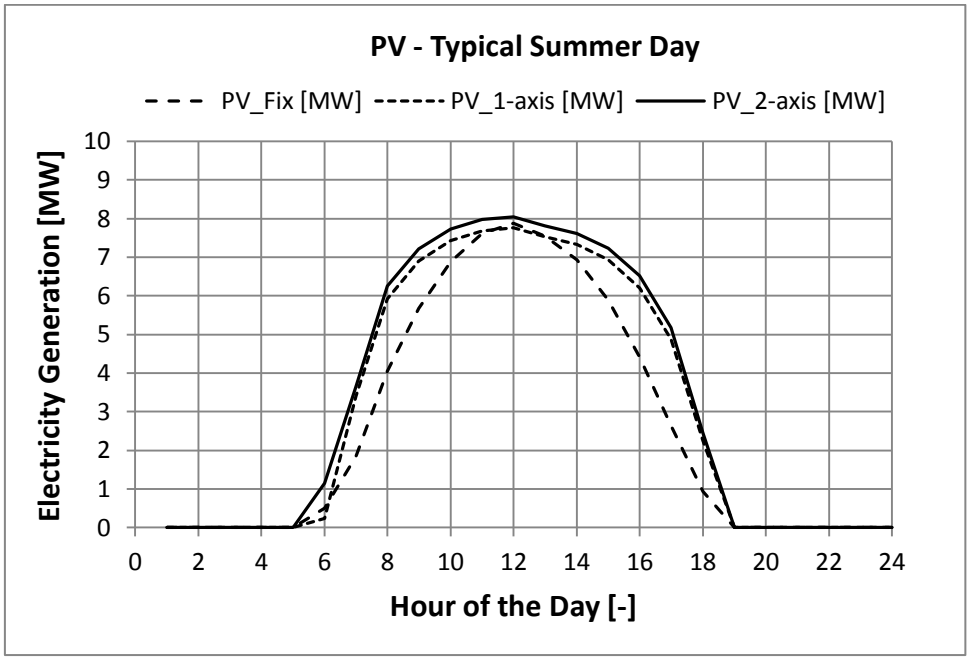

Figure 57: Comparison of daily electricity generation profiles of PV plants; typical summer day, Marsa Alam

The seasonal differences in electricity generation between the considered PV systems can be appreciated in Figure 58. The bars represent the relative monthly power yields of fix, 1-axis tracking and 2-axis tracking PV plants, respectively. The 100 % case is defined as the highest absolute power production (August, 2-axis tracking PV). As one would expect, the 2-axis PV system is characterized by a higher power production than the other two systems along the whole year. The tracking allows maximizing the utilization of the available solar resources. Table 18 shows that the global annual irradiance of 2-axis tracking PV systems is approx. 3,150 kWh/m²/y, while fixed PV plants dispose of just 2,520 kWh/m²/y global annual irradiance.

The performance differences between fix PV and 1-axis PV are significantly larger than between 1-axis and 2-axis plants. Almost independent of the tracking system, yield differences between summer and winter months amount to approx. 20 %.

Table 18 summarizes the key design parameters as well as the main technical and economic results of the simulated PV plants. 2-axis tracking PV systems present more than 2,550

equivalent full load operation hours per year and a capacity factor of more than 29 %. However, although 2-axis PV plants present an approx. 23 % higher annual electricity generation than fixed PV plants, the levelized cost of electricity of t fixed PV plants is lower. This can be explained by the high additional investment in tracking systems. Such results are in line with data provided in the literature [Goodrich 2012].

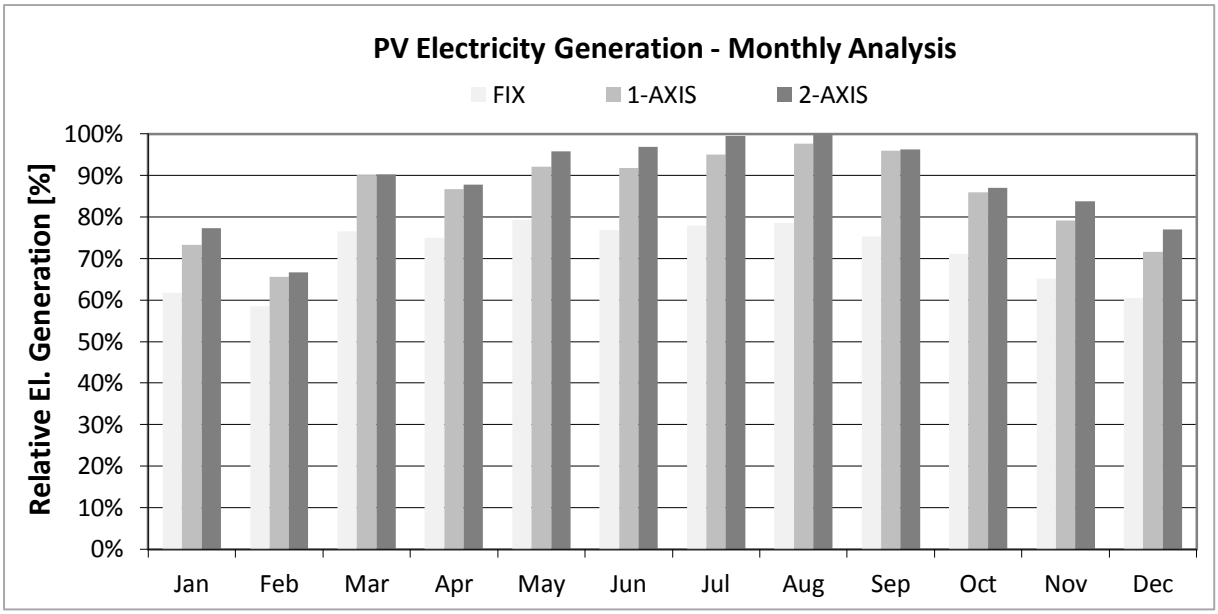

Figure 58: Monthly sum of PV electricity generation; comparison of different sun tracking technologies

	Unit	FIX	1-AXIS	2-AXIS
Key Design Parameters				
Capacity	MW_p		10.0	
Technology	-		Polycrystalline	
Nominal efficiency	%		12.93	
Tracking type	-	Fix	1-axis tracking	2-axis tracking
Annual solar irradiance (Global Irradiance)	$kWh/(m^2 y)$	2,520	3,031	3,153
Annual Yield Analysis				
Average inverter efficiency	%	92.8	93.5	93.8
Average components´ efficiency[1]	%	85.6	86.2	86.5
Net elec. generation at grid connection	GWh_{el}/y	20.7	24.7	25.5
Full load hours	h	2,066	2,472	2,552
Capacity factor	-	23.6	28.2	29.1
Net annual solar-to-electricity efficiency	%	10.8	12.9	13.3

Table 18: Summary of technical and economic parameters of PV plants; [1]including inverter and wiring

b) Impact of long-term Resource Availability

In contrast to CSP, PV is characterized by a much lower uncertainty of power output (Figure 59). This may appear surprising. However, such differences can be explained by the fact that CSP and PV use different solar resources. CSP plants only use the direct share of the irradiance (i.e. DNI), which is prone to higher seasonal and year-by-year variations than global irradiance.

Global irradiance consists of direct and diffuse share. Whenever direct irradiation is reduced due to the presence of clouds or aerosols, a portion of the scattered irradiation impinges the PV collectors as diffuse irradiation can also be converted into electricity. Diffuse irradiation cannot be used by CSP as it reaches the collectors from several different directions and therefore cannot be concentrated.

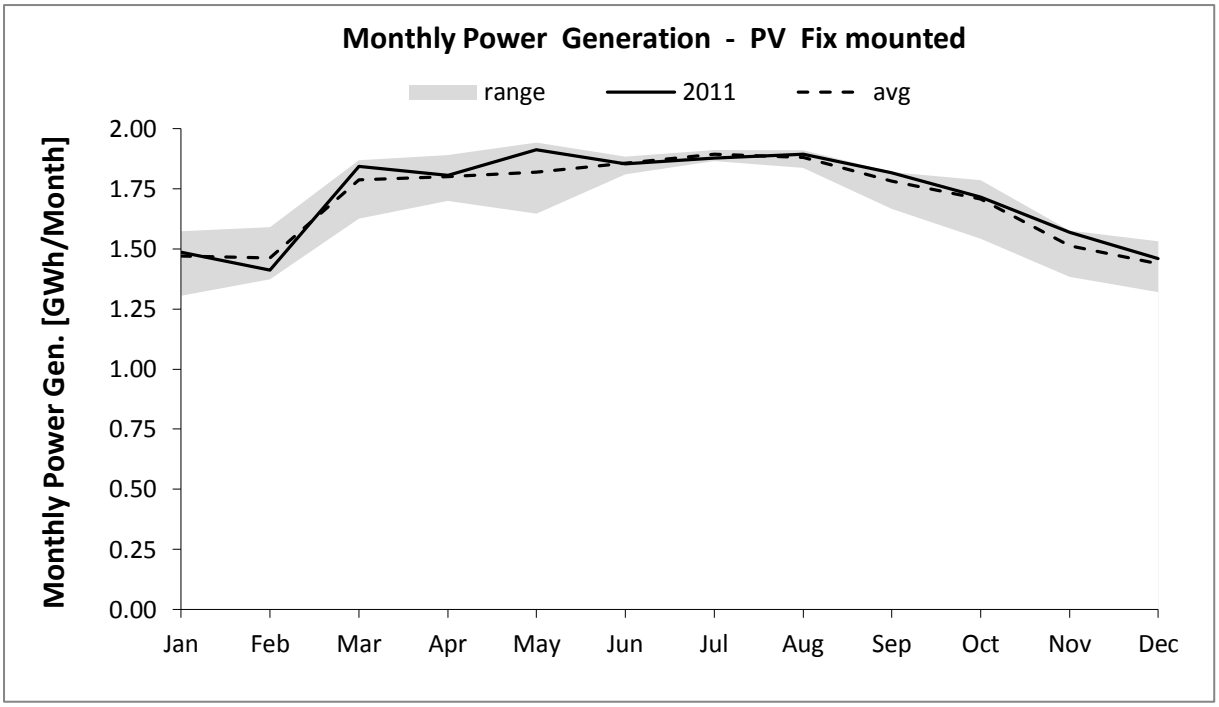

Figure 59: Monthly sum of power generation (PV, fix mounted, long-term analysis)

During the summer months (June to September), the variability of the monthly electricity generation is constantly below 10 %, with a minimum in July (2.4 %). In winter, the uncertainty is higher and reaches 17.1 % in January. Due to its low variability PV seems to be best suited for the coupling with daily storages such as batteries. In addition, PV can be considered as a secure form of renewable power supply, in particular during summer months.

However, it should be underlined that electricity generation by PV is characterized by daily intermittency, which cannot be recognized in a diagram of monthly cumulated production such that of Figure 59. Storage devices and backup power plants will be required to guarantee a continuous power supply. The impact of such intermittency within an electricity network will be assessed in 8.4.

8.2.3 Wind Power

a) Impact of long-term Resource Availability

Wind power plants were not analyzed as in detail as CSP and PV. No technology selection has been performed; instead, standard 2 MW wind turbines have been selected [Gamesa 2014]. However, the impact of long-term resource availability has been assessed in order to highlight the main differences in comparison to CSP and PV (Figure 60).

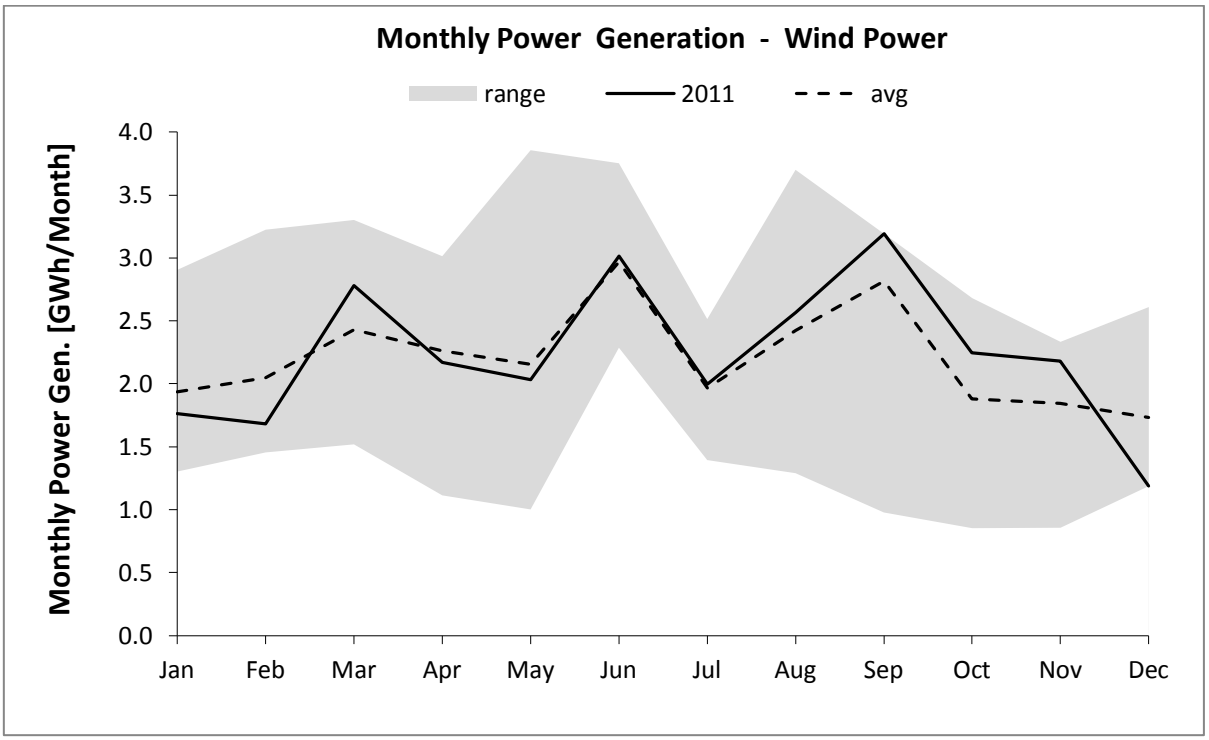

Figure 60: Monthly sum of power generation (wind power, long-term analysis)

Wind power production does not present any regularity patterns and is characterized by a high output uncertainty. For most of the months, the maximal year-by-year variability exceeds 50 % and reaches a maximum of 74 % in May. Wind power currently is among the cheapest renewable technologies. However, due to their unpredictable power generation patterns, wind power plants seem to be best suited for integration in relatively large power supply systems, as such systems are likely to be equipped with sufficient balancing options, e.g. backup plants, storages and well-developed electricity networks. Wind power can be used as an effective fossil fuel saver, but external cost for backup and power balancing should be carefully evaluated.

Similarly to PV, electricity generation by wind power is characterized by intermittency, which cannot be recognized in a diagram of monthly cumulated production. Storage devices and backup power plants will be required to guarantee a continuous power supply. The impact of such intermittency within an electricity network will be assessed in 8.4.

8.3 Seawater Desalination

The flexibility of the developed models allows the analysis of a large number of layouts. Concerning MED, parametric studies are carried out on the number of stages and on the pressure of the heating steam (including thermal vapor compression). The effect of economic parameters such as intake cost, material cost and heat cost on LWC is also assessed. The economics and the energy consumptions of RO are mainly affected by the type of pre-treatment, the temperature and the salinity of the feed water as well as by the design recovery ratio (Table 19).

Technology	Description	Objective
MED (8.3.1)		
a) Power source and fuel price	Techno-economic analysis of the impact of number of stages, power source (conventional turbine and CSP) and fossil fuel price on LWC	Selection of Min. LWC as function of energy source and fuel price; cost breakdown of MED plants
b) Steam pressure	Impact of heating steam pressure on techno-economic figures (in addition, variation of number of effects and fossil fuel price)	Selection of Min. LWC as function of heating steam pressure
c) Metal price	Economic effect of metal price fluctuations over time on LWC and optimal number of stages	Selection of Min. LWC as function of metal price
MED-TVC (8.3.2)		
a) Power source, fuel price and steam pressure	Techno-economic analysis of the impact of number of stages, power source (conventional steam turbine and CSP), fossil fuel price and heating steam pressure on LWC	Selection of Min. LWC as function of energy source, fuel price and steam pressure
b) MED / MED-TVC comparison	Summary of economic results of 8.3.1 and 8.3.2	Selection of best thermal desalination technology (to be used in 8.4)
RO (8.3.3)		
a) Water salinity, water temperature and recovery ratio	Analysis of the influence of water salinity, water temperature and recovery ratio on specific energy requirements and economic figures	Basic understanding of the impact of key parameters on the design of SWRO plants; selection of Min. energy requirements and Min. LWC (to be used in 8.4)
b) Fuel cost	Economic impact of fuel cost on LWC; breakdown of cost structures	Sensitivity of LWC on fuel price variations
c) MED / RO comparison	Breakdown of cost structure of MED and RO (Assumption: CSP-only power supply)	Preliminary economic comparison on technology level

Table 19: Overview of the second section of the case study (8.3): analysis and pre-selection of desalination plants

8.3.1 MED

The technical performance and the economics of MED plants depend on a wide number of parameters. The most relevant of them are evaluated and discussed within this case study. An overview of the calculations is provided in Table 20. The analysis starts with the discussion of the impact of technical and economic parameters on the optimal number of stages. Other parameters such as the pressure of the heating steam and the energy source (i.e. based on fossil fuels or renewable) have a significant impact on LWC.

Finally, the water price is influenced by other parameters such as the metal price, which contributes to a notable extent to the investment cost of the MED evaporator. The impact of the intake cost is discussed in Annex 10.4.4.

Parameter	Unit	Range
Number of stages	-	4 - 14
Heating steam pressure	bar	0.2 - 0.4
Electricity and heat source	-	Fossil steam turbine / CSP
Metal price	-	Base case / 0.5x / 2x

Table 20: Overview of parameters of the MED case study

a) Impact of Power Source and Fuel Price

The number of stages is the most important design parameter of an MED plant. Table 21 summarizes the main design parameters used for the simulation and some key technical results. The analysis includes three cases, i.e. 4, 8 and 12 stages. Common input parameters have been chosen for the top brine temperature, the condenser temperature and the heating steam mass flow. The first obvious consideration is that the higher the number of stages, the higher the GOR. In fact, the higher the number of stages, the more efficient the MED process, as the latent heat of condensation and evaporation of the steam can be re-used several times. For the same reason the specific heat consumption decreases at a high number of effects.

The cooling water mass flow also depends on the number of stages; in particular it depends on the amount of steam which is produced in the last effect. For this purpose, cold seawater enters the condenser and condensates the steam flow produced in the last effect. After the condenser, only a portion of the pre-heated seawater is directed toward the MED (feed water), while the remaining part (cooling water) is mixed with the brine before it is discharged to the sea. As a first approximation, it can be assumed that the steam generation is almost the same in each effect. At first sight one would think that the amount of distillate decreases at each successive step, as a share of the steam generated in the previous step has to be used for feedwater pre-heating. This share cannot be used for distillate production in the successive stage. However, this loss is partially counterbalanced by the flashing of brine and distillate, whose impact is particularly important at a high number of stages (the amount of flash is proportional to the cumulated brine and distillate mass flow). In conclusion, it can be stated that the amount of required cooling water is approx. inversely proportional to the number of stages. The cooling water mass flow also influences the specific electricity consumption (SEC) of the MED plant. The SEC consists of two main components, i.e. MED process and feed water intake. In the model, the MED process electricity consumption is assumed to be independent of the number of stages and equal to 0.6 kWh/m³.

The remaining portion of electricity consumption is due to the water intake and is proportional to the cooling water mass flow. The specific electricity consumption of efficient MED plants (12 effects or higher) can fall below 1.5 kWh/m³. In addition, the type of intake and its layout (elevation difference and pipe length) impact on the SEC. The SEC values reported in Table 21 have been obtained assuming an open intake.

MED Plant - Number of Stages	**-**	**4**	**8**	**12**
Motive steam temperature	°C		74.0	
Top brine temperature	°C		70.0	
Condenser temperature	°C		37.6	
Average ΔT per stage	K	10.8	4.6	2.9
Distillate production	m³/h	490	920	1,310
GOR	-	3.88	7.28	10.33
Spec. cooling water mass flow	-	17.0	7.0	3.5
Spec. feed water mass flow	-	2.6	2.8	2.9
Spec. heat transfer area	m²/(kg/s)	205	321	480
Spec. heat consumption	kWh_{th}/m^3	172.6	96.1	70.9
Spec. electricity consumption	kWh_{el}/m^3	3.28	1.94	1.48

Table 21: Key results of the technical MED model

So far, all of the analyzed parameters would lead to the conclusion that there is no benefit in choosing a low number of stages. However, higher GOR and lower energy consumption has to be paid in terms of the higher heat exchanger area and higher capital cost. The reason is simple: the driving force of MED processes is the net temperature difference between two consecutive stages (i.e. the brine temperature difference between two stages minus the boiling point elevation and pressure losses). As a consequence, the higher the number of stages, the lower the available temperature difference per stage and the higher the required specific heat transfer area of the heat exchangers.

The discussion of Table 21 highlighted that a trade-off exists between technical efficiency and economics. The following case studies analyze in detail these aspects. Figure 61 shows the results of such an optimization. A fossil fuel fired steam turbine has been assumed as a source for heat and electricity. The results present the levelized water cost as a function of the number of stages. A differentiation is made between fix costs and variable costs. In addition, the impact of the fossil fuel price escalation on LWC is considered. Fix costs include capital cost, personnel and maintenance and repair cost. Such an additional cost's breakdown is shown in Table 22. Fix costs present a quite wide minimum between 6 and 10 stages. At a lower number of stages, fix costs increase due to the higher intake cost. In fact, the lower the number of effects, the higher the specific intake water mass flow. At a high number of effects the fix costs' share increases again. Such behavior is due to the reduction of the available temperature differences between stages and of the consequent increase of the heat exchanger area, which is described in detail in Annex 10.3.1.

Maintenance and repair (M&R) cost and personnel cost are almost independent of the number of stages.

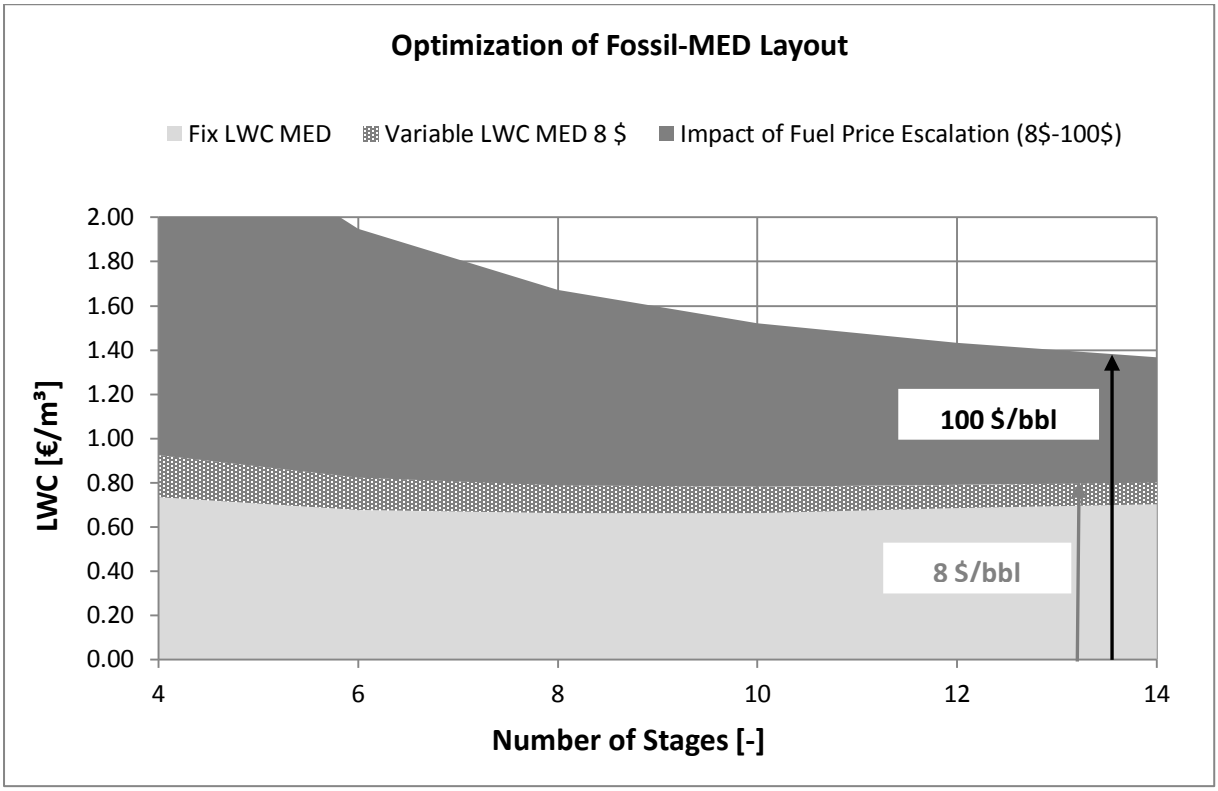

Figure 61: Impact of number of stages on LWC (fossil-fired steam turbine); Assumption: 30,000 m³/d capacity

In addition, the higher the number of effects, the lower the specific electricity cost. It may appear surprising that the heat cost is almost negligible (0.07 €/m³ to 0.03 €/m³ under the assumption of low fossil fuel price). However, this can be explained by the reference cycle method (7.2). In the considered case, the reference cycle is a steam turbine equipped with a conventional cooling unit (evaporative cooling). The average annual costs are calculated for both power blocks, i.e. MED case and conventional cooling. In the first case the cooling cost is set to zero, as the cooling is provided by the MED plant, whose costs are assessed separately. In the second case (i.e. the reference cycle), the cooling cost has to be added.

Number of Stages	**-**	**4**		**8**		**12**	
Capital Cost	€/m³	0.49		0.43		0.45	
Personnel Cost	€/m³	0.02		0.01		0.01	
M&R Cost	€/m³	0.22		0.22		0.22	
Sum of fix LWC	€/m³	0.73		0.66		0.69	
Electricity Cost	€/m³	0.09	(0.44)	0.06	(0.28)	0.04	(0.22)
Heat Cost	€/m³	0.07	(1.32)[1]	0.04	(0.70)	0.03	(0.49)
Chemical Cost	€/m³	0.03		0.03		0.03	
Sum of variable LWC	€/m³	0.19	(1.79)[1]	0.13	(1.01)	0.10	(0.75)
LWC	€/m³	0.92	(2.52)[1]	0.79	(1.67)	0.79	(1.43)

Table 22: Breakdown of LWC cost; Assumptions: energy source fossil fired steam turbine; Fossil fuel price: 8 $/bbl and [1](100 $/bbl)

Finally, the impact of a possible escalation of the fossil fuel price is assessed. The results discussed so far refer to a fuel price of 8 $/bbl. This price is far below market prices. However, most of MENA countries -and in particular oil producing countries- still subsidize oil for national use [IEA 2014]. The additional case assumes a market fuel price (100 $/bbl). The increase of LWC due to fossil fuel price increases is represented at the top of and in Table 22 (values in brackets). Depending on the number of stages, the increase of LWC in comparison to the case of a low fossil fuel price amounts from approx. 1.60 €/m³ to 0.64 €/m³. Such an impact is higher at a lower number of effects, as in this case the MED plant is less efficient.

The figures change when taking CSP as a heat and electricity source instead of a conventional power plant (Figure 62). Although most of the considerations previously exposed remain true, i.e. the minimum of LWC occurs in correspondence with the trade-off between MED efficiency and overall cost, the position of such a minimum as well as the impact of the fuel price differ from the conventional case. The assumed CSP configuration is a molten salt-based central receiver power plant. The solar multiple is 3.0 and the TES capacity 14 FLH. The plant is operated round-the-clock (as in the conventional case). Whenever the TES is discharged, operation is continued in hybrid mode. Such a CSP plant is able to achieve an annual solar share of approx. 86 %, so that the consumption of fossil fuels can be minimized.

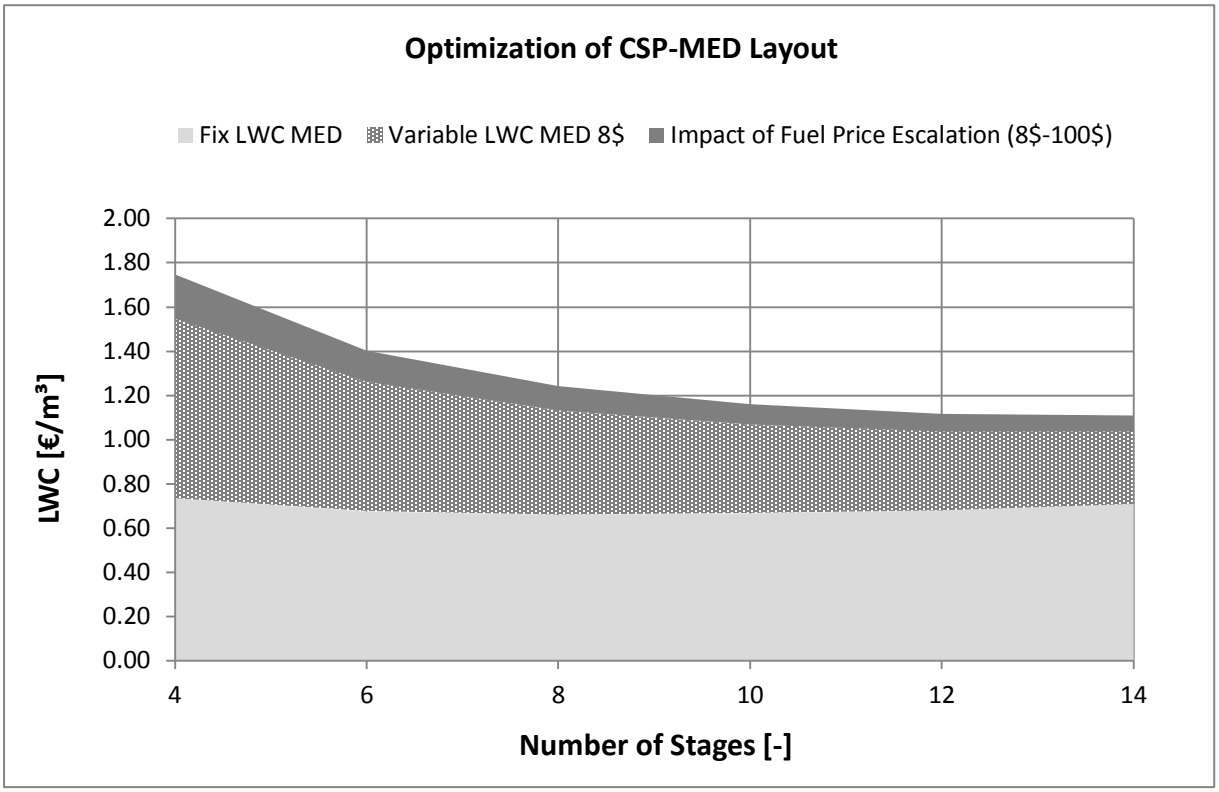

Figure 62: Impact of number of stages on LWC (CSP hybrid)

Two main differences in comparison to the previous case can be observed: the first one is the higher weight of variable costs, while the second one is the lower impact of fossil fuel

price escalation on LWC. Fix costs do not change, as neither capital cost nor personnel nor M&R are affected by the type of energy supply. The higher variable costs are mainly due to the higher heat cost and -secondarily- to the slightly higher electricity cost. The CSP-MED case is characterized by higher capital investment (solar field, thermal energy storage) which is required to compensate lower turbine efficiency in comparison to the CSP reference cycle. In the 4-stage MED, heat cost amounts to 0.52 €/m³ and is so the largest cost contributor, followed by the MED investment cost (0.49 €/m³). In contrast to the previous case, cooling cost only plays a marginal role in the total investment costs. However, heat cost can be reduced by over 60 % increasing the number of stages from 4 to 12. The higher CSP investment cost also reflects on the higher specific electricity cost for MED. The advantage of CSP becomes visible at high fossil fuel price. In contrast to the conventional case, the impact of the fossil fuel price escalation is lower. For a 12-stage MED, the difference of specific energy cost between low and high fuel price amounts to 0.64 €/m³ in the conventional case and 0.08 €/m³ in the CSP case. It should be noted that such figures change if another CSP configuration (e.g. solar multiple) is chosen. As an example, assuming a lower solar multiple would lead to lower capital cost, but higher consumption of fossil fuels.

Finally, the comparison of Figure 61 and Figure 62 makes clear that the optimal number of stages of an MED plant depends on the power supply technology and the fossil fuel price. In the case of conventional power supply and low fossil fuel price, the optimal number of stages is 9. This optimum shifts to the right part of the diagram (14 stages) when assuming market fuel price. In the case of CSP, the high heat supply cost leads to a high optimal number of stages (13-14), which is only marginally influenced by the price of fossil fuel. This trend mainly reflects the general fact that additional investments in efficiency are convenient only if investment or operation costs are sufficiently high.

Number of Stages	**-**	**4**		**8**		**12**	
Capital Cost	€/m³	0.49		0.43		0.45	
Personnel Cost	€/m³	0.02		0.01		0.01	
M&R Cost	€/m³	0.22		0.22		0.22	
Sum of fix LWC	€/m³	0.73		0.66		0.68	
Electricity Cost	€/m³	0.26	(0.31)[1]	0.17	(0.19)	0.13	(0.15)
Heat Cost	€/m³	0.52	(0.67)[1]	0.27	(0.36)	0.19	(0.25)
Chemical Cost	€/m³	0.03		0.03		0.03	
Sum of variable LWC	€/m³	0.81	(1.01)[1]	0.47	(0.58)	0.36	(0.44)
LWC	€/m³	1.55	(1.75)[1]	1.13	(1.24)	1.04	(1.12)

Table 23: Breakdown of LWC cost; Assumptions: energy source CSP; Fossil fuel price: 8 $/bbl and [1](100 $/bbl), large scale plant

b) Impact of Steam Pressure

The pressure of the heating steam also has an important impact on LWC. Low steam pressure means that the available temperature difference of the MED process is relatively low. As a result, the heat transfer area of the evaporators´ heat exchangers and -in turn- the

capital costs become noticeable also at a rather low number of stages. In addition, the lower the pressure of the heating steam, the lower the heat cost. The combination of these factors is expected to lead to a lower optimal number of stages.

Similarly to the previous case study, two heat sources are considered, i.e. a conventional steam turbine and a CSP plant. Figure 63 presents the results of the first case, which includes the analysis of two steam pressures (0.20 bar and 0.40 bar) and of a variation of the fossil fuel price (8 $/bbl and 100 $/bbl). It should be noted that the high pressure case would lead in practice to scaling problems on the surface of the heat exchangers, as the maximal solubility of salts would be exceeded (at least in the first stages). Thus, this case had an academic value only. As one would expect, in the case of low steam pressure (0.20 bar) the optimal number of stages is lower than in the previous case (Figure 61), which assumed a steam pressure of 0.37 bar. In the case of low fossil fuel price, the optimal number of stages is 6, while it shifts to 10 in the case of high fossil fuel price. At a pressure of 0.40 bar, the optimal number of stages is higher (10 and 14, assuming low and high fossil fuel prices, respectively). This is due to the higher overall available temperature difference in the MED process, which reduces the required heat transfer area of the heat exchangers. In addition, the heat cost is higher because -according to the reference cycle method- a higher steam extraction temperature corresponds to a higher amount of virtually non-generated electricity.

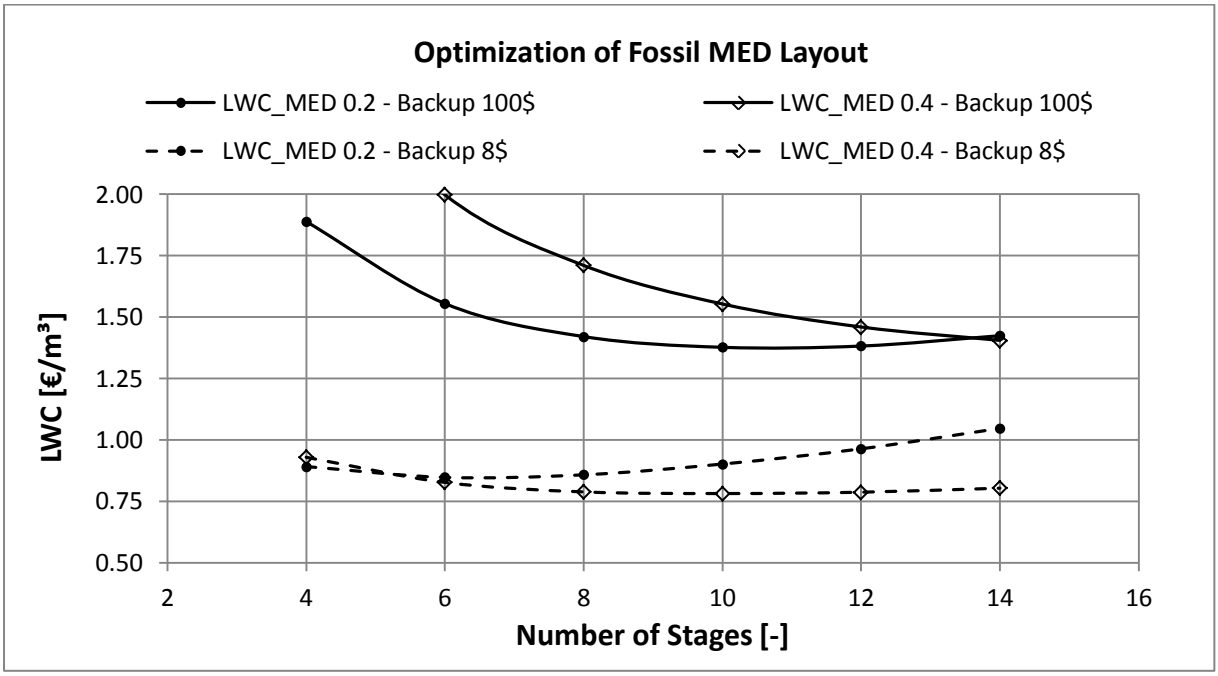

Figure 63: Impact of steam pressure on fossil MED; Assumptions: base intake and material cost; fossil fuel price: 8 $/bbl and 100 $/bbl

The price of fossil fuels also impacts the optimal heating steam pressure. The lower the price of the fuel, the lower the cost of heat. If the price of the fossil fuel is low, higher steam pressure provides lower LWC, except for the 4-stage configuration. The figures change if high fuel price is assumed. In this case the heat cost has a preponderant weight. The heat cost

can be minimized selecting a higher number of stages and a lower pressure of the heating steam, which reduces the cost penalty according to the reference cycle method. Figure 64 shows the impact of the heating steam pressure on the LWC of a CSP-MED plant.

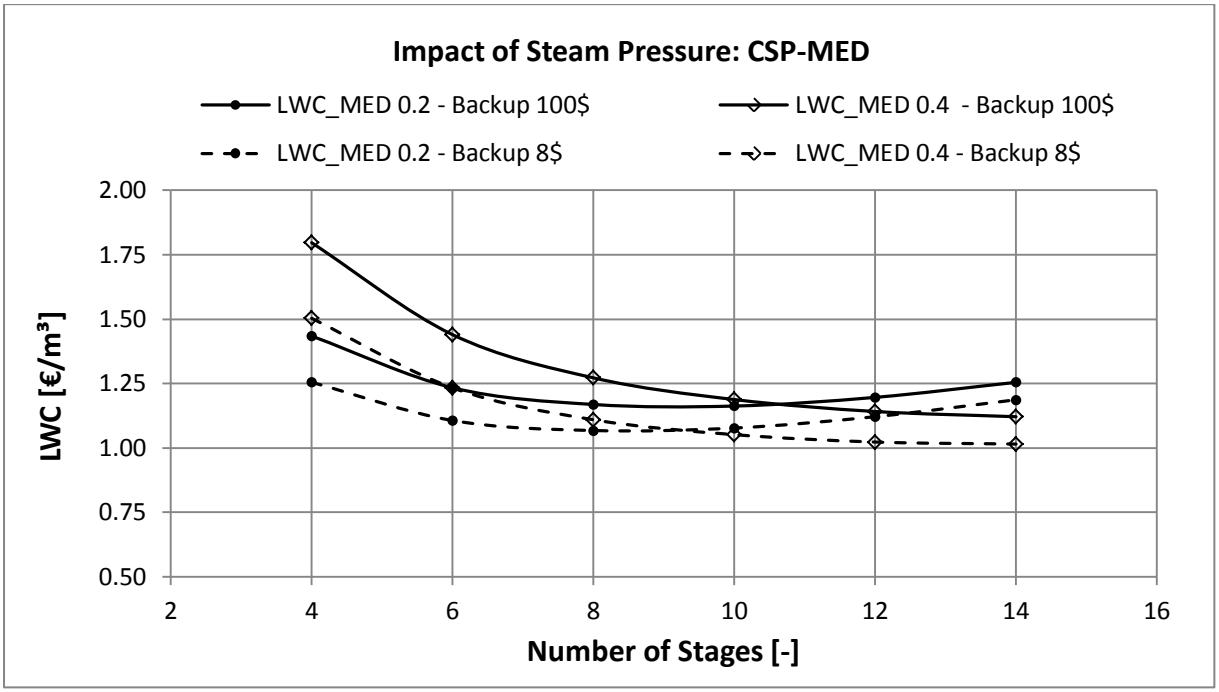

Figure 64: Impact of heating steam pressure on LWC of a CSP-MED plant; Assumptions: base intake and material cost; fossil fuel price: 8 $/bbl and 100 $/bbl

If the number of stages is lower than 9 - 11, 0.20 bar steam provides lower LWC than 0.40 bar steam. In contrast, at a high number of stages 0.4 bar steam performs better. At this point of the discussion it should be evident that such behavior is the result of a trade-off between capital cost and heat cost. If the pressure of the steam is lower, the heat cost is relatively low, but the CAPEX of the evaporator is high even at an intermediate number of stages. In contrast, if the pressure of the steam is high, the capital cost remains relatively low also at a high number of stages, while the heat cost is higher. For this particular case, it turns out that lowest LWC is provided by relatively high steam pressure and a high number of effects. This remains true independent of the price of the fossil fuels.

c) Impact of Metal Price

Different metals such as copper and nickel are commonly used in MED plants. Their price fluctuations over the last 30 years can be appreciated in Figure 65; it is interesting to note that the metal price trends correlate with the oil price (dashed grey line). Metals such as copper and nickel have experienced extreme price volatility during the last few years. The prices are mainly dictated by speculative processes, as the developments between the years 2006 and 2010 show. The metal price contributes to a relatively large extent to the CAPEX of MED evaporators. In highly efficient plants (e.g. 12 stages or more), the evaporator cost almost achieves 60 % of the total plant CAPEX (Annex Figure 104). Of this 60 %, approx. 40 % is constituted by metallic components such as evaporator tubes and clad sheets. As a result,

up to 24 % of the total capital cost of an MED plant may be prone to the price variations of metals. Figure 66 presents the impact of the metal price and the number of stages on LWC. Three cases have been considered. The base case assumes a metal price of 50 US$/ton (MED BASE). In addition, a price of 25 US$/ton and 100 US$/ton is taken into account, in the two other cases MED 0.5x and MED 2x, respectively. The continuous operation of the desalination plant is guaranteed by a hybrid CSP power plant. The price of the backup fossil fuel is assumed to be 8 $/bbl.

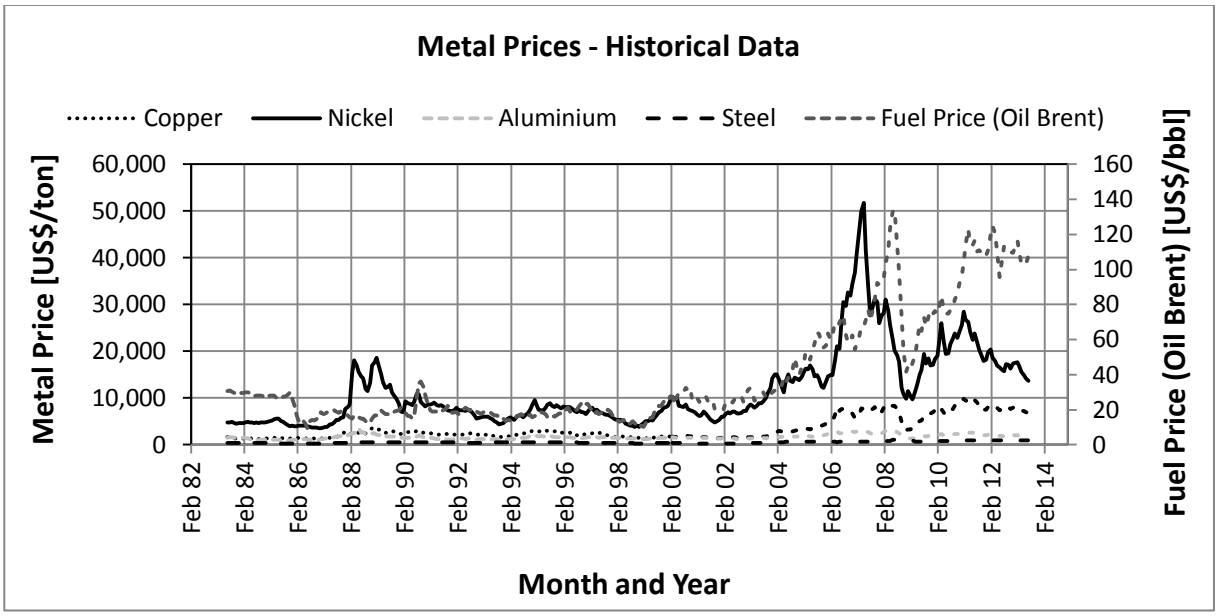

Figure 65: Historical development of selected metal prices and qualitative comparison with fuel price (Brent oil) [indexmundi 2013]

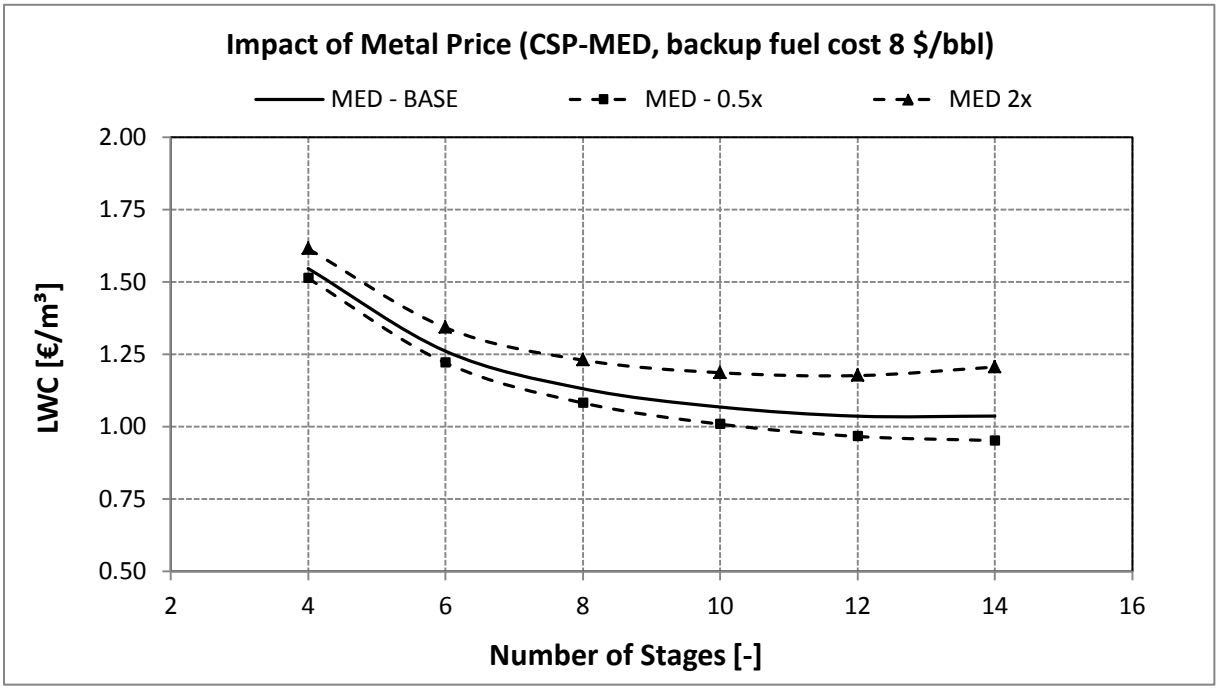

Figure 66: Impact of metal price on LWC; Assumptions: CSP CR, hybrid mode; fossil fuel price: 8 $/bbl

The results show that an increase in the metal price (MED 2x) causes an increase in capital expenditures and of LWC. In addition, the higher the number of stages is, the larger the difference to the base case, which can be explained with the increasing weight of the evaporator cost and other metal components on the total CAPEX. The metal price also impacts the optimal number of stages: the higher the metal price, the lower the optimal number of stages. In contrast, lower metal prices imply lower LWC, while the optimal number of effects is shifted towards the right part of the diagram.

8.3.2 MED-TVC

a) Impact of Power Source, Fuel Price and Steam Pressure

Technical and economic performances of MED plants with thermal vapor compression present a number of differences in comparison to MED without TVC. The structure of this case study is similar to that used in 8.3.1. First, key technical features of MED-TVC plants are presented. As a second step, a sensitivity on LWC has been carried out, which takes into account different levels of steam pressure as well as two power supply technologies (i.e. conventional steam turbine and CSP). In addition, the impact of the variation of the price of fossil fuels is taken into account (8 $/bbl and 100 $/bbl).

Table 24 summarizes the main design parameters used for the simulation of MED-TVC plants and some key technical result. The analysis includes three cases, i.e. 4, 8 and 12 stages.

Number of Stages	**-**	**4**	**8**	**12**
Motive steam temperature	°C		151.8	
Gross turbine efficiency	%		24.3	
Top brine temperature	°C		65.0	
Condenser temperature	°C		37.6	
Distillate production	m^3/h	590	1,100	1,550
GOR	-	5.62	10.50	14.79
Spec. cooling water mass flow	-	16.4	6.7	3.2
Spec. feed water mass flow	-	2.6	2.8	3.0
Spec. heat transfer area	$m^2/(kg/s)$	234	429	683
Spec. heat consumption	kWh_{th}/m^3	119.9	67.0	50.0
Spec. electricity consumption	kWh_{el}/m^3	3.21	1.90	1.45

Table 24: Key results of the technical MED-TVC model; Assumption: motive steam pressure is 5.0 bar

Common input parameters have been chosen for top brine temperature, condenser temperature and steam mass flow. The temperature of the motive steam is higher than in the case of MED without TVC. The mid pressure steam is used to entrain a share of the distillate produced in the last effect and to upgrade its level. The two steam flows are mixed and they serve as a heat supply in the first stage of the MED. The re-cycling of a portion of the produced distillate makes possible to improve the GOR. However, it will be shown that

such an improvement has to be paid in terms of higher heat cost. Almost independently of the number of stages, the GOR increase of MED-TVC in comparison to simple MED amounts to more than 35 %.

Most of the issues previously discussed in 8.3.1 also apply to the MED-TVC case. Figure 67 shows the results of the optimization of the number of stages in a conventional MED-TVC plant. A total of four cases is analyzed, which include two steam pressures (1.5 bar and 5.0 bar) and two fossil fuel prices (8 $/bbl and 100 $/bbl). The choice of the two values of motive steam pressure is justified as follows: 5.0 bar (or similar values) are commonly used in commercial MED-TVC plants, while the additional value of 1.5 bar has been selected in order to reduce the impact of heat cost, as this cost item is expected to be particularly relevant in the CSP case. So far, no MED-TVC plants use such low pressure. The technical feasibility of such a layout should be therefore critically assessed.

Similarly to Figure 63 (simple MED, conventional power supply), Figure 67 shows that at a low number of stages the LWC is mainly defined by the price of the fossil fuel. As long as the price of the energy supply is low, the impact of the steam pressure plays a minor role also at a low number of stages. In MED-TVC plants an increase in the steam pressure at the exit of the turbine (also called motive steam) does not imply a change in the top brine temperature (which is a design parameter). Rather, the pressure of the motive steam impact the entrainment ratio (Eq. 3.25) and in turn the GOR.

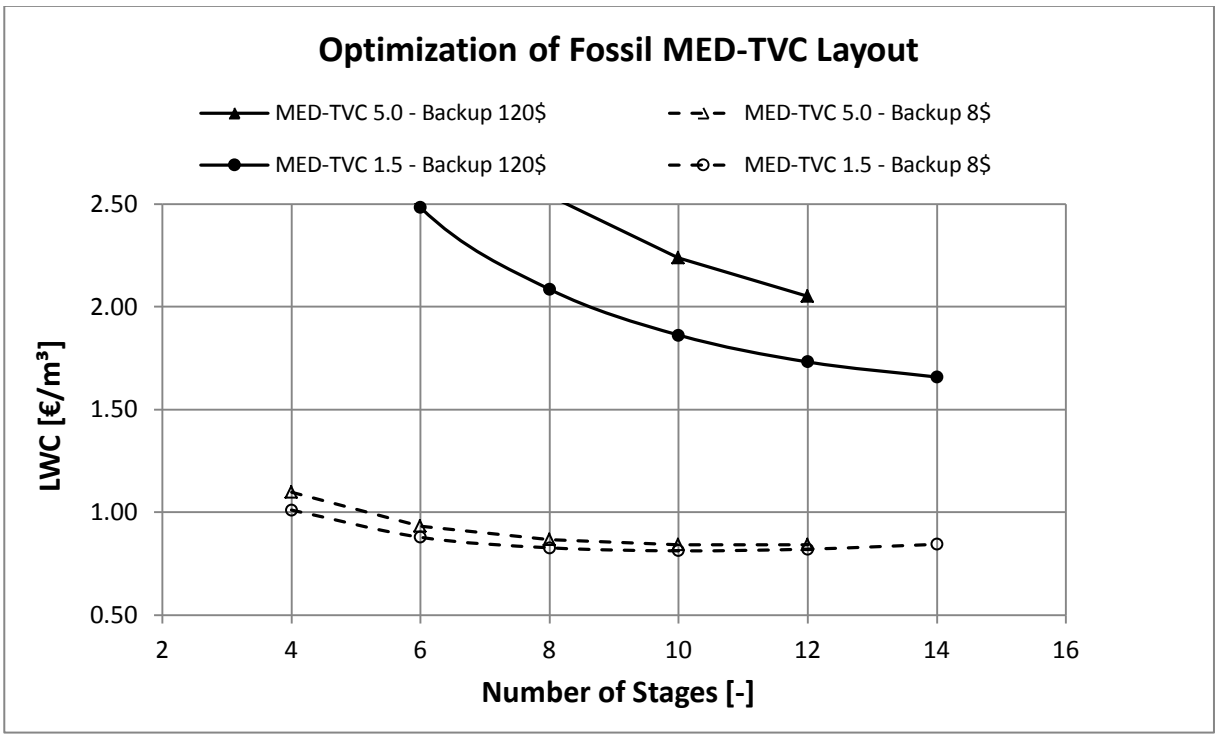

Figure 67: Impact of steam pressure on fossil MED-TVC; Assumptions: base case intake and material cost

The upper lines of Table 25 summarize the cost differences among the four analyzed cases. The majority of the cost items (capital cost, personnel, M&R and chemicals) are independent of the steam pressure and the fossil fuel price. The only differences are in the electricity cost

and in the heat cost. As a general remark, the heat cost of MED-TVC is higher than that of MED without TVC. This is due to the fact that the saved expenditures for the cooling unit (in comparison to the reference cycle) are more than balanced by the heat cost. The higher the pressure of the motive steam, the higher the heat cost. Such an impact is exacerbated in the case of a high fuel price.

For a given number of stages, the price of fossil fuels only impacts the heat cost but not the electricity cost. In other words, the electricity cost is independent of the pressure of the motive steam. This may appear confusing; however, this is a direct consequence of the definition of the reference cycle method (7.2). Depending on the price of the fossil fuel, the optimal number of stages varies between 10 (low fossil fuel price) and 14 (high fossil fuel price). Most of the existing MED-TVC plants have however a number of stages between 4 and 6. Such differences may be motivated by different assumptions on the intake cost (Annex 10.4.4), and the metal price (8.3.1).

The same sensitivity of motive steam pressure and of price of fossil fuels is carried out taking CSP as a power supply (Figure 68). Several differences can be observed in comparison to the conventional MED-TVC case. First the LWC is higher, in particular at a low number of stages, which is due to the high heat cost. In addition, the pressure of the motive steam has a large impact on the heat cost (Table 25), which is due to the high CAPEX of the CSP plant. Finally, similarly to the MED case without TVC, the optimal number of stages is 14.

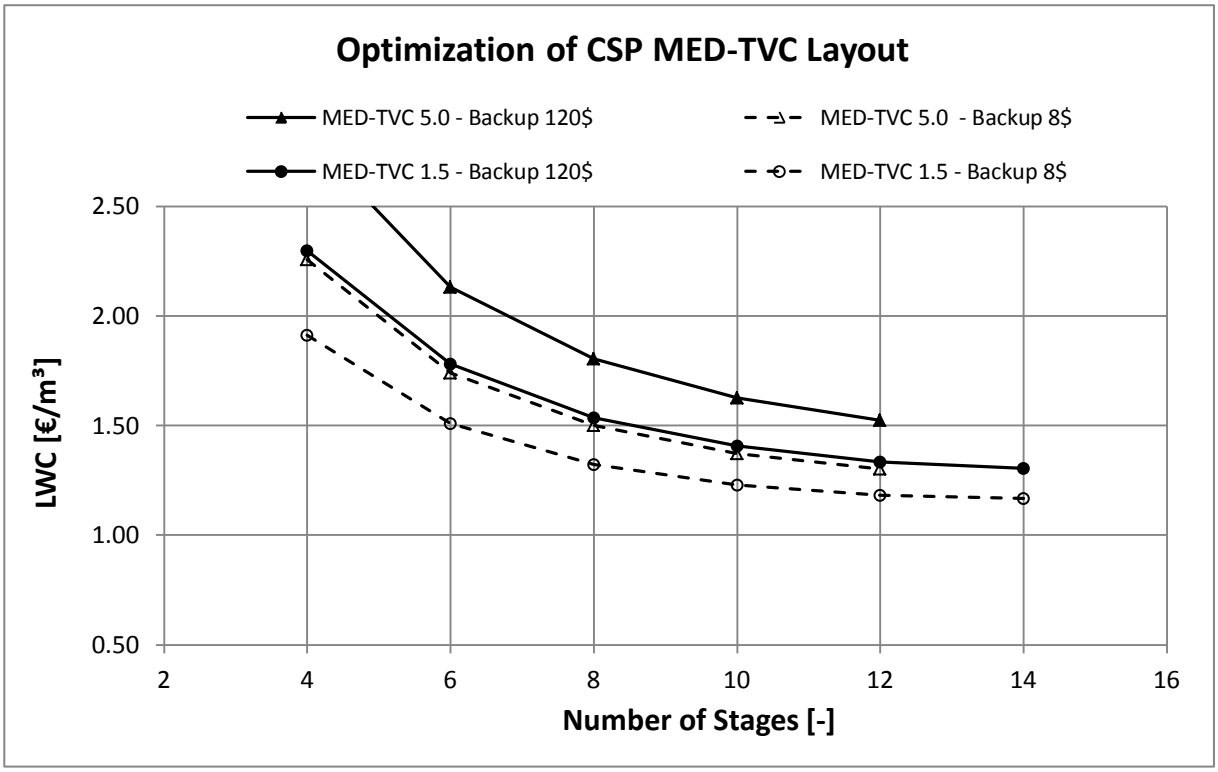

Figure 68: Impact of number of stages on CSP MED-TVC; Assumptions: base case intake and material cost

Heating steam pressure	1.5 bar		5.0 bar	
Fossil fuel price	8 $/bbl	100 $/bbl	8 $/bbl	100 $/bbl
Fossil MED-TVC				
Electricity cost	0.06	0.27	0.06	0.27
Heat cost	0.10	1.15	0.15	1.61
CSP MED-TVC				
Electricity cost	0.17	0.21	0.17	0.21
Heat cost	0.48	0.66	0.67	0.94

Table 25: Summary of the main differences among the considered MED-TVC scenarios; Assumption: 8-stage MED-TVC, large scale plant

b) Comparison of MED and MED-TVC

Table 26 summarizes the cost breakdown of MED and MED-TVC plants. A differentiation is made between conventional and CSP power supply. All values refer to 12-stage processes and to a low fossil fuel price (8 $/bbl). The comparison shows that the main differences relate to capital cost, electricity cost and heat cost, while the remaining cost items (i.e. personnel, M&R and chemicals) do not experience significant variations. In the case of conventional power supply, the LWC of both desalination processes is very similar.

		MED	**MED-TVC**	**MED**	**MED-TVC**
Heating steam pressure	bar	0.37	1.5	0.37	1.5
Power supply	-	Conventional (Fossil)		CSP Hybrid	
Capital cost	€/m³	0.45	0.43	0.45	0.43
Personnel cost	€/m³	0.01	0.01	0.01	0.01
M&R cost	€/m³	0.22	0.22	0.22	0.22
Sum of fix LWC	€/m³	0.69	0.67	0.69	0.67
Electricity cost	€/m³	0.04	0.05	0.13	0.14
Heat cost	€/m³	0.03	0.07	0.19	0.34
Chemical cost	€/m³	0.03	0.03	0.03	0.03
Sum of variable LWC	€/m³	0.10	0.15	0.36	0.51
LWC	€/m³	0.79	0.82	1.04	1.18

Table 26: Exemplary cost breakdown of MED and MED-TVC; Assumptions: 12-stage process, low fossil fuel price (8 $/bbl)

The cost breakdown shows that capital cost is lower in the MED-TVC case, which is due to the higher GOR. Despite the GOR difference between MED and MED-TVC is approx. 35 %, this results in only approx. 5 % capital cost reduction. In fact, the GOR increase only reduces the specific evaporator cost, while the cost of other plant components does not change. In addition, the lower CAPEX is completely counterbalanced by the higher heat cost. In the case CSP is used as a power supply, both heat cost and electricity cost are higher.

Finally, the analysis has shown that MED without TVC performs lower LWC than MED-TVC in a wide range of cases. Therefore, MED without TVC has been selected as the reference thermal desalination technology in the following case studies.

8.3.3 RO

a) Impact of Water Salinity, Water Temperature and Recovery Ratio

This case study presents the sensitivity analysis of a typical SWRO plant using partial two-pass configuration. In such a configuration, the permeate produced within the first pass is divided into two streams. Only one stream is processed by the second stage. The main motivation for the development of this configuration is primarily the reduction of the investment cost of the second pass. In addition, such a configuration allows increasing the flexibility of the plant operation. During summer the seawater temperature is higher and so is the water passage and the salt passage through the membranes. In this case, the required permeate salinity level is reached by increasing the amount of feed processed by the second stage.

Table 27 summarizes the main performance parameters of the analyzed reference SWRO plant. The total plant recovery (i.e. taking into account first and second pass) is 42.0 %, which is an input parameter. It will be shown in the following discussion that the choice of the optimal recovery ratio mainly depends on the seawater quality, i.e. salinity, temperature and biofouling potential.

SWRO Plant	**Unit**	**Value**
Total recovery rate	%	42.0
Spec. membrane area	$m^2/(m^3/h)$	84.1
Water salinity after post-treatment	ppm	250
Specific electricity consumption (SEC)	kWh_{el}/m^3	3.74
1st pass		
Feed salinity	ppm	40,150
Feed pressure SWRO membranes	bar	68.1
Design flux rate	$l/(m^2\ h)$	13.7
Permeate salinity	ppm	640
2nd pass		
Feed salinity	ppm	640
Feed pressure BWRO membranes	bar	8.5
Design flux rate	$l/(m^2\ h)$	31.1
Permeate salinity	ppm	11

Table 27: Key results of the technical SWRO model

The water salinity target after remineralization has been set to 250 ppm. This implies that the average TDS of the permeate upstream of the post-treatment should not exceed approx. 100 ppm. A differentiation exists between the first and the second pass. The feed of the first pass has a pressure of barely 70 bar. Such a high pressure is required in order to counterbalance the osmotic pressure of the feed and to guarantee a sufficiently high net driving pressure. In fact, it has been shown (Eq. 3.28) that the net water flow is proportional to the pressure difference between feed and permeate, while the salt passage solely

depends on the salinity gradients across the membrane. In contrast, the second stage processes brackish water (approx. 640 ppm). As a result, the required feed pressure is almost an order of magnitude lower than in the first pass (8.5 bar). The high pressure requirement in the first pass is the main contributor to the electricity consumption of RO plants.

The salinity of the feed also impacts the used flux rates, i.e. the ratio between permeate and membrane area within a RO module. Such flux rates are relatively low (between 11 l/m²/h and 14 l/m²/h) in the first pass in order to avoid excessive concentration polarization and to minimize the risk of fouling. In the second pass the feed salinity is lower and so the permeate flow rate is higher (28 l/m²/h - 32 l/m²/h). Finally, the electricity consumption (3.74 kWh/m³) consists of the sum of the consumption of each plant component, i.e. intake, pre-treatment, main RO process and post-treatment.

Figure 69 presents the effect of seawater salinity and temperature on the specific energy consumption (SEC). The first consideration is that the higher the salinity of the feed, the higher the electricity consumption. This is not surprising, as water salinity, required feed pressure and SEC are closely inter-related. In contrast, the dependency of SEC on the seawater temperature necessitates some additional explanation. Water and salt passage increase approx. 3 %/K within the typical RO temperature operation range (10 °C – 35 °C). Accordingly, the higher the temperature of the seawater, the lower the required pressure. This behavior can be explained with the decreasing viscosity of water by increasing temperature. The impact of varying temperature on the plant performance is taken into account by means of the temperature correction factor for water and salt passage.

However, the positive impact of the temperature increase on energy consumption tends to level off above 25 °C, due to the increase of osmotic pressure in the downstream elements of the vessel. In fact, a high water passage across the membrane mainly results in a relatively rapid decline of feed mass flow along the vessel, while most of the salt remains on the feed side of the elements. The salinity of the feed increases more rapidly than at lower temperatures and the average net driving pressure is lower. This has to be compensated by higher feed pressure, which results in higher SEC.

The minimal SEC also depends on the seawater salinity. According to the results, the higher the salinity of the feed, the lower the optimal seawater temperature. The eventual impact of high boron concentrations, which could influence SEC, is not considered in the implemented model. However, boron has to be carefully considered in the final assessment of a RO plant as it may be a source of additional technical and economic constraints.

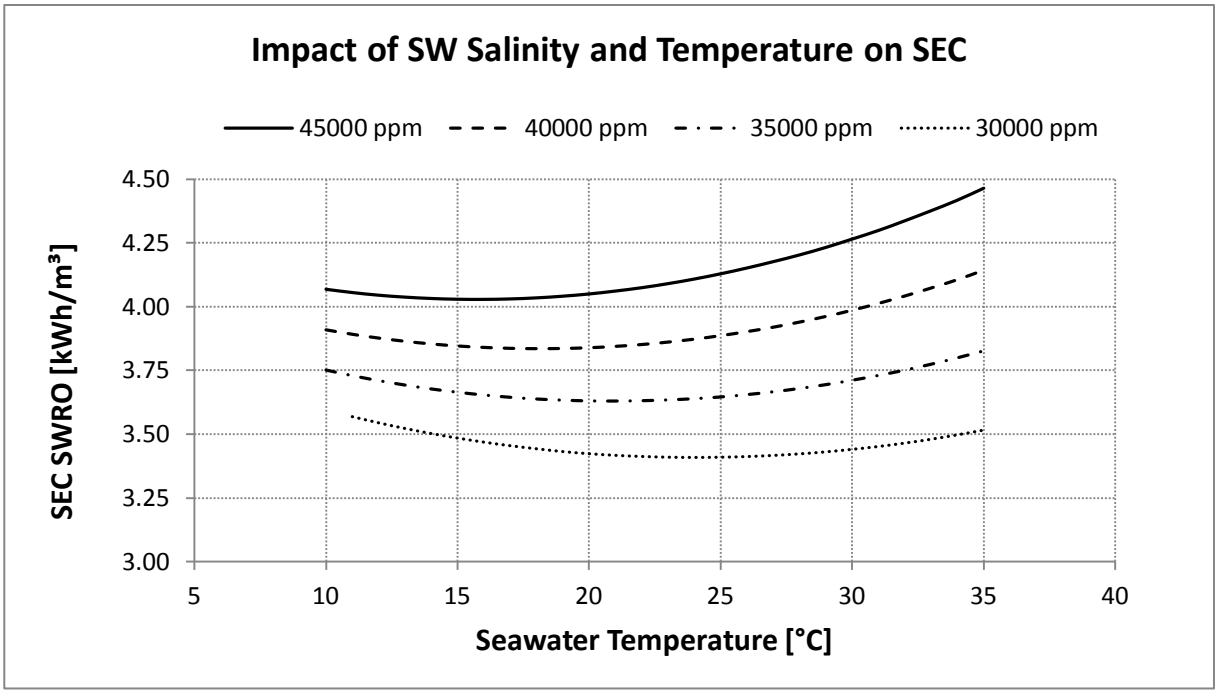

Figure 69: Impact of SW Salinity and Temperature on SEC (reverse osmosis)

Finally, Figure 70 compares the dependency of SEC and of LWC on the recovery ratio. It is interesting to note that the minimum of the specific electricity consumption does not correspond to a minimum of the LWC. The course of both curves has a similar behavior at a low recovery rate. Both curves decrease driven by the lower power requirement. In addition, the LWC falls also due to the saving of investment cost (intake unit and number of required pressure vessels). In contrast, at high recovery rate the LWC still continues to decrease while SEC increases again. Such a reduction is due to the fact that in the considered case capital cost is higher than energy cost. As a result, an increase of R implies a reduction of the required number of vessels. Such an effect over-compensates the impact of the higher SEC and of the higher electricity cost. More insight into the general behavior of SEC as function of R is presented in Annex 10.4.4.

A last question which may arise from the discussion of Figure 70 is why a higher recovery ratio than 42 % has not been selected, taking into account that R = 42 % does not correspond to the minimum LWC. The answer is that the implemented model does not consider the risk of fouling. In fact, the higher the recovery ratio, the higher the probability of occurrence of fouling. Such damages would increase the operation cost of the plant: more chemicals would be used in order to keep the membranes clean. In addition, more frequent cleaning procedures would be required, which would lead to a reduction of the plant availability. Finally, the lifetime of the membranes is likely to be reduced in the case of fouling, which increases the membrane replacement cost. The consideration of such issues would require additional and detailed techno-economic input data. Such data are not in the public domain and -in addition- they are very site-specific. Finally, a recovery ratio of 42 % has been used for the following analyses (8.4), which is a best-practice value for SWRO plants in the Red Sea region according to the available literature [Wilf 2007].

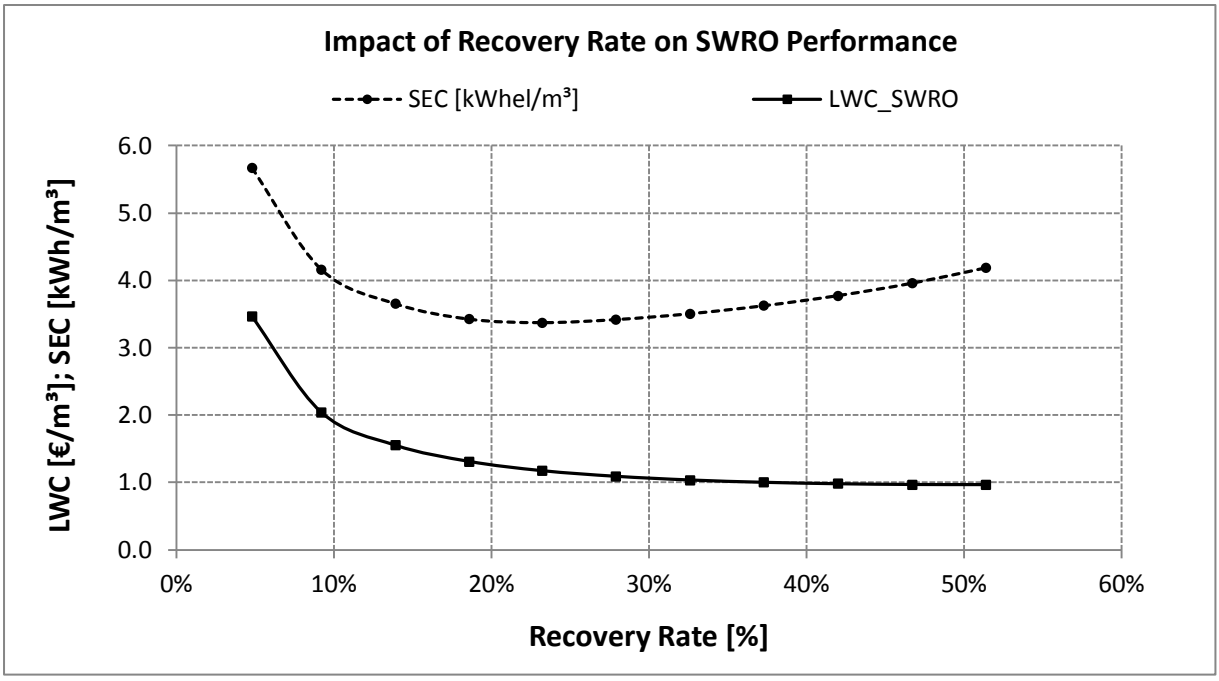

Figure 70: Specific electricity consumption and LWC of SWRO plant as function of recovery rate; Assumptions: conventional intake water pre-treatment; power supply: hybrid CSP, low fossil fuel price (8 $/bbl)

b) Impact of Fuel Cost

The specific energy consumption and the electricity price significantly impact on LWC of RO plants. Figure 71 shows the impact of the fossil fuel price escalation on the levelized electricity cost, assuming that the power supply is provided by a conventional steam turbine. Two fossil fuel prices have been analyzed: 8 $/bbl and 100 $/bbl. These prices correspond to an electricity price of 3.13 €c/kWh and 15.26 €c/kWh, respectively.

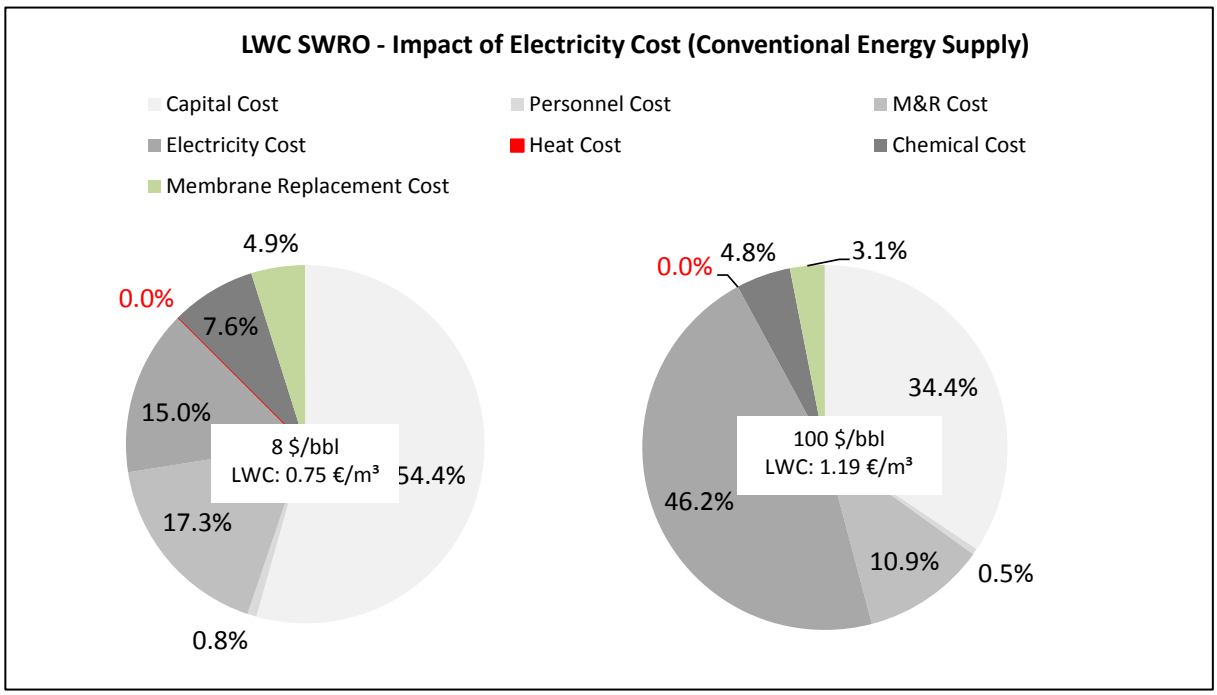

Figure 71: Impact of electricity price on the LWC of an RO plant; currency exchange rate: 1.33 [$/€]

In the low-price scenario, the LWC amounts to 0.75 €/m³. More than 54 % of this price is determined by the capital cost. The second largest cost item is maintenance and repair (approx. 17 %). Electricity cost and chemical cost follow with a share of 15 % and 7.6 %, respectively. The other two minor cost shares are membrane replacement cost and personnel.

An eventual increase of the price of fossil fuels reflects on both the LWC and on the relative weight of each item in the cost breakdown. Assuming a fossil fuel price of 100 $/bbl, the LWC increases to 1.19 €/m³, which is an increase of roughly 58 % in comparison to the previous case. In addition, the electricity cost becomes the major cost item. Its relative weight to LWC increases from 15.0 % to 46.2 %. As the other cost items are assumed to be constant in absolute terms, their relative weight is proportionally reduced. Accordingly, the capital cost becomes the second largest cost item with a relative weight of 34.4 %.

c) Comparison of MED and RO

This section compares the economic performances of MED and SWRO plants in Marsa Alam. The two reference desalination plants consist of a 12-stage MED and a SWRO plant using partial two-pass configuration. Both plants have a capacity of 30,000 m³/d.

The LWC breakdown of both plants is shown in Figure 72. Under these assumptions, MED provides higher LWC than SWRO. Such an LWC difference is lower than 0.1 €/m³. The largest cost contribution of both plants is the capital cost. For both MED and SWRO plants, the capital cost consists of approx. 40 % of the total specific water cost. In such a high-efficiency MED, the temperature difference between two consecutive stages is low (approx. 2.7 K), which has to be balanced by high heat transfer areas of the evaporator. However, such a layout allows minimizing the heat cost, which nevertheless accounts for 22.4 % of LWC. SWRO only uses electricity, so in this case the heat cost does not have any contribution. The third largest cost item of MED plants is maintenance and repair (19.6 %), which is approx. 7 % higher than in the case of RO.

Electricity cost is the major cost item for RO after capital cost. The SEC of RO is approximately 2.7 times higher than the SEC of MED. While in MED electricity is mainly needed to operate intake and feed water pumps, RO plants use electricity to increase the pressure of the feed, which despite the use of energy recovery systems (3.2.3) is a relatively energy consuming process. Two other minor cost items are personnel and -only in the case of RO- membrane replacement.

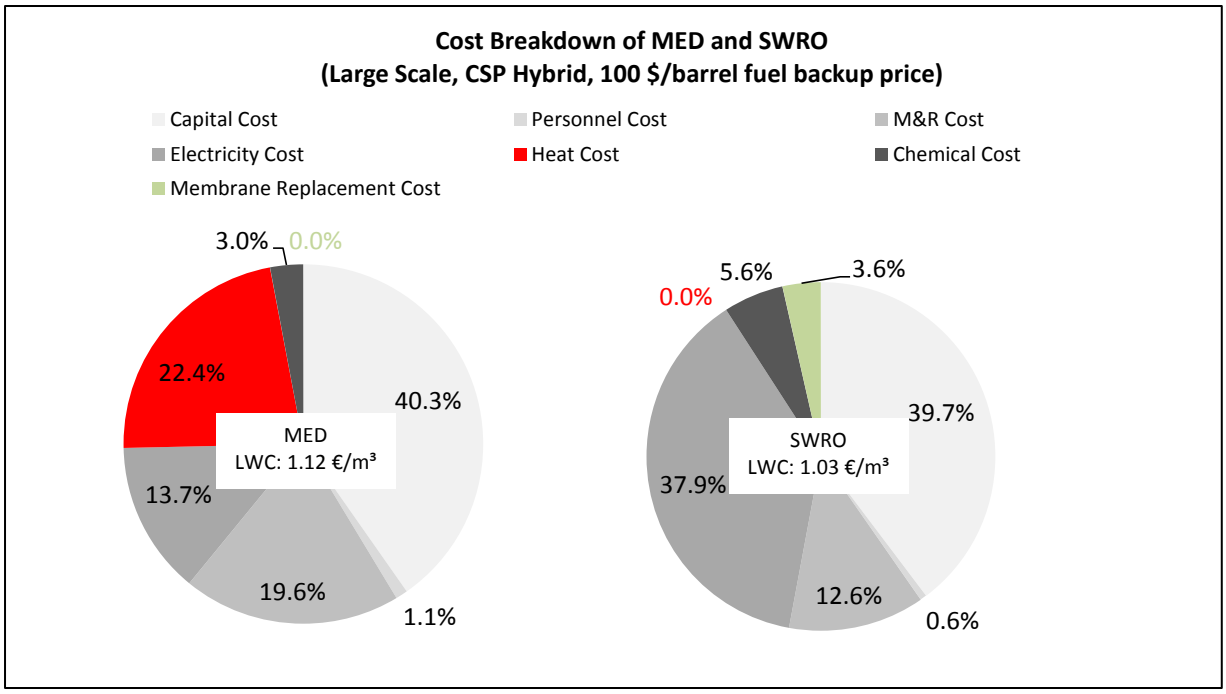

Figure 72: Breakdown of levelized water cost by plant components (MED and RO); Assumptions: 30,000 m³/d capacity, CSP hybrid power supply; high fossil fuel price (100 $/bbl)

8.4 Combined Systems for Water and Power Supply

The previous case studies focused on the separated analysis of renewable energy technologies (8.2) and desalination technologies (8.3). Sensitivity analysis on key technical design parameters as well as economic parameters have been shown and discussed. This section provides the analysis of combined electricity and water supply systems (Table 28).

System	Description	Objective
Power Supply Mix with SWRO (8.4.1)	Economic assessment of a large number of power supply mixes consisting of renewable and conventional technologies; water production by RO; Main assumptions: cost scenario 2020, high fossil fuel price, flexible CSP operation	Minimization of average annual supply cost for electricity and water produced by RO
Power Supply Mix with CSP-MED (8.4.2)	Economic assessment of a large number of power supply mixes consisting of renewable and conventional technologies; water production by MED; Main assumptions: cost scenario 2020, high fossil fuel price, base-load CSP operation	Minimization of average annual supply cost for electricity and water produced by MED
Final Assessment (8.4.3)	Comparison of results of 8.4.1 and 8.4.2 and impact of fossil fuel price on results	Overall minimization of average supply cost for electricity and water

Table 28: Overview of the third section of the case study (8.4): final assessment of combined systems for the production of electricity and desalinated water

The total cost of supply (capital and operation cost for electricity and water supply) have been calculated for a wide range of configurations. Further, optimal configurations have been identified as a function of the “renewable share” (i.e. the percentage of the annual

load covered by RE plants) and of the price of fossil fuels. Two main cases have been taken into account:

- An optimized electricity generation mix (consisting of renewable and fossil-based power plants) combined with an SWRO plant (8.4.1)
- An optimized electricity generation mix combined with a MED plant. In this case, the heat supply is provided by an hybrid CSP plant (8.4.2)

The final assessment (8.4.3) presents the impact of the variation of fossil fuel prices on the previous results.

8.4.1 Power Supply Mix with SWRO

The sensitivity analysis previously carried out in 8.3.3 has shown that the levelized water cost of SWRO plants depends on the cost of electricity. Under the assumption of conventional power supply and high price of fossil fuels, the energy cost may consist of up to roughly 50 % of the total LWC. The cost of an optimal power generation mix depends on a series of factors such as power demand profiles, available renewable resources as well as capital and operation cost (in particular fossil fuel cost), just to cite the most relevant of them. The following optimization has been carried out taking into account a large set of configurations, as summarized in Table 29.

Technology	Unit	Considered Range	
CSP solar multiple	-	1.5 - 3.5, step 0.5	
CSP TES capacity	h	8 - 14, step 2	
CSP turbine capacity	MW_{el}	0 / 50[1]	
PV	MW_{el}	0 / 35 / 70 / 150	
Wind	MW_{el}	0 / 25 / 75 / 100 / 175 / 250	
Cost Scenario		**CAPEX & OPEX**	**Fossil Fuel Price**
Cost scenario 1	-	Year 2014	8 $/bbl
Cost scenario 2		Year 2020	120 $/bbl

Table 29: Summary of analyzed configurations for the optimization of the power park; [1]load specification depends on the analyzed configuration

A fixed CSP turbine capacity has been selected: 50 MW, which is slightly below the annual minimal load. The solar multiple and the capacity of the thermal energy storages have been varied in a consistent range. In addition, a wide range of PV and wind power capacities has been taken into account. For each of the listed configurations, an annual yield simulation has been performed. The same boundary conditions have been assumed for each of the considered cases (main assumptions in 8.1). In particular, this implies that each configuration has to cover the same load. The model does not take into account the optimization of the commitment of each power plant at each time step. Rather, a simplified merit order has been assumed. Two scenarios have been taken as a basis for the economic assessment: the first one considers the current capital and operation cost for renewable and conventional power plants as well as strongly subsidized fossil fuel price (8 $/bbl). The second one

assumes capital cost projections for the year 2020 (i.e. consideration of the learning curve of renewable technologies) as well as the possible market price for fossil fuels (120 $/bbl). These two choices may be interpreted as two extreme scenarios. The analysis of the differences between the two cases will highlight the importance of renewable energy as a cost stabilizing factor in the power and -as a consequence- in the water supply.

The results of the power supply optimization are summarized in Figure 73. On the vertical axis the specific electricity supply cost is reported (weighted average of the LEC of each power plant). A first differentiation is made between configurations with CSP and without CSP. In addition, the supply costs obtained assuming low and high fossil fuel price are represented. The results are shown as a function of the renewable share, i.e. the portion of the annual load which is covered by renewable energy.

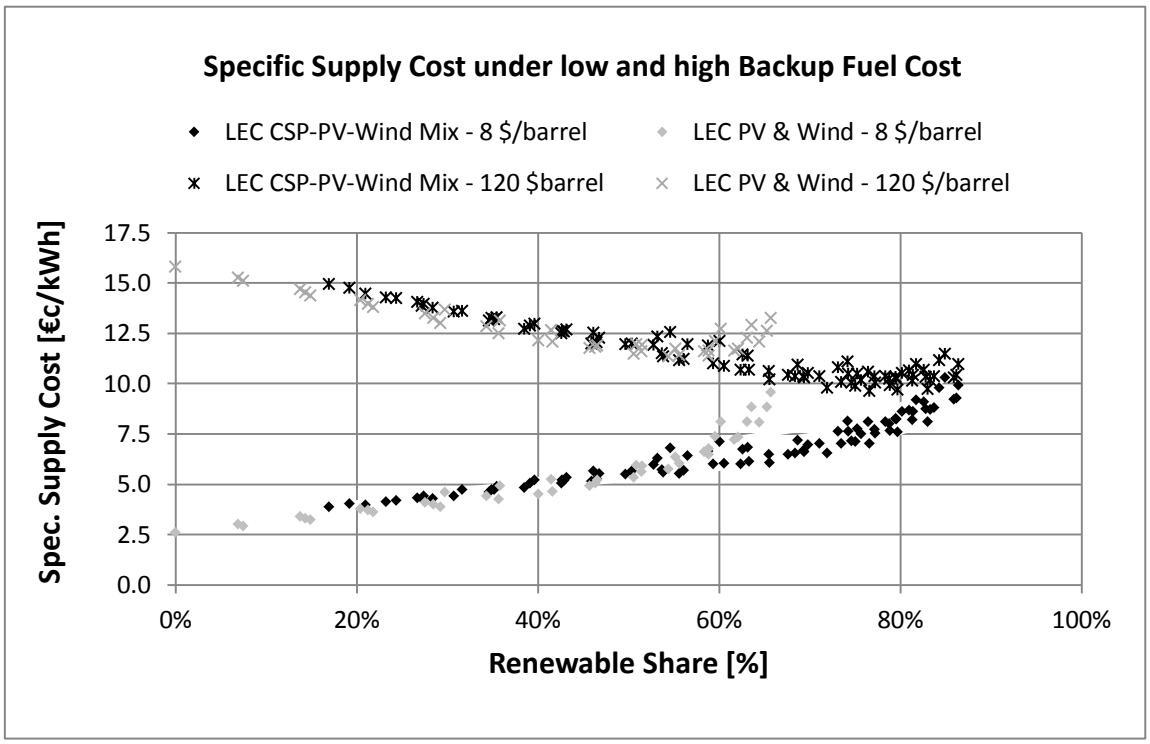

Figure 73: Impact of renewable share and backup fossil fuel price on cost of supply

A series of interesting considerations can be made:

- The assumption of subsidized fossil fuel prices does not make the introduction of renewable energy technologies appear very favorable from an economic point of view. Despite the fact that the analyzed site has excellent solar and wind resources at its disposal, renewable technologies are not able to compete with subsidized fuel prices. Nevertheless, such a conclusion does not take into account a number of important considerations. First, subsidies have to be paid by someone. This may happen in the form of direct state subsidies, which is the case for fossil fuel importing countries. Alternatively, in fossil fuel exporting countries such subsidies correspond to the lost opportunity to sell the fuel on the market at non-subsidized prices. To this

adds the impact of environmental costs, which have not been quantified in this case study.

- The higher the level of subsidies, the higher the risk of dramatic electricity cost increase due the eventual inability to further pay such subsidies. Assuming a 100 % conventional electricity supply, an increase of the electricity cost of up to approx. 500 % could be expected. For this reason, specific efforts should be initiated as soon as possible in order to avoid or at least reduce the risk of severe shocks in the future.
- Moving in due time towards an electricity supply system based on a mix of renewable and conventional technologies is not only convenient in the case of high fossil fuel price, but it also includes strategic advantages such as the reduction of the dependence on scarce resources and the stability of the supply cost. Under the assumption of high fossil fuel prices (120 $/bbl), the minimum of the supply cost roughly corresponds to a renewable share between 70 % and 80 %. Once renewable energy technologies are in operation, their annual yield and their annual cost is known with a low degree of uncertainty, related to the year-to-year variability of solar and wind resources. The impact of a possible fossil fuel price escalation is much lower than in a fossil-based power supply, as the consumption of fossil fuels is minimized. The supply cost gap between low and high fossil fuel prices has its maximum at the 100 % conventional case and tends to close at a renewable share above 80 %.
- As long as the renewable share is below approx. 50 %, the lowest costs of supply are provided by a mix of conventional and intermittent renewable technologies, i.e. PV and wind power (Table 30). Within this range, power supply mixes which include CSP are slightly more expensive, due to the fact that the LEC of PV and wind is lower than the LEC of CSP. The backup is provided by conventional power plants. The figures change at renewable shares higher than 50 %. The reason is simple: the higher the renewable share, the higher the required installed capacity of PV and wind power. However, at the same time power curtailments increase, as electricity generation surpluses become more frequent. As the simplified model does not consider the option of transporting the surpluses over long distances, such surpluses finally result in increasing cost of supply. This can be observed in the increase of the grey marks in the middle of Figure 73.
- Renewable shares higher than 50 % can be achieved at a competitive cost and without excessive power curtailments by the introduction of options which increment the flexibility of the power supply. Several measures may be considered such as storages, extension of the electricity grid (long-distance transport) and load-management. A detailed consideration of all of these options would be beyond the scope of this thesis. However, the introduction of CSP with integrated thermal energy storage is demonstrated to be an excellent option to complement the analyzed power generation mix. The optimal power park at high renewable shares (e.g. last case in Table 30) is a mix of all available renewable technologies (PV, wind power and CSP) and fossil backup. In particular, electricity generation by relatively cheap but

variable renewable power plants is balanced by the power generation on-demand, which is provided by the CSP power plant operated in hybrid mode. Figure 74 presents the typical power generation patterns of a winter week in Marsa Alam. Such a power park corresponds to the cost-optimal mix under the assumption of a high fossil fuel price (120 $/bbl). The power park consists of a 50 MW CSP power plant with high solar multiple (3.0) and large thermal energy storage (14 full load hours). In addition, the installed PV and wind power capacity amounts to 70 MW_p and 100 MW, respectively. In the sample week the wind power generation is relatively high. Nevertheless, the power curtailments are almost negligible (shaded areas above the electricity demand). This is due to the fact that the CSP power plant can be flexibly operated at a minimum load during periods of high wind or PV power generation. The solar field of the CSP plant is -however- in operation and the collected heat is almost completely stored in the TES (red dashed line). At times of low or absent power generation from intermittent renewable technologies, the TES is discharged. Whenever the storage is empty, operation is guaranteed by the integrated backup boiler, which makes use of fossil fuel. In contrast, during summer (Figure 75) the average power demand is approx. 50 % higher than in winter. At that time, the CSP power plant is able to deliver base load operation without any fossil fuel consumption.

- A final remark on Figure 73 should be made with regard to the increase of the cost of supply above an 80 % renewable share. In fact, after a minimum at approx. 77 % renewable share, the cost of supply increases again, driven by the increased need for redundant infrastructures (e.g. storages and over-sized plants) and the rising amount of power curtailments due to the intermittent nature of renewable sources. This underlines the fact that very high renewable shares will be related to high efforts. In addition, new and cost-efficient solutions for long-term energy storages (thermal, electrical and chemical) will be required to achieve this target.

Renewable Share	**%**	**0.0%**	**21.8%**	**41.6%**	**62.4%**	**76.6%**
Cost scenario 1	€c/kWh	2.61	3.62	4.65	6.00	7.03
Cost scenario 2	€c/kWh	15.82	13.81	12.08	10.67	9.62
CSP turbine capacity	MW	0.0	0.0	0.0	50.0	50.0
CSP SM	-	0.0	0.0	0.0	2.0	3.0
CSP TES capacity	h	0.0	0.0	0.0	8.0	14.0
PV	MW	0.0	30.0	60.0	35.0	70.0
Wind	MW	0.0	50.0	100.0	100.0	100.0
Fossil backup	MW	154.8	154.8	154.8	104.8	104.8

Table 30: Selection of cost optimal power park configurations as function of the renewable share (with reference to Figure 73)

Table 31 summarizes the main technical and economic results of the optimized SWRO plant. The plant nominal capacity is slightly higher than the scheduled 30,000 m³/d (32,600 m³/d) in order to cope with the planned off-line periods due to cleaning, maintenance or

unforeseen outages. The average plant availability is assumed to be 92.0 %. Accordingly, the SWRO plant operates at full load for more than 8,000 h/y and produces roughly 11 Mio. m^3/y of desalinated water. The specific electricity demand amounts to 3.74 kWh_{el}/m^3, which corresponds to 4.9 MW.

SWRO Parameter	Unit	Value
Plant nominal capacity	m^3/d	32,600
Average availability	%	92.0%
Plant yearly output	Mm^3/y	10.9
Specific electricity demand (incl. intake)	kWh_{el}/m^3	3.74
Electricity demand	MW_{el}	4.90
Annual electricity consumption	GWh_{el}/y	39.0
LWC (8 $/bbl – 120 $/bbl)	€/m^3	0.89 - 0.98

Table 31: Main results of the optimized SWRO plant

The integration of the power park with the desalination plant is straightforward, as RO is considered an additional electricity demand. In contrast to MED, RO does not put any further boundary condition on the layout of the power plants. The total electricity demand (i.e. the black line in Figure 74 and Figure 75) consists of the sum of the hourly load curve and the 4.9 MW for the desalination plant.

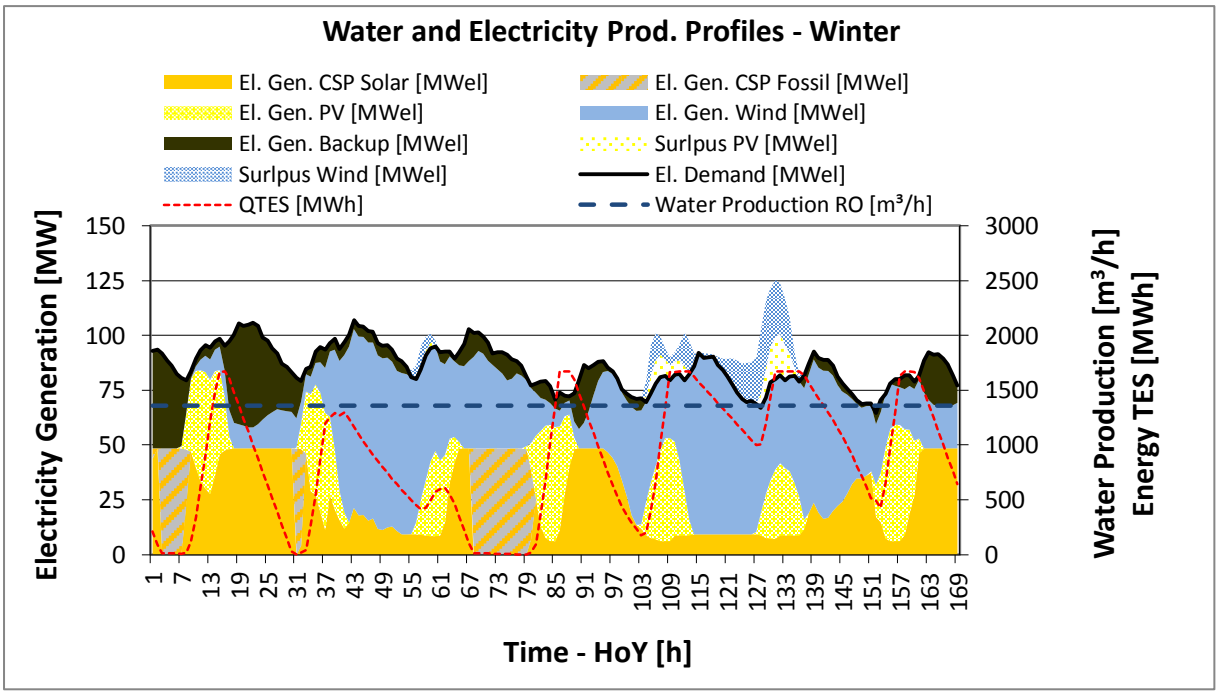

Figure 74: Exemplary electricity and water production profiles in the first week of the year (optimal configuration for 30,000 m^3/d SWRO; fossil fuel price = 120 $/bbl)

The annual electricity consumption of the SWRO plant is 39 GWh, which represents 4.3 % of the total demand of Marsa Alam. Assuming an electricity price of 9.62 €c/kWh (2020 scenario with a high fossil fuel price), the electricity cost of the analyzed SWRO plant amounts to 0.34 €/m^3. The final LWC of the base case reverse osmosis plant is 0.98 €/m^3.

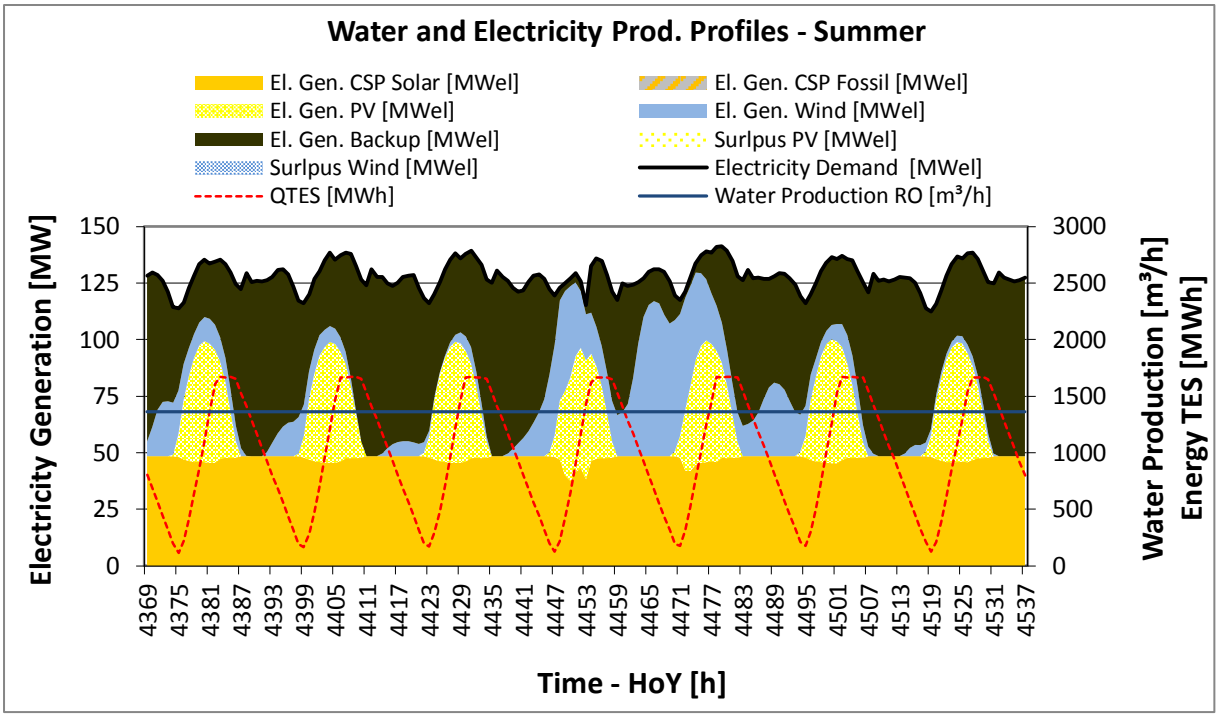

Figure 75: Exemplary electricity and water production profiles in a summer week (optimal configuration for 30,000 m³/d SWRO; fossil fuel price = 120 $/bbl)

8.4.2 Power Supply Mix with CSP-MED

Most of the considerations exposed above remain true when considering the integration of an MED plant into an electricity supply system. In this case an optimum power park also exists, which minimizes the cost of the energy supply. However, in contrast to the previous case, both electricity and heat have to be continuously provided to the desalination plant. The required heat supply introduces a further boundary condition, i.e. in this case the CSP power plant cannot operate flexibly as in the SWRO case. Rather, it has to be operated as a base load power plant. It has already been shown that -due to the thermal energy storage and to the integrated fossil fired backup- this is technically and economically feasible.

The design of the MED plant and of its heat supply is closely interrelated and requires some explanation. The main design parameters are summarized in the first part of Table 32. Given an average plant availability of 92 %, the nominal plant capacity has to be over-sized (32,600 m³/d). The continuous drinking water supply is guaranteed also during scheduled cleaning periods or short-time outages due to this over-capacity. A 1-day capacity drinking water storage serves to bridge these off-line periods.

A series of calculations has been performed over a number of steam pressure levels and a number of stages, in order to minimize the specific cost of power supply. The pressure of the heating steam has been varied between 0.3 bar and 0.37 bar, and the number of stages between 12 and 14. The selected ranges result from the discussion of 8.3.1. Under the assumption of a high fossil fuel price, a minimum has been found for a steam pressure of 0.35 bar and 13 stages. This corresponds to a GOR of approx. 11.5 and to a required heating

steam mass flow of 34.5 kg/s. Finally, the capacity of the CSP turbine has been scaled in order to fulfil these conditions. The resulting turbine capacity is approx. 50 MW, which is below the annual minimum load of approx. 55 MW.

Similarly to the SWRO, the annual water production amounts to 10.9 Mio. m^3/d (Table 32). The specific electricity consumption of the MED process is 1.42 kWh/m^3. This corresponds to a consumption of barely 2 MW. The annual electricity consumption is 14.8 GWh, which is approx. one third of the electrical consumption of the SWRO. In addition, the specific heat consumption of the MED is 64.3 kWh_{th}/m^3.

Figure 76 and Figure 77 show the power generation patterns of the optimized power park with MED desalination in a typical winter and summer week, respectively. The 2020 cost scenario and a high fossil fuel price (120 $/bbl) have been assumed.

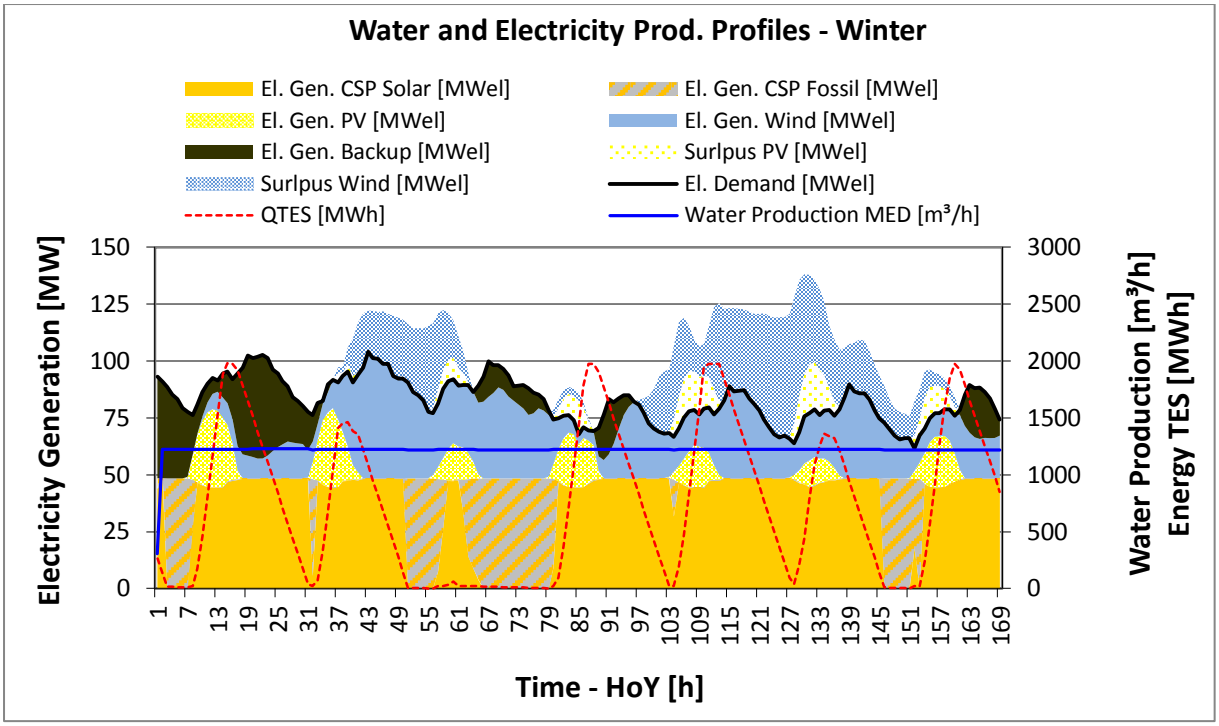

Figure 76: Exemplary electricity and water production profiles in the first week of the year (optimal configuration for 30,000 m^3/d MED; fossil fuel price = 120 $/bbl)

It can be observed that -similarly to the SWRO case- the optimal power supply consists of a mix of all available renewable and conventional technologies.

However, the optimal capacity of each of the renewable power plants differs from the SWRO case. A comparative analysis of such differences as well as the detailed economic assessment of the two cases is provided in 8.4.3.

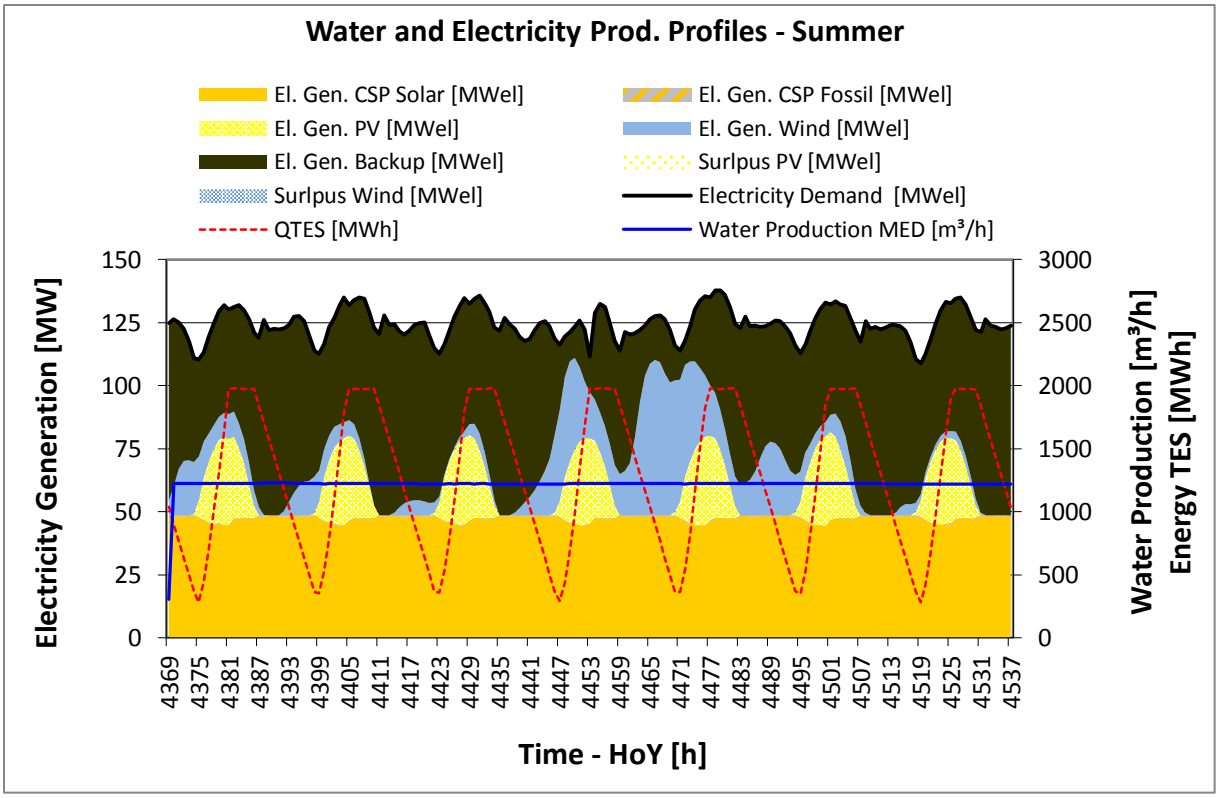

Figure 77: Exemplary electricity and water production profiles in a summer week of the year (optimal configuration for 30,000 m³/d MED; fossil fuel price = 120 $/bbl)

MED Parameter	Unit	Value
Plant net capacity	m³/d	30,000
Average availability	%	92.0%
Plant nominal capacity	m³/d	32,600
GOR	-	11.5
Required steam mass flow	kg/s	34.5
Required turbine capacity	MW_{el}	50.0
Plant yearly output	Mm³/y	10.9
Specific electricity demand (incl. intake)	kWh_{el}/m^3	1.42
Electricity demand	MW_{el}	1.95
Annual electricity consumption	GWh_{el}/y	14.8
Specific heat demand	kWh_{th}/m^3	64.3

Table 32: Main results of the optimized MED plant

8.4.3 Final Assessment

This section summarizes the results of the techno-economic analysis carried out in 8.4.1 and 8.4.2 for SWRO and MED, respectively. Table 33 presents the results of the optimized power mix in the two considered cases. In the SWRO case the solar multiple and the storage capacity of the CSP plant are slightly smaller than in the MED case, while the capacity of PV and wind power is higher. These differences can be mainly explained by the different boundary conditions on the CSP plant. It has already been discussed that in the SWRO case

the CSP plant is able to act as a balancing renewable power plant. This way the electricity generation of the CSP turbine can be reduced to the minimum load whenever the residual load, i.e. the difference between the current load and the sum of the PV and wind power generation, falls below the nominal capacity of the CSP turbine (50 MW). This allows minimizing the annual power curtailments (1.7 % on annual basis) as well as maximizing the renewable share (76.6 %). The power curtailments are more frequent during winter, due to the relatively low demand. In contrast, in summer the electricity demand is higher and power cut-offs are negligible (Figure 75 and Figure 77).

In the MED case, the CSP plant is also used for the continuous heat supply to the MED. This adds rigidity to the power supply system. In fact, the CSP plant cannot balance the fluctuations of the intermittent renewable technologies. As a consequence, the residual load is systematically lower and leads to more frequent power curtailments (7.1 % on annual basis). This also implies a demanding optimization procedure, which includes a compromise between the minimization of the power curtailments and the minimization of the fossil fuel consumption. As a result, the optimal power park configuration consists of a CSP plant with a very high solar multiple (3.5), which maximize the solar share of the CSP plant, and slightly lower PV and wind power capacities in comparison to the SWRO case. The total annual electricity demand is lower in the MED case, due to the fact that the SWRO consumes more electricity than the MED (899.3 GWh/y vs. 873.2 GWh/y). The average levelized electricity cost is similar in both cases (SWRO: 9.62 €c/kWh, MED: 9.92 €c/kWh) under the assumption of a high fossil fuel price (120 $/bbl).

Configuration	Unit	Mix-SWRO	Mix-CSP-MED
CSP turbine capacity	MW	50.0	50.0
CSP SM	-	3.0	3.4
CSP TES capacity	h	14.0	15.0
PV	MW	70.0	45.0
Wind	MW	100.0	90.0
Fossil backup	MW	104.8	101.5
Renewable share	%	76.6	73.8
Electricity curtailment	%/annual demand	1.7	7.1
Annual demand	GWh/y	899.3	873.2
Specific cost of supply (8 $/bbl – 120 $/bbl)	€c/kWh	7.03 - 9.62	6.89 - 9.92
LWC (8 $/bbl – 120 $/bbl)	€/m³	0.89 - 0.98	0.99 - 1.06
Cost of supply (8 $/bbl – 120 $/bbl)	Mio. €/y	69.7 - 93.0	69.0 - 95.8

Table 33: Comparison of power plant configurations and key economic results of SWRO and MED power mix; Assumption: the power park is optimized for a fossil fuel price of 120 $/bbl

Finally, the LWC of the SWRO plant is lower than the LWC of the MED. However, such a difference is low (SWRO: 0.98 €/m³, MED: 1.06 €/m³) and should be considered critically due to the relative uncertainty of the cost assessment. For example, it has been discussed that the price of metals plays a significant role in the definition of the CAPEX of the MED

evaporator. Such prices have been prone to dramatic fluctuations in the few last years (8.3.1).

Finally, Figure 78 shows a comparison of the average power and water supply cost. Three cases have been considered, i.e. the two optimized SWRO and MED cases as well as a 100 % conventional case. In addition, two prices of the fossil fuels have been taken into account, i.e. 8 $/bbl and 120 $/bbl. The bars show the absolute value of the supply cost as well as its breakdown into each of the main cost items (CSP, PV, wind power, fossil backup and desalination). Similarly to the results reported in Figure 73, under the assumption of low fossil price it seems to be no economic benefit in choosing renewable energies. However, it should be stressed that behind such a low fossil fuel price subsidies are hidden, which have to be paid even if they do not appear explicitly in these calculations.

The three bars on the right part of Figure 78 highlight the impact of the possible price escalation of fossil fuels on the cost of supply. In the case RE power plants are included in the power supply mix (fourth and fifth bar), the escalation of the average annual supply cost is moderate in comparison to the scenario with a low fossil fuel cost (first and second bar). In contrast, the 100 % conventional case (third and sixth bar) is prone to dramatic cost escalation of almost 400 %. Under the cost scenario in the year 2020, the break even between the annual supply cost of the RO-fossil case and the annual supply cost in the case of RO-renewable mix is approx. 50 US$/bbl, which corresponds to an average energy supply cost of 22.4 €/MWh.

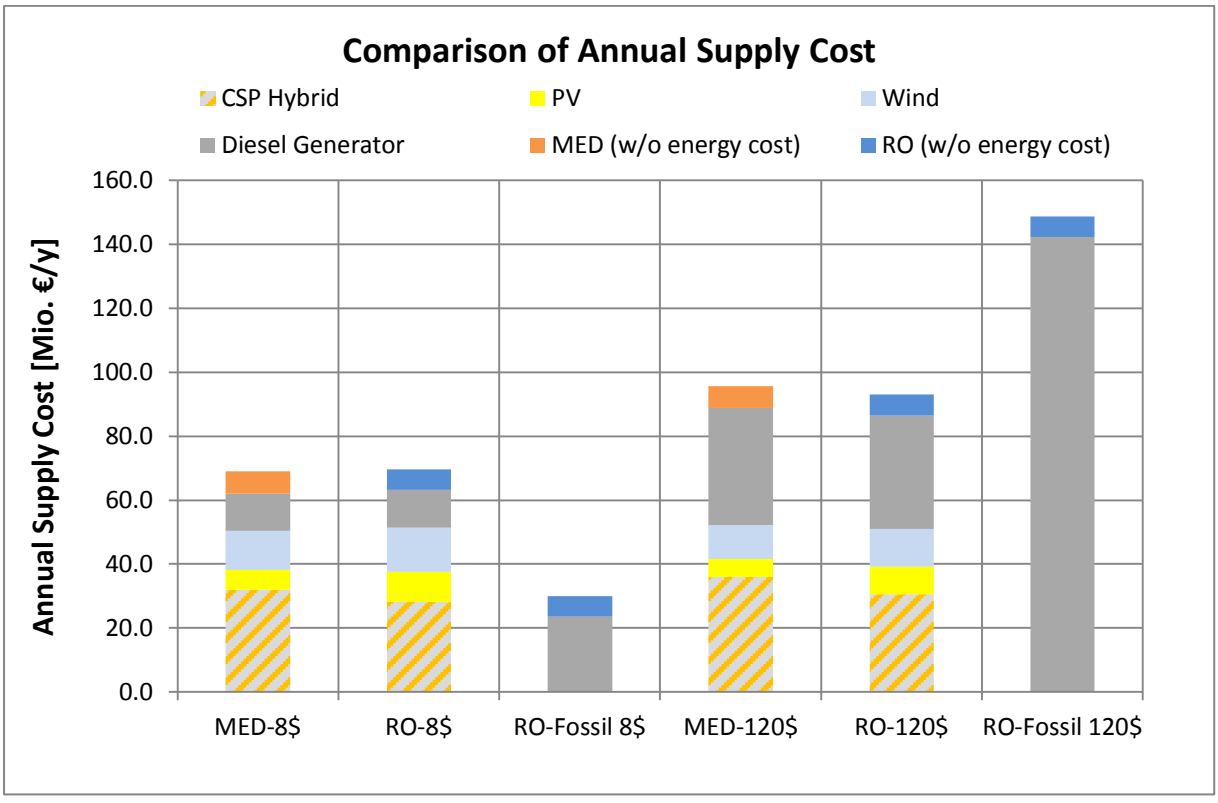

Figure 78: Comparison of annual average supply cost (electricity and water); Technical assumptions as described in Table 33; cost scenario 2020

The difference in the annual supply cost between the MED and the SWRO case are approx. 2.8 Mio. €/y. Such a difference is due only to a minimum extent to the higher MED cost in comparison to the SWRO. In fact, the MED presents annual costs (without energy cost according to Eq. 7.10) which are only marginally higher than the SWRO cost (6.88 Mio. €/y vs. 6.46 Mio. €/y). The main cost difference is due to the lower renewable share in the case of the MED (73.8 % vs 76.6 %) and to the consequently higher fossil fuel cost. Also the CSP capital cost is higher in the case of the MED; this is related to the larger solar multiple and to the slightly lower turbine conversion efficiency. The supply cost of the MED case could be further reduced by increasing the flexibility of the CSP plant. This would allow increasing the installed capacity of PV and wind power plants as well as reducing the consumption of fossil fuels. The continuous heat supply to the MED plant should be guaranteed by the introduction of a low-temperature energy storage.

9 Conclusions and Outlook

A unique and flexible tool for the integrated simulation and evaluation of renewable power plants and seawater desalination systems has been implemented within this doctoral thesis based on the commercially available tool INSEL and on own developments. The work carried out involved three main steps:

1. New technical models have been implemented in INSEL. Such models include two desalination technologies, i.e. MED and RO. A large number of parameters such as intake layout, pre-treatment type and process design values can be flexibly adapted. In addition, CSP models have been integrated in INSEL. Such models include line focusing systems (parabolic trough and linear Fresnel) and point focusing systems (central receiver). Optical and geometrical efficiency, heat balances on receivers and plant layout have been taken into account. In addition, transient effects are considered by means of a simplified approach. The power block model consists of a detailed thermodynamic model which takes into account several cooling technologies such as evaporative cooling and dry cooling.
2. The key results provided by the annual yield simulations with INSEL have been used as inputs for the economic model. This model has been developed in Excel and mainly consists of the evaluation of the investment and operation cost of each plant component. The calculation of levelized electricity cost (LEC) and levelized water cost (LWC) has been performed. In addition, the average annual cost for power and water supply turned out to be a relevant objective function for the evaluation of multi-purpose systems.
3. The potentialities of the INSEL models and of the economic model are exemplarily shown within a number of case studies. The analysis has been carried out for Marsa Alam, a remote touristic location in the South-East of Egypt. The analysis aimed at the identification and the evaluation of key parameters which influence technical

performance and economics of utility-scale renewable desalination plants. The analyses consider local requirements (electricity, water), available resources (solar irradiation, wind speed, air temperature, seawater quality) as well as economic parameters (investment cost, back-up fuel cost etc.).

The main findings of the case studies are:

- CSP: The comparison among several CSP technologies and plant configurations shows that the molten-salt-based central receiver technology with a 14-16 hours thermal storage performs lowest levelized electricity cost. The main advantages of CR are high efficiency and relatively low capital cost of the thermal energy storage. However, the LEC of all three considered CSP technologies is in a quite narrow range between 12.5 €c/kWh (PT) and 10.0 €c/kWh (CR). As local factors like DNI potential, presence of aerosols in the atmosphere as well as capital and operation cost impact the technical and economic results, case-by-case assessment remains necessary.
- MED: The optimal number of stages depends on several parameters. A trade-off exists between heat cost and intake cost on the one hand, and evaporator cost on the other hand. In conventional MED plants, the optimal number of effects ranges between 6 and 8 stages. However, if the cost of the heat supply is high (e.g. high fossil fuel price, or CSP as heat source) the optimum number of effects is 13 - 14. Due to the relatively high quality of the required heating steam, MED-TVC is cost-competitive only in the case low-cost heat is available (e.g. waste heat, low fuel cost).
- RO: In the last few years RO has gained a dominant position in the global desalination market. This success is due to low capital cost, improvements in membranes (salt rejection rate, life time) and the reduction of specific energy consumption (energy recovery systems). Membrane fouling can be a challenging issue for RO plants. Experience has shown that the selection of a too high recovery ratio increases the risk of fouling. Such damage would increase the operation cost of the plant and reduce the average life time of the membranes.
- Electricity supply systems: Renewable shares higher than 50 % can be achieved at competitive cost and without excessive power curtailments by the introduction of options which increase the flexibility of the power supply. The introduction of CSP with integrated thermal energy storage demonstrates to be an excellent option to complement a power generation mix consisting of intermittent renewable energy technologies and fossil backup. The optimal power plant fleet at high renewable shares is a mix of conventional and all available renewable technologies. In particular, the electricity generation by relatively cheap but variable renewable power plants is balanced by the slightly more expensive but dispatchable power provided by CSP. At even higher renewable shares (e.g. higher than 80 %), the cost of supply increases sharply, which is driven by the increased need for additional infrastructures and rising power curtailments due to the intermittent nature of renewable sources.

- Combined power and desalination systems: In the SWRO case the CSP plant is electricity-driven. In this way, the electricity generation of the CSP turbine can be reduced to the minimum load whenever the residual load is low. This allows minimizing the annual power curtailments and reflects on the lower LWC (0.98 €/m³) and lower cost of supply of the SWRO case. In contrast, in the MED case the CSP plant is heat-driven. This adds rigidity to the power supply system. The continuous heat supply to the MED plant may be alternatively guaranteed by the introduction of a low-temperature energy storage.

In conclusion, it has been shown that renewable desalination is technically and economically feasible as long as fair economic boundary conditions are set for the comparison with conventional power supply systems. Reverse osmosis provides approx. 10 % lower LWC than MED. Such a result is confirmed by a number of sensitivity analyses. However, such a conclusion cannot be generalized for other locations. A final decision between SWRO and MED should be taken case-by-case. The reason is that the water production cost of RO plants significantly depends on seawater quality and on the type of pre-treatment. In the case of low-quality feed water (e.g. Arabic Gulf), RO plants would require additional pre-treatment steps, which results to a LWC increase of approx. 20 %. The implemented INSEL models represent an important milestone for the DLR Department of System Analysis. System optimization models such as REMix will profit from the integration with INSEL in terms of reliability and quality of results. As an example, the performance of single plants in REMix may be validated. In addition, detailed hourly yields of CSP solar fields calculated with INSEL may be used in REMix to improve the accuracy of the results. At the same time, the development of such a flexible tool constitutes an important pre-requisite for future research work. The INSEL models developed within the framework of this thesis can be flexibly used within a wide range of applications in the field of renewable energy and sustainable seawater desalination. These topics include the assessment of enhanced dry-cooling for CSP. Technically available approaches such as hybrid dry-wet cooling as well as optimized condenser design and plant dispatch still need to be systematically evaluated and compared. In addition, the reduction of the environmental impact of seawater desalination plants may also represent a focus of the future work. Innovative concepts, which allow minimizing the impact of infrastructures for feedwater intake and brine discharge on the marine ecosystem as well as reducing the addition of chemicals to the feedwater, are needed. Key aspects will be the substitution of chemicals by natural or membrane-based filters (whose additional energy requirement will be covered by renewable energy), optimized plant design and operation strategies, hybrid desalination configurations and adequate material selection. New INSEL models will be implemented to expand the range of analysis to further applications such as the assessment of different paths for the production of liquid synthetic fuels for the long-distance transport sector (e.g. diesel and kerosene). The use of renewable energy and the system integration of a number of technical processes such as seawater desalination, electrolysis, carbon dioxide capture from the atmosphere and Fischer-Tropsch synthesis will enable the production of carbon-neutral fuels.

10 Annex

10.1 Desalination

Classification of Desalination Processes

Desalination processes can be classified according to the following criteria (Table 34):

- modality of salt separation (water extraction, salt extraction)
- separation process (thermal, membrane)
- used energy (mechanical, thermal, electrical)

The first criterion indicates if salt is removed from the water main stream or vice versa. Salt separation processes seem to be more convenient than water separation processes at first glance, as salt content of seawater typically does not exceed 4.5 %. However, several technical constrains have so far limited the development of salt separation processes, concluding in the preference of water separation technologies. Water extraction technologies may involve water phase change (evaporation or solidification). Alternatively, water extraction occurs without phase change by means of salt-rejecting membranes. In both cases energy has to be provided, as water separation does not happen spontaneously. In the beginning desalination plants were based on thermal processes. An overview on the historical development of desalination can be found in [El-Dessouky 2002].

Desalination Process	Separation Process	Used Energy	Separation Modality
Multi-Stage Flash	Thermal	Thermal	Water extraction
Multi-Effect Distillation	Thermal	Thermal	Water extraction
Reverse Osmosis	Membrane	Mechanical	Water extraction
Mechanical Vapor Compression	Thermal	Mechanical	Water extraction
Multi-Effect Humidification	Thermal	Thermal	Water extraction
Membrane Distillation	Thermal/Membrane	Thermal	Water extraction
Solar Stills	Thermal	Thermal	Water extraction
Electro Dialysis	Membrane	Electrical	Salt extraction

Table 34: Classification of desalination technologies - Adapted from [Cipollina 2009]

10.1.1 Preliminary Comparison of Desalination Technologies

Comparison of desalination technologies is a rather complex topic. Therefore, a number of technical and economic issues should be taken into account, such as plant component susceptibility to water quality, use of chemicals, energy requirements, quality of drink water, reliability, simplicity of operation, investment and maintenance costs, just to cite the most relevant of them. Table 35 presents an overview of preliminary comparison of the three main commercial desalination technologies, i.e. RO, MSF and MED.

Desalination Process	Advantages	Disadvantages
RO	For BW or SW applications Relatively low energy consumption Modular layout; Lower CAPEX than thermal systems; Lower feed water consumption than MED/MSF	Dependency on pre-treatment effectiveness More complex operation than MED Lower product water quality (ca. 200 – 500 ppm for single pass units) Higher requirements for Boron removal
MED	Also for high saline/low-quality water High product water quality (< 20 ppm) Reliability / long operation periods without cleaning Higher efficiency than MSF Low spec. electrical consumption	High investment cost (dependency on metal price fluctuations) Higher feed water consumption than RO
MSF	Also for high saline/low-quality water High product water quality (< 20 ppm) Reliability / simplicity of operation Long operation experience Large units (up to 90,000 m^3/day)	High investment cost (dependency on metal price fluctuations) Elevate feed water consumption High energy consumption

Table 35: Preliminary comparison of main desalination processes [DesalData 2011]

Comparing different processes with regard to energy consumption, a method is required which allows comparing energy forms with different value such as heat and electricity. This also applies to desalination processes. It is assumed that the energy required by different desalination technologies is supplied by steam turbines, without further specification of the used type of fuel (fossil or renewable). Alternatively, heat may be directly supplied by a boiler without any electricity generation. In dual purpose plants the question has to be answered, which cost share should be allocated for the heat. This problem is solved using the so-called “reference-cycle method”, which is based on the lost electricity generation in the dual-purpose case in comparison to a reference case (electricity generation only) [Gebel 2008], [Greffrath 2009]. The energy requirements of the main desalination processes have been calculated for typical configurations. The results are shown in Figure 79.

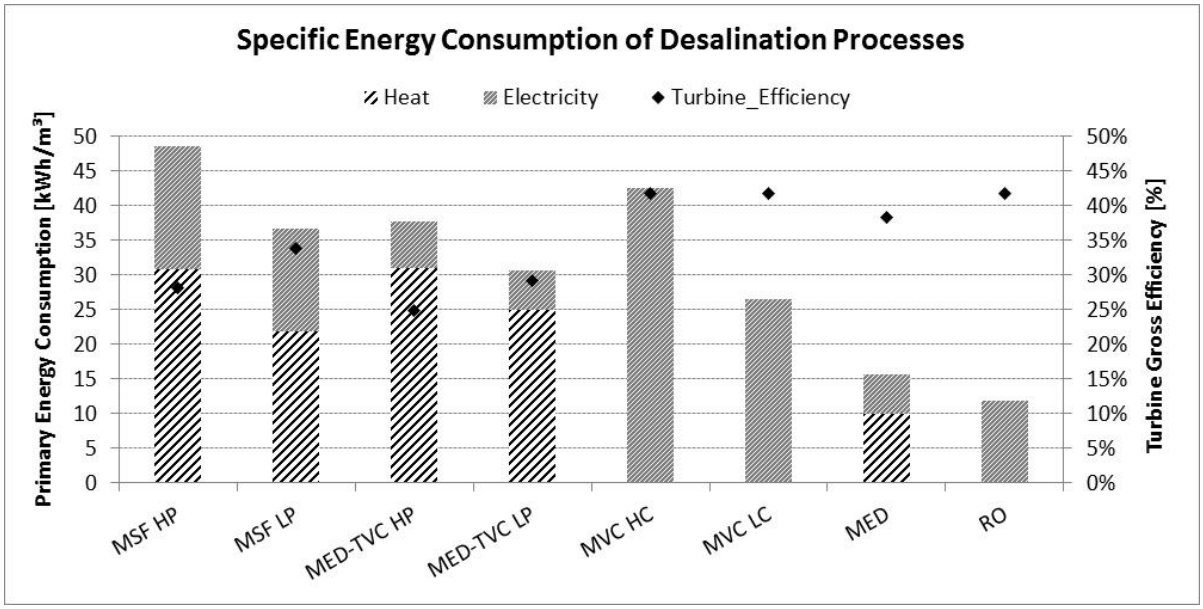

Figure 79: Specific energy consumption (as defined in [Gebel 2008]) of main desalination processes – Adapted from [Greffrath 2009]; HC = high electrical consumption, LC = low electrical consumption

In addition, the energy consumption of thermal desalination plants significantly depends on the number of stages. In particular, the higher the number of stages is, the lower is the specific energy consumption (Figure 80). This is because plants with a high number of stages make use of motive steam more efficiently, as the vapor's heat of evaporation/condensation can be "recycled" at each new stage. However, the installation of each additional stage causes investment cost, so that an optimum number of stages can be identified under given economic assumptions.

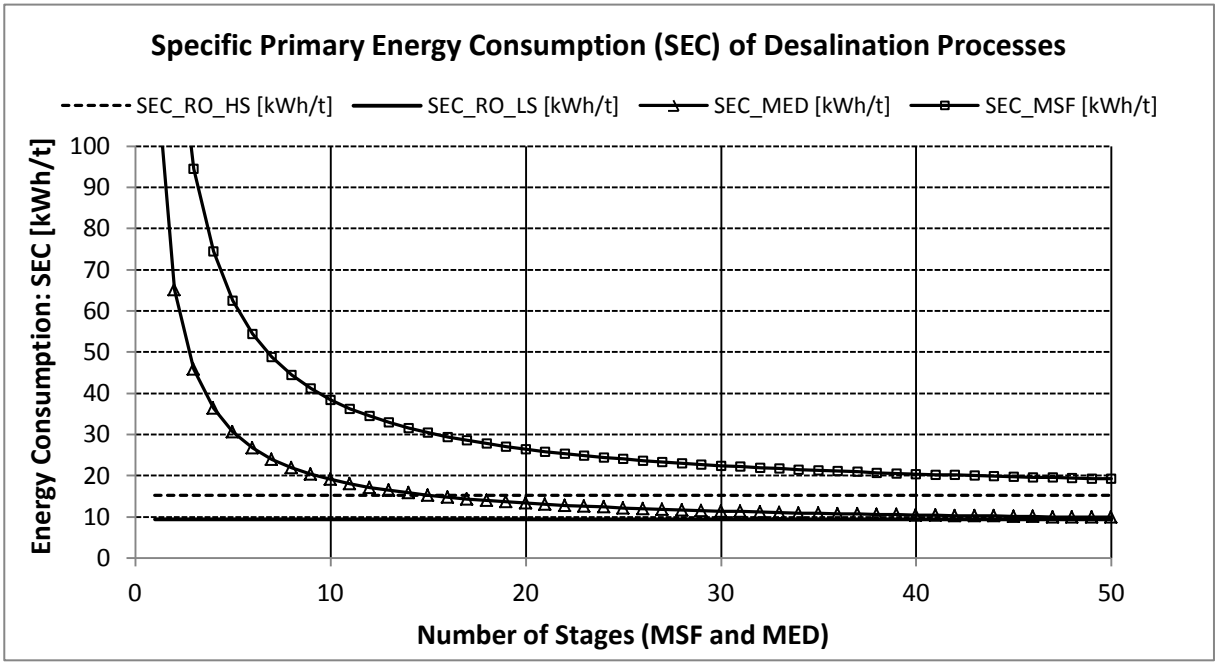

Figure 80: Specific primary energy consumption of thermal desalination processes (dual purpose) compared with RO; HS = high salinity (45,000 ppm); LS = low salinity (30,000 ppm) – Adapted from [Gebel 2008]

Following equations have been used for the generation of Figure 79 and Figure 80 [Gebel 2008].

For MSF:

$$SEC_{MSF} = \left[\frac{\Delta h_v}{N} \cdot \left(1 + N \cdot \frac{\Delta T_{TTD} + \Delta T_{BPE} + \Delta T_{Losses}}{\Delta T_0}\right)\right] \cdot \frac{\eta_T \cdot \eta_{C,HS}}{\eta_{PP}} + \frac{sP_{el\_MSF}}{\eta_{PP}} \quad \text{Eq. 10.1}$$

For MED:

$$SEC_{MED} = \left[\frac{\Delta h_v}{N} + \frac{CF}{CF - 1} \cdot c_p \cdot \left(\Delta T_{Stage} + \Delta T_{TTD} + \Delta T_{BPE}\right)\right] \cdot \frac{\eta_T \cdot \eta_{C,HS}}{\eta_{PP}} + \frac{sP_{el\_MED}}{\eta_{PP}} \quad \text{Eq. 10.2}$$

For RO:

$$SEC_{RO} = \frac{1}{\rho_{sw}} \cdot \left(\frac{\Delta p_{RO} + \Delta p_{Loss} + k_{OSM} \cdot X_{sw} \cdot CF}{1 - 1/CF} \cdot \frac{1}{\eta_{PP}} - \frac{\Delta p_{RO} + k_{OSM} \cdot X_{sw} \cdot CF}{CF - 1} \right) \cdot \eta_{ER} \cdot \frac{1}{\eta_{PP}} + \frac{sP_{el\_MED}}{\eta_{PP}} \quad \text{Eq. 10.3}$$

The definition of the parameters used in the previous equations and their typical values are summarized in Table 36. Details about the derivation of the formulas can be found in [Gebel 2008].

Parameter	Symbol	Unit	Value
Terminal temperature difference	ΔT_{TTD}	K	1.5
Boiling point elevation	ΔT_{BPE}	K	0.7
Non-equilibrium losses	ΔT_{Losses}	K	0.6
Heating steam temperature MSF	T_{T_MSF}	°C	110
Heating steam temperature MED	T_{T_MED}	°C	70
Theoretical condensing temperature	T_{MIN}	°C	40
Overall temperature difference MSF	ΔT_{0_MSF}	K	70
Overall temperature difference MED	ΔT_{0_MED}	K	30
Heat of evaporation	Δh_v	kJ/kg	2,200
Power plant efficiency	η_{PP}	%	41.8%
Steam turbine efficiency	η_T	%	90.0%
RO high pressure pump efficiency	η_P	%	80.0%
RO energy recovery turbine efficiency	η_{ERT}	%	70.0%
Driving pressure difference	ΔP_{RO}	bar	30
Friction pressure losses	ΔP_{Loss}	bar	4
Osmotic pressure coefficient	k_{OSM}	bar/%TDS	8
Feed concentration	X_{sw}	%TDS	4.2%
Concentration factor RO	CF_{RO}	-	1.5
Concentration factor MED	CF_{MED}	-	2.0
Seawater density	ρ_{sw}	kg/m³	1,041
Specific energy demand for auxiliaries RO	sP_{AUX_RO}	kWh/m³	0.5
Specific energy demand for auxiliaries MED	sP_{AUX_MED}	kWh/m³	2.0
Specific energy demand for auxiliaries MSF	sP_{AUX_MSF}	kWh/m³	2.0

Table 36: Overview of typical parameters for the calculation of specific energy consumption of desalination processes [Gebel 2008]

10.1.2 Water Intake and Pre-Treatment

Water intake is one of the most important components of each desalination plant, as it accounts for the supply of the desalination process with adequate water source quality [Voutchkov 2010]. The required water quality at the inlet of the desalination plant depends on the desalination technology [Gille 2003]. MED does not have as stringent water quality requirements as RO. The intake type and its layout have a major impact on the feed water composition (e.g. concentration of foulants) and on the requirements to the downstream pretreatment system. The two most used water intake types are open intakes and subsurface (beach well) intakes. Subsurface intakes include different layouts such as vertical

beach wells and seabed filtration systems (Figure 81). These intake types make use of the seafloor as a natural filter and provide high quality feed water, as most of the solids, organic compounds, silt and microorganisms are retained by the ground layer. This intake system's main advantages are avoided impingement and entrainment of marine organisms, lower required investment for pretreatment equipment and minimization of the use of chemicals. However, the realization of this intake type underlies a number of constraints such as the availability of a well flushed ocean bottom and sufficient seabed permeability (e.g. limestone). In addition, the capacity of a single well is rather limited and the required intake area is high (approx. 0.6 $m^2/(m^3/day)$), so that this intake type is economically justifiable only for small and medium (e.g. up to 20,000 m^3/day) desalination capacities [Voutchkov 2010].

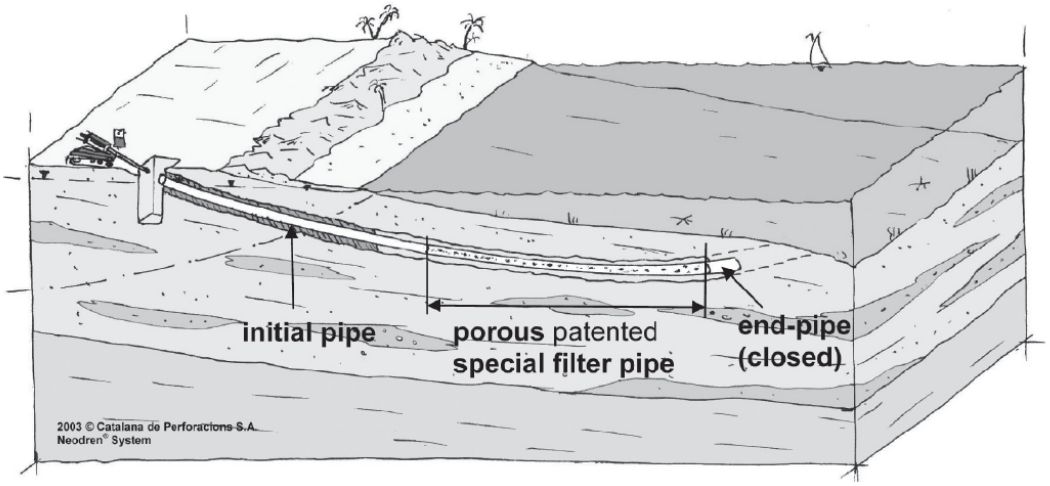

Figure 81: Scheme of the horizontal directionally drilled intake (Neodren, Catalana de Perforaccions) [Peters 2008]

Open intakes are the typical choice for large desalination plants. They can be divided into surface and submerged intakes. Surface intakes consist of a series of coarse and fine screens. All the equipment is located on-shore, which makes the investment cost low and the maintenance easier. However, as surface seawater is affected by high debris concentration, often problems of organisms' growth (mussels, fishes, and algae), chipping of concrete tubes and scaling occurs along the feed water pipes [Kohls 2010]. Submerged intakes are typically used for small and medium-size desalination plants or in the case particular seawater temperature and quality are required. Such intakes consist of off-shore intake structure, intake pipeline, screens, pump station and chemical feed equipment. The intake structure is typically placed at a water depth of approx. 30 meters to insure sufficient water quality. The water inlet is located 2 meters over the seabed in order to avoid the entry of silt and sand. The velocity of the water inlet should not exceed 0.2 m/s to prevent impingements of water organisms such as jellyfish. In contrast, along the transport tubes a minimal velocity of 1 m/s has to be guaranteed to avoid particle sedimentation [Wilf 2007]. During the last few years the company Taprogge has developed a number of patented submerged intake systems equipped with air powered backwash systems (Figure 82). The main advantages of this intake are high filtration efficiency, short backwash time (few seconds) and relatively low investment and operation cost [Taprogge 2014] [Gebel 2008]. If the desalination plant is

located in the proximity of a once-through cooled power plant, co-location (i.e. sharing) of water intake could be a favorable option from both the economic and the environmental point of view. However, a number of potential disadvantages due to higher water temperature (higher biofouling risk, lower boron rejection) and possible presence of metals (iron, copper and nickel) due to corrosion in the power plant cooling section reduce the attractiveness of this solution [Voutchkov 2010].

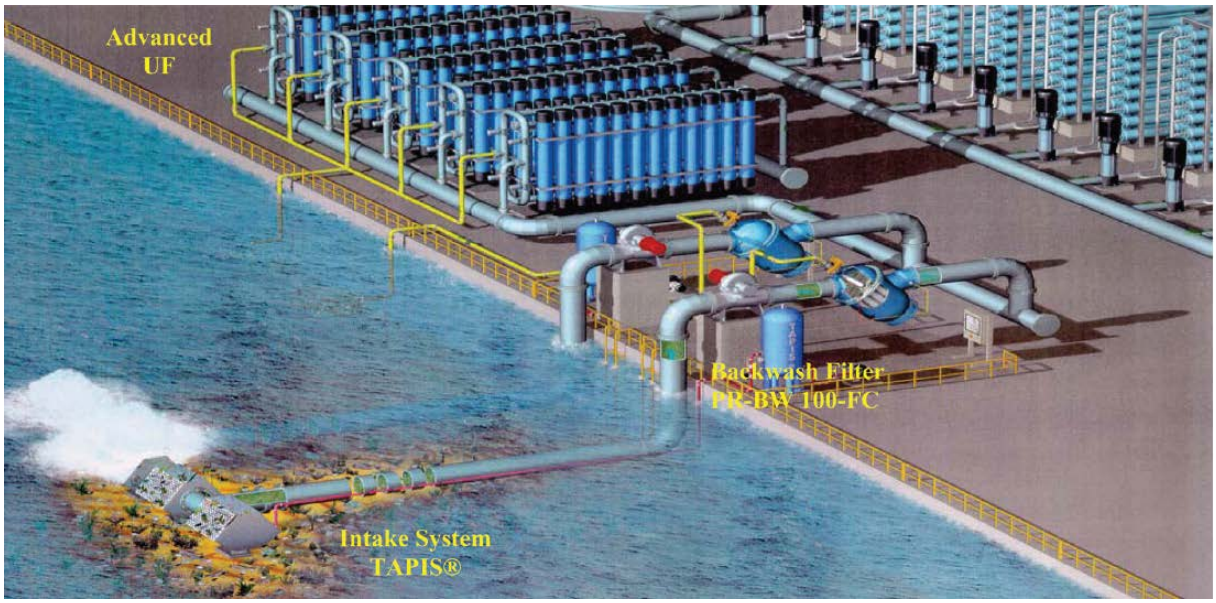

Figure 82: Scheme of the Taprogge submerged intake system for SWRO [Gille 2005]

Alternative Membrane Pretreatment

Over the last ten years significant improvement of microfiltration (MF) and ultrafiltration (UF) technologies has been reached. Nanofiltration (NF) membranes are typically used for softening or treatment of low salinity water. Currently, more than 20 desalination plants make use of MF/UF pretreatment systems [Voutchkov 2010 b]. MF/UF pretreatment is based on mechanical particle removal through fine pore membranes. Such systems are able to retain particles as small as 0.1 μm (MF) and 0.01 μm (UF) almost without coagulant addition. Turbidity and silt density can be typically reduced to very low values (turbidity < 0.05 NTU and SDI < 3). In addition, UF membranes effectively reject viruses and other pathogens and are less prone to variations in seawater quality. A detailed comparison between the feedwater quality of conventional and membrane pretreatment is presented in [Gille 2005]. Fouling agents such as dissolved organics and microorganisms are not removed, which increases the biofouling risk to downstream RO equipment. Another critical issue for MF/UF pretreatment is the presence of algae. In [Voutchkov 2010] is shown that MF/UF still are characterized by relatively high costs and lack of compatible, standardized products (high dependence on suppliers). Several advantages such as excellent particulate removal, lower requirement of chemicals, relative performance stability and simple operation will probably make MF/UF systems the preferred pretreatment technology in the future.

10.1.3 Desalination Processes

MED Configurations

Configuration	Description
Forward Feed	The feed water is only introduced in the first effect. The brine of the first stage is used as feed for the second effect and so on. As a result, the solute concentration in the brine gradually increases along the path to the last effect. If used in desalination plants, this configuration would lead to scaling problems.
Backward Feed	This configuration is the opposite of the previous one, i.e. the complete feed is introduced in the last effect. The brine is successively pumped though the stages. In the first effect, high temperature and solute concentration would favor the formation of scaling (even more than in forward feed configuration). Therefore also this layout is not used for desalination applications.
Parallel Feed	The feed water is distributed in each stage, thus allowing better scaling control, high efficiency and flexible operation. This configuration is the standard for MED seawater desalination plants.
Parallel-Cross Feed	This layout is a further improvement of the previous configuration. Similarly to MSF plants, the brine of the first effect flows directly to the bottom of the second effect. Additional vapor is produced by flashing, whereas the main distillate generation process remains temperature-driven evaporation on the tube bundle. The brine temperature is lower (approx. 40 °C) than in the previous case, which reduces the thermal load of the discharged water.

Table 37: Overview of MED configurations [El-Dessouky 2002]

RO Plant Configurations

Four main stage configurations are used in RO units. An overview is presented in Table 38.

Configuration	Description
Concentrate Staging	
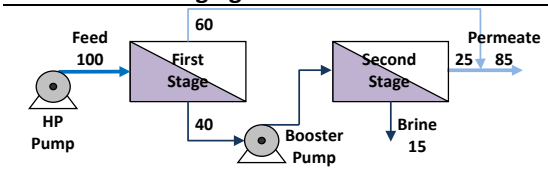	This is the typical configuration of commercial two-stage RO plants. In such a layout, the concentrate of the first stage serves as feed for the second stage.
Permeate Staging	
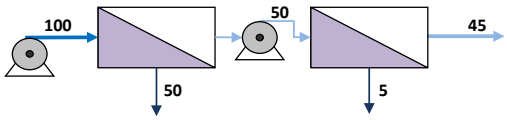	If the permeate from a single RO pass exceeds the required salinity level, a second pass is required. Thus, the permeate of the first stage is reprocessed in the second stage.
Partial Two-Pass	
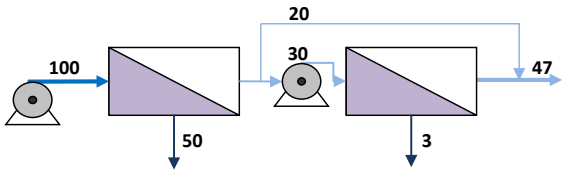	The permeate from the first pass is divided into two streams. Only one portion of permeate is processed by the second stage. This allows reducing the capacity of the second stage.
Split-Partial Two-Pass	
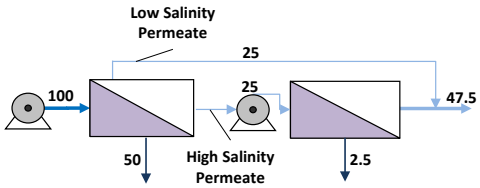	The permeate of the first stage is collected at both ends of the vessel. The permeate from the initial elements has sufficiently low salinity, due to the lower osmotic pressure of the feed, and does not need to be further processed. The remaining permeate is fed into the second stage.

Table 38: Possible configurations of RO stages – Adapted from [Wilf 2007]

While concentrate staging is a typical configuration in existing RO plants, two other layouts such as partial two-pass and split-partial two-pass have been introduced in the last few years. The main motivation for the development of these two alternative configurations is primarily the reduction of investment cost for the second pass. In addition, these two innovative configurations allow a more flexible plant operation. During summer seawater temperature and -as a consequence- salt passage through the membranes are higher. In this case, the required permeate salinity level is reached by increasing the amount of feed processed in the second stage [Wilf 2007].

Pressure Exchange Systems

PX devices consist of three pistons with each four valves, two on the brine side and two on the feed side. The basic layout is shown in Figure 83 [Gebel 2008].

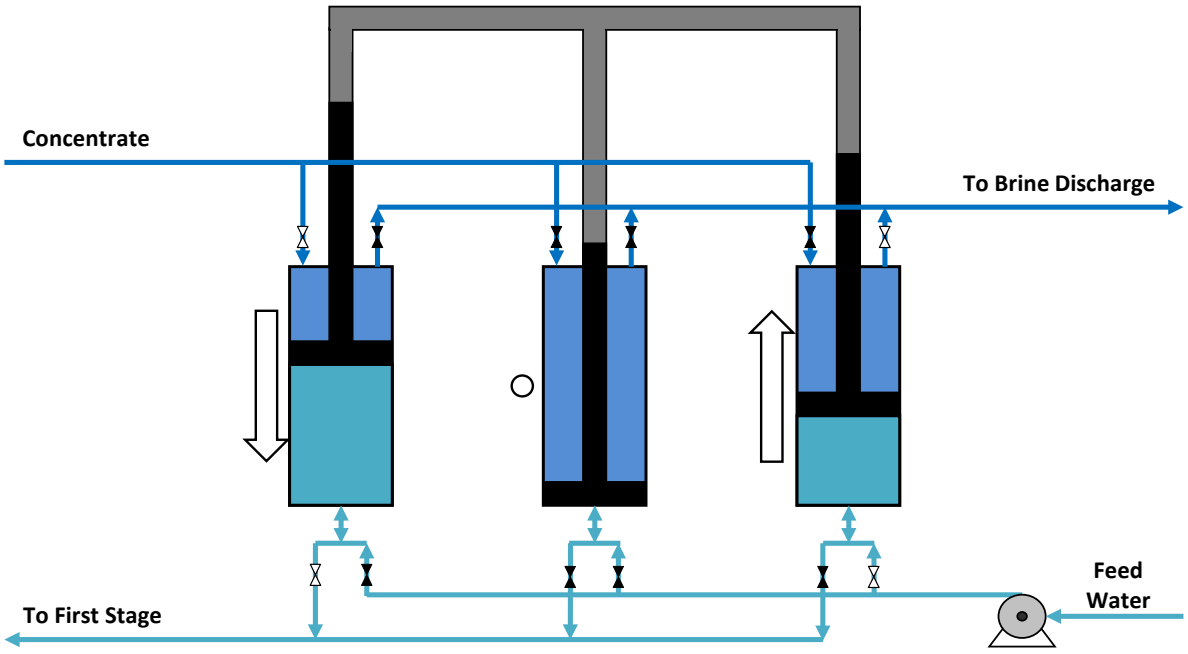

Figure 83: Operating principle of a PX unit [Gebel 2008]

The operating principle of PX systems goes as follows [Gebel 2008]: the pressurized concentrate moves the first piston down, while the exit valve of this piston is closed (black valve in Figure 83). On the other side of the same piston, the feed gets pressurized and flows toward the vessels of the first stage. Simultaneously, piston three is filled by low-pressure feed water. The second piston is on stand-by, but it is essential to guarantee the operation of the PX system without interruptions.

10.1.4 Brine Discharge

The magnitude of environmental impact depends on a number of factors such as individual sensitivity of organisms on osmotic, thermal and chemical stress, brine composition, discharge layout as well as shore morphologic and hydrodynamic conditions (i.e. shore bathymetric profile and presence of currents) (Figure 84).

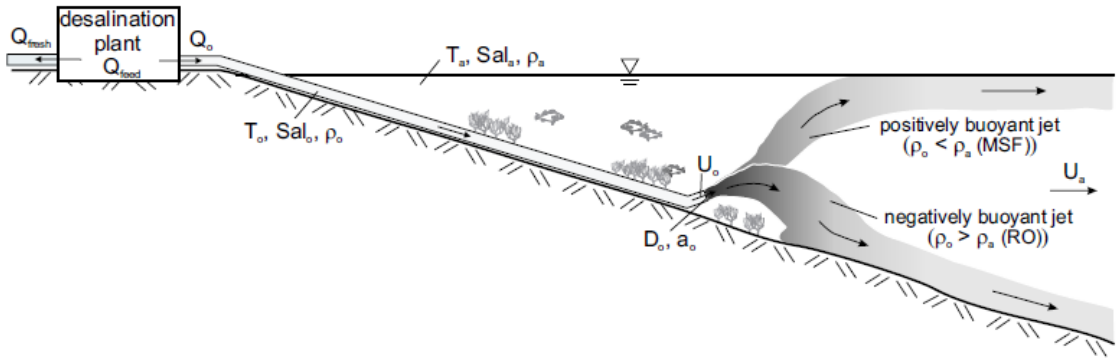

Figure 84: Brine discharge of thermal desalination and reverse osmosis [Niepelt 2007]

Desalination plants should be integrated into environmental integrated assessment (EIA) plans that regulate the use of water resources and desalination technology on a regional scale. The evaluation of each single desalination project starting from the planning phase should be taken into account. A standard EIA for desalination projects should include collection of comprehensive information on all environmental impacts of desalination, conduction of monitoring activities, establishment of criteria for analysis of monitoring data, and finally the comparison of different water intake and discharge solutions. Such a procedure currently is not state of the art [Lattemann 2008]. Environmental impacts of brine discharge can be minimized by a number of measures such:

- Horizontal drains below the sea bottom should be considered for water intake where suitable topographic and geologic conditions are available [Peters 2008]. Impingement and entrainment of larger organisms as well as the addition of chemicals can be minimized. Alternatively, pre-filtration with UF or MF membranes should be taken into consideration. This option may contribute to the reduction of chemical pre-treatment needs.
- Chlorine may be replaced by the use of ultraviolet light (200–300 nm) for disinfection purposes. Environmentally friendly additives may also replace other commonly added chemicals.
- Entrainment of plankton organisms (e.g. eggs, larvae) can be avoided by optimized intakes, which should be located in deeper waters, offshore, or underground.
- Brine dilution with other waste streams. Co-location of desalination and power plants allows mixing of cooling water from the power plant and waste water from the desalination plant. At the same time, a multi-port diffuser can be implemented to improve dilution [Bleninger 2008]. Thereby, a series of brine outfalls should be located at successive distances of approx. 50 m – 100 m. The velocity at the port outlet should be higher than 3.5 m/s in order to enhance turbulence and mixing.
- Impacts of high temperature in the discharged brine can be reduced by heat dissipation prior to disposal (e.g. cooling towers).

Material selection for heat exchangers: titanium is expensive but presents the best corrosion resistance. Therefore it should be preferred to copper, which constitutes a hazardous pollutant in the brine discharge [Lattemann 2003].

10.1.5 Desalination Markets

The desalination market has experienced remarkable growth in the last few years. While in 2005 the worldwide desalination capacity amounted to approx. 40 million m^3/day [Gebel 2008], in October 2013 that value reached 80.9 million m^3/d [waterworld 2013]. During 2013, new desalination plants with a capacity of 6 million m^3/day were expected to start operation. Up to date comprehensive data about existing and planned desalination plants can be found in the commercial platform DesalData [DesalData]. The leading desalination technology is RO, which holds approx. 60 % of the global market. MSF and MED follow with 26.8 % and 8.0 % market share, respectively. The most used water sources are seawater (60.0 %), brackish water (21.5 %), river water (8.3 %) and wastewater (5.7 %).

Desalination plants are mainly located in the Gulf States (in particular Saudi Arabia, UAE, Kuwait and Qatar), in Algeria and in the Unites States of America. The USA leads the membrane desalination market, whereas mainly brackish water is used as a water source. The Gulf States traditionally favor thermal desalination of seawater, also due to still large availability of low-cost fossil fuels for energy supply [desalination.com]. Product water is mainly used in the municipal sector (63.0 %), followed by industry applications (25.8 %) and power stations (5.8 %). Currently, only 1.9 % is destined for irrigation.

10.1.6 Renewable Desalination

A large number of studies, projects and mainly small-scale demonstration plants have appeared in the last decades. Several European research centers are involved in the development of such systems. Among them are CIEMAT-Plataforma Solar de Almería, Canary Islands Institute of Technology, Fraunhofer Institute for Solar Energy Systems, DLR and many others. Also, companies have been founded that commercialize some of the proposed concepts. This chapter briefly describes a selection of renewable desalination solutions (Table 39). For additional information, specific literature should be consulted. A comprehensive review of the state-of-the-art of renewable desalination is presented in [Cipollina 2009] and [PRODES 2010]. These publications also include detailed information about currently operating renewable desalination plants.

Even if several renewable desalination concepts have been proposed and developed in demonstration plants, their commercial application is still limited to small capacities applied in remote locations. Additionally, they are characterized by high capital and water cost. On the other hand, large desalination capacities will be required in the near future in order to cover the increasing water demand of the MENA countries as well as of other water-scarce regions.

Concept	Typical Capacity	Energy Consumption		Development Stage	Water Cost
		Electrical	Thermal		
	[m³/d]	[kWh/m³]	[kWh/m³]		[€/m³]
Solar Stills	< 0.1	-	Solar passive	Application	1.1 – 5.3
Solar-MEH	1 - 100	1.5	100	Application	2.1 – 5.3
Solar-MD	0.15 - 10	-	150 - 200	R&D	8.5 - 16
Solar Pond MED	< 3,000	1.5	60 - 70	R&D	0.6 – 0.8
CSP-MED	> 5,000	1.5	60 - 70	R&D	1.9 – 2.3
CSP-RO	> 5,000	3 – 4.5	-	R&D	1.9 – 2.3
PV-RO	< 100	3 – 4-5	-	Application	9.5 – 12.8
Wind-RO	50 - 2000	3 – 4-5	-	Application	1.6 – 4.3
Geothermal-MED	-	-	-	Basic Research	-

Table 39: Preliminary comparison of renewable seawater desalination concepts – Adapted from [IRENA 2012] and [Al-Kharagouli 2013]

10.2 CSP

10.2.1 CSP Basics

The knowledge of the thermodynamic basics of CSP is helpful to understand advantages and disadvantages of each technology (e.g. linear vs. point focusing systems, different HTFs etc.) and to make clear where potentials for further technology development are on. According to the Carnot´s theorem, higher efficiencies in heat engines can be achieved by high cycle top temperatures and low bottom temperatures. High inlet temperatures can be obtained using concentrated solar energy, while low outlet temperatures are obtained with efficient cooling. At this regard, it is opportune to define the concentration ratio cr:

$$cr = \frac{Ap}{D_{rec}} \qquad \text{Eq. 10.4}$$

Ap	[m]	collector aperture
D_{rec}	[m]	receiver external diameter

The higher is the concentration ratio, the higher is the temperature which in principle can be achieved. The concentration ratio is limited however by the non-ideal apparent size of the sun (32´as seen from the Earth). If D_{rec} is lower than $32´ \cdot Ap$, the share of the radiation reflected by the mirrors on the receiver (intercept factor) will be reduced and the spillage will be higher [Riffelmann 2012]. In addition, inaccuracies and optical errors of collector components further reduce the practical achievable concentration ratio of CSP applications, which is ca. 10,000 for point focusing systems and ca. 80 for line focusing systems [Zarza 2012].

In addition, the realization of high temperatures is related to higher heat losses (conductive, convective and radiative). A simplified approach for the calculation of the solar field output of a concentrating parabolic reflector is [Sokrates 2004]:

$$\dot{Q}_{sf} = \dot{Q}_{abs} - \dot{Q}_{loss} \quad \text{Eq. 10.5}$$

$$\dot{Q}_{sf} = Ap \cdot \left[DNI \cdot \eta_{opt} \cdot \eta_{geo} - \frac{k \cdot \pi}{cr} \cdot (T_{rec} - T_{amb}) - \frac{\varepsilon \cdot \sigma \cdot \pi}{cr} \cdot \cdot \left(T_{rec}^4 - T_{sky}^4 \right) \right] \quad \text{Eq. 10.6}$$

η_{opt}	[-]	collector optical efficiency
η_{geo}	[-]	collector geometrical efficiency
k	[W/m²/K]	conduction/convection loss factor
ε	[-]	receiver emissivity
σ	[W/m^2/K^4]	Stefan-Boltzmann constant
T_{rec}	[K]	receiver temperature
T_{amb}	[K]	ambient temperature
T_{sky}	[K]	sky temperature

The fist term on the right side of the equation is the absorbed heat $\dot{Q}_{abs}$. The second term - $\dot{Q}_{loss}$- consists on two members, i.e. convective/conductive losses on one hand, which increase linearly with rising receiver temperature, and radiative losses on the other hand, which depend on the difference between the fourth power of receiver and sky temperature. Eq. 10.6 put in evidence two CSP design basics:

- the thermal losses -in particular radiative losses- increase with increasing receiver temperature
- the thermal losses are inversely proportional to the concentration factor cr

These both aspects are shown in Figure 85, where the solar field efficiency is defined as:

$$\eta_{sf} = \frac{\dot{Q}_{sf}}{DNI \cdot Ap} \quad \text{Eq. 10.7}$$

If there is no temperature difference between receiver and ambient (left part of the diagram), the efficiency of the solar field is only function of the optical losses and is independent from the concentration ratio. If the temperature difference rises, the effect of the concentration ratio for the limitation of thermal losses becomes more important.

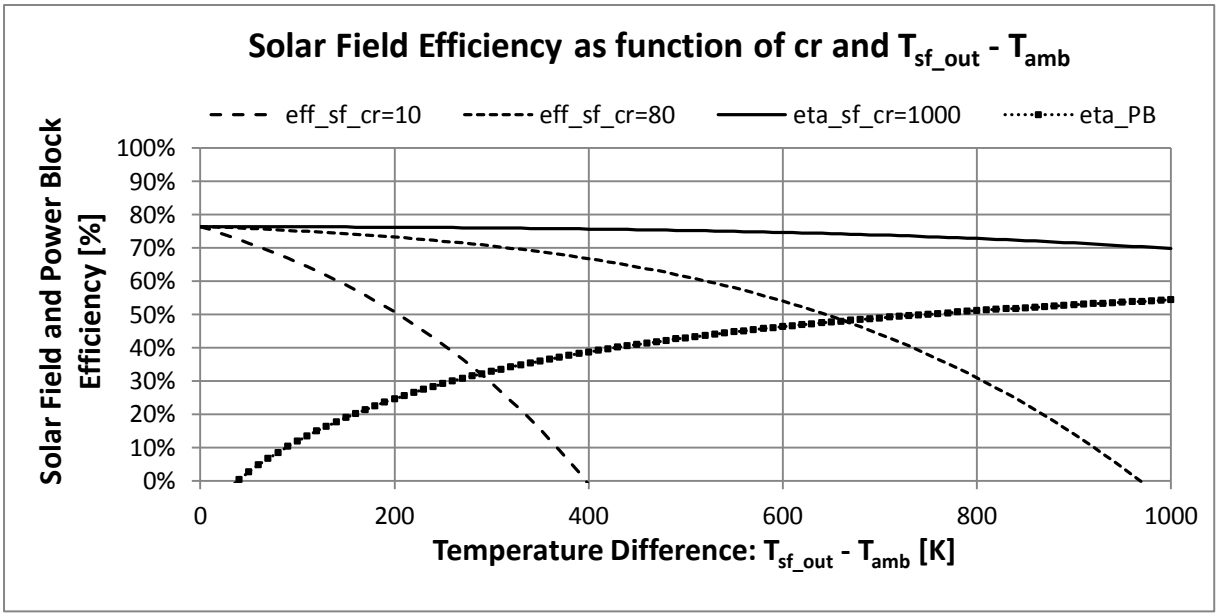

Figure 85: Solar field efficiency as function of concentration ratio and outlet solar field temperature

10.2.2 Incident Angle Calculation (General Case)

The general calculation of the solar incident angle θ is performed according to [Duffie 1991]:

$$\begin{aligned}\cos\theta = \quad & \sin\delta \cdot \sin\phi \cdot \cos\beta \\ & - \sin\delta \cdot \cos\phi \cdot \sin\beta \cdot \cos\gamma \\ & + \cos\delta \cdot \cos\phi \cdot \cos\beta \cdot \cos\omega \\ & + \cos\delta \cdot \sin\phi \cdot \sin\beta \cdot \cos\gamma \cdot \cos\omega \\ & + \cos\delta \cdot \sin\beta \cdot \sin\gamma \cdot \sin\omega\end{aligned} \qquad \text{Eq. 10.8}$$

10.2.3 Heat Transfer Fluids and Collectors Data

VP-1

	a_0	a_1	a_2	a_3	a_4
ρ(kg/m³)	1083.25	-0.90797	7.811610^{-4}	$-2.367\ 10^{-6}$	0
c_p (kJ/kg/K)	1.498	$2.414\ 10^{-3}$	5.959110^{-6}	$-2.9879\ 10^{-8}$	$4.4172\ 10^{-11}$
p_{vap} (kPa)	2.12329	-1.190859	$4.35824\ 10^{-3}$	$3.6106\ 10^{-5}$	$1.08408\ 10^{-7}$
h (kJ/kg)	-18.9777	1.51351	$1.2908\ 10^{-3}$	$1.20149\ 10^{-7}$	0

Table 40: Main VP-1 physical properties expressed as polynomial functions [EnerMENA 2012]

Additional information on VP-1 as well as other HTF can be found in [Raade 2010]. An overview on physical properties of oil-based HTF is given by [Therminol] and [Dowtherm].

Molten Salt

The features of the "solar salt" are calculated according to [Ferri 2008]:

$$\rho_{HTF} = 2{,}090 - 0.636 \cdot T_{fl} \qquad \text{Eq. 10.9}$$

$$c_{p\_HTF} = \left(1{,}443 + 0.172 \cdot T_{fl}\right) \cdot 10^{-3} \qquad \text{Eq. 10.10}$$

Collectors Data

Main geometrical and optical parameters of a series of commercial parabolic trough collectors are summarized in Table 41 [Cordes 2011].

These data are also included in the INSEL model. The collector selection is performed by the INSEL user in the block parameter window. A comprehensive and detailed overview on available parabolic trough collectors can be found in [Fernandez-Garcia 2010].

Collector	**Manufacturer** -	**Reflectance Area** [m²/module]	**Aperture** [m]	**Length** [m]	$\eta_{opt,peak}$ [%]
LS-2	Luz	235	5	49	76
LS-3	Luz	545	5.76	100	80
SKAL-ET 150	Flagsol	817.5	5.76	150	80
SGX-1	Acciona	417	5	100	77
Senertrough	Sener	> 800	5.76	150	n.s.[1]
Heliotrough	Flagsol	n.s.	6.78	191	n.s.

Table 41: Geometrical and optical data of parabolic trough commercial collectors; adapted from [Cordes 2011]. Sources: [Price 2002], [SAM], [Kearney 2007], [Riffelmann 2009], [Kötter 2010]; [1]n.s. = not specified.

10.2.4 Details of CSP Model

Piping Model

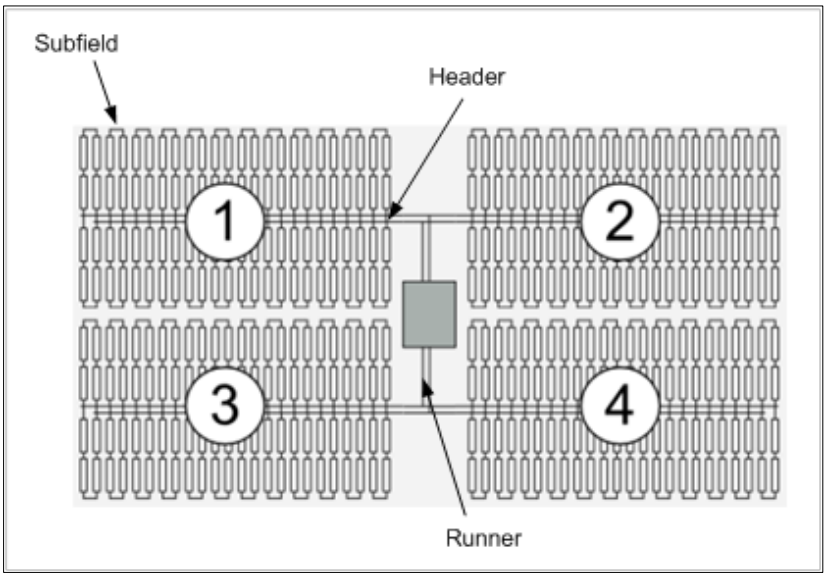

Figure 86: Possible field layout for oil or salt cooled parabolic trough CSP systems [Wagner 2011]

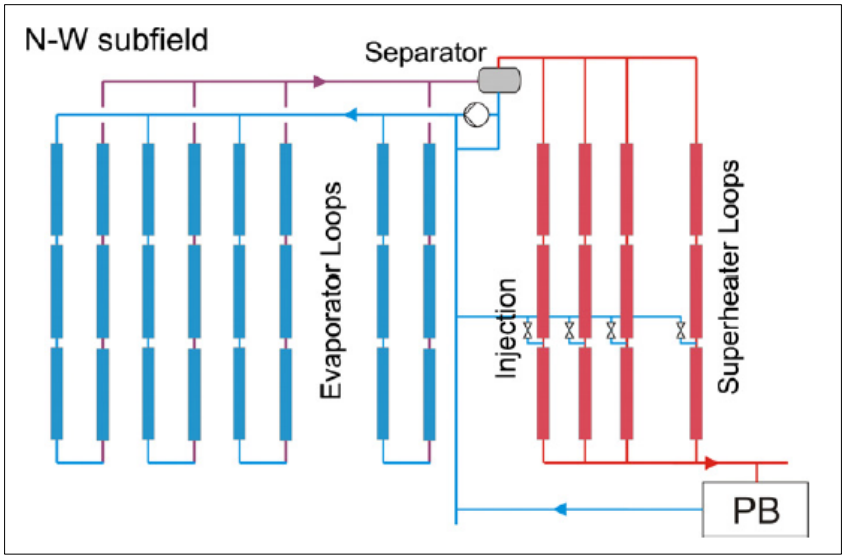

Figure 87: Solar field layout of a recirculation mode DSG system [Birnbaum 2011]

The total number of extractions along the runner pipe i_{r_max} is a function of $n_{subfields}$:

$$i_{r\_max} = \begin{cases} \dfrac{n_{subfields}}{4} \\ \dfrac{n_{subfields} - 2}{2} \end{cases} \Bigg| \begin{matrix} (n_{subfields}\ mod\ 4) = 0 \\ (n_{subfields}\ mod\ 4)\ \neq 0 \end{matrix} \qquad \text{Eq. 10.11}$$

In FORTRAN this condition is expressed with the command *floor*. Considering a CSP plant with a North-South axis of symmetry and a number of subfield $n_{subfields} \geq 4$ (as for $n_{subfields} = 2$ no runner is necessary), the HTF mass flow rate in the runner $\dot{m}_{HTF\_runner}$ can be calculated as:

$$\dot{m}_{HTF\_r}(i_r) = \begin{cases} \dot{m}_{subfield} \cdot \left[\dfrac{n_{subfields}}{2} - 2 \cdot (i_r - 1)\right], (n_{subfields}\ mod\ 4) = 0 \\ \dot{m}_{subfield} \cdot \left[\dfrac{n_{subfields}}{2} - (2 \cdot i_r - 1)\right], (n_{subfields}\ mod\ 4)\ \neq 0 \end{cases} \qquad \text{Eq. 10.12}$$

i_r	[-]	runner extraction-counter
$\dot{m}_{HTF\_r}(i_r)$	[kg/s]	HTF mass flow as function of runner extraction-counter
$n_{subfields}$	[-]	total number of subfields

In the runner sections the tube diameter can be estimated as:

$$D_{runner} = \sqrt{\frac{4 \cdot \dot{m}_{HTF\_r}(i_r)}{\rho_{HTF} \cdot v_{HTF} \cdot \pi}} \qquad \text{Eq. 10.13}$$

The length of the runner pipes can be calculated as follows for solar field layouts with at least four subfields:

$$L_{runner}(n_{subfields}) = L_{runner\_pb} + \left(\frac{L_{loop}}{2} + 2 \cdot \Delta L_{row}\right) \cdot \left(\frac{n_{subfields} - 4}{2} + 1\right) \quad \text{Eq. 10.14}$$

L_{runner}	[m]	total runner length
L_{runner_pb}	[m]	runner length around the power block (50 m)
L_{loop}	[m]	length of a collector loop
ΔL_{row}	[m]	distance between two parallel collector loops

Header

In contrast to receiver diameters, which are fixed along their whole length, header diameters needs to be adapted step-wise in order to match the changing mass flow rates along the HTF extractions to the collector loops. In this case the optimum diameter results from a trade-off between investment cost on the one hand (higher for large D_{runner}) and mounting cost and pressure losses on the other hand (higher for small D_{runner}). The problem is practically solved by setting a tolerance range to the HTF flow velocity, i.e. HTF minimum and maximum acceptable velocity values. If the HTF velocity is outside this given tolerance range in a given pipe step (e.g. in the way to the collectors), the diameter is recalculated setting the HTF velocity equal to the maximum acceptable value.

Next to the runner, the header diameter is designed for the upper velocity limit considering the subfield HTF mass flow rate:

$$\dot{m}_{HTF\_subfield} = \frac{\dot{m}_{HTF\_tot}}{n_{subfields}} \quad \text{Eq. 10.15}$$

The number of extractions $n_{estractions}$ in a subfield is:

$$n_{extractions} = \frac{n_{loops}}{2 \cdot n_{subfields}} \quad \text{Eq. 10.16}$$

n_{loops}	[-]	number of collector loops

According to Figure 88, the HTF mass flow along the header is:

$$\dot{m}_{HTF\_header}(i_h = k) = \dot{m}_{HTF\_subfield} - \sum_{i_h=1}^{k-1} 2 \cdot \dot{m}_{HTF\_loop} \quad \text{Eq. 10.17}$$

With

i_h	[-]	any header step, $i_h \in (1..n_{extractions})$

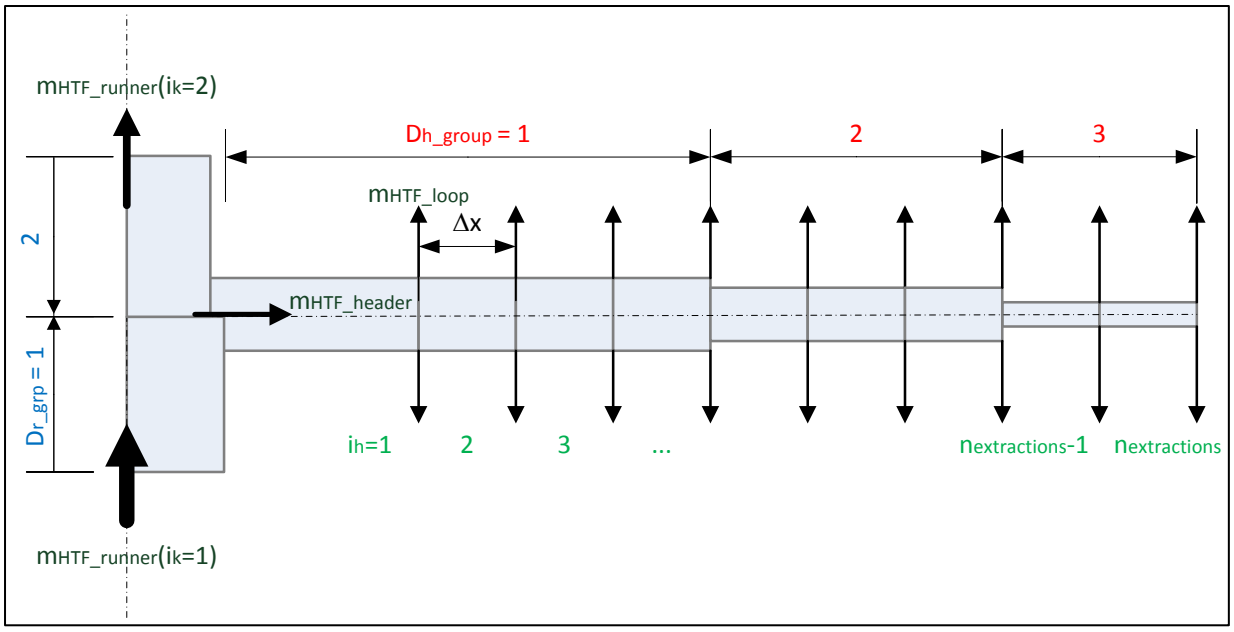

Figure 88: Overview of runner and header HTF mass flow distributions with relative numerations and symbols; Adapted from [Wagner 2011]

The diameters of the header sections have been calculated separately for the cold and hot sections in order to take into account the higher HTF density in the hot header. Figure 89 shows the results of the upper and lower limitations on the HTF velocity. As one could expect, the required adjustment of the header diameter is more frequent toward the end of the header, as there the ratio between HTF mass flow before and after one extraction is much higher than in the first steps.

The total length of the header can be estimated as:

$$L_{header} = n_{extractions} \cdot (\Delta L_{row} + 4.275) \qquad \text{Eq. 10.18}$$

where the factor 4.275 is added to the distance between two parallel collector loops in order to take into account the requirements for thermal expansion and contractions (Kelly and Kearney 2007).

Collector loops

The HTF mass flow in the collector loops (receiver and header-receiver connections) is constant ($\dot{m}_{HTF\_loop}$). The total length of a loop is expressed as:

$$L_{loop} = L_{receiver} + \Delta L_{h\_r} \qquad \text{Eq. 10.19}$$

ΔL_{h_r} [m] length of the header-receiver connection [Wagner 2011]

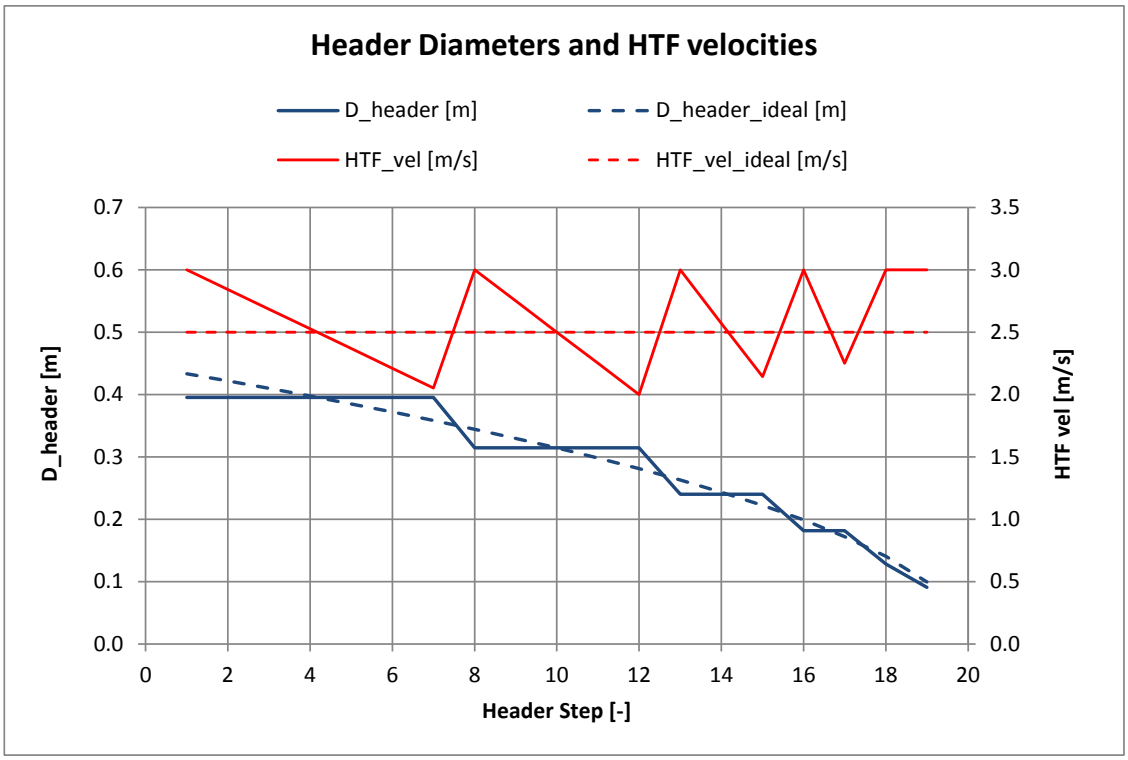

Figure 89: Header diameter and HTF velocity as function of header steps (HTF extractions are located at the end of each step); broken lines represent the ideal case (i.e. 2.5 m/s HTF velocity)

Concentrate Losses

Additional pressure losses are due to several devices and components as elbows, valves, ball joints etc. Table 42 gives an overview on their distribution in the solar field (runner, header and loop) and their typical loss coefficients.

Devices	ξ_k	Devices/Runner	Header	Loop
Expansions/Contractions	0.5	$if\ (D_i \neq D_{i-1})$	$if\ (D_i \neq D_{i-1})$	-
Elbows	0.9	-	-	12
Long Elbows	0.6	$max\left[4 \cdot \left(\frac{L_{runner}}{70} + 0.5\right); 8\right]$	1	-
Weldolets	1.8	-	-	2
Ball joints	8.7	-	-	$n_{coll} + 3$
Valves	0.2	2	-	2
Loop control valves	10	-	-	1

Table 42: Overview on coefficients and distribution of concentrate pressure losses; Adapted from [Wagner 2011]

Details of Transient Model

The heat capacities of HTF and steel tubes are calculated taking into account tube lengths and diameters which have been calculated for the different components in the piping layout section according to [Wagner 2011], [Cordes 2011].

$$M_{HTF} = M_{HTF,loop} + M_{HTF,header} + M_{HTF,runner} + M_{HTF,vessel} \qquad \text{Eq. 10.20}$$

$$M_{HTF,loop} = \rho_{HTF} \cdot \frac{\pi}{4} D_{abs,i}^2 \cdot L_{loop} \quad \text{Eq. 10.21}$$

$$M_{HTF,header} = \sum_{j=1}^{n_{header\_sections}} \rho_{HTF} \cdot \frac{\pi}{4} D_{header,j}^2 \cdot L_{header,j} \quad \text{Eq. 10.22}$$

$$M_{HTF,runner} = \sum_{l=1}^{n_{runner\_sections}} \rho_{HTF} \cdot \frac{\pi}{4} D_{runner,l}^2 \cdot L_{runner,l} \quad \text{Eq. 10.23}$$

$$M_{steel} = M_{steel,loop} + M_{steel,header} + M_{steel,runner} + M_{steel,vessel} + M_{steel,PB} \quad \text{Eq. 10.24}$$

$$M_{steel,loop} = \rho_{steel} \cdot \frac{\pi}{4} (D_{abs,e}^2 - D_{abs,i}^2) \cdot L_{loop} \quad \text{Eq. 10.25}$$

$$M_{steel,header} = \sum_{j=1}^{n_{header}} \rho_{steel} \cdot \frac{\pi}{4} (D_{header,j}^2 - (D_{header,j} - t_{wall})^2) \cdot L_{dist} \quad \text{Eq. 10.26}$$

$$M_{steel,runner} = \sum_{l=1}^{n_{runner\_sections}} \rho_{steel} \cdot \frac{\pi}{4} D_{runner,l}^2 \cdot L_{runner,l} \quad \text{Eq. 10.27}$$

As the specific volume of the synthetic oil increases with rising temperature, during nominal operation of the solar field a relevant part of the HTF is buffered in the expansion vessel (around 25 % of the total HTF [Rheinländer 2010]). The additional HTF mass $M_{HTF,vessel}$ is not calculated explicitly in this model. The tube wall thickness of header and runner sections is proportional to the tube diameter [Wagner 2011]:

$$t_{wall} = 0{,}0194 \cdot D \quad \text{Eq. 10.28}$$

Short-term DNI Fluctuations

As the implemented model works with one-hour input data resolution, in principle a low DNI value could physically mean both one hour with constant low irradiation or one hour with strong DNI fluctuations because of broken clouds conditions. Although these two conditions have the same arithmetical DNI value, the dynamic solar field response in these two cases is different. In particular, in the second case there will be certain times with high DNI alternated with other times with very low or no DNI. During these periods, the solar field starts to cool down, so that whenever DNI is again available, a new start-up process has to be completed before operation at nominal conditions can be continued. These processes cannot be easily captured by models with hourly input data resolution. However, a rough approach can consist in the consideration of the clear sky index (CSI), i.e. the ratio between actual DNI and clear sky DNI:

$$CSI = \frac{DNI}{DNI_{clear\_sky}}$$ Eq. 10.29

The main idea of this approach is that if the CSI is below a given threshold limit, in order to exclude from these considerations the effects due to aerosols), the irradiation conditions are likely to be characterized by cloud transients. In these cases, a very simple method is proposed, which does not require high time-resolution meteorological information. The considered hour is split in two parts, the first one with clear sky DNI and the second part with no DNI. The duration of the clear sky conditions are calculated by the rule of proportion:

$$t_{clear\_sky} = CSI \cdot 1h$$ Eq. 10.30

During the second part of the hour (where the DNI is 0 W/m²) a cool-down process occurs. The required start-up heat is then subtracted from the thermal yield of the successive hour. If required, the INSEL user has the possibility to switch this calculation option off in the graphical interface or to adjust the threshold limit to the site-specific atmospheric conditions.

Details of DSG Model

Parameter	One-phase Liquid Flow	Two-phase Flow	One-phase Gas Flow
h	$h \le h'$	$h' < h < h''$	$h \ge h''$
k_{conv}	$Nu_{D_{abs,i}} \cdot \frac{\lambda_{fl}}{D_{abs,i}}$	$k' \cdot \left\{(1-x)^{0,01}\left[(1-x) + 1{,}2x^{0,4}\left(\frac{\rho'}{\rho''}\right)^{0,37}\right]^{-2,2} + x^{0,01}\left[\frac{\alpha''}{\alpha'}\left(1+8(1-x)^{0,7}\left(\frac{\rho'}{\rho''}\right)^{0,67}\right)\right]^{-2}\right\}^{0,5}$	$Nu_{D_{abs,i}} \cdot \frac{\lambda_{fl}}{D_{abs,i}}$
Nu_D	$\frac{\left(\frac{\xi}{8}\right) Re \,\mathrm{Pr}}{1 + 12{,}7\sqrt{\left(\frac{\xi}{8}\right)}\left(\mathrm{Pr}^{\frac{2}{3}} - 1\right)} \cdot \left[1 + \left(\frac{D}{L}\right)^{\frac{2}{3}}\right] \cdot \left(\frac{Pr}{Pr_w}\right)^{0,11}$	-	$\frac{\left(\frac{\xi}{8}\right) Re \,\mathrm{Pr}}{1 + 12{,}7\sqrt{\left(\frac{\xi}{8}\right)}\left(\mathrm{Pr}^{\frac{2}{3}} - 1\right)} \cdot \left[1 + \left(\frac{D}{L}\right)^{\frac{2}{3}}\right] \cdot \left(\frac{T}{T_w}\right)^{-0.18}$
ξ	$(1{,}8 \log_{10} Re - 1{,}5)^{-2}$	-	$(1{,}8 \log_{10} Re - 1{,}5)^{-2}$

Table 43: General procedure for the calculation of the absorber-fluid heat transfer [Gnielinski 1976], [Forristall 2003], [VDI 2010]; Pr = Prandtl number; Nu = Nusselt number

It is interesting to analyze the behavior of the heat transfer coefficient as function of the enthalpy (Figure 90): due to the pronounced convection mechanisms in the two-phase flow,

the heat transfer coefficient of wet steam increases up to around a factor four in comparison to the single-phase flow.

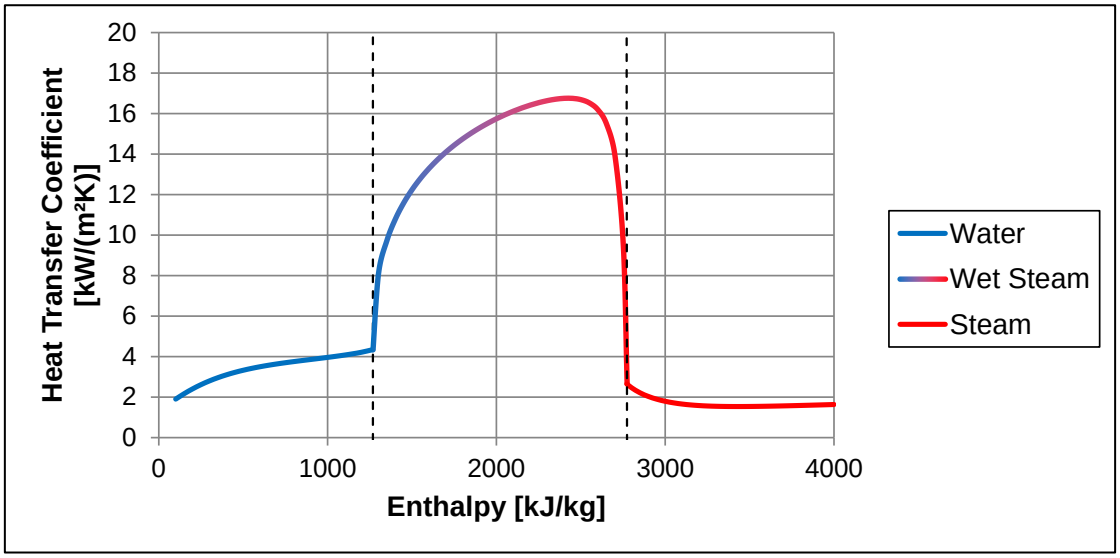

Figure 90: Heat transfer coefficient between inner absorber tube surface and water/steam as function of enthalpy

Finally, the pressure losses of the two-phase flow are calculated according this empirical equation [VDI 2010]:

$$\Delta p_{verl} = f_m \cdot \frac{L \cdot 2 \cdot \rho_m \cdot v_m^2}{D} \qquad \text{Eq. 10.31}$$

Where

$$f_m = 0.0925 \cdot Re^{-0,2534} + \frac{(13,98 \cdot Re^{-0,9501} - 0.0925 \cdot Re^{-0,2534})}{\left(1 + \left(\frac{Re}{293}\right)^{4,864}\right)^{0,1972}} \qquad \text{Eq. 10.32}$$

In Eq. 10.31 and Eq. 10.32 all fluid parameters are averaged values between liquid and gaseous phase, with exception of the Reynolds number Re which is calculated using the kinematic viscosity of the pure liquid phase.

10.2.5 PT-CSP Plant Model Validation

Thermo-oil

In this section some result of the developed model are presented and compared with two different reference models of the DLR Department of Solar Research. The first reference model is a detailed transient model which is applied for the simulation of the dynamic behavior of oil-based CSP plants during single days. The second reference model is a more simplified tool for annual yield analysis.

Single Days against dynamic model

As a first step, the CSP model developed in INSEL is tested with a detailed transient model. The analysis has been carried out for two sample days -"day one" with nearly clear-sky conditions and "day two" with broken clouds conditions- for a virtual Andasol-like power plant sited at the Plataforma Solar de Almería. For the detailed reference model DNI data with minute-resolution are available, while the INSEL model is fed with hourly averages calculated from the high-resolution data. Finally, the results from the detailed reference model have been cumulated to hourly values in order to make them comparable with those of INSEL.

Figure 91 shows the results of the comparison of the solar field output Q_{sf} and of the average HTF temperature T_{HTF_avg} for "day one". The results from the INSEL model show a good agreement with the reference model. All in all, the difference of the daily cumulated heat from the solar field is below 1 %. Looking more in detail into the hourly values, the most relevant difference is found during the start-up, whereas the difference is probably due to the fact that the reference model counts as Q_{sf} only the heat which can be directly used for electricity generation or thermal storage charge, while the INSEL model includes in Q_{sf} also the heat for the power block start-up. Furthermore, the INSEL model allows for power block start-up not before the HTF temperature has reached its nominal value. This could explain the difference of HTF temperature during heat-up. After the start-up procedure is terminated, the agreement of the INSEL model is very good, also in the afternoon after the thermal energy storage is fully charged and a share of the receiver has to be defocussed.

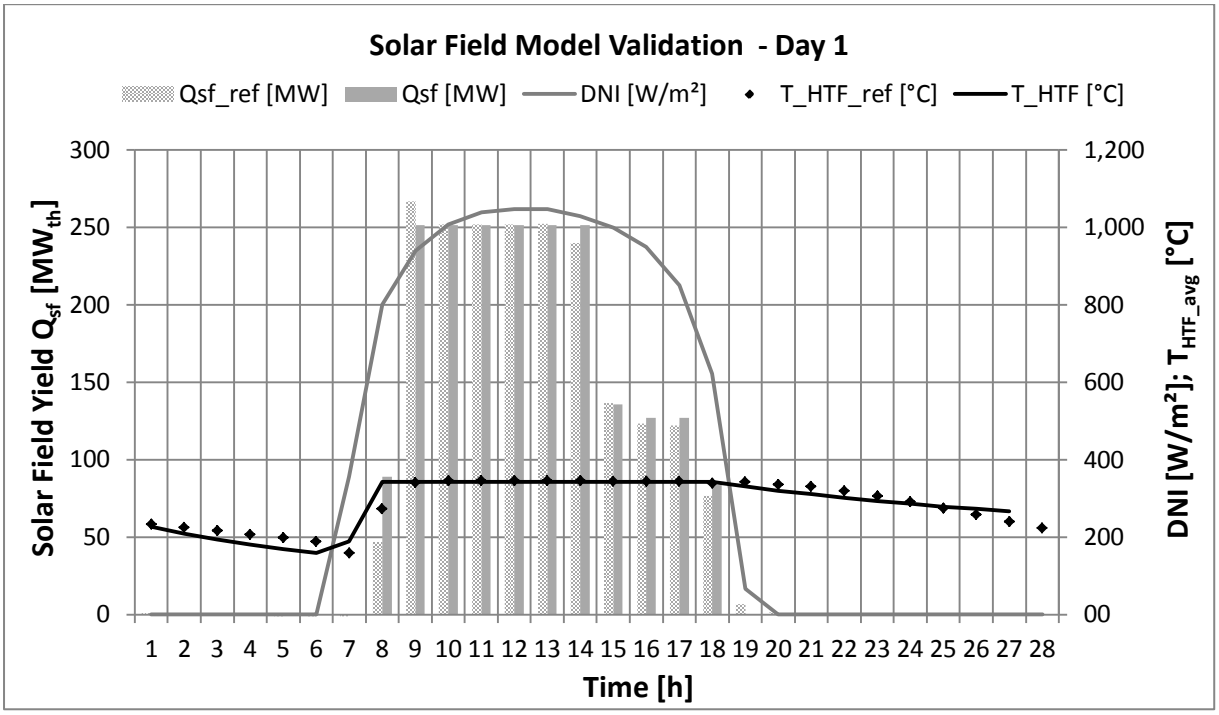

Figure 91: Solar field model validation on transients under nearly clear-sky conditions

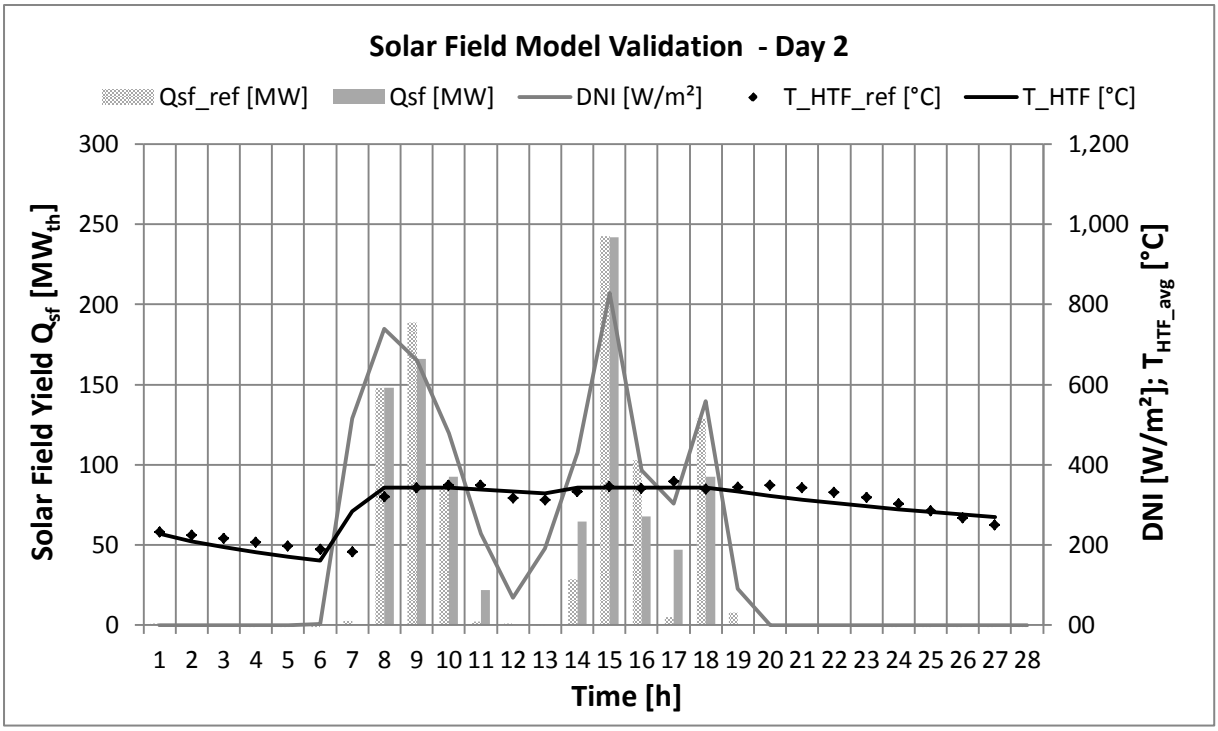

Figure 92: Solar field model validation on transients under partly cloudy weather conditions

Larger mismatches among single hour values can be found looking at the second analyzed day (Figure 92). This is little surprising, as "day two" is characterized by strongly fluctuating DNI. Largest discrepancies between the two models are for DNI values between 300 W/m² and 600 W/m². The INSEL model is fed with hourly input data and therefore cannot capture the real course of the short-term DNI fluctuations and the consequent cool-down and heat-up processes. Furthermore, the detailed reference model could use different operation strategies than the INSEL model under mid and low DNI conditions. However, it seems that overestimations in certain hours always are balanced by underestimations in the following hour, so that also in this case the daily cumulated error is still below 1 %.

Yearly simulation and comparison with DLR-Solar Research tool

As a second step in the model validation process, two annual yield simulations have been carried out with INSEL for two different CSP (oil-based parabolic trough) configurations, i.e. without and with thermal energy storage (indirect two-tank molten salt). The main results of the simulations (solar field output and gross power generation) have been compared with another tool of the DLR Solar Research Department. In this case, both models use hourly input data. Table 44 summarizes the key input parameters of the two analyzed configurations. The first CSP plant is a 20 MW_{el} plant without storage, while the second is a larger plant with thermal energy storage (50 MW_{el}, ca. 19 hours full load storage operation) which is able to deliver base load operation during most of summer days.

The results of the simulations reveal an excellent agreement between INSEL and the reference model. The differences between the annual cumulated gross electricity generation of INSEL and reference model are in both cases ca. 1 %, which is better than expected. Figure

93 shows the results of three sample days in July for the configuration without thermal energy storage. While the differences of the solar field output are exiguous, some small discrepancy can be found in the power production during start-up and shut-down processes.

CSP Power Plant	Unit	ALG-1	ALG-2
Power Block			
Type	-	single re-heat, condensing	single re-heat, condensing
Installed gross capacity	MW_{el}	20.0	50.0
Life steam conditions	bar / °C	100 / 377	100 / 377
Re-heat conditions	bar / °C	16.5 / 377	16.5 / 377
No. of pre-heaters (HP/LP)	-	3 / 2	3 / 2
Gross Nominal Efficiency	%	39.0%	39.0%
Solar Field & HTF System			
Number of loops	-	42	288
Collector net aperture area	m^2	817.5	817.5
Collector spacing	m	16.5	16.5
HTF		Therminol VP-1	Therminol VP-1
HTF temp.(in/out)	°C / °C	293 / 393	293 / 393
Thermal Energy Storage			
Type	-	-	Indirect two-tank molten salt
Storage medium	-	-	60% $NaNO_3$ / 40% KNO_3
Storage capacity	MWh_{th}	0	2,639
Molten salt mass	tons	0	69,450

Table 44: Overview of main simulation parameters for the two analyzed configurations

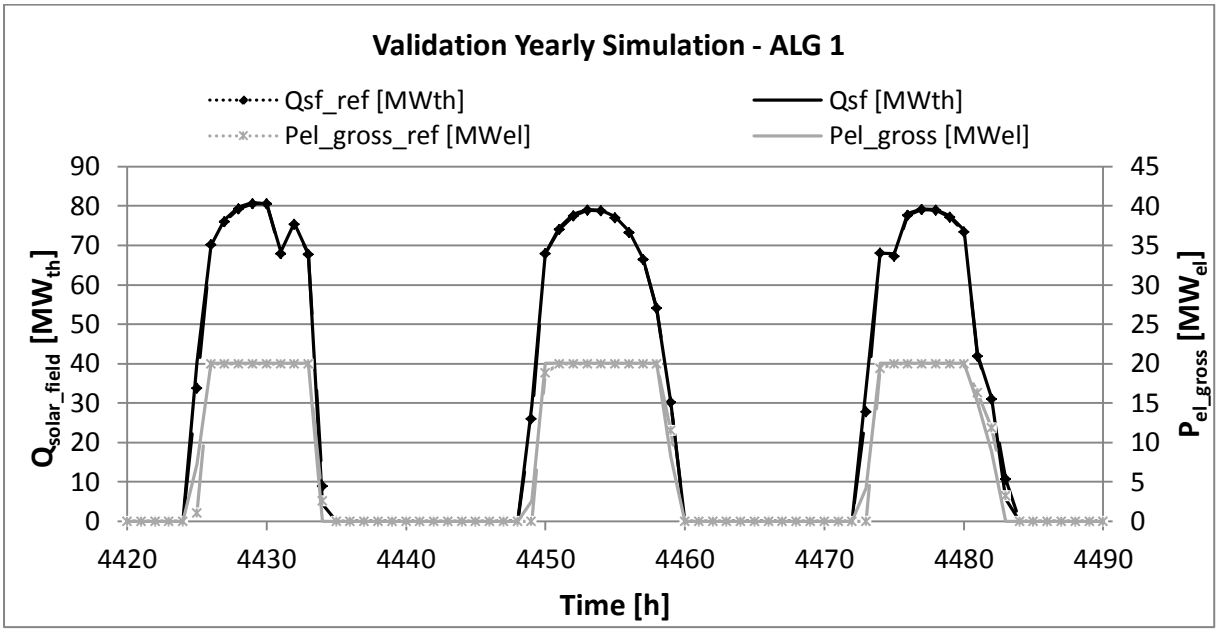

Figure 93: validation of CSP model – Oil based parabolic trough solar field without thermal storage

The apparently larger mismatch between the solar field output of the two models for the second configuration (Figure 94) is because the reference model first calculates Q_{sf} independently of the storage charge status (i.e. without mirror defocussing), while the solar

field INSEL model receives each hour information about the storage charge status and automatically defocusses part of the receivers if required. In both models the power generation at night hours is slightly lower than nominal conditions due to lower HTF temperature and capacity limitation of the molten salt pump.

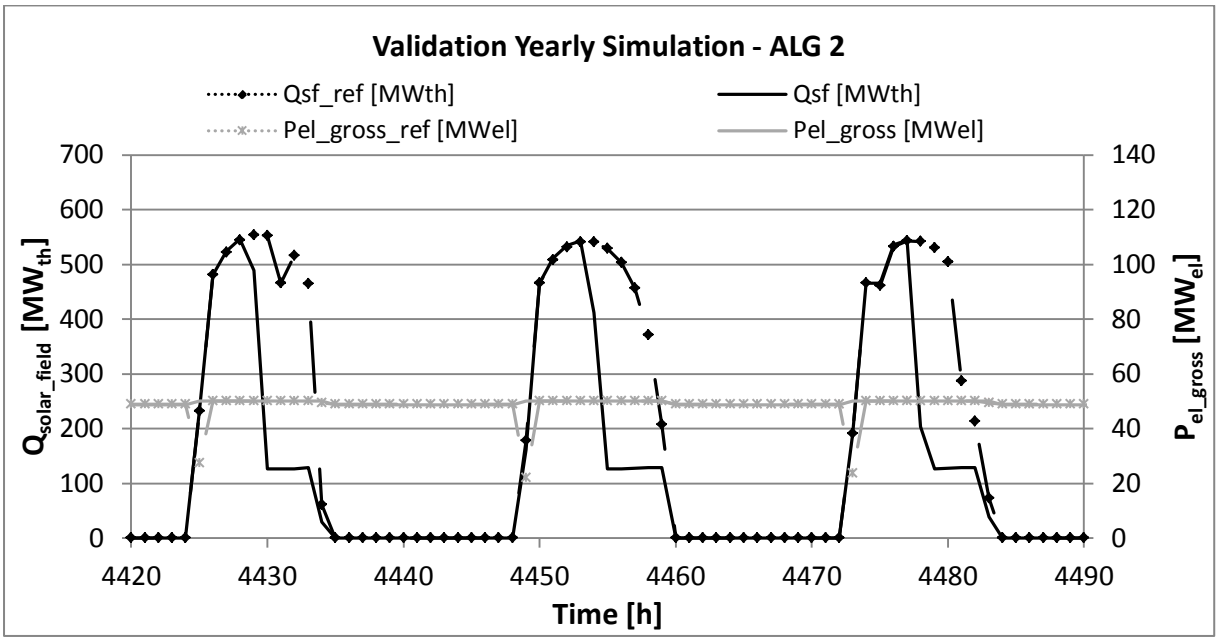

Figure 94: Validation of CSP model – Oil based parabolic trough solar field with thermal storage

Molten Salt Model

The implemented parabolic trough molten salt INSEL module has been validated with the simulation tool EBSILON. The current chapter summarizes the main results of this comparison. The work of [Wagner 2012] has been taken as reference for the current analysis. This study focuses on the annual yield simulation of a 125 MW_{el} CSP plant with a SM of ca. 2.2 and a 10 full load hours thermal storage located near Las Vegas (Table 45), a site with excellent DNI resources (2,650 kWh/m²/y). Table 45 gives an overview on the most relevant plant specifications.

As mentioned in paragraph 4.2.5, a molten salt plant presents some particularities in comparison with a VP-1 plant. The most important of them is that the HTF freezes at high temperature (ca. 240 °C). In order to deal with this restriction, the salt is recirculated through the solar field whenever the temperature falls below 270 °C. The anti-freeze heat is taken from the cold tank of the thermal energy storage, or -if the TES is completely discharged- from the auxiliary fossil heater.

Table 46 compares the results of the INSEL and of the EBSILON model. The agreement between the two models is very good (differences below 1 % referred to annual sums) for the net solar heat as well as for the gross and the net power generation. The other listed parameters such as parasitic and thermal losses present a discrepancy below ca. 5 %, which is acceptable for the purpose of this work.

For the majority of the other parameters however hourly values are available. This makes the identification and the correction of eventual mismatches between models easier.

CSP Power Plant	Unit	Value
Power Block		
Type	-	single re-heat, condensing
Installed gross capacity	MW_{el}	125.0
Life steam conditions	bar / °C	150 / 500
No. Low / high pressure pre-heater	-	3 / 2
HTF heater capacity	MW_{th}	25
Condenser cooling system	-	Fixed Pressure (0.08 bar)
Gross Nominal Efficiency	%	44.25%
Solar Field & HTF System		
Collector net aperture area	m^2	817.5
Number of Loops	-	352
Collector spacing	m	16.5
Heat transfer fluid (HTF)	-	Solar Salt
HTF temperature (in / out)	°C / °C	310 / 510
Thermal Energy Storage		
Type	-	Direct two-tank molten salt
Storage medium	-	60% $NaNO_3$ / 40% KNO_3
TES capacity (Full load hours)	h	10
Molten salt mass	tons	33,555
Location and DNI Data		
Site	-	Las Vegas
Latitude / Longitude	°	36.06 / -115.08
Annual DNI Sum	$kWh/m^2/y$	2,650

Table 45: Plant specifications and DNI Data

Figure 95 presents a comparison of INSEL and EBSILON results for three sample days. The INSEL model seems to describe very good the behavior of the solar field (start-up, operation, defocussing of part of the collector after noon due to the full storage). A slight difference can be found on the thermal output of the solar field in the evening hours directly after sunset.

Results	Reference Model [GWh_{th}/y]	INSEL Model [GWh_{th}/y]	Difference [%]
Irradiation on Net Aperture	**3,057.2**	**3,050.6**	**0.22%**
Heat Losses Receiver	293.9	285.1	2.99%
Dumping	140.9	182.2	-29.33%
Solar Field Net Heat	**1,345.7**	**1,341.3**	**0.32%**
Heat Losses TES Tanks	8.3	8.5	-2.19%
Auxiliary Heater	45.2	43.2	4.44%
Power Block Start-up Losses	48.2	46.3	4.05%
Gross Power Generation	572.1	567.3	0.84%
Solar Field + TES Parasitics	12.6	12.5	0.78%
Power Block Parasitics (w/o cooling)	12.2	11.7	4.50%
Net Power Generation	**547.3**	**543.8**	**0.64%**

Table 46: Molten Salt model validation - Result summary

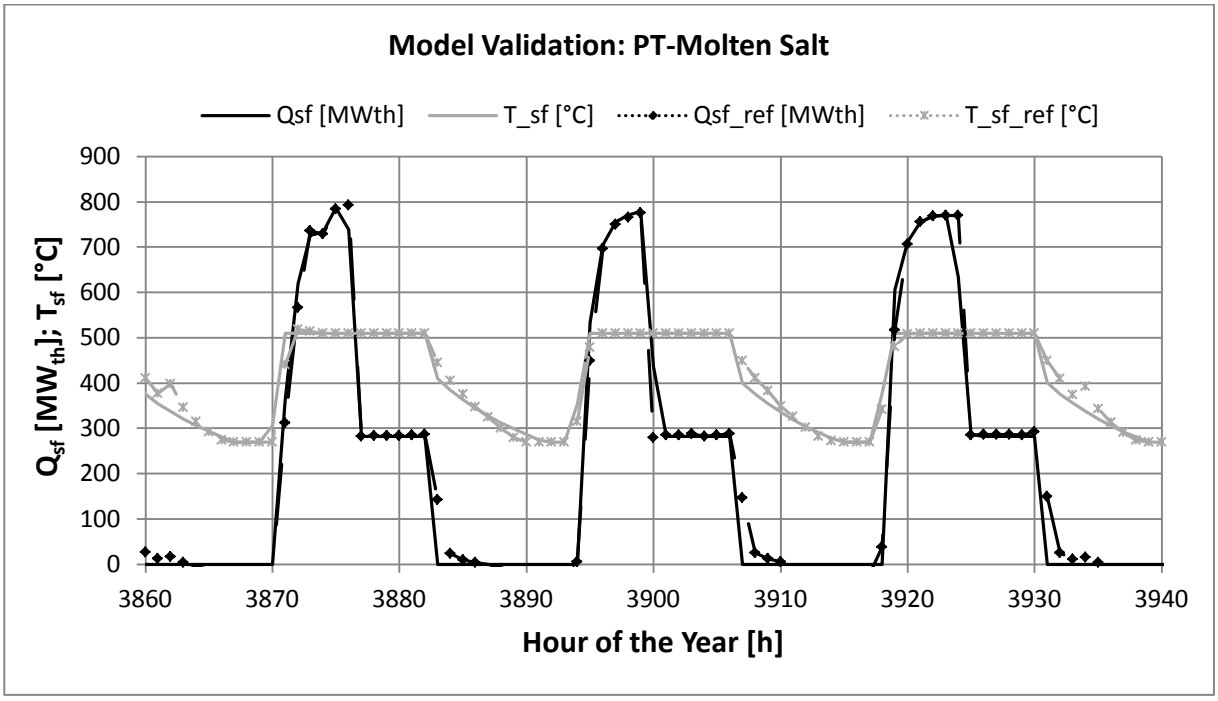

Figure 95: Molten salt parabolic trough model – Solar field collected heat and HTF temperature profiles

Finally, in Figure 96 the status of charge of the thermal energy storage and the gross power generation are compared. Besides marginal differences during start-up and shut-down times, the power generation modeled with INSEL reproduces well the production patterns of the EBSILON model.

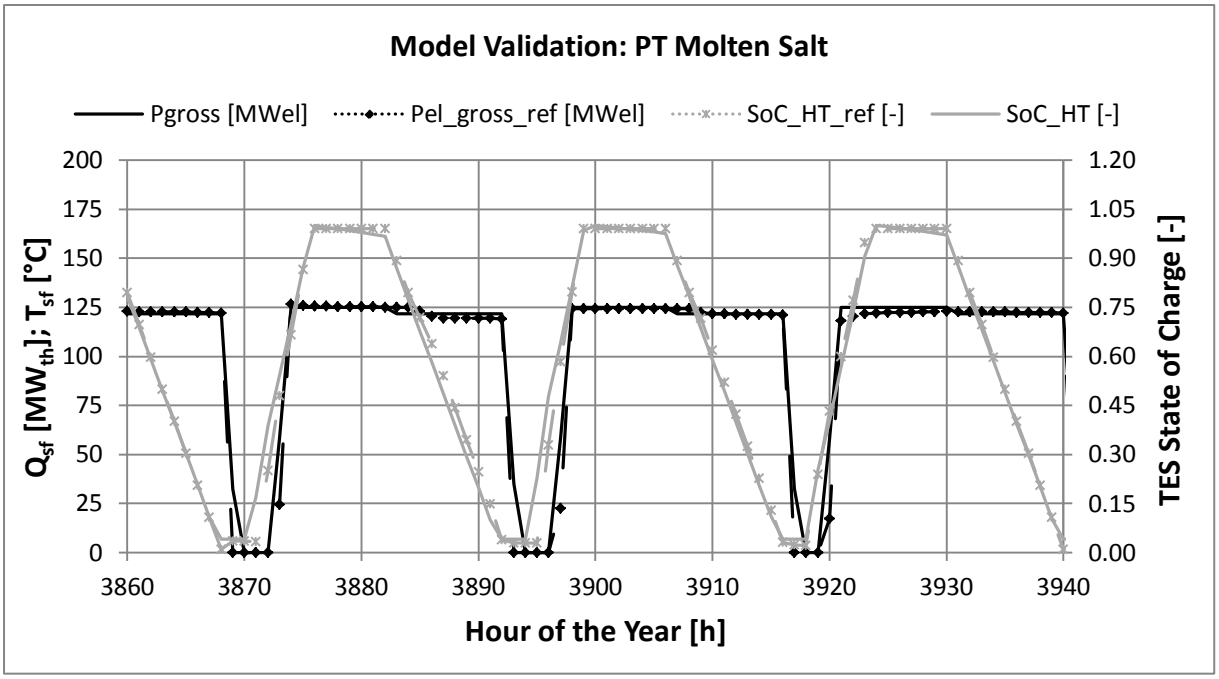

Figure 96: Molten salt parabolic trough model – TES State of Charge and Gross Power Production

DSG Model

The validation of the DSG model has been carried out by a comparison of the INSEL model with an Excel-based tool developed by the Department of Solar Research of the DLR. The reference model is used in order to perform yearly simulations with reasonable time effort. An even more detailed commercial simulation tool called IPSEpro is utilized in order to analyze the behavior of the solar field and of the power block in few characteristic operating points such as nominal operation condition, storage discharge and some selected part load cases.

The gained data are then used to generate several characteristic lines for the annual simulation tool. The reference Excel tool also takes into account the start-up behavior by consideration of an additional mass integrated with the solar field. This mass is characterized by temperature-dependent energy losses. Wind effects on the performance of the solar field are neglected. Concerning the thermal energy storage, PCM is assumed even if this option is still not commercially available up to now. The energy losses of the PCM may lead, in particular during prolonged times without irradiation, to negative values of the state of charge. In these cases, before starting normal plant operation, the heat collected by the solar field is firstly used to compensate for these energy losses till a state of charge major than zero is reached. Within this model, additional co-firing is not provided. The required heat for the start-up of the power block is a fixed heat amount (half full-load hour) which has to be delivered by the solar field after a defined offline time of three hours.

Table 47 summarizes the main design parameters which have been used for the validation of the INSEL DSG model. Eurotrough-like collectors have been selected. The layout of the solar

field -other than in oil-based CSP plants- is divided in evaporation section and superheating section, so that the ratio between the two sections has also to be specified.

The results of the comparison are presented in Figure 97. Here is shown that the matching of the hourly values of heat collected by solar field, state of charge of the thermal storage and generated electricity is very good. Nominal operation, start-up, storage discharge and part load conditions are well-reproduced. Accordingly, also the annual sums of solar field collected heat and gross electricity generation of the two models are very similar. The relative errors are lower than 1.7 %.

The results of the simulation also show that during storage discharge the gross electricity generation is clearly lower than during direct operation from the solar field. This is due to the particular characteristics of the PCM; during storage discharge the steam parameters (temperature and pressure) which can be reached are both lower than under nominal conditions. This leads to lower turbine efficiency. The same effect can be observed to a smaller extent also in oil-based CSP plants with 2-tank molten salt storage.

CSP Power Plant	Unit	Value
Power Block		
Type		Single re-heat, condensing
Installed gross capacity	MW_{el}	120.0
Life steam conditions	bar / °C	100 / 500
No. Low / high pressure pre-heater	-	3 / 2
HTF heater capacity	MW_{th}	-
Condenser cooling system	-	Fixed pressure (0.08 bar)
Gross nominal efficiency	%	41.1%
Solar Field & HTF System		
Solar multiple (SM)	-	2.0
Collector type	-	Eurotrough
Evaporator/Superheater ratio	-	1.71
Number of loops	-	148
Area solar field	m^2	967,920
Collector spacing	m	16.5
Heat transfer fluid (HTF)	-	Water/Steam
HTF temperature (in / out)	°C / °C	260 / 500
Thermal Energy Storage		
Type	-	Phase change material (PCM)
TES capacity (Full load hours)	h	8.0
Location and DNI Data		
Site	-	Daggett
Latitude / Longitude	°	34.86 / -116.89
Annual DNI sum	$kWh/m^2/y$	2,723

Table 47: Key design data used for the validation of the DSG model

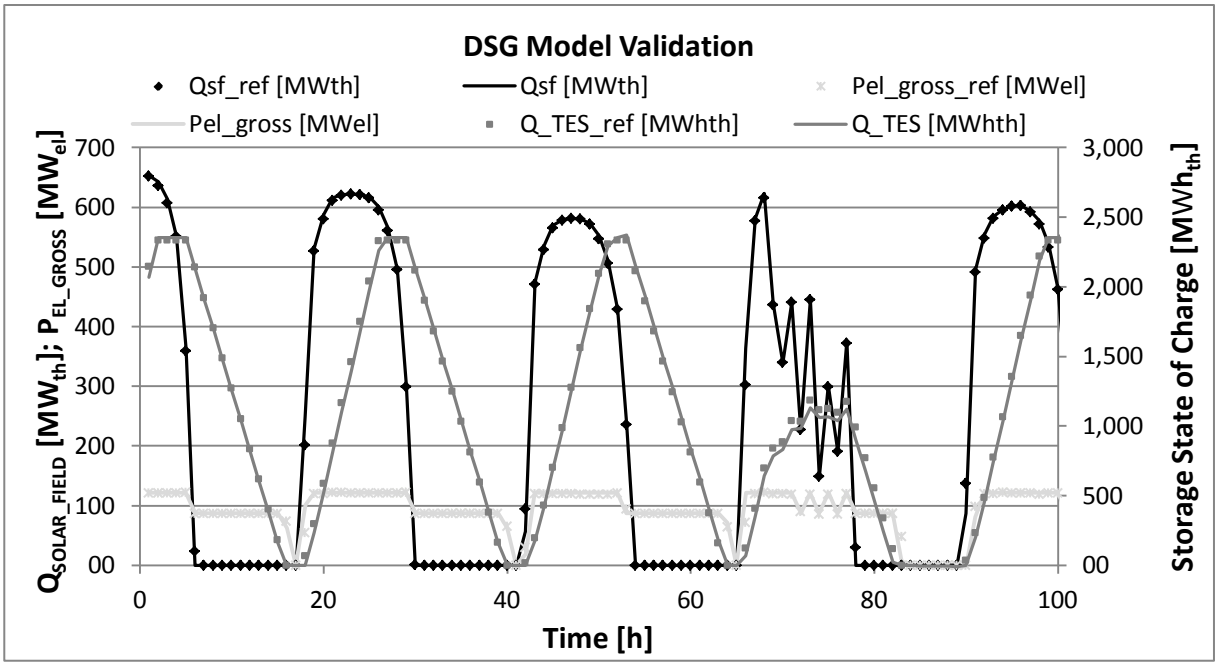

Figure 97: Results extract from the validation of the DSG model

10.2.6 Alternative Thermal Energy Storage Concepts

Concrete Storage

The application of passive storage systems such as concrete storage is mainly motivated by the potential reduction of investment and operating cost in comparison to molten salt systems [Laing 2006]. The basic storage module is made up of a tube register which serves as a heat exchanger between HTF and storage medium, as shown in Figure 98 [Bahl 2009].

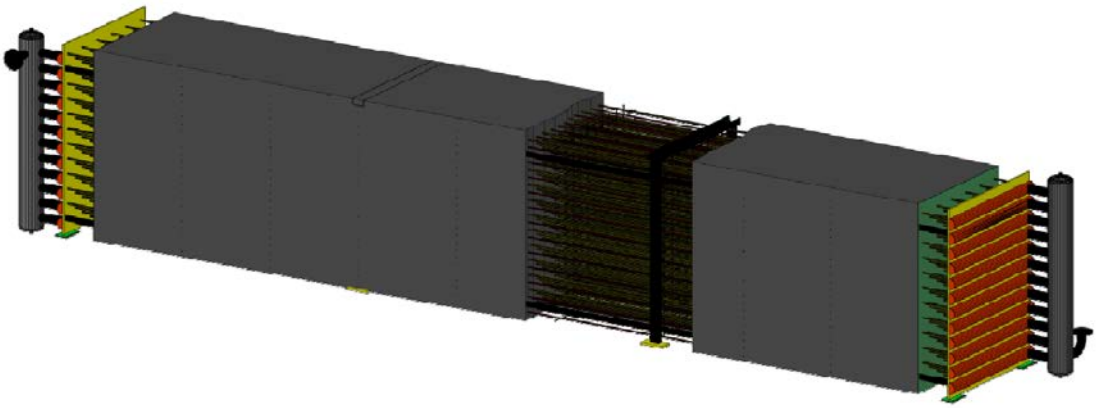

Figure 98: Storage module with visible tube register [Bahl 2009]

In [Bahl 2009] it has been evaluated that the set-up of a concrete storage suitable for the Andasol plant would consist of several parallel rows with each row consisting of a series of basic modules. The needed area would amount to approx. 1.5 % of the total land requirements, which corresponds to a 300 m x 100 m rectangle. The main disadvantage of this storage concept is that the temperature decreases during the discharge. Particular care has to be taken during the first heating-up. In this, the concrete has to expel the excess

water in order to avoid breaking in the modules. Finally, the low material cost is counterbalanced by the low heat conductivity of the concrete and by the relatively high cost required for the heat exchanger. Alternative designs which aim at the reduction of these disadvantages such as the Cell-flux concept are currently the object of research [Steinmann 2011].

Concrete Storage Model

The concrete storage consists of a tubular heat exchanger which is integrated into the concrete volume [Steinmann 2005]. The implemented model assumes that the basic concrete module is made up of a series of parallel concrete cylinders with a heat exchanger tube in the middle. Figure 99 exemplifies the geometrical setup of the model. In radial direction, only two temperatures are considered: HTF temperature and average storage temperature (i.e., infinite thermal conductivity of the storage medium in radial direction is assumed).

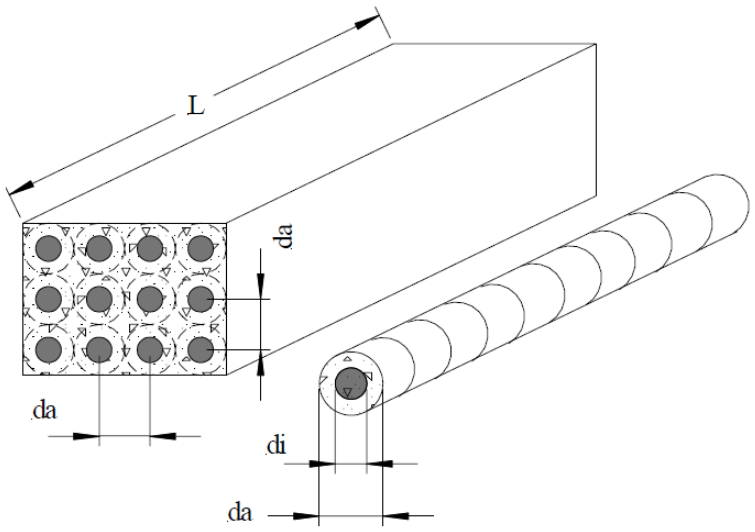

Figure 99: Modeling scheme of the concrete storage module with axial discretization [Steinmann 2005]

In axial direction, a discretization is made in order to take into account the temperature changes over the x-coordinate of the heat exchanger. During the charging process, the hot HTF enters the storage and cools down as it flows through the heat exchanger tube. The thermal energy balance of the HTF passing through a finite concrete volume is [Schmidt 1981]:

$$\frac{k \cdot A \cdot \Delta x}{L} \cdot (T_c - T_{HTF}) + \dot{m}_{HTF} \cdot c_{p\_HTF} \cdot T_{HTF}\big|_x = \dot{m}_{HTF} \cdot c_{p\_HTF} \cdot T_{HTF}\big|_{x+\Delta x} + S_{HTF} \cdot \Delta x \cdot \rho_{HTF} \cdot c_{p\_HTF} \cdot \frac{\partial T_{HTF}}{\partial \tau} \quad \text{Eq. 10.33}$$

k	[W/m²/K]	heat transfer coefficient between concrete and fluid
A	[m²]	lateral surface of the heat exchanger tube

L	[m]	total tube length
S_{HTF}	[m²]	internal cross-surface of the heat exchanger tube

The left part of Eq. 10.33 represents the heat transfer between storage medium and HTF (first term) and the energy content of the HTF entering the considered volume. These two terms are equal to the energy content of the HTF at the outlet of the section plus the energy accumulation of the transfer fluid over time. The last term is negligible and can be therefore removed from the equation. The physical and geometrical constants are summarized as a non-dimensional distance factor:

$$\xi = \frac{h \cdot A \cdot x}{\dot{m}_{HTF} \cdot c_{p\_HTF} \cdot L} \qquad \text{Eq. 10.34}$$

Finally, Eq. 10.33 is simplified as follows:

$$\frac{T_{HTF}|_{x-\Delta x} - T_{HTF}|_x}{\Delta x} = \xi \cdot (T_c - T_{HTF})|_{x-\Delta x} \qquad \text{Eq. 10.35}$$

A similar energy balance can be stated for the storage side:

$$\frac{T_c|_{t-\Delta t} - T_c|_t}{\Delta t} = \chi \cdot (T_{HTF} - T_c)|_{t-\Delta t} \qquad \text{Eq. 10.36}$$

The non-dimensional time χ is:

$$\chi = \frac{h \cdot A \cdot \Delta t}{S_c \cdot L \cdot \rho_{HTF} \cdot c_{p\_HTF}} \qquad \text{Eq. 10.37}$$

Eq. 10.35 and Eq. 10.36 can be solved if the initial temperature distribution in the storage is known. The values of Δt and Δx have to be selected accurately in order to avoid numerical instability in the solution process. In particular, the typically used Δt of one hour has been reduced to 15 minutes. The heat losses of the reference storage module (8.6 m x 1.7 m x 1.3 m) are a function of the average storage temperature and of the ambient temperature [Bahl 2009]:

$$\dot{Q}_{TES\_loss\_ref} = 9.35 \cdot (\bar{T}_{TES} - T_{amb})^{1.201} \qquad \text{Eq. 10.38}$$

$\bar{T}_{TES}$	[°C]	average temp. of the reference storage module

For other module geometries, the heat losses are assumed to be proportional to the ratio between the current lateral area and the reference lateral area. The auxiliary electrical power required for the pumping of the HTF through the heat exchanger is:

$$P_{parasitic\_TES} = \frac{\Delta p_{HTF} \cdot \dot{m}_{HTF}}{\rho_{HTF} \cdot \eta_{pump}} \qquad \text{Eq. 10.39}$$

The design pressure losses Δp_{HTF} are assumed to be 6 bar [Johnson 2010].

Phase Change Material (PCM)

Direct steam generation (DSG) is a promising option for further cost reduction of CSP [Laing 2011]. However, DSG requires specific and innovative storage concepts. Thus, the water/steam phase change poses a major challenge. In fact, large amounts of heat at a constant temperature level have to be supplied by the storage during the discharge in order to evaporate the water. This purpose cannot be efficiently fulfilled by sensible heat storages. The main difference between sensible heat storage and PCM lies in the different temperature profiles which can be realized in the heat exchanger (HX) between water/steam and storage, as exemplified in Figure 100. The temperature profile in the HX of sensible heat storage is affected by several constraints (Figure 100 - left). Firstly, the temperature change of the storage medium is linear, while the temperature change in the steam/water system involves three phases: sensible steam de-superheating, isothermal condensation and sensible undercooling. Secondly, a minimum driving temperature difference -e.g. 10 K- is required in the heat exchanger (ΔT_{HX_min}). Due to these constraints, the temperature that can be realized in the storage is significantly lower than the steam temperature at the inlet of the storage T_{steam_in}. Further, the maximum steam temperature during storage discharge is lower. According to the saturation curve, the steam pressure is also lower [Laing 2010]. The reduction of the steam parameters has a negative impact on the turbine efficiency.

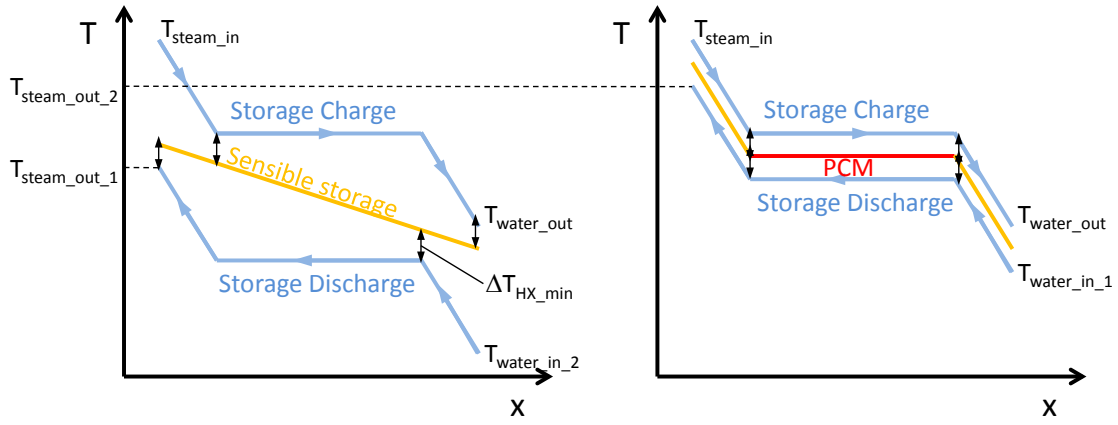

Figure 100: Thermal profiles in the heat exchanger of a DSG storage. Left: sensible thermal storage only; Right: combined sensible/PCM storage [Laing 2010, adapted]

The right part of Figure 100 shows a combined storage concept as it has been proposed by DLR and Züblin for DSG applications. The water preheating and the steam superheating are provided by sensible heat storage modules (e.g. concrete) and the heat of evaporation is supplied by a PCM module [Laing 2010]. A number of variations of this basic storage layout has been evaluated and compared in the DETOP project [Feldhoff 2012 b]. The introduction

of the PCM module allows delivering large amounts of heat in a very narrow temperature range, which exactly matches the temperature profile of the steam/water system. Therefore, the plant efficiency can also be maintained on a high level during storage discharge, because the steam saturation temperature is only approx. 20 K lower than during solar operation. The main disadvantages of PCM storage systems are the early stage of development and the high investment cost.

Buffer Storage for DSG

Due to the fact that PCM is still not commercially available, buffer storages are used so far in DSG applications. Buffer storages aim at the compensation of short-time and mostly unpredictable transients of solar irradiation [Steinmann 2006]. Therefore, plant components can be protected from the impact of such transients. Due to the fact that steam has low volumetric energy density, the direct storage of steam is not economically feasible. Steam accumulators consist of pressurized tanks which are partially filled with saturated water in the liquid phase (Figure 101). During charge procedures, steam enters the storage and condenses, increasing the temperature of the water. Alternatively, saturated liquid water is additionally fed into the storage.

During the discharge, steam is generated by gradually lowering the pressure. Such systems are called sliding pressure systems or Ruths systems. Constant pressure concepts exist as well [Steinmann 2006], which also allow maintaining constant temperature during discharge. Such systems are equipped with an external depressurization chamber (flash evaporator). Steam buffer storages are cost-competitive only for small storage capacities (not longer than approx. one hour) and for low pressures, as can be seen in Figure 101 (right).

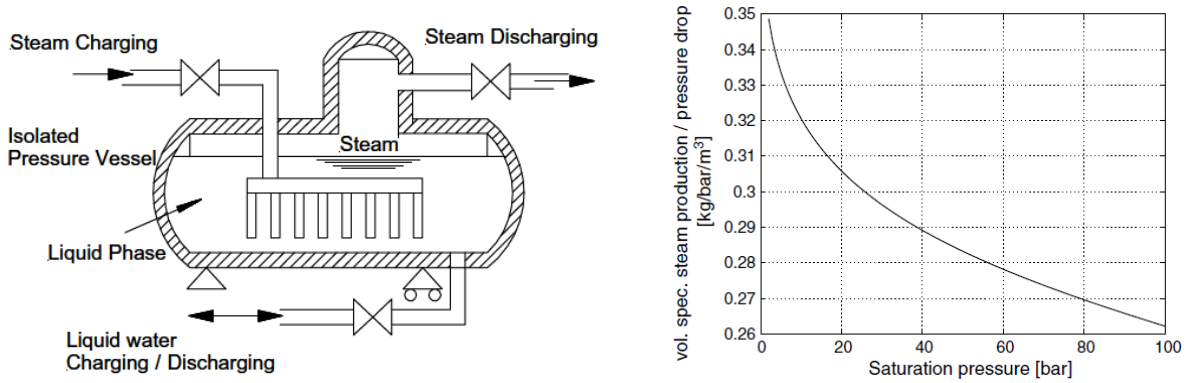

Figure 101: Scheme of a buffer storage (left) and specific steam production as function of saturation pressure [Steinmann 2006]

10.3 Details of Economic Models

10.3.1 Desalination

Operation Cost Calculation

Operation cost consists of fixed and variable costs (Table 48).

Fixed Costs	Variable Costs
Annual capital Cost	Thermal Energy
Personnel	Electrical Energy
Maintenance and Repair	Chemicals and Additives
	Membrane Replacement

Table 48: Breakdown of operating costs for desalination plants

The annual capital costs are calculated by means of the capital factor method. The calculation has been carried out with the same procedure used for the LEC calculation. The annual water production calculated in the technical model is multiplied by the plant availability in order to take into account the off-times of the plant due to cleaning and maintenance.

Personnel cost can be simply assessed as far as the number of employees and their qualification are known (Table 53):

$$C_{pers} = \sum_{i=1}^{n} n_{pers\_i} \cdot c_{pers\_i} \qquad \text{Eq. 10.40}$$

C_{pers}	[Mio. €/y]	annual personnel cost
c_{pers_i}	[€/y/cap]	annual salary per employee for position i
n_{pers_i}	[-]	number of persons for position i

The fixed annual costs for maintenance and repair can be expressed as:

$$C_{M\&R} = C_{CAPEX} \cdot f_{M\&R} \qquad \text{Eq. 10.41}$$

$C_{M\&R}$	[Mio. €/y]	annual cost for maintenance and repair
$f_{M\&R}$	[%]	percent of CAPEX for M&R

The $f_{M\&R}$ parameter depends on the plant layout; typical values are between 3.0 % and 3.3 % for MED units and approx. 2.7 % for SWRO plants [MENAWATER 2011]. The electricity cost of the desalination plant is calculated as:

$$C_{el} = E_{el\_y\_des} \cdot LEC \qquad \text{Eq. 10.42}$$

C_{el}	[Mio. €/y]	annual cost for electricity supply
$E_{el\_y\_des}$	[GWh/y]	annual electricity consumption for desalination

The annual electricity consumption of desalination plants is the sum of electricity requirements for the process itself and the energy needed for seawater intake and brine discharge. The detailed explanation of the assessment of these factors has been given in 3.1.3 and 3.2.3.

The variable costs also include the costs for chemical and consumables for water pre-treatment, desalination process and post-treatment. The determination of these costs is typically carried out by means of a mass-flow-based approach (Table 54):

$$C_{chem} = \sum_{i=1}^{n} \dot{m}_i \cdot \frac{x_i}{x_i^*} \cdot h/y_i \cdot c_{chem\_i} \qquad \text{Eq. 10.43}$$

C_{chem}	[Mio. €/y]	annual chemical cost
$\dot{m}_i$	[kg/s]	receiving mass flow
x_i^*	[%]	commercial chemical concentration
x_i	[mg/l]	chemical concentration to receiving flow
h/y_i	[h/y]	annual operation time of chemical dosing
c_{chem_i}	[€/ton]	specific chemical cost

The specific chemical cost for MED mainly consist of antiscalant cost and remineralization agents cost. Specific chemical cost for MED are approx. 0.03 €/m³. Membrane desalination technologies present significantly higher specific chemical costs (approx. 0.06 €/m³) due to high cost for coagulants, which are required in the demanding pretreatment section. The antiscalants used in the RO process also contribute to the high chemical costs. A further remark should be made in respect to the membrane replacement costs. Membranes are subject to deterioration and after a certain amount of operation hours they have to be exchanged. Due to the fact that large desalination units are characterized by relatively high membrane replacement costs, the depreciation method should be used for a correct cost assessment [Gebel 2008]. In particular, the depreciation of investment for membranes should be carried out for the guarantee period of the membranes (given by the supplier) instead for the whole life time of the desalination plant. A depreciation period of 5 years has been chosen for the reference case [Gebel 2008].

MED

The calculation of the capital cost is performed by breaking down the whole MED plant into functional groups. For each group a cost assessment is carried out, i.e. intake, pump station and brine discharge, feed water pre-treatment, steam supply, evaporator (incl. erection and commissioning), potabilization plant, drinking water storage, civil works as well as instrumentation and control (I&C) and electrical works (Figure 102).

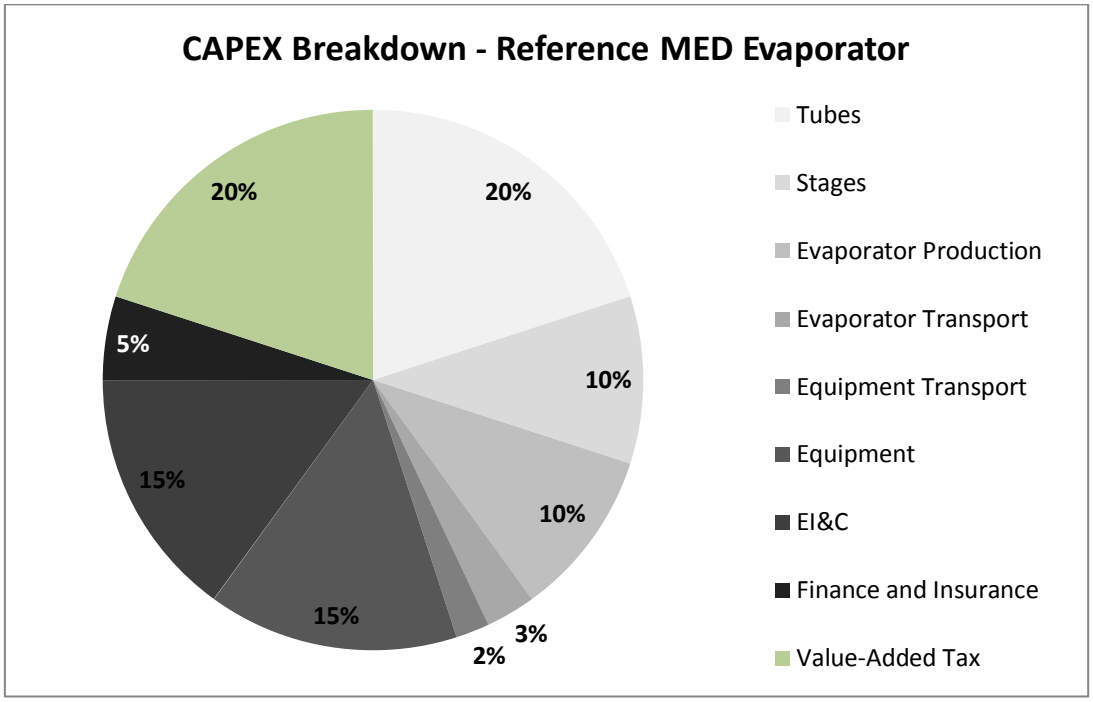

Figure 102: CAPEX breakdown for the MED reference evaporator (CIF price, September 2010)

The assessment of the specific costs of the evaporator -which is the core of the MED plant- is carried out in two steps: in the first step the cost breakdown of a reference plant is selected, for which the price is known. The selected reference is a 6-stages MED with a total evaporator CAPEX of 720 €/(m³/day) [SIDEM 2010].

In the second step, the reference costs are adapted for a general case taking into consideration the impact of the number of stages on the CAPEX. Figure 103 shows that the higher the number of stages is, the higher is the cost of the evaporator tube bundle. This is due to the larger area of the heat exchangers. As the geometry of each effect is the same, a linear trend could be expected. However, the increase of the number of stages also implicates a reduction of the effective temperature difference between two stages, which results in a hyperbolic cost escalation. The value of the specific heat transfer area sA is calculated in the MED technical model as presented in 3.1.3.

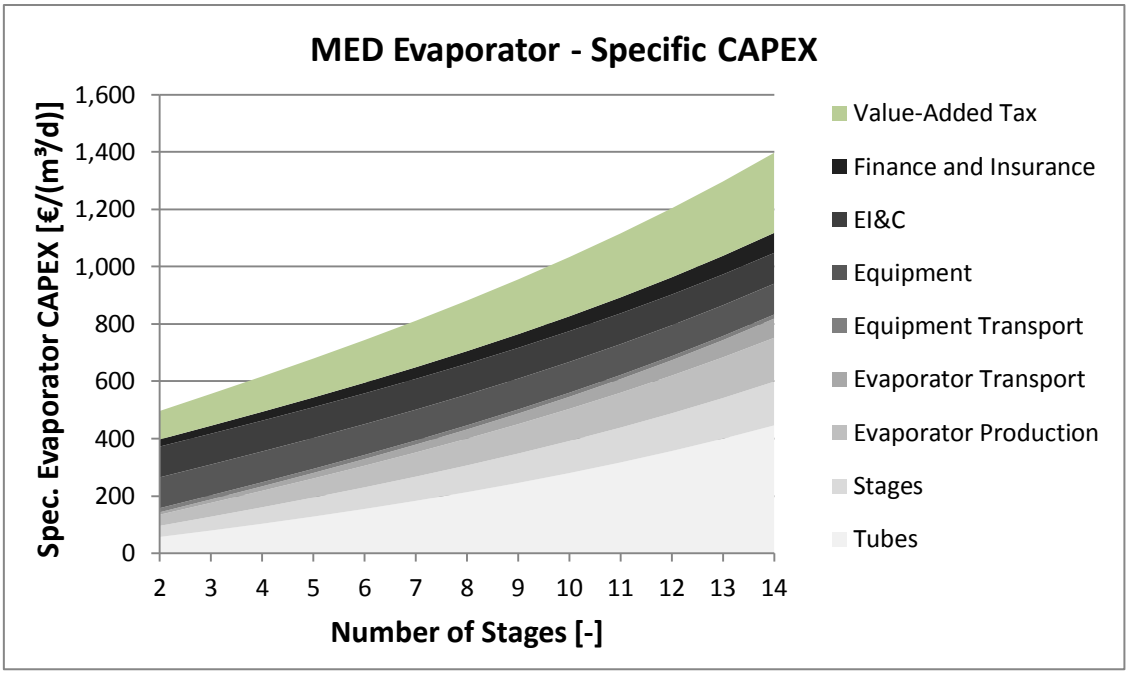

Figure 103: MED CAPEX breakdown as a function of the number of stages (large unit capacity)

The costs for the evaporator production and transportation are assumed to be proportional to the ratio between the specific heat transfer area of the evaporator in a particular case and in the reference case. The finance and insurance cost and the added value tax are 5 % and 20 % of the total MED CAPEX, respectively [SIDEM 2010]. The costs of the other functional groups of the MED plant are calculated with a procedure similar to the one used for the evaporator costs, i.e. the selection of a reference plant and a successive adjustment of the cost model for the general case. The selected reference plant is a 14-stages plant [MENAWATER 2011]. The total specific investment cost is approx. 2,250 €/(m³/day). The MED evaporator cost accounts for barely 60 % of the total CAPEX (Figure 104).

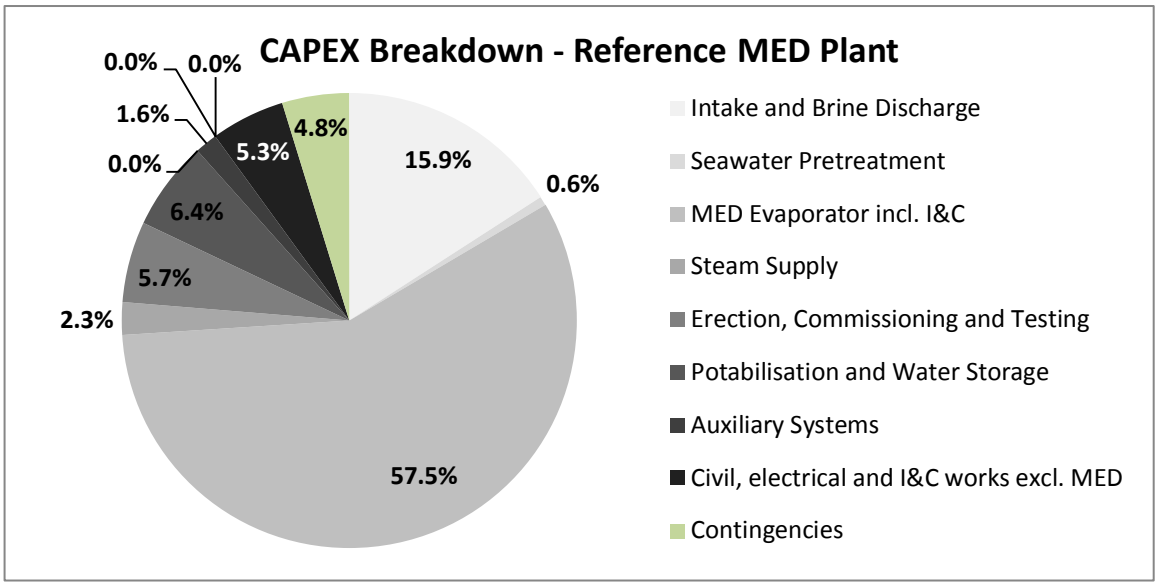

Figure 104: CAPEX breakdown of the reference MED plant

Another important share is represented by the intake system and the brine discharge system (around 16 %). The seawater pretreatment (mainly chlorination) accounts for less than 1 % of the total CAPEX. Finally, the investment costs of the reference case have to be adapted for the general case. The impact of the number of stages on the evaporator cost has already been taken into account in the previous analysis. It remains to consider the effect of the seawater intake. This is a very site-specific issue. In fact, the intake cost depends on several parameters such as the bathymetric profile of the shore, the intake type (e.g. open intake, submerged intake, beach well) and the required water flow, which in turn is a function of the design seawater temperature rise in the condenser. Due to environmental protection regulations, some sites have salinity and temperature rise limits, which may require additional seawater for dilution [Desportes 2013]. The efficiency of the MED plant also influences the necessary cooling water flow. The lower the number of stages is, the higher is the required cooling water flow. Finally, a differentiation can be made in the outfall options (e.g. open channel, pipe in the sea with diffusers).As a base case submerged intake and pipe brine discharge have been selected. The allowed temperature increase of seawater in the condenser is 8 K.

Reference Evaporator CIF	Unit	Value
Tubes	$/(m³/d)	200
Clad Sheets	$/(m³/d)	100
Fabrication	$/(m³/d)	100
Transport evaporator	$/(m³/d)	30
Transport equipment	$/(m³/d)	20
Equipment	$/(m³/d)	150
EI&C	$/(m³/d)	150
Finance & Insurance	$/(m³/d)	50
Added Value	$/(m³/d)	200
Sum	$/(m³/d)	1,000

Table 49: Reference MED evaporator cost; assumption: 6-stage evaporator (CIF), 100,000 m³/d capacity [Sidem 2010]; CIF = cost, insurance and freight; EI&C = electrical, instrumentation and controls

MED Plant	Unit	Value
Intake , pump station and outfall incl. civil	$/(m³/d)	500
Seawater chlorination	$/(m³/d)	20
Process incl. Electrical and I&C	$/(m³/d)	1,810
Steam supply and condensate return	$/(m³/d)	72
Erection, commissioning and testing	$/(m³/d)	181
Potabilization Plant	$/(m³/d)	100
Drinking Water Storage & pumping	$/(m³/d)	100
Auxiliary Systems	$/(m³/d)	50
Civil Works MED	$/(m³/d)	91
Civil infrastructure	$/(m³/d)	30
Electrical works excluding MED	$/(m³/d)	30
I&C works excluding MED	$/(m³/d)	15
Direct Cost	$/(m³/d)	2,999
Contingencies	% of Direct Cost	5.0
Total MED Plant	$/(m³/d)	3,149

Table 50: MED plant capital cost; assumption: 14-stage evaporator, 100,000 m³/d capacity [MENAWATER 2011]; I&C = instrumentation and controls

Chemicals	Commercial Concentration	Chemical 100 % to receiving Flow	Operation Time	Specific Cost
-	%	mg/l	h/h	US$/t
Seawater Pretreatment				
Liquid chlorine as Cl^2	100.0%	0.0	1.0	1,200
MED Process				
Antiscalant	100.0%	3.0	1.0	2,500
Antifoam	100.0%	0.2	1.0	5,000
Post-treatment				
Hydrated Lime $Ca(OH)^2$	94.0%	35.0	1.0	180
Polyelectrolyte (lime sat. feed)	100.0%	2.0	1.0	2,500
Carbon Dioxide CO^2	99.5%	40.0	1.0	180
Chlorine	100.0%	0.0	1.0	1,200

Table 51: Overview of assumed chemical dosage and cost for MED plants [MENAWATER 2012]

SWRO

Also in the case of SWRO, the calculation of capital cost is performed by breaking down the whole plant into functional groups. Where applicable, the same functional groups as for the MED are used. Figure 105 presents the CAPEX breakdown for the selected reference SWRO plant. The breakdown applies for a large SWRO plant with open intake and a demanding pre-treatment consisting of dissolved air flotation, gravity filters and pressure filters (common choice in the Arabian Gulf). The total CAPEX amounts to 1,730 €/(m^3/day).

Similarly to the MED case, the investment cost needs to be adapted in order to take into account the case-specific intake cost, which are a function of intake type, plant capacity and SWRO design recovery ratio. In addition, different pre-treatment systems may also be used (e.g. sand filters, dissolved air flotation etc.). The selection of the recovery ratio as well as of the most adapted pre-treatment is affected by the feed water quality and salinity (3.2.3).

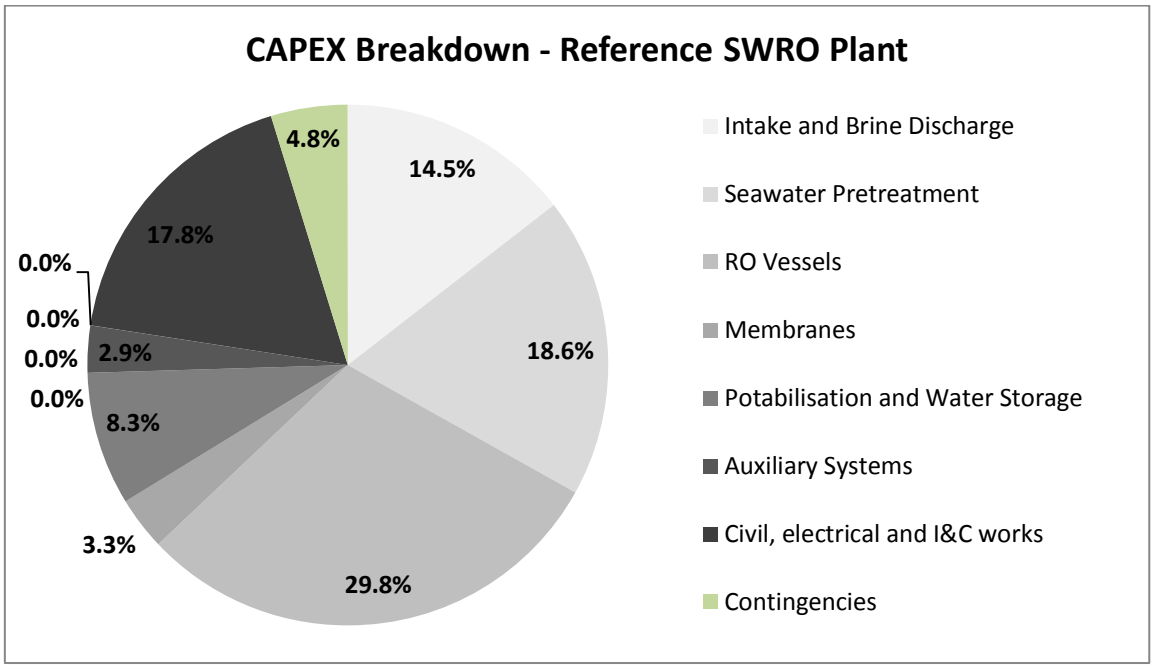

Figure 105: CAPEX breakdown of the reference SWRO plant [MENAWATER 2011]

SWRO Plant		
Intake , pump station and outfall	$/(m³/d)	300
Pretreatment System	$/(m³/d)	250
Membranes (without vessels)	$/(m³/d)	80
Reverse osmosis without membranes	$/(m³/d)	720
Potabilization Plant	$/(m³/d)	100
Drinking Water Storage & pumping	$/(m³/d)	100
Wastewater collection & treatment	$/(m³/d)	50
Auxiliary Systems	$/(m³/d)	70
Civil works	$/(m³/d)	160
Electrical works	$/(m³/d)	150
I&C works	$/(m³/d)	70
Total	$/(m³/d)	2,050
Contingencies	% DC	103
Total SWRO Plant	$/(m³/d)	2,153

Table 52: SWRO plant capital cost; assumption: two-pass system, conventional pre-treatment, 100,000 m³/d capacity [MENAWATER 2011], adapted

Position	**Number of Persons**	**Salary**	**Annual Costs**
	-	$/y/Person	$/y
Plant manager	1	90,000	90,000
Administration	2	40,000	80,000
Secretary	1	30,000	30,000
Process Engineer	1	70,000	70,000
Electrical Engineer	1	70,000	70,000
I&C Engineer	1	70,000	70,000
O&M planning supervision eng.	1	70,000	70,000
Operator	4	40,000	160,000
Chemist	1	50,000	50,000
Lab Assistant	1	40,000	40,000
Support staff	6	30,000	180,000
Total	20		
Total Personnel Cost			**910,000**

Table 53: Exemplary personnel cost breakdown for a 100,000 m³/day SWRO desalination plant [MENAWATER 2011]

Chemicals	Commercial Concentration	Chem. 100 % to receiving Flow	Operation Time	Specific Cost
-	%	mg/l	h/h	US$/t
Pretreatment SWRO				
Chlorination Seawater				
Liquid chlorine as Cl_2	100.0%	0.0	0.0417	1,200
Sodium Hypochlorite (as NaOCl)	12.5%	8.4	0.0417	250
Flocculation				
Coagulant Ferric Chloride	42.0%	20.0	1.0	220
Flocculant (Polyelectrolyte)	100.0%	1.0	1.0	3,000
Sulphuric Acid	98.0%	15.0	1.0	180
Dual Media Filtration				
Coagulant Ferric Chloride (2. filter stage)	42.0%	5.0	1.0	220
Flocculant (Polyelectrolyte - 2. filter stage)	100.0%	0.0	1.0	3,000
Membrane Filtration - BW & CEB				
BW Sodium Hypochlorite	12.5%	0.0	0.5455	250
CEB Sodium Hypochlorite	12.5%	0.0	0.0007	250
CEB Caustic Soda	40.0%	0.0	0.0007	350
CEB Hydrochloritic acid	36.0%	0.0	0.0007	120
SWRO				
Sulphuric Acid H_2SO_4 - 1st pass feed	98.0%	0.0	1.0	180
Caustic Soda NaOH - 1st pass feed	40.0%	0.0	1.0	350
Bisulphite $NaHSO_3$	35.0%	2.9	0.0417	400
Antiscalant 1st pass feed	100.0%	6.0	1.0	2,500
Chlorine 1st pass feed				
Liquid Chlorine (as Cl_2)	100.0%	0.0	0.0	1,200
Sodium Hypochlorite (as NaOCl)	12.5%	0.0	0.0	200
Antiscalant 2nd pass feed	100.0%	3.0	1.0	3,000
Caustic Soda 2nd pass feed	40.0%	8.6	1.0	350
Wastewater Treatment (WWT)				
Coagulant WWT Ferric Chloride	42.0%	15.0	1.0	220
Polyelectrolite WW	100.0%	1.0	1.0	4,000
Polyelectrolyte Sludge Dewatering kg/t DS	100.0%	4.0	0.6667	4,500
Post-treatment				
Hydrated Lime $Ca(OH)_2$	94.0%	35.3	1.0	180
Carbon Dioxide CO_2	99.5%	40.0	1.0	180
Sodium Hypochlorite	12.5%	4.0	1.0	200

Table 54: Overview of assumed chemical dosage and cost for SWRO plants [MENAWATER 2012]

10.3.2 Renewable Energies

CSP

Investment costs of CSP plants are divided in direct and indirect costs. Direct costs consist of material, labor and other expenses which are related to the construction of the plant. Indirect costs include non-hardware project costs such as permitting, interest during construction, owner's cost and engineering, procurement and construction (EPC) [Turchi 2013]. EPC cost estimate includes engineering, procurement, transportation and commissioning of the plant components [MENAWATER 2011]. The plant investment costs are estimated for each of the categories described in Table 55. A differentiation for the operating costs is also made between personnel, water, equipment (spare parts), insurance

and miscellaneous (utilities and contract services). The uncertainty of the resulting direct cost is assumed to be ± 10 % for well-established technologies such as utility-scale parabolic trough plants with thermo-oil as HTF and two-tank molten salt storage.

CAPEX Item	Description
Land	Land costs (separate item because of large cost variability)
Site Improvements	Land clearing and grading, roads, fences, water supply infrastructure, eventually evaporation pond
Solar Field	Mirrors, receivers (linear focusing system only), support structure, tracking system, foundations, I&C and installation
HTF System	HTF, HTF pumps, piping system, eventually expansion tank, I&C
Tower (for CR only)	Tower, piping and insulation
Receiver (for CR only)	Receiver, horizontal piping incl. insulation, cold salt pumps, controls and heat tracing
Thermal Storage	Hot tank, cold tank, storage medium, piping, insulation, foundations, I&C
BOS	Heat exchangers for steam generation incl. associated components (piping, valves, I&C), other auxiliary systems
Power Block	Steam turbine, pre-heaters, generator, feed water and blowdown system, cooling, I&C
Fossil Backup	Auxiliary boiler
Contingency	Unforeseen costs occurring during construction
EPC and Owners´ Cost	Management, EPC profit, commissioning, permitting and legal, insurance

Table 55: Overview and description of investment cost items of CSP plants [Turchi 2013], [CSP Today 2013] – I&C = instrumentation and control

For other CSP technologies which still are in early or medium development stage, the uncertainty is higher. Further, it has to be taken into account that each CSP project is characterized by a series of very site-specific and time-specific constraints. For example, the bid price of a particular project may be influenced by the general order situation of the CSP industry in a particular time frame, by the possibility to receive follow-up orders, by the risks involved in the project development etc. Therefore the spread of indirect cost which has been found in the literature (Table 56) is much higher than the differences in direct costs. In addition, two relevant issues for the cost estimation are the size of the plant and the construction year.

Note for conventional backup power plants: the start-up cost of conventional power plants is taken into account by means of an amount of fossil fuels which is needed to heat up certain parts of the plant to operating temperature [DEWI 2005]. The impact of part-load on efficiency has been considered according to [Chacartegui 2011].

Technology	Unit	Parabolic Trough			Linear Fresnel			Central Receiver		
HTF	**-**	**VP-1**	**Solar Salt**	**DSG**	**VP-1**	**Solar Salt**	**DSG**	**VP-1**	**Solar Salt**	**DSG**
PLANT REFERENCE										
Solar field ref.	m^2	800,000	800,000	900,000	860,000	860,000	860,000	-	1,300,000	800,000
Thermal Storage ref.	MWh_{th}	1,800	1,800	2,300	1,800	1,800	2,300	-	2,800	0
Power Block ref.	MW_{el}	100	100	100	100	100	100	-	100	100
INVESTMENT COST										
Land	€/m^2	1.8	1.8	1.8	1.8	1.8	1.8	-	1.8	1.8
Site Improvements	€/m^2 mirror	31.4	31.4	31.4	20.9	20.9	20.9	-	15.7	15.7
Solar Field (excl. HTF)	€/m^2	210.1	220.6	237.0	178.8	134.1	178.8	-	132.4	132.4
HTF System (incl. HTF)	€/m^2	61.3	31.0	27.0	61.3	31.0	27.0	-	0.0	0.0
Tower	Mio. €	-	-	-	-	-	-	-	$=f(z_{tower}(Q_{rec}))$	$=f(z_{tower}(Q_{rec}))$
Receiver	€/kW_{th}	-	-	-	-	-	-	-	110.0	138.6
Thermal Storage	€/kWh_{th}	45.5	19.0	77.4	45.5	19.0	77.4	-	19.0	77.4
BOS	€/kW_{el}	225.0	0.0	0.0	225.0	0.0	0.0	-	257.4	0.0
Power Block (Wet Cooling)	€/kW_{el}	695.0	695.0	691.5	695.0	695.0	691.5	-	1007.8	1002.7
Power Block (Dry Cooling)	€/kW_{el}	871.0	871.0	867.5	871.0	871.0	867.5	-	1,183.8	1,178.7
Fossil Backup	€/kW_{th}	0.0	0.0	0.0	0.0	0.0	0.0	-	0.0	0.0
Contingency	% of DC	5.00%	5.00%	5.00%	5.00%	5.00%	5.00%	-	5.00%	5.00%
EPC and Owners´ Cost	% of DC	13.00%	15.60%	15.60%	13.00%	15.60%	15.60%		15.60%	15.60%
OPERATION COST										
Personnel Cost	% DC/y	0.40%	0.40%	0.40%	0.28%	0.28%	0.28%	-	0.40%	0.40%
Equipment (spare parts)	% DC/y	0.75%	0.75%	0.75%	0.63%	0.63%	0.63%	-	0.53%	0.53%
Insurance Rate	% DC/y	0.50%	0.50%	0.50%	0.50%	0.50%	0.50%	-	0.50%	0.50%
Misc. (utilities & contract services)	% DC/y	0.30%	0.30%	0.30%	0.30%	0.30%	0.30%	-	0.30%	0.30%

Table 56: Overview of CSP investment and operational costs [Ruegamer 2013], [CSP Today 2013], [CSP Today 2013 b], [SAM], [Singer 2013], [Weinrebe 2013], [Mertins 2009], [Feldhoff 2012 c], [MENAWATER 2011], [IDAE 2011], [IRENA 2012 d]

PV

The investment cost of PV systems consists of a series of items, which can be divided into two main categories, i.e. PV module costs and balance of system costs (BOS). The BOS costs include all direct costs items other than the PV modules, i.e. site preparation, structural installation, civil and electrical works. A breakdown of investment cost for utility scale PV plants (reference plant capacity is 10 MW_p) is presented in Table 57.

CAPEX Item	Description
Land	Land costs (considered as separate item because of large cost variability)
Site Improvements	Land clearing and grading, roads, fences
Modules	Raw material costs (mainly silicon price), cell manufacturing and module assembly costs
Inverters	Inverter
Electrical Works	Transformer, wiring, grid connection
Mounting Structure	Structural system, racks
Tracking System	Tracking system, I&C
Civil Works	Foundation, monitoring system, security
Contingency	Unforeseen costs occurring during construction
EPC and Owners´ Cost	Project management, EPC profit, commissioning, permitting and legal insurance

Table 57: Overview and description of investment cost items of PV plants [Goodrich 2012], [IRENA 2012 c]

The investment cost data reported in Table 58 are for conventional c-Si modules and are understood as average costs. However, significant cost differences exist due to regional and site-specific cost factors (e.g. labor, installer experience etc.) [Goodrich 2012]. A differentiation is made between fixed axis, one-axis tracking and two-axes-tracking PV systems. Tracking PV systems are typically 10 % - 20 % more expensive than fixed axis systems. On the other hand, the energy yield of tracking plants is higher. The operating costs are sub-divided into personnel, water, equipment and insurance costs.

Similarly to CSP, PV investment costs are influenced by the size of the plant. This is also due to the fact that permitting costs, project management costs and engineering are amortized over a larger system size [Goodrich 2012]. Scale effects are calculated with Eq. 7.6. The specific size scaling factors have been adjusted in order to match literature data [Goodrich 2012].

The price of PV systems has significantly decreased in recent years. The main cost driving factor was the substantial reductions in PV module prices [Goodrich 2012]. Learning effects have been taken into account based on a number short-term costs projection scenarios [EPIA 2013], [Feldman 2012], [IRENA 2012 c].

Technology	Unit	Crystalline Silicon PV		
Tracking System	**-**	**Fixed-Axis**	**1-Axis Tracking**	**2-Axes Tracking**
Plant Reference				
Plant Capacity	MW_p	10.0	10.0	10.0
Year	-	2013	2013	2013
INVESTMENT COST				
Land	€/m²	1.8	1.8	1.8
Site Improvements	€/m² module	11.7	11.7	11.7
Modules	€/kW_p	947.7	947.7	947.7
Inverters	€/kW_p	155.5	233.3	163.3
Electrical Works	€/kW_p	190.0	190.0	197.6
Mounting Structure	€/kW_p	224.5	224.5	224.5
Tracking System	€/kW_p	0.0	346.0	454.0
Civil Works	€/kW_p	165.1	165.1	165.1
Contingency	% of DC	1.00%	2.00%	2.00%
EPC and Owners´ Cost	% of DC	8.00%	8.00%	8.00%
OPERATION COST				
Personnel	% DC/y	0.63%	0.63%	0.63%
Water	% DC/y	0.06%	0.06%	0.06%
Spare Parts	% DC/y	1.00%	2.50%	2.50%
Insurance	% DC/y	0.50%	0.50%	0.50%

Table 58: Overview of PV investment and operational costs [Goodrich 2012], [IRENA 2012 c], [MENAWATER 2011], [EPIA 2013]; EPC = engineering, procurement and construction

Wind Power

The capital cost of a wind power park can be subdivided into a number of categories, as shown in Table 59. The three major cost components are wind turbine, BOS -which includes permitting, transport and installation- and indirect costs (EPC and owners' cost).

CAPEX Item	Description
Wind Turbine	Blades, tower and transformer
Grid Connection	Connection to the local distribution network
Construction	Site preparation and tower foundations, transportation and installation, access roads
Other Capital Cost	Construction of buildings, control systems
Contingency	Unforeseen costs occurring during construction
EPC and Owners´ Cost	Project management, EPC profit, commissioning, permitting and legal, insurance

Table 59: Overview and description of investment cost items of wind power plants [Tegen 2013], [IRENA 2012 b]; EPC = engineering, procurement and construction

The capital costs of wind power projects are dominated by the cost for the wind turbine (approx. 70 % of total CAPEX) (Table 60). The costs are average costs for large scale (e.g. 10 MW) on-shore turbines. The total CAPEX may vary in a wide range (± 35 %) driven by a series of factors such as terrain conditions, site access and regional labor costs [Tegen 2013]. Additional costs incur in the case automatic power control equipment (e.g. for scheduled power curtailments) is required.

Technology	Unit	Wind Power Plant
Plant Reference		
Plant Capacity	MW	10.0
Year	-	2013
INVESTMENT COST		
Wind Turbine	€/kW	1,034.4
Grid Connection	€/kW	134.9
Construction	€/kW	135.6
Other Capital Cost	€/kW	52.2
Contingency	% of DC	5.55%
EPC and Owners´ Cost	% of DC	1.44%
OPERATION COST		
Personnel	% of DC	0.53%
Spare Parts	% of DC	1.50%
Insurance	% of DC	0.75%

Table 60: Overview and description of investment cost items of wind power plants [Tegen 2013], [IRENA 2013], [MENAWATER 2011], [Prognos 2013]; EPC = engineering, procurement and construction

Operation and maintenance costs include personnel, replacement of equipment and insurance. For simplicity, these items are expressed as percentage of the direct costs.

10.4 Case Studies

10.4.1 Meteorological Site Characterization

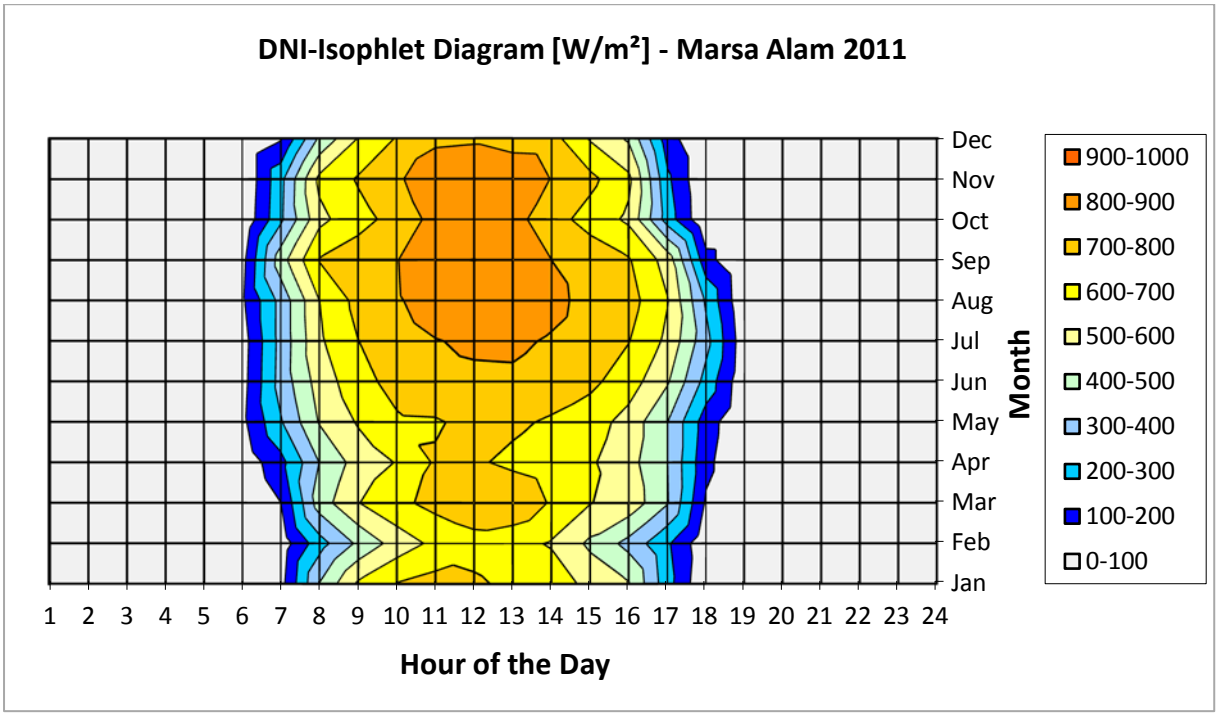

Figure 106: DNI-Isopleth diagram, Marsa Alam

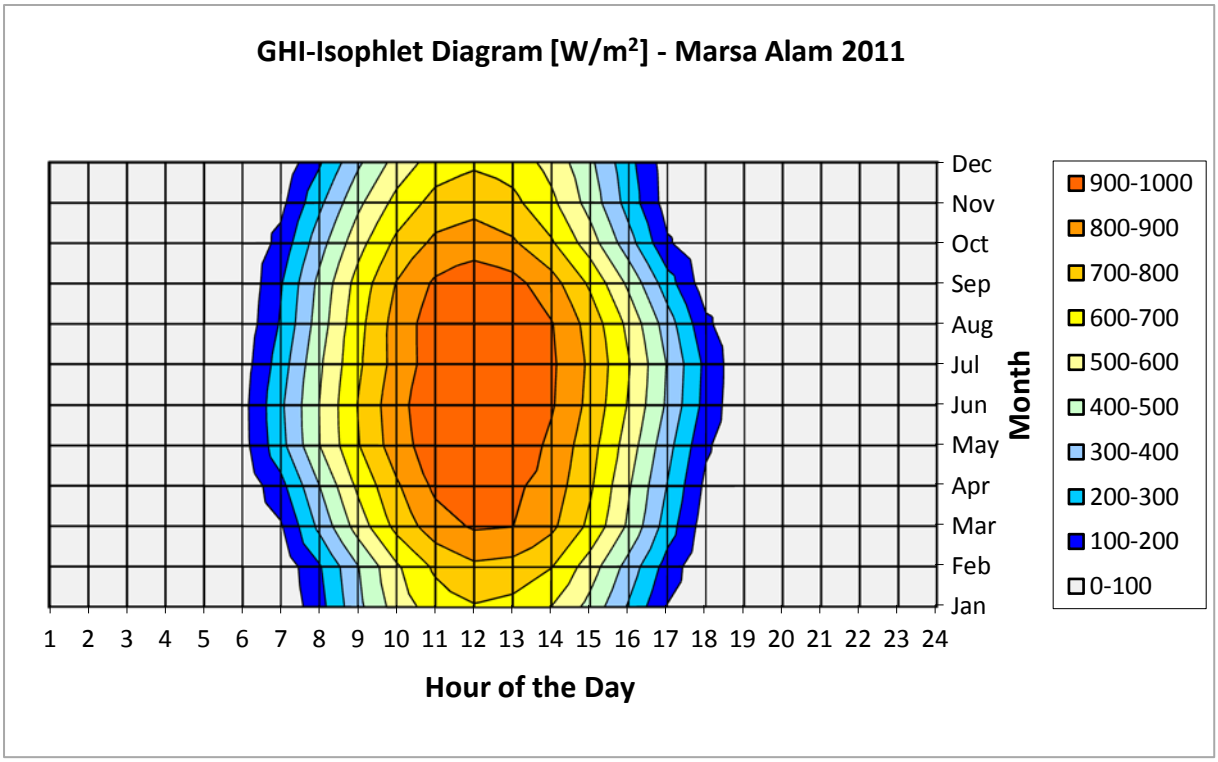

Figure 107: GHI-Isopleth diagram, Marsa Alam

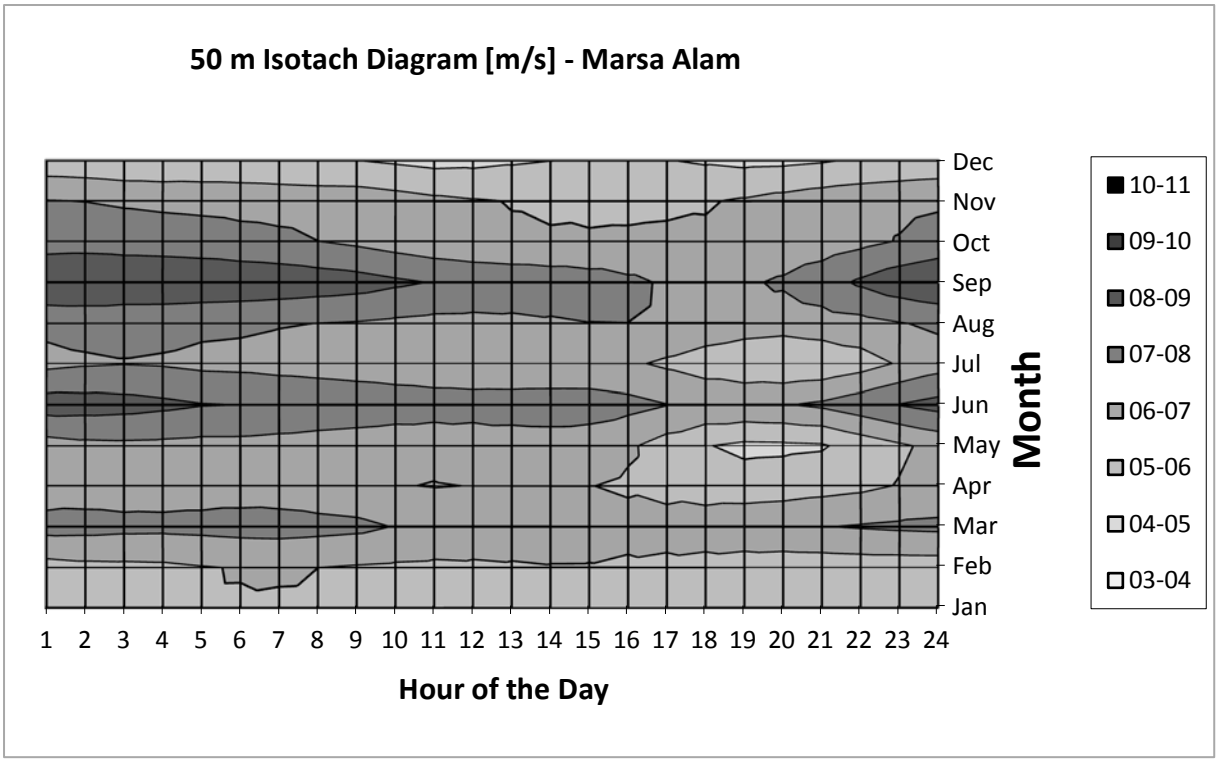

Figure 108: Wind speed isolines at 50 m height, annual average distribution in Marsa Alam

10.4.2 Technical and Economic Inputs

Solar Field		**Parabolic Trough**	**Linear Fresnel**	**Central Receiver**
Collector Type	-	SKAL-ET 150	SUPERNOVA	Abengoa Heliostats
Collector Aperture	m²	817.5	741.9	121
Collector Spacing	m	16.5	4.5	Optimized by HFLCAL[2]
HTF	-	VP-1/Solar Salt/DSG	VP-1/Solar Salt/DSG	Solar Salt
Max HTF Temperature[1]	°C	393/500/500	393/500/500	565
Min HTF Temperature	°C	293		
Thermal Energy Storage		2-tank molten salt storage (for VP-1 and solar salt); DSG w/o storage		
Cold Tank Temperature	°C	285 (Anti-freezing if T < 270 °C)		
Hot Tank Temperature	°C	385 - 565 (dependent on HTF)		
Power Block		Single-Reheating		
Capacity	MW	50 (30)		
Inlet Steam Pressure	bar	100		
Inlet Steam Temperature	°C	373 – 545 (dependent on HTF)		
Steam Extractions	-	4-6 (dependent on condensation pressure)		
Cooling Type	-	Once-through/dry cooling/MED or MED-TVC		

Table 61: CSP plant design data; [1]values refer to different heat transfer fluids (HTF specifications in 10.2.3 Table 40); [2]heliostat field layout calculation, tool developed by the solar research institute of DLR (4.4)

PV Technology	Unit	Polycrystalline
Module Type	-	Solarwatt 210
Module Aperture	m²	1.66
Mounting Type	-	Fix/1-axis tracking/2-axis tracking
Modules per String	-	21
String per Inverter	-	23
Inverter Type		Ingecon Sun 100 kW
Inverters per Transformer	-	10

Table 62: PV plant design data [MENAWATER 2012]

Common Assumptions	Unit	MED and SWRO	
Plant Nominal Capacity	m³/d	30,000	
Availability	%	92.0	
Intake Type	-	Submerged with air backwash	
Intake Length	m	Open intake / 500	
Intake Elevation Difference	m	20	
Technology-Specific Assumptions		**MED (MED-TVC)**	**SWRO**
Pretreatment Type	-	Filtration, conditioning	Flocculation, filtration
Number of Stages[1] / Modules[2]	-	4 – 14, step 2	First pass: 8 (SWC) Second pass: 7 (ESPA)
Drinking Water Post-Treatment	-	Blending, limestone filtration, conditioning and disinfection	Limestone filtration, conditioning and disinfection

Table 63: Summary of key design parameters of MED and SWRO plants; [1]applies to MED; [2]applies to SWRO

Technology	Interest Rate [%/y]	Debt Period [y]	Operational Life [y]	Cost Assumptions
CSP	8.0	25	35	Table 56
PV		20	25	Table 58
Wind Power		20	25	Table 60
Backup Plant		20	35	Table 56
MED		25	35	Table 49; Table 50
SWRO		25	30	Table 52

Table 64: Overview of economic and financial assumptions

10.4.3 CSP

Comparison of HTF in PT Plants

The LEC calculation is based on the assessment of investment and operation costs (Table 65). Land cost and site improvement cost are linearly proportional to the net aperture area. Their specific value (i.e. €/m²) is independent of the used HTF. The same applies for the solar field cost, whereas the specific investment cost is slightly lower in the first case than in the other two cases. In molten salt plants, approx. 10 €/m² are assumed as an additional cost for heat tracing along the piping system [Ruegamer 2013].

Investment Cost		**PT-OIL**	**PT-SALT**	**PT-DSG**
Land cost	Mio. €	5.2	4.5	1.8
Site improvement cost	Mio. €	23.9	20.7	8.7
Solar field	Mio. €	159.7	145.4	65.9
HTF system	Mio. €	46.6	20.4	7.5
Thermal storage	Mio. €	82.6	35.5	0.0
BOS	Mio. €	13.1	0.0	0.0
Power block	Mio. €	36.9	36.9	36.7
Cooling	Mio. €	3.7	3.5	3.5
Back-up boiler	Mio. €	8.4	7.1	7.6
Total direct cost	Mio. €	380.1	274.0	131.9
Contingency	Mio. €	19.01	13.70	6.59
EPC and owners´ cost	Mio. €	49.8	44.1	24.7
Total CAPEX	Mio. €	448.9	331.8	163.2
Operation Cost				
Annual capital cost	Mio. €/ y	42.1	31.1	15.3
Personnel cost	Mio. €/ y	1.5	1.1	0.5
Equipment (spare parts)	Mio. €/ y	2.9	2.1	1.0
Insurance rate	Mio. €/ y	1.9	1.4	0.7
Miscellaneous	Mio. €/ y	1.1	0.8	0.4
Water cost	Mio. €/ y	0.51	0.46	0.19
Fuel cost	Mio. €/ y	0.0	0.1	0.0
Total OPEX	Mio. €/ y	50.0	36.9	18.0
LEC	€cent/kWh	17.40	12.48	14.76

Table 65: Economic comparison of optimized PT systems; Assumptions: cost scenario 2014, low fossil fuel price (8 $/bbl)

In addition, DSG receivers are assumed to be approx. 25 €/m² more expensive than conventional receivers due to a higher operation pressure (100 bar vs. approx. 25 bar in conventional oil-based CSP plants). According to the data available in the literature, the investment cost per m² solar field of oil-based HTF systems (including the heat transfer fluid) is 61.3 €/m², which is almost twice as much as the specific cost of molten salt HTF systems. The most significant cost difference between the first and second case is the TES cost. Even if both systems present similar TES layouts and comparable storage capacity (approx. 1,800 MWh), the PT-SALT plant has the advantage of an approx. 2.5 higher temperature difference between the hot and the cold tank in comparison to the PT-OIL system. As a direct consequence, the required molten salt mass is significantly lower. The item "BOS" (i.e. balance of system) takes into account the cost of additional equipment such as the oil/salt heat exchangers and the HTF expansion vessel. The contingency is assumed to be 5.0 % of the direct cost in all the considered cases, while a differentiation is made with regard to EPC and owners´ cost. PT-OIL systems are assumed to be state-of-the-art and so the EPC and owners´ costs are slightly lower than in the other two cases (13.0 % vs. 15.6 %). Concerning operation costs, most of the items (e.g. personnel, equipment, insurance and miscellaneous) are expressed as a percentage of direct costs and no differentiation is made between the three considered cases. This means that such costs just reflect the differences in direct costs.

Fuel costs are higher in the molten salt case due to the higher anti-freezing requirements. However, this item only plays a secondary role (approx. 0.2 % of the operation cost in the case of a low fossil fuel price, up to 2.2 % in the case of a market fuel price).

Comparison of CSP Technologies

Most of the considerations about land cost, site improvement, HTF system, TES, contingency and EPC have already been discussed with regard to Table 65. The central receiver system is characterized by high receiver and tower costs, whereas the specific investment cost for the heliostat field is lower than for the parabolic trough (132 €/m² vs. 221 €/m²). According to [SAM], the specific investment cost for the power block is approx. 45 % more expensive than for PT (916 €/kW vs. 632 €/kW). This assumption should be critically assessed. Despite such differences, PT and CR come to a very similar direct cost, while LF is approx. 15 % lower.

Investment Cost		**PT-SALT**	**LF-SALT**	**CR-SALT**
Land cost	Mio. €	4.5	3.7	5.8
Site Improvement cost	Mio. €	20.7	16.9	10.3
Solar field	Mio. €	145.4	108.1	86.9
HTF system	Mio. €	20.4	25.0	0.0
Tower	Mio. €	0.0	0.0	6.5
Receiver	Mio. €	0.0	0.0	48.4
Thermal storage	Mio. €	35.5	31.7	33.4
BOS	Mio. €	0.0	0.0	15.0
Power block	Mio. €	36.9	36.9	53.6
Cooling	Mio. €	3.5	3.5	3.3
Back-up boiler	Mio. €	7.1	6.9	6.9
Total direct cost	Mio. €	274.0	232.8	270.1
Contingency	Mio. €	13.70	11.64	13.50
EPC and owners´ cost	Mio. €	44.1	36.7	46.9
Total CAPEX	Mio. €	331.8	281.1	330.4
Operation Cost				
Annual capital cost	Mio. €/ y	31.1	26.3	31.0
Personnel cost	Mio. €/ y	1.1	0.7	1.1
Equipment (spare parts)	Mio. €/ y	2.1	1.5	1.4
Insurance rate	Mio. €/ y	1.4	1.2	1.4
Miscellaneous	Mio. €/ y	0.8	0.7	0.8
Water cost	Mio. €/ y	0.46	0.44	0.52
Fuel cost	Mio. €/ y	0.1	0.1	0.0
Total OPEX	Mio. €/ y	36.9	30.9	36.1
LEC	€cent/kWh	12.48	11.01	10.08

Table 66: Economic comparison of optimized molten salt systems; Assumptions: cost scenario 2014, low fossil fuel price (8 $/bbl)

Additional Case Studies

Land costs also have an impact on LEC. Linear Fresnel reflectors have highest land use factor among CSP technologies and are less negatively affected by higher land cost than solar tower and parabolic trough (Figure 109).

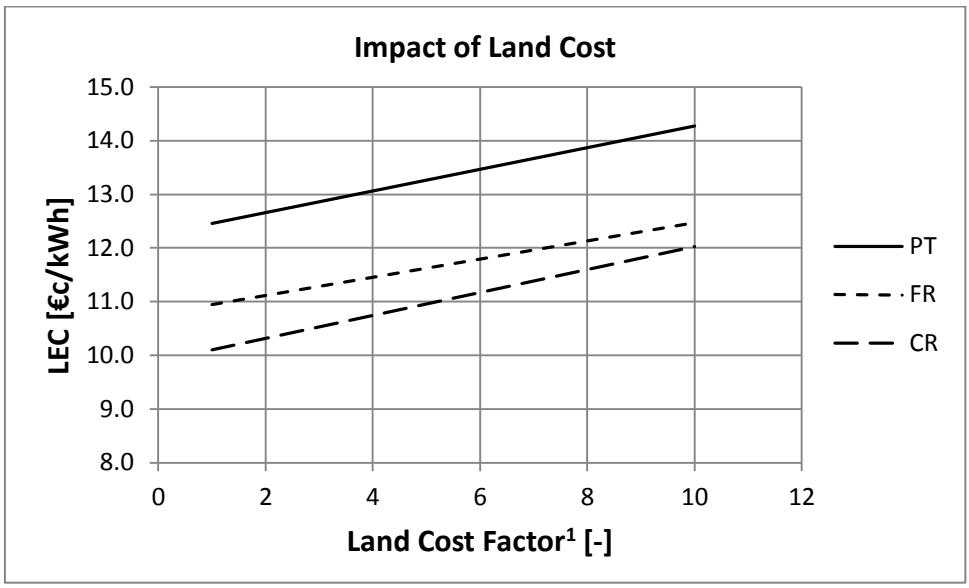

Figure 109: Impact of land cost of LEC of various CSP technologies ([1]land cost factor 1.0 corresponds to 1.8 €/m²)

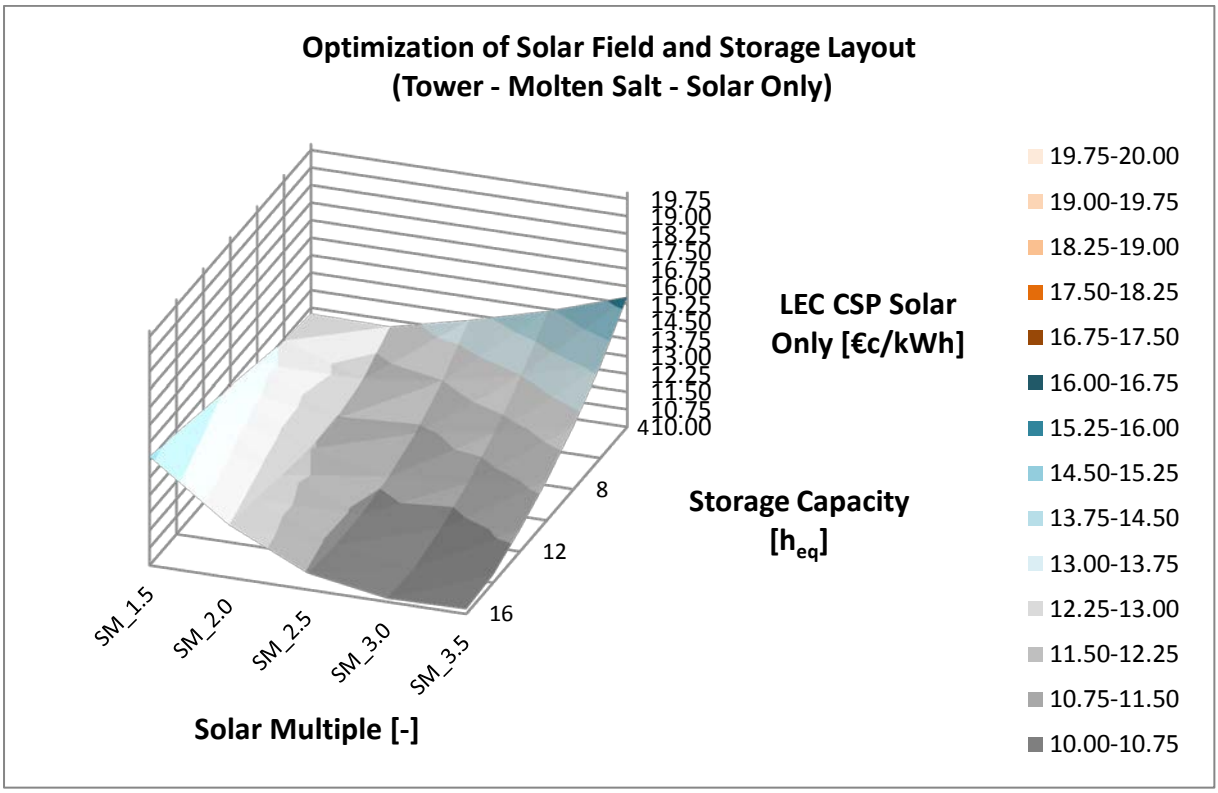

Figure 110: CSP layout optimization (solar tower, solar-only operation)

	h_{TES} 4	h_{TES} 6	h_{TES} 8	h_{TES} 10	h_{TES} 12	h_{TES} 14	h_{TES} 16
SM 1.5	12.74	12.92	13.29	13.64	13.98	14.32	14.66
SM 2.0	12.71	11.80	11.47	11.51	11.74	12.00	12.26
SM 2.5	13.51	12.24	11.34	10.83	10.57	10.55	10.70
SM 3.0	14.42	13.01	11.91	11.07	10.47	**10.10**	10.15
SM 3.5	15.54	13.93	12.70	11.71	10.93	10.34	10.21

Table 67: LEC values related to Figure 110

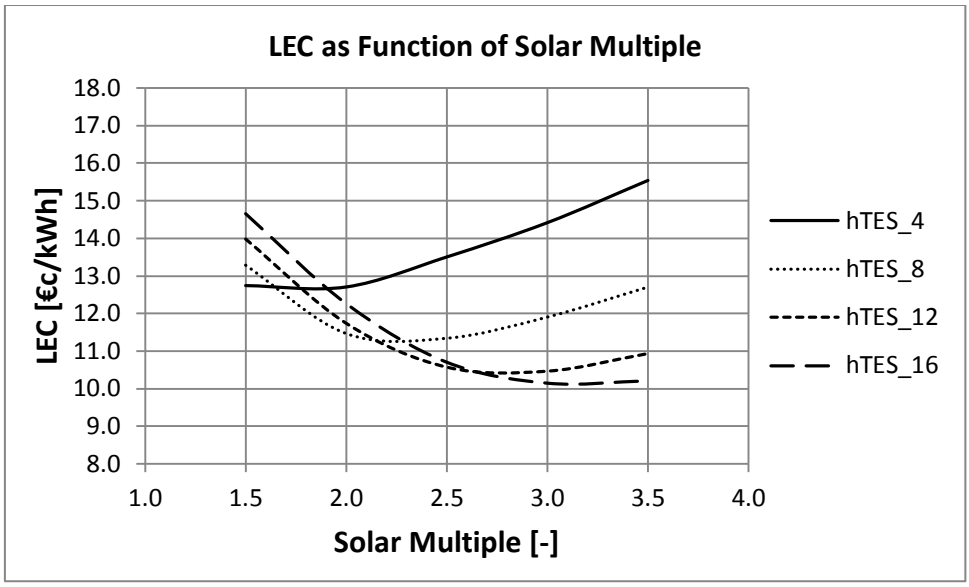

Figure 111: Section lines (constant storage capacity) with reference to Figure 110

Power Block

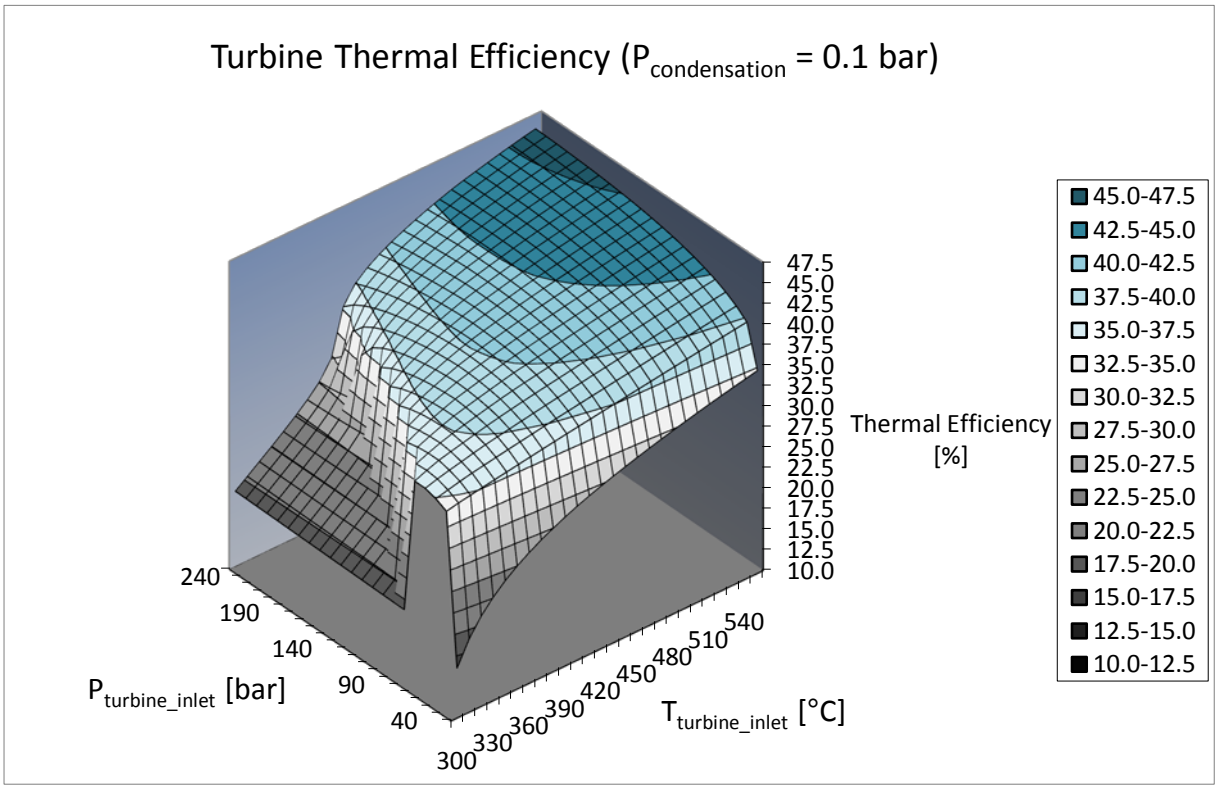

Figure 112: turbine thermal efficiency as function of inlet steam parameters (temperature and pressure)

10.4.4 Desalination

MED

The GOR of MED units (with and without TVC) also depend on the top brine temperature (Figure 113). In MED units, the lower the process temperature is, the higher the GOR, due to the lower amount of heat which has to be used for feed water pre-heating. In MED-TVC systems, the GOR reduction at high TBT can be explained as follows: the higher the discharge temperature is (i.e. steam temperature at the inlet of the first MED stage), the higher the entrainment ratio (i.e. the ratio between motive steam and entrained steam). As a result, more steam is provided by the turbine and the GOR is lower.

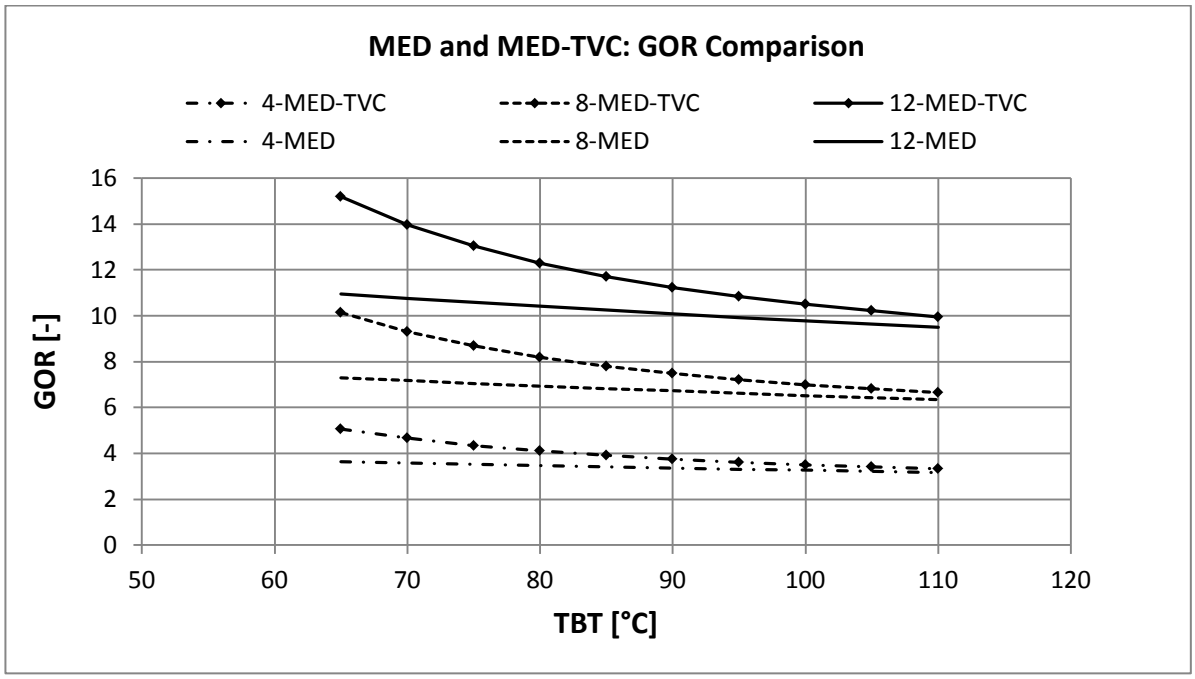

Figure 113: Impact of TBT on the GOR of MED and MED-TVC

RO

Impact of Salinity and Recovery Ratio on SEC

Figure 114 shows the impact of recovery ratio and salinity on SEC. Four salinities have been analyzed: the second and the third case roughly represent the maximum (45,000 ppm; however few exceptions with even higher salinity exist) and the minimum (30,000 ppm) seawater salinity in the MENA region, respectively. In addition, two other extreme cases have been taken into account in order to highlight the impact of salinity on the optimal recovery rate. These two additional cases, i.e. 90,000 ppm and 10,000 ppm, are only used for illustrative purposes. As it has already been discussed, the higher the salinity is, the higher the SEC. In addition, for each of the analyzed salinities, a minimum SEC exists as a function of the recovery ratio. Such behavior can be explained as follows: at low recovery rate, high amounts of feed water have to be pumped through the intake unit and brought to operation pressure, while the permeate production is relatively low. Although the analyzed

RO plant is equipped with an efficient energy recovery system (PX, Figure 83), a portion of the feed pressure is lost. At higher recovery rates (R) the intake water flow can be reduced as well as the energy consumption; however, this positive effect levels off and inverts at even higher R. Due to the fact that high recovery has to be achieved, the feed mass flow decreases rapidly along the vessel. This causes an increase in the feed salinity whose negative impact is exacerbated by the polarization concentration (Eq. 3.31). Finally, this leads to a reduction of the available net driving pressure (in particular in the final elements of the vessel). Due to such considerations, the higher the seawater salinity is, the lower the optimal recovery rate.

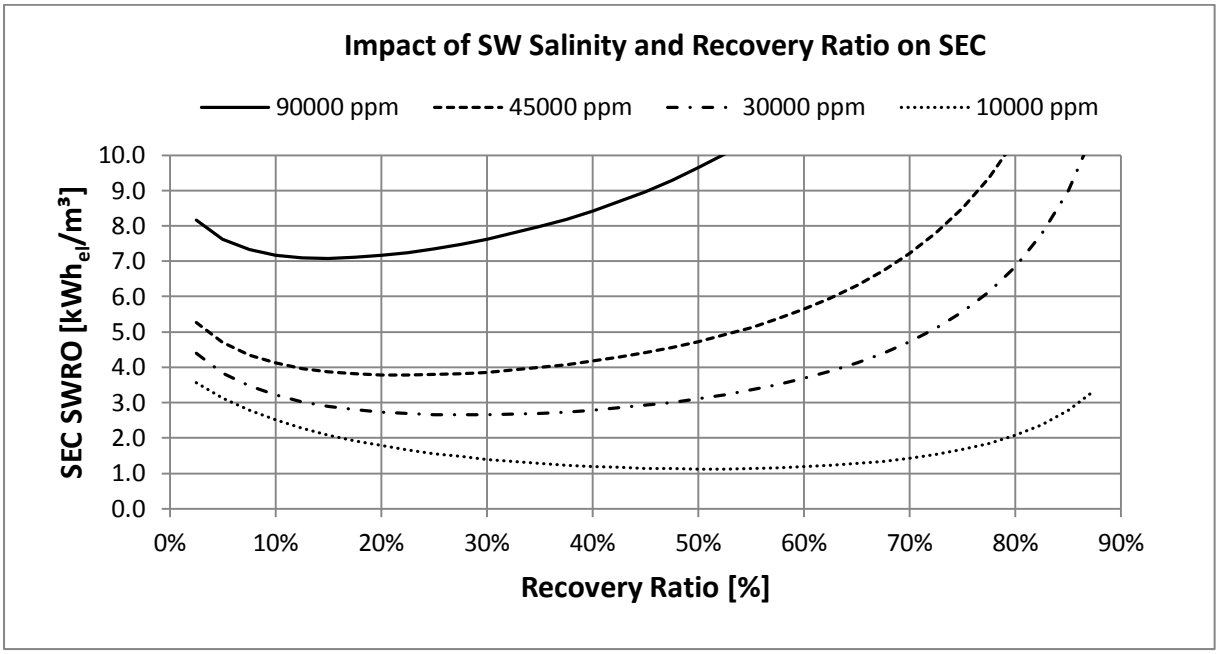

Figure 114: Impact of RO recovery ratio and seawater temperature on the specific electricity consumption (SEC)

Impact of Pre-treatment

The intake water still contains several contaminants (e.g. particulate, colloids, organic and mineral compounds, bacteria) that -if not removed with targeted measures- would reduce the plant efficiency and increase the replacement cost of the components. These measures mainly include the use of several chemical additives, which are partially discharged into the sea and cause local marine pollution. The reduction of the use of chemicals would contribute to the minimization of the environmental impact of desalination processes. The typical pretreatment steps in MED units are rather simple. In addition, such measures are almost independent of the quality of the raw water source. Thermal processes have proven to be suitable for a wide range of seawater qualities. In contrast, RO membranes are highly susceptible to a wide range of water impurities. The best pretreatment design should be selected after a detailed analysis of composition and concentration of these impurities and their variation over time. The following case study shows the impact of two pre-treatment designs. The conventional pre-treatment consists of dual media filters and cartridge filters. Such a layout is the common choice in commercial SWRO applications as long as turbidity

spikes are lower than 30 NTU and the TOC is below 4 mg/l. However, some sites are characterized by even higher turbidity and TOC values, which may be related to algal blooms and oil spills. Such conditions -which are likely to happen e.g. in the Arabic Gulf- require additional pretreatment upstream the filtration step. The second analyzed pre-treatment option includes sedimentation basins and dissolved air flotation (DAF) prior to the conventional filtration steps, which are used to reduce turbidity down to approx. 1.5 NTU. Table 68 presents the impact of pre-treatment and of fossil fuel price on LWC, under the assumption that the power is supplied by a conventional steam turbine. The comparison shows that DAF pre-treatment is related to higher capital cost (0.46 €/m³) in comparison to the conventional pre-treatment case (0.41 €/m³), which is due to the additional efforts for the construction of sedimentation basins and DAF unit. As a direct consequence, maintenance and repair cost (M&R) are also slightly higher. The DAF pre-treatment also impacts chemical and electricity cost, which is higher due to additional pumping requirements. In addition, the higher the price of the fossil fuel is, the higher the LWC difference between conventional and demanding pre-treatment.

Fossil Fuel Price	**$/bbl**	**8**		**100**	
Pretreatment Type	**-**	**Conventional**	**DAF**	**Conventional**	**DAF**
Capital cost	€/m³	0.41	0.46	0.41	0.46
Personnel Cost	€/m³	0.01	0.01	0.01	0.01
M&R cost	€/m³	0.13	0.15	0.13	0.15
Sum of fix LWC	€/m³	0.54	0.61	0.54	0.61
Electricity cost	€/m³	0.11	0.14	0.55	0.70
Chemical cost	€/m³	0.06	0.09	0.06	0.09
Membrane replacement cost	€/m³	0.04	0.05	0.04	0.05
Sum of variable LWC	€/m³	0.21	0.28	0.64	0.84
LWC	€/m³	0.75	0.90	1.19	1.45

Table 68: Impact of pre-treatment type and of fossil fuel price on LWC of an SWRO plant; Assumptions: conventional steam turbine as power supply, open intake

Scale Effects

In the next case study (Figure 115 to Figure 116) the impact of plant capacity on LWC has been analyzed. Two power supply technologies (conventional and CSP) and two fossil fuel prices (8 $/bbl and 100 $/bbl) have been considered.

Figure 115 shows the impact of plant capacity on LWC, under the assumption of conventional (fossil) power supply. Three cases have been selected, i.e. 20,000 m³/d, 30,000 m³/d and 100,000 m³/d. The second case is the reference plant capacity of this case study, which also roughly corresponds to the state-of-the-art capacity of MED plants (approx. 38,000 m³/d for a single unit). The results show that the capacity of the plant significantly impacts the LWC. The larger the size of the plant is, the lower the cost. Such an impact is more accentuated for MED than for RO plants. This difference is due to the assumed dependency of the specific capital cost on the plant capacity (Eq. 7.9).

Concerning MED, it is also interesting to note that the LWC differences between small and medium sizes are larger than the LWC differences between medium and large sizes. This may appear surprising; however, the capital cost curve described in Eq. 7.9 is assumed to be valid as long as the MED unit does not exceed the maximal capacity of a single unit, i.e. 38,000 m³/d. For larger MED capacities, no further reduction of capital cost is expected. In contrast, the capital cost curve of RO is assumed to be valid also at large capacity. SWRO performs lower LWC than MED for all analyzed cases. The lower the capacity of the desalination plant is and the lower the price of the fuel, the higher the LWC differences between the two technologies.

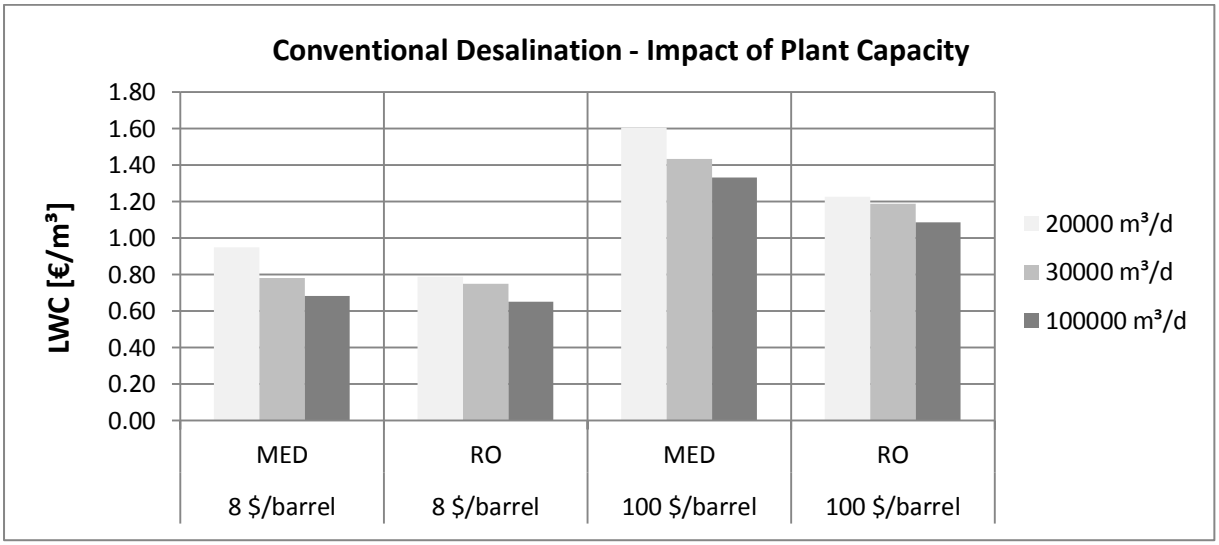

Figure 115: Impact of plant capacity on LWC; Assumption: conventional (fossil) power supply

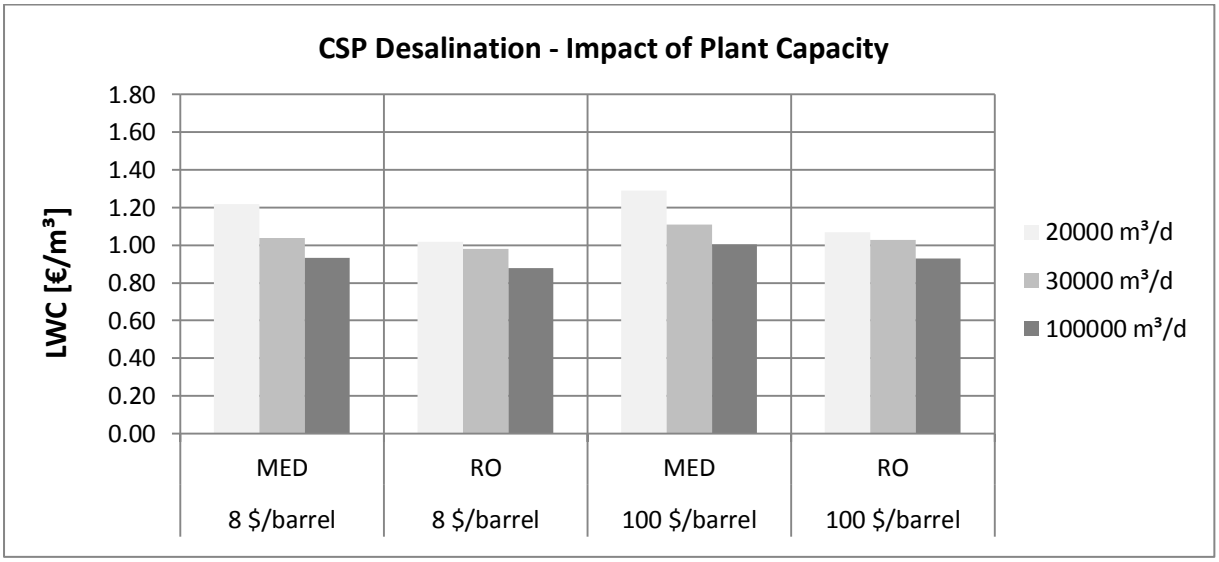

Figure 116: Impact of plant capacity on LWC; Assumption: CSP fossil power supply

Feed Water Intake

The choice of the most convenient intake type and its layout are very site-specific issues. In fact, several parameters have to be carefully considered such as plant capacity, sea bottom geology and bathymetric profile. In addition, the eventual option of a shared intake with an adjacent power plant should be taken into account. For these reasons, a high sensitivity on the optimal feed water intake configuration is expected. The case study reported in Figure 117 shows the impact on LWC of two exemplary intake types, i.e. open intake and deep (or submerged) intake. MED as well SWRO are considered. In the case of a submerged intake, a pipe length of 500 m has been taken into account, which is assumed to be required in order to reach an acceptable water quality. The results show that MED is particularly sensitive to variations of the intake layout. This is due to the fact that MED plants need significantly more intake water per unit of drinking water than RO plants. The lower the number of stages is, the higher the required cooling water mass flow per unit of produced distillate. In addition, the longer the intake piping system is (as in the deep intake case), the higher the capital cost. The optimization of the number of stages in the two considered cases shows that in the case of open intake the optimal number of stages is around 9 - 10, while in the second case the optimum slightly shifts to the right part of the diagram, due to the fact that higher investment cost has to be compensated be higher efficiency of the desalination process. Concerning RO, the sensitivity of LWC on the intake layout is less accentuated than for MED. In fact, membrane desalination processes do not need any cooling water, so that the required intake water is defined by the optimal recovery ratio of the plant. For typical seawater conditions, the ratio between intake water and permeate is approx. 2.5. Accordingly, the economic impact of the intakes´ layout is not as relevant as for MED.

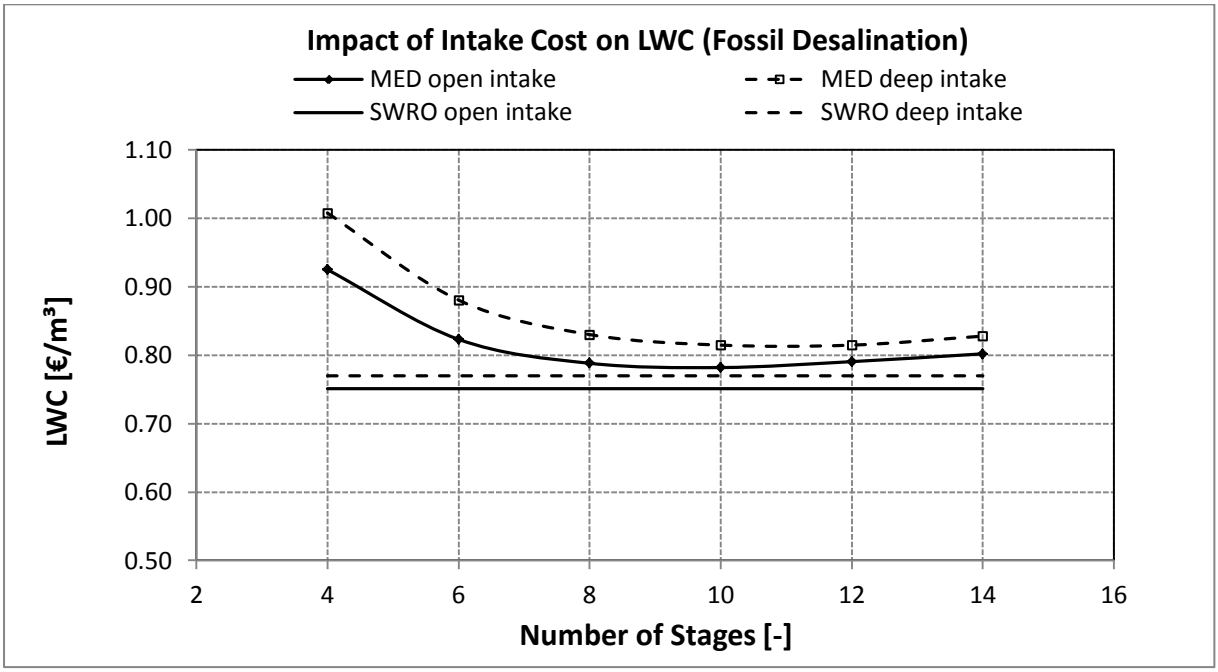

Figure 117: Impact of intake type (open intake vs. deep intake) on LWC. Assumptions: fossil desalination, low fuel cost (8 $/bbl)

10.5 Parameters of Developed INSEL Blocks

List of hourly INSEL Outputs

INSEL Block	n	n_Block	Symbol	Unit	Description
Time	1	1	HoY	-	Hour of the year
	2	2	HoD	-	Hour of the day
	3	3	DoM	-	Day of the month
	4	4	MoY	-	Month of the year
INPUTS	5	1	DNI	W/m²	Direct normal irradiance
	6	2	GHI	W/m²	Global horizontal irradiance
	7	3	Diff	W/m²	Diffuse irradiance
	8	4	T_{amb}	°C	Ambient Temperature
	9	5	wv @ meas	m/s	Wind velocity (measurement)
	10	6	Rel. Hum.	-	Relative Humidity
	11	7	p_{atm}	mbar	Atmospheric pressure
	12	8	T_{cw}	°C	Cooling Water temperature
	13	9	X_{sw}	ppm	Seawater salinity
	14	10	P_{Demand}	MW_{el}	Electricity demand
	15	11	H_2O_{Demand}	m³/h	Water demand
Solar Angles	16	1	α_s	°	Sun elevation angle [Day: > 0]
	17	2	γ_s	°	Solar azimuth
	18	3	θ_Z	°	Zenith angle
SOLAR FIELD CSP	19	1	Q_{sf}	MW_{th}	Thermal energy flow from solar field
	20	2	T_{HTF}	°C	HTF temperature at collector exit
	21	3	Q_{af_SF}	MW_{th}	Q anti-freezing solar field
	22	4	$P_{parasitics\_SF}$	MW_{el}	Pumping parasitics in solar field
	23	5	η_{opt}	-	Optical efficiency
	24	6	η_{sf}	-	Solar field efficiency
	25	7	Q_{dump_sf}	MW	Qump heat in solar field
	26	8	A_{sf}	m²	Mirror area solar field
THERMAL ENERGY STORAGE CSP	27	1	Q_{TES}	MWh	Thermal energy in storage
	28	2	T_{2HX}	°C	HTF temp. before water/steam HX
	29	3	Q_{2HX}	MW	Thermal heat flow to the heat exchanger
	30	4	$P_{parasitics\_TES}$	MW	Pumping parasitics in storage
	31	5	Q_{dump_TES}	MW	Dump heat heat in storage
	32	6	$Q_{TES\_residual}$	MW	Residual heat in storage
	33	7	T_{ht}	°C	Hot tank temperature
	34	8	T_{ct}	°C	Cold tank temperature
	35	9	Q_{AF}	MW	Required backup heat for anti-freezing
	36	10	Q_{TES_max}	MWh_{th}	Storage capacity
CO-FIRING CSP (part of CSP turbine)	37	1	$Q_{after\ cofir}$	MW	Thermal heat flow after co-firing
	38	2	T_s	°C	Live steam temperature at turbine inlet
	39	3	Q_{cofir}	MW	Thermal heat flow in co-firing (fossil)
	40	4	cofir switch	-	0 = co-firing out; 1=co-firing on
STEAM TURBINE CSP	41	1	$P_{elgross}$	MW_{el}	Gross electricity production
	42	2	η_{gross}	-	Gross turbine efficiency
	43	3	T_{cond}	°C	Condenser temperature
	44	4	m_s*X_s	kg/s	Steam flow condenser (uncond. fraction)
	45	5	$P_{parasitics\_turb}$	MW_{el}	Pumping parasitics feed water pump
	46	6	$P_{parasitics\_cool}$	MW_{el}	Cooling parasitics
	47	7	$P_{parasitics\_plant}$	MW_{el}	CSP plant parasitics
	48	8	P_{CSP_sol}	MW_{el}	Solar electricity production

	49	9	P_{CSP_cof}	MW_{el}	Fossil electricity production
	50	10	$Q_{residual\ TES}$	MW_{th}	Residual heat to storage
	51	11	P_{el_net}	MW_{el}	Net power generation
	52	12	$P_{el\_CSP\_demand}$	MW_{el}	Electricity demand CSP
	53	13	$Q_{sf\_dump\_turb}$	MW_{th}	Qsf dump in the turbine
PV	54	1	n PV sys	-	Number of systems
	55	2	GTI	W/m^2	Global tilted irradiance on collector
	56	3	tilt Angle	°	Tilt angle collector
	57	4	γ_c	°	Collector azimuth
	58	5	Pel_PV	MW_{el}	Electricity production PV
	59	6	losses PV	-	Inverter-to-grid, array, wiring etc.
	60	7	$\eta_{inverter}$	-	PV inverter efficiency
WIND	61	1	wv @ hub	m/s	Wind velocity (hub elevation)
	62	2	P_{el_Wind}	MW_{el}	Electricity production wind
	63	3	P_{Wind_dump}	MW_{el}	Dump electricity wind
	64	4	n wind turb	-	Number of installed wind turbines
	65	5	hub height	m	Hub height of the wind turbine
DESALINATION MED	66	1	m_{sw}	m^3/h	Seawater mass flow
	67	2	m_d	m^3/h	Desalinated water mass flow
	68	3	X_p	ppm	Product water salinity
	69	4	R	-	Recovery ratio
	70	5	partload	-	Partload behaviour (Md/Md_nom)
	71	6	m_{out}	m^3/h	Brine water flow
	72	7	$X_{discharge}$	ppm	Brine salinity (evtl. mixed)
	73	8	$T_{discharge}$	°C	Brine temperature (evtl. mixed)
	74	9	SEC_{DES}	kWh/m^3	Specific energy consumption for DESAL
	75	10	SEC_{INTAKE}	kWh/m^3	Specific energy consumption for Intake
	76	11	$P_{parasitics\_DES}$	MW_{el}	Pumping parasitics in desalination
	77	12	GOR	-	GOR for MED
	78	13	n MED	-	Number of stages MED
	79	14	sA	$m^2/(kg*s)$	Specific heat transfer area
	80	15	sQ_{th}	kWh_{th}/m^3	Specific thermal energy consumption
BACK-UP GENERATOR	81	1	P_{el_rest}	MW	Electricity demand back-up generator
	82	2	η_{gen}	-	Generator net efficiency
	83	3	P_{el_gen}	MW	Electricity produced by the generator
	84	4	Q_{th_cofir}	MW_{th}	Thermal heat flow in the generator
DESALINATION SWRO	85	1	m_{sw}	m^3/h	Seawater mass flow
	86	2	Water Production	m^3/h	Desalinated water mass flow
	87	3	X_p	ppm	Product water salinity
	88	4	RR	-	Recovery ratio
	89	5	partload	-	Partload behaviour (Md/Md_nom)
	90	6	m_{out}	m^3/h	Brine water flow
	91	7	X_{out}	ppm	Brine salinity (evtl. mixed)
	92	8	T_{out}	°C	Brine temperature (evtl. mixed)
	93	9	SEC_{DES}	kWh/m^3	Specific energy consumption for DESAL
	94	10	SEC_{INTAKE}	kWh/m^3	Specific energy consumption for Intake
	95	11	P_{par_DES}	MW_{el}	Pumping parasitics in desalination
	96	12	p_{RO}	bar	Feed pressure 1st Stage
	97	13	A_M	m^2	Membrane area
Ref. Turbine	98	1	η_{gross_REF}	-	Ref. gross efficiency MED heat cost calc.

Table 69: Standardized (i.e. independent of analyzed configuration) list of INSEL hourly output parameters

Sun Position Block

Input	Unit	Block Parameter	Unit	Value	Output	Unit
DoY	-	ϕ	°	0-90	HoY	h
HoD	-	φ	°	-180-180	θ_z	°
Minute	min	Time step	min	60	θ	°
		UTC/local time[1]	-	0/1	α_s	°
		Site altitude	m	> 0	γ_s	°
		Site name	-	-	ϕ	°
					φ	°
					Site altitude	m
					$\theta_{30°}$	°
					ϖ	°
					Solar time	h
					$\vartheta_\perp$	°
					θ_i	°

Table 70: Summary of inputs, block parameters and outputs of the block SUNPOS

[1]0=UTC (Universal Time Coordinates); 1=local time

Parabolic Trough Solar Field

Input	Unit	Block Parameter	Unit	Value	Output	Unit
HoY	h	Collector Type[1]	-	1/2/3/4/5	$\dot{Q}_{sf}$	MW_{th}
θ	°	Row Distance	m	16.5	T_{sf_out}	°C
α_s	°	Max. HTF Flow	kg/s/loop	8.0 (VP-1)	$\dot{m}_{HTF}$	kg/s
γ_s	°	Nom. Demand	MW_{el}	0-250	η_{sf}	-
DNI	W/m²	Cooling[2]	-	1/2/3/4	$\dot{Q}_{dump}$	MW_{th}
T_{amb}	°C	SM	-	1.0-3.5	$P_{parasitic\_sf}$	MW_{el}
v_{wind}	m/s	L Collector	M	150	A_{sf}	m²
P_{atm}	mbar	n subfields	-	4	n Collector Row	-
Q_{TES_rest}	MWh_{th}	HTF Type[3]	-	1/2/3	η_{geo}	-
Elec. Demand	MW_{el}	k_{CSI}[4]	-	0-1	IAM	-
		Opt. loss. correction	-	1.0	η_{cos}	-
		$k_{startup}$[5]	-	1.0-1.75	η_{shad}	-
		η_{turb_nom}	-	0.30-0.45	$\eta_{endgain}$	-
		$T_{sf\_out\_design}$	°C	390-565	$Q_{startup}$	MWh_{th}
					Δp_{HTF}	bar
					HTF Type	-

Table 71: Summary of inputs, block parameters and outputs of the block SFPIPE

[1]1=LS-2;2=LS-3;3=SKAL-ET 150; 4=SGX-1; 5=AT150

[2]0=once-through; 1=evaporative tower; 2=dry cooling; 3=MED; 4=fixed pressure

[3]1=oil (VP-1); 2=solar salt; 3=DSG

[4]transient correction: only if clear sky index (CSI) < k_{CSI}, else steady-state

[5]non-ideal startup of solar field (>= 1.0 and < 1.5)

Linear Fresnel Solar Field

Input	Unit	Block Parameter	Unit	Value	Output	Unit
HoY	h	Collector Type	-	1	$\dot{Q}_{sf}$	MW_{th}
θ	°	Max. HTF Flow	kg/s/loop	8.0 (VP-1)	T_{sf_out}	°C
θ_i	°	Nom. Demand	MW_{el}	0-250	$\dot{m}_{HTF}$	kg/s
$\theta_\perp$	°	SM	-	1.0-4.0	η_{sf}	-
DNI	W/m²	HTF Type[3]	-	1/2/3	$\dot{Q}_{dump}$	MW_{th}
T_{amb}	°C	$k_{startup}$[5]	-	1.0-1.75	$P_{parasitic\_sf}$	MW_{el}
v_{wind}	m/s	η_{turb_nom}	-	0.30-0.45	A_{sf}	m²
P_{atm}	mbar	$T_{sf\_out\_design}$	°C	390-565	η_{geo}	-
Q_{TES_rest}	MWh_{th}				η_{sf}	-
P_{el}	MW_{el}				$Q_{startup}$	MWh_{th}
					Δp_{HTF}	bar
					HTF Type	-

Table 72: Summary of inputs, block parameters and outputs of the block NOVA

Heliostat Field and Receiver

Input	Unit	Block Parameter	Unit	Value	Output	Unit
HoY	h	h_{rel}	-	0.7-1.3	$\dot{Q}_{eff}$	MW_{th}
α_s	°	SM	-	1.0-3.5	T_{sf_out}	°C
γ_s	°	φ	°	20-40	$\dot{m}_{HTF}$	kg/s
η_{sf}[1]	-	Avg. Reflectivity	-	0.87	η_{sf}	-
DNI	W/m²	k wind Loss	-	0	$\dot{Q}_{dump}$	MW_{th}
T_{amb}	°C	$T_{rec\_in\_nom}$	°C	293	$P_{parasitic\_sf}$	MW_{el}
v_{wind}	m/s	$T_{rec\_out\_nom}$	°C	565	A_{sf}	m²
Q_{TES_rest}	MWh_{th}	$\eta_{opt\_receiver}$	-	0.93	η_{wind_sf}	-
P_{el}	MW_{el}	$\alpha_{loss\_convection}$	°	13	η_{sf}	-
		$\dot{Q}_{rec}/\dot{Q}_{rec\ max}$	-	1.1	$Q_{startup}$	MWh_{th}
		k_{T_rec}	1/K	0.5	Δp_{HTF}	bar
		ΔT_{wall_design}	K	25	$\dot{Q}_{inc\_rec}$	MW_{th}
		ε_{rec}	-	0.83	$\dot{Q}_{inc\_rec\_design}$	MW_{th}
		Δp_{rec_design}	bar	15	$\dot{Q}_{loss\_opt}$	MW_{th}
		Max. Rec. Flux	kW/m²	575	$\dot{Q}_{loss\_conv}$	MW_{th}
		Calc. Mode[2]	-	0/1	$\dot{Q}_{loss\_rad}$	MW_{th}
		P_{el_nom}	MW_{el}	0-250	$\dot{Q}_{loss}$	MW_{th}
		η_{turb_nom}	-	0.40-0.45	Rec. Flux	kW/m² rec.

Table 73: Summary of inputs, block parameters and outputs of the block TOWER

[1]calculated by interpolation matrix (if calculation mode = 2)

[2]0=from file; 1=from matrix

Molten Salt Thermal Energy Storage

Input	Unit	Block Parameter	Unit	Value	Output	Unit
HoY	h	Tank Diameter	m	38.5	$\dot{m}_{sf}$	kg/s
T_{amb}	°C	$\eta_{turb\ nom}$	-	0.30-0.45	$\dot{m}_{HTF\ TES}$	kg/s
T_{HTF_sf}	°C	P_{el_nom}	MW_{el}	0-250	T_{TES_out}	°C
$\dot{Q}_{sf}$	MW_{th}	SoC_0 [2]	-	0.01-0.1	Q_{TES}	MWh_{th}
P_{el}	MW_{el}	$\dot{q}_{loss}$	%/day	1.5	$\dot{Q}_{turb}$	MW_{th}
$\dot{m}_{HTF}$	kg/s	SoC_{min}	-	> 0.01	$\dot{Q}_{cofir}$	MW_{th}
η_{turb}	-	h_{TES_design}	h	0 - 16	SoC	-
$P_{parasitic\_sf}$	MW_{el}	$T_{cold\_tank\_0}$	°C	290	dM_{salt}	ton/h
$\dot{Q}_{rest\_from\_turb}$ [1]	MW_{th}	$T_{hot\_tank\_0}$	°C	565	$\dot{m}_{HTF\_turb}$	kg/s
HTF Type	-	Calc. Mode [3]	-	0/1	$\dot{m}_{HTF\_turb\_design}$	kg/s
					$P_{parasitic\_TES}$	MW_{el}
					M_{hot_tank}	ton
					M_{cold_tank}	ton
					T_{hot_tank}	°C
					T_{cold_tank}	°C
					$\dot{Q}_{dump}$	MW_{th}
					Q_{TES_rest}	MWh_{th}
					Q_{TES_design}	MWh_{th}

Table 74: Summary of inputs, block parameters and outputs of the block STOMS

[1] for INSEL simulation only

[2] initial state of charge

[3] demand cover mode: 0=demand cover with gross power; 1=demand cover with net power

Steam Turbine

Input	Unit	Block Parameter	Unit	Value	Output	Unit
$\dot{Q}_{turb}$	MW_{th}	T_{in_HP}	°C	370-545	P_{el_gross}	MW_{el}
T_{steam_in}	°C	T_{in_LP}	°C	370-545	η_{turb_gross}	-
HoY	-	p_{in_HP}	bar	100	$\dot{Q}_{in}$	MW_{th}
$\dot{Q}_{sf}$	MW_{th}	Cool. Type[1]		0/1/2/3/4	$\dot{Q}_{out}$	MW_{th}
T_{amb}	°C	p_{cond}[2]	bar	0.08-2.5	$\eta_{turb\ net}$	-
P_{el}	MW_{el}	$P_{el\ nominal}$	MW_{el}	0-250	$\dot{m}_{steam\_in}$	kg/s
$P_{parasitic\_sf}$	MW_{el}	Max. Overload	-	1.1	Part Load	-
$P_{parasitic\_TES}$	MW_{el}	Cofir. Switch[3]	-	0/1	$\dot{m}_{steam\_in}$	kg/s
Q_{TES}	MWh_{th}	$P_{el_{design}(cofir=on)}$	MW_{el}	0-250	$\dot{Q}_{in\_design}$	MW_{th}
T_{cool_water}	°C	η_{gen_design}	-	0.97	$\dot{m}_{steam\_in\_LP}$	kg/s
Cofir. Switch	-	TTD	K	5.0	T_{steam_LP}	°C
Rel. Humidity	-	DCA	K	4.0	p_{steam_LP}	bar
P_{atm}	mbar	Δp_{steam_line}	bar/bar	0.05	p_{cond}	bar
HTF Type	-	$\Delta p_{steam\ bleed}$	bar/bar	0.03	$\dot{m}_{steam\ cond}$	kg/s
		η_{pump_design}	-	0.83	T_{cond}	°C
		$\eta_{exp\_HP\_design}$	-	0.86	$P_{parasitic\_plant}$	MW_{el}
		$\eta_{exp\_LP\_design}$	-	0.85	P_{el_net}	MW_{el}
		T_{amb_design}[4]	°C	25-45	P_{el_solar}	MW_{el}
		Rel. Hum. design	-	0.2-0.6	Q_{cofir}	MWh_{th}
		$T_{cool\_water\_design}$	°C	20-35	$P_{parasitic\_pump}$	MW_{el}
		$k_{startup}$	-	0.0-0.5	$P_{parasitic\_cooling}$	MW_{el}
		ITD	K	20	$\dot{Q}_{rest\_from\_turb}$	MW_{th}

Table 75: Summary of inputs, block parameters and outputs of the block STEAMTURB

[1]0=once-through; 1=MED; 2=dry; 3=evaporative tower; 4=fixed pressure

[2]pressure for cooling type=4

[3]1=ON; 0=OFF

[4]relevant for cooling =2-3

Multi-Effect Distillation

Input	Unit	Block Parameter	Unit	Value	Output	Unit
$\dot{m}_{steam\_cond}$	kg/s	TVC Mode[1]	-	0/1	$\dot{m}_d$	m³/h
p_{steam_cond}	bar	n Stages	-	2-14	GOR	-
$T_{seawater}$	°C	$p_{motive\_steam\_0}$	bar	0.20-2.5	$\dot{m}_{seawater}$	m³/h
$X_{seawater}$	ppm	$\dot{m}_{motive\_steam\_0}$	kg/s	> 0	$\dot{m}_{cool\ water}$	m³/h
Water Demand	m³/h	$T_{seawater\_0}$	°C	20-35	$\dot{m}_{feed\_water}$	m³/h
		$X_{seawater\_0}$	ppm	30,000-50,000	$\dot{m}_{brine}$	m³/h
		$X_{\max\_stages}$	ppm	65,000	$\dot{m}_{discharge}$	m³/h
		$T_{steam\ (n=1)}$[2]	°C	< 70	$T_{discharge}$	°C
		Δt_{cond}	K	7-12	$X_{discharge}$	ppm
		L Intake Pipe	m	> 0	sA	m²/(kg/s)
		Δz Intake Pipe	m	0-20	$\dot{q}_{th\_consumption}$	kWh_{th}/m^3
		Feed Preheat[3]	-	0/1	$P_{parasitic\_MED}$	MW_{el}
		$t_{startup}$	h	0.0-1.0	SEC	kWh_{el}/m^3
					Part Load	-
					$\dot{m}_{d\_dump}$	m³/h
					TVC Mode	-
					Plant Capacity	m³/day
					n Stages	-
					RR	-
					X_d	ppm
					SEC_{intake}	kWh_{el}/m^3

Table 76: Summary of inputs, block parameters and outputs of the block MED

[1]0=off; 1=on

[2]relevant for TVC

[3]0=off;1=on

Reverse Osmosis

Input	Unit	Block Parameter	Unit	Value	Output	Unit
$T_{seawater}$	°C	Water Demand$_0$	m³/h	> 0	$\dot{m}_p$	m³/h
$X_{seawater}$	ppm	X_{p_0}	ppm	80-150	Part Load	-
Water Demand	m³/h	R 1st Stage	-	0.35-0.50	$p_{feed\_1st\_stage}$	bar
		R 2nd Stage	-	0.75-0.90	SEC_{intake}	kWh_{el}/m^3
		n Elements 1st	-	8	X_p	ppm
		n Elements 2nd	-	0-8	RR	-
		Membr. Age	y	3-5	$\dot{m}_{feed\_water}$	m³/h
		PT Type[1]		0/1	$X_{seawater}$	ppm
		Δz Intake Pipe	m	0-20	$\dot{m}_{concentrate}$	m³/h
		L Intake Pipe	m	> 0	$X_{concentrate}$	ppm
					$A_{membrane}$	m²
					EC	MW_{el}
					SEC	kWh_{el}/m^3

Table 77: Summary of inputs, block parameters and outputs of the block SWRO

[1]pretreatment type: 1\=conventional; 2\=with DAF

References

[Abou Rayan 2003] Abou Rayan, M., Djebedjian, B., Khaled, I., El-Sarraf, S., Desalination option within water demand management and supply for Red Sea Coast in Egypt, paper presented at the 7th international Water Technology Conference, IWTC 2003, Cairo, Egypt

[Ackermann 2000] Ackermann, T., Söder, L., Wind energy technology and current status: a review, Renew. Sustain. Energy Rev., 4 315-374 (2000)

[Al-Kharagouli 2013] Al-Kharagouli, A., Kazmerski, L., Energy consumption and water production cost of conventional and renewable-energy-powered desalination processes, Renewable and Sustainable Energy Reviews 24 (2013) 343–356

[AQUA-CSP 2007] Trieb, F., Schillings, C., Viebahn, P., Paul, C., Altowaie, H., Sufian, T. et al., AQUA-CSP: Concentrating Solar Power for Seawater Desalination. German Aerospace Center (DLR), Study for the German Ministry of Environment, Nature Conservation and Nuclear Safety, Stuttgart 2007

[AQUASTAT] Online [Apr. 2014]: http://www.fao.org/nr/water/aquastat/data/query/index.html

[Arribas 2011] Arribas, L., Bopp, G., Vetter, M., Lippkau, A., Mauch, K., Worldwide overview about design and simulation tools for hybrid PV systems, IEA 2011, Online [Nov. 2014]: http://www.iea-pvps.org/fileadmin/dam/public/report/technical/rep11_01.pdf

[Bahl 2009] Bahl, C., Laing, D., Hempel, M., Stückle, A., Concrete thermal Energy Storage for solar thermal Power Plants and industrial Process Heat, Paper presented at the SolarPACES Conference 2009, Berlin

[Barlev 2011] Barlev, D., Vidu, R., Stroeve, P., Innovation in concentrated solar power, Solar Energy Materials & Solar Cells 95 (2011) 2703–2725

[Bauer 2011] Bauer, T., Laing, D., Tamme, R., Recent Progress in Alkali Nitrate/Nitrite Developments for Solar Thermal Power Applications, Molten Salts Chemistry and Technology, MS9, Trondheim, Norway 5 - 9 June 2011

[Birnbaum 2011] Birnbaum, J., Feldhoff, J.F., Fichtner, M., Hirsch, T., Jöcker, M., Pitz-Paal, R., Zimmermann, G., Steam temperature stability in a direct steam generation solar power plant, Solar Energy 85 (2011) 660–668

[Bleninger 2008] Bleninger, T., Jirka, G.H., Modeling and environmentally sound management of brine discharge from desalination plant, Desalination, 221 (2008), 585-59

[Bognar 2012] Bognar, K., Personal communication, 2012

[Bonacina 1992] Bonacina, C., Cavallini, A., Mattarolo, L., Trasmissione del calore, cleup editore, Padova, Italy, 1992

[Buck 2008] Buck, R., Solare Turmtechnologie - Stand und Potentiale, presentation at the solar colloquium 2008, Cologne, Germany

[Casimiro 2013] Casimiro, S., Cardoso, J., Alarcon-Padilla, D.-C., Turchi, C., Ioakimidis, C., Farihna Mendes, J., Modeling multi effect distillation powered by CSP in TRNSYS, paper presented at the SolarPACES Conference 2013, Las Vegas

[Chacartegui 2011] Chacartegui, R., Sanchez, D., Munoz, A., Sanchez, T., Real time simulation of medium size gas turbines, Energy Conversion and Management, 52 (2011) 713-724

[Cipollina 2009] Cipollina, A., Micale, G., Rizzuti, L., Seawater Desalination – Conventional and Renewable Desalination Processes, Springer 2009

[Cordes 2011] Cordes, M., Weiterentwicklung eines Solarfeldmodells für das Simulationstool INSEL mit anschließender Untersuchung regenerativer Energiesysteme, Diploma Thesis, University of Siegen, 2011

[CSP Today 2013] Chamberlain, K., CSP Parabolic Trough Report: Cost, Performance and Key Trends

[CSP Today 2013 b] Chamberlain, K., CSP Solar Tower Report: Cost, Performance and Key Trends

[DEEP] Desalination Economic Evaluation Program, International Atomic Energy Agency (IAEA), Online [Apr. 2014]: http://www.iaea.org/NuclearPower/Desalination/

[Dersch 2009] Dersch J., Eck M., Häberle A., Comparison of linear Fresnel and parabolic trough collector systems - System analysis to determine break-even costs of linear Fresnel collectors, SolarPACES Conference, 2009, Berlin

[Dersch 2010] Dersch, J., Schwarzbözl, P., Richert, T., Implementation of solar towers in Greenius - A tool for fast assessment of technical and economic performance of CSP systems, Presentation at the SolarPACES Conference 2010, Perpignan

[Dersch 2010 b] Dersch, J., Schwarzbözl, P., Richert, T., Annual Yield Analysis of Solar Tower Power Plants with GREENIUS, Journal of Solar Energy Engineering 133 (2011)

[DesalData] DesalData, Online [Jan. 2014]: www.desaldata.com

[DesalData 2011] Desalination Markets 2010 Report,Online [Feb. 2014]: www.desaldata.com

[desalination.com] Online [Jan. 2014]: http://www.desalination.com/market/desal-markets

[Desportes 2013] Desportes, C., Aquatech, Personal communication, 2013

[DEWI 2005] DEWI, eon, ewi, RWE, Vattenfall, Energiewirtschaftliche Planung für die Netzintegration von Windenergie in Deutschland an Land und Offshore bis zum Jahr 2020. Köln: Deutsche Energie-Agentur GmbH (DEWI), 2005

[DOE 2001] U.S. Department of Energy, Concentrating Solar Power Commercial Application Study: Reducing Water Consumption of Concentrating Solar Power Electricity Generation - Report to Congress, 2001

[Doenitz 2009] Doenitz, F.D., Solarthermische Kraftwerke – Europas erstes kommerzielles Parabolrinnenkraftwerk ANDASOL 1 am Netz – Solar Millennium AG, Hannover, Apr. 2009, Online [Nov. 2014]: http://files.messe.de/cmsdb/001/14468.pdf

[Dowtherm] Dowtherm A heat transfer fluid, Form No. 176-1337-397 AMS, Dow Chemical Company, 1997

[Dudley 1994] Dudley V. E., Kolb G. J., et al.: Test Results - SEGS LS-2 Solar Collector. SANDIA Report, SAND94-1884, 1994

[Duffie 1991] Duffie, J.A., Beckman, W. A., Solar Engineering of Thermal Processes, 1991, New York

[EBSILON] EBSILON® Professional, STEAG Energy Services GmbH - System Technologies, Online [Nov. 2014]: http://www.steag-systemtechnologies.com/ebsilon_professional.html

[Eck 2001] Eck, M., Steinmann, W.-D., Direct Steam Generation in Parabolic Troughs: first Results of the DISS Project, Proceedings of Solar Forum 2001: Solar Energy: the Power to choose – April 2001, Washington D.C.

[Eck 2007] Eck, M., Steinmann, W.-D., Dynamics and Control of Parabolic Trough Collector Loops with Direct Steam Generation, Solar Energy 81 (2007) 268-279

[EDF 2010] Methodological Manual for Financial Analysis of Concentrated Solar Power and Desalination Plants in Mediterranean Countries, EDF R&D Report, 2010

[El-Dessouky 2002] El-Dessouky, H.T., Ettouney, H.M., Fundamentals of Seawater Desalination, Elsevier, Kuwait University, 2002

[El-Nashar 1999] El-Nashar, A.M., Cost allocation in a cogeneration plant for the production of power and desalted water comparison of the exergy cost accounting method with the WEA method, Desalination 122 (1999) 15-34

[Emeis 2013] Emeis, S., Wind Energy Meteorology – Atmospheric Physics for Wind Power Generation, Green Energy and Technology, Springer, 2013

[EnerMENA 2012] Schenk, H., Yield Analysis for Parabolic Trough Solar Thermal Power Plants, Technical Report, 2012

[enolcon 2010] enolcon gmbh, Schneider, G., Maier, H., Workshop Innovative Cooling Systems for CSP-Applications, presentation at the 2nd MENASOL Conference, May 2010, Cairo, Egypt

[EPIA 2013] EPIA, main authors: Masson, G., Latour, M., Rekinger, M., Theologitis, I.-T., Papoutsi, M., Global Market Outlook for Photovoltaics 2013-2017

[Falchetta 2012] Falchetta, M., private communication, 2012

[Feldhoff 2007] Feldhoff, J.F., „Vergleichende Analyse und Bewertung von Solarthermischen Kraftwerken mit solarer Direktverdampfung“, Diploma Thesis, DLR and RWTH Aachen, 2007

[Feldhoff 2010] Feldhoff, J. F., Benitez, D., Eck, M., Economic Potential of Solar Thermal Power Plants with Direct Steam Generation Compared With HTF Plants, Journal of Solar Energy Engineering, 132 (4)

[Feldhoff 2011] Feldhoff, J.F., Schmitz, K., Eck, M., Laing, D., Ortiz-Vives, F., Schnatbaum-Lauman, L., Schulte-Fischedick, J., Comparative System Analysis of Parabolic Trough Power Plants with DSG and Oil using Integrated Thermal Energy Storage, paper presented at the SolarPACES Conference 2011, Perpignan

[Feldhoff 2012] Feldhoff, J.F., Linear Fresnel Collectors – A Technology Overview, Presentation at the SFERA Summer School 2012, June 28, 2012, Almeria, Spain

[Feldhoff 2012 b] Feldhoff, J.F., Direct Steam Generation (DSG) – Technology Overview, Presentation at the SFERA Summer School 2012, June 28, 2012, Almeria, Spain

[Feldhoff 2012 c] Feldhoff, J. F., Schmitz, K., Eck, M., et al., 2012, Comparative system analysis of direct steam generation and synthetic oil parabolic trough power plants with integrated thermal storage, Solar Energy, 86 (1), 520-530

[Feldman 2012] Feldman, D., Barbose, G., Margolis, R., Wiser, R., Darghouth, N., Goodricht, A., Photovoltaic (PV) Pricing Trends: Historical, Recent, and Near-Term Projections, NREL and LBNL Technical Report: DOE/GO-102012-3839, November 2012

[Fernandez-Garcia 2010] Fernández-García, A., Zarza, E., Valenzuela, L., et al., 2010, Parabolic-trough solar collectors and their applications, Renewable and Sustainable Energy Reviews, 14, pp. 1695 - 1721.

[Ferri 2008] Ferri, R., Cammi, A., Mazzei, D., Molten salt mixture properties in RELAP5 code for thermodynamic solar applications, International Journal of Thermal Sciences 47 (2008) 1676–1687

[Fichter 2014] Fichter, T., Trieb, F., Moser, M., Optimized Integration of Renewable Energy Technologies Into Jordan's Power Plant Portfolio, Heat Transfer Engineering, 35:3, 281-301, DOI: 10.1080/01457632.2013.825183

[Flagsol 2005] Öffentliches Statusseminar Erforschung und Entwicklung der Parabolrinnentechnik Stuttgart, Juli 2005

[Forristall 2003] Forristall, R., Heat Transfer Analysis and Modelling of a Parabolic Trough Solar Receiver Implemented in Engineering Equation Solver, National Renewable Energy Laboratory Technical Report, NREL/TP-550-34169, 2003, Online [Nov. 2014]: www.nrel.gov/csp/troughnet/pdfs/34169.pdf

[Fritzmann 2007] Fritzmann, C., Löwenberg, J., Wintgens, T., Melin, T., State-of-the-art of Reverse Osmosis Desalination, Desalination 216 (2007) 1–76

[FutureWater 2011] Immerzeel, W., Droogers, P., Terink, W., Water Demand Model Report, MENA Regional Water Outlook, 2011

[Gamesa 2014] GAMESA G87-2.0 MW Specification Brochure, Online [Mar. 2014], http://iberdrolarenewables.us/deerfield/Zimmerman/DFLD-JZ-Rev5a-GamesaBrochure.pdf

[Garcia 2008] Garcia, P., Ferriere, A., Bezian, J.-J., Codes for solar flux calculation dedicated to central receiver system applications: A comparative review - Solar Energy 82 (2008) 189–197

[Gathmann 2011] Gathmann, N., Scholz, W., Analysis of novel thermal Energy Storage System Design with 3 Tanks, paper presented at the SolarPACES Conference 2011

[GEA 2013] Online [Jun. 2013]: www.gea-heatexchangers.com, Brochure GEA ACC

[Gebel 2008] Gebel, J., Yüce, S., An Engineer´s Guide to Desalination, VGB PowerTech, Essen, Germany, 2008

[Gemasolar 2013] torresolenergy, Online [Apr. 2013]: www.torresolenergy.com/TORRESOL/gemasolar-plant/en

[Gil 2010] Gil, A., Medrano, M., Martorell, I., Lazaro, M., Dolado, P., Zalba, B., Cabeza, L.F., State of the art on high temperature thermal energy storage for power generation - Part 1: Concepts, materials and modellization

[Gille 2003] Gille, D., Seawater intakes for desalination plants, Desalination 156 (2003) 249-256

[Gille 2005] Gille, D., Czolkoss, W., Ultrafiltration with multi-bore membranes as seawater pre-treatment, Desalination 182 (2005) 301–307

[Giuliano 2013] Giuliano, S., private communication, 2013

[Glade 2009] Glade, H., MED, MED-TVC: Fundamentals, Main Components, Configurations, Presentation at the DME Workshop, September 2009, Duisburg, Germany

[Gnielinski 1976] Gnielisnki, V., New equations for heat and mass transfer in turbulent pipe and channel flow, International Chemical Engineering 16 (1976) 359-368

[Goodrich 2012] Goodrich, A., James, T., Woodhouse, M., Residential, Commercial, and Utility-Scale Photovoltaic (PV) System Prices in the United States: Current Drivers and Cost-Reduction Opportunities, NREL Technical Report, NREL/TP-6A20-53347, February 2012

[Greenius] DLR and HTW Berlin, Greenius, Online [Apr. 2014]: http://freegreenius.dlr.de/

[Greffrath 2009] Greffrath, R., Process Comparison with Respect to primary Energy, Greffrath Consulting, Presentation at the DME Workshop, September 2009, Duisburg, Germany

[GWEC 2014] Global Wind Energy Council (GWEC), Global Wind Statistics 2013, Online [Mar. 2014]: http://www.gwec.net/global-figures/graphs/

[Haar 1984] Haar, L., NBS/NRC Steam Tables: Thermodynamic and Transport Properties and Computer Programs for Vapor and Liquid States of Water in SI Units, Hemisphere Publishing Corporation, Washington, 1984, Online [Nov. 2014]: http://people.sc.fsu.edu/~jburkardt/f77_src/steam_nbs/steam_nbs.html

[Hanrieder 2012] Hanrieder, N., Wehringer, F., Wilbert, S., Wolfertstetter, F., Pitz-Paal, R., Campos, A., Quaschning, V., Determinatn of Beam Attenuation in Tower Plants, Paper presented at the SolarPACES Conference 2012, Marrakesh

[Hirsch 2010] Hirsch, T., Schenk, H., Dynamics of Oil-Based Parabolic Trough Plants - A detailed transient simulation model – Paper presented at the SolarPACES Conference 2010, Perpignan

[Hirsch 2011] Hirsch, T., private communication, 2011

[Ho 2008] Ho C., Software and Codes for Analysis of Concentrating Solar Power Technologies, SANDIA, 2008, SAND2008-8053

[IDAE 2011] Evaluacion del Potencial de energia solar termoelectrica - Estudio Tecnico per 2011-2020 (spanish), 2011

[IEA 2010] Projected Costs of Generating Electricity, 2010 Edition, International Energy Agency and Nuclear Energy Agency, 2010

[IEA 2014] International Energy Agency, Online [May 2014]: www.iea.org/subsidy/index.html

[indexmundi 2013] Online [Sept. 2013]: http://www.indexmundi.com/commodities/

[INSEL] INSEL, developed by Doppelintegral GmbH, Online [Apr. 2014]: http://www.insel.eu/index.php?id=301&L=1

[IPSEpro] IPSEpro, SimTech Simulation Technology, Online [Apr. 2014]: http://www.simtechnology.com/IPSEpro/english/IPSEpro.php

[IRENA 2012] IRENA, ESTAP, Water Desalination Using Renewable Energy – Technology Brief, 2012

[IRENA 2012 b] RENEWABLE ENERGY TECHNOLOGIES: COST ANALYSIS SERIES – Wind Power, Technical Report, 2012

[IRENA 2012 c] IRENA working paper: Renewable Energy Technologies: Cost Analysis Series – Volume 1: Power Sector, Issue 4/5, Solar Photovoltaics, Jun. 2012

[IRENA 2012 d] IRENA working paper: Renewable Energy Technologies: Cost Analysis Series – Volume 1: Power Sector, Issue 2/5, Concentrating Solar Power, Jun. 2012

[IRENA 2013] IRENA, IEA, ESTAP, Solar Photovoltaics - Technology Brief E11, Online [Jan. 2013]: http://www.irena.org/DocumentDownloads/Publications/IRENA-ETSAP%20Tech%20Brief%20E11%20Solar%20PV.pdf

[ISE 2012] Studie Stromgestehungskosten erneuerbare Energien, Fraunhofer-Institut für Solare Energiesysteme ISE, Mai 2012

[Jensen 2007] Jensen, P.H., Meyer, N.I., Mortensen, N.G., Oster, F., International Solar Energy Society (ISES), Wind Energy Pocket Reference, ISES, 2007

[Johnson 2010] Johnson, M., private communication, 2010

[Kearney 2007] Kearney, D.: Parabolic Trough Collector Overview, NREL Parabolic Trough Workshop, Golden CO, 2007

[Kleemann 1993] Kleemann, M., Meliß, M., Regenerative Energiequellen, Springer Verlag, Heidelberg, 1993

[Kögler 2009] Kögler, D., de Lalaing, J., Hellen, D., Mauelshagen, T., Evaluation of Usable Secondary Effects of Linear Fresnel Collector Operation, SolarPACES 2009, Berlin

[Kohls 2010] Kohls, M. (Taprogge), Intake and Filtration Systems for Thermal and Membrane Desalination Plants, Presentation at the DME Seminar: Chemicals and Pretreatment in Seawater Desalination, 9.-10. June 2010, Duisburg

[Koschikowski 2003] Koschikowski, J., Wieghaus, M., Rommel, M., Solar thermal-driven desalination plants based on membrane distillation, Desalination 156 (2003) 295-304

[Kötter 2010] Kötter, J., Riffelmann, K.J., Decker, S., Fellmuth, J., Macke, A., Nava, P., Weinrebe, G., Schiel, W., Steindorf, A., Dracker, R., Heliotrough: One Year Experience with the Loop in a Commercial Solar Power Plant, Proceedings of the 16th SolarPACES Conference, Perpignan, 2010

[Laing 2006] Laing, D., Steinmann, W.-D., Tamme, R., Richter, C., Solid media thermal storage for parabolic trough power plants, Solar Energy, Volume 80, Issue 10, October 2006, Pages 1283–1289

[Laing 2010] Laing, D., Bauer, T., Lehmann, D., Bahl, C., Development of a Thermal Energy Storage System for Parabolic Trough Power Plants with Direct Steam Generation, Journal of Solar Energy Engineering Copyright, ASME, May 2010, Vol. 132 / 021011-1

[Laing 2011] Laing, D., Bahl, C., Bauer, T., Lehmann, D., Steinmann, W.-D., Thermal energy storage for direct steam generation, Solar Energy 85 (2011) 627–633

[Lata 2010] Lata, J., Alcalde S., Fernendez, D., Lekube, X., First surrounding field of heliostats in the world for commercial solar power plants – Gemasolar, presentation at the SolarPACES Conference 2010, Perpignan

[Lattemann 2003] Lattemann, S., Höpner, T., Seawater Desalination: Impacts of Brine and Chemical Discharge on the Marine Environment, Institute for Chemistry and Biology of the Marine Environment (ICBM), University of Oldenburg, 2003

[Lattemann 2008] Lattemann, S., Höpner, T., Environmental impact and impact assessment of seawater desalination, Desalination 220 (2008), 1-15

[Lippke 1995] Lippke, F., Simulation of the Part Load Behavior of a 30MWe SEGS Plant, Prepared for Sandia National Laboratories, Albuquerque, NM, SAND95-1293, June 1995

[Ludwig 2004] Ludwig, H., Hybrid systems in seawater desalination – practical design aspects, present status and development perspectives, Desalination 164 (2004) 1-18

[Ludwig 2010] Ludwig, H., SWRO Energy Consumption: Expectations and Reality for State-of-the-Art Technology, updated version of the paper presented at the IDA World Congress 2009, Nov. 7-9, Dubai

[Mason 2011] Mason, S., Worldwide overview of concentrating solar thermal simulation tools, paper presented at the SolarPACES Conference 2011, Granada, Spain

[Maulbetsch 2004] Maulbetsch, J., Zammit, K., Technical Report: Comparison of Alternate Cooling Technologies for U.S. Power Plants Economic, Environmental, and Other Tradeoffs, EPRI, 2004

[MED-CSD 2010] Allal, H., Trieb, F., Moser, M., Scharfe, J., Tomasek, M.L., Kern et al., M., Technology Review and Selection of CSP and Desalination Configurations adapted for Application in the Southern and Eastern Mediterranean Region, MED-CSD Final Report - WP1: Combined Solar Power and Desalination Plants: Techno-Economic Potential in Mediterranean Partner Countries, Online [Nov. 2014]: http://www.med-csd-ec.eu/eng/

[MENAWATER 2011] Verdier, F., (Fichtner) Trieb, F., Fichter, T., Moser, M., (DLR) 2011. Desalination Using Renewable Energy, Task 2 - Energy Requirement, MENA Regional Water Outlook, Part II, Online [Nov. 2014]: www.dlr.de/tt/menawater

[MENAWATER 2012] Laukemann, T., Verdier, F., Baten, R., (Fichtner) Trieb, F., Moser., M., Fichter, T., (DLR) MENA Regional Water Outlook, Phase II, Desalination using Renewable Energy, study commissioned by the World Bank, 2012

[MERRA] MERRA Database, Online [Nov. 2014]: http://gmao.gsfc.nasa.gov/research/merra, data analysis by DLR

[Mertins 2009] Mertins, M., Doctoral Thesis: Technische und wirtschaftliche Analyse von horizontalen Fresnel-Kollektoren, Universität Karlsruhe, 2009

[Meteonorm] Meteonorm: Global meteorological Service; Online [Nov. 2014]: http://meteonorm.com/en/

[Mittelman 2010] Mittelman, G., Epstein, M., A novel power block for CSP systems, Solar Energy 84 (2010) 1761-1771

[Montes 2009] Montes, M.J., Abanades, A., Martinez-Val, J.M., Valdes, M., Solar multiple optimization for a solar-only thermal power plant, using oil as heat transfer fluid in the parabolic trough collectors, Solar Energy 83 (2009) 2165–2176

[Morillo 2014] Morillo, J., Usero, J., Rosado, D., El Bakouri H., Riaza, A., Bernaola, F.-J., Comparative study of brine management technologies for desalination plants, Desalination 336 (2014) 32–49

[Morin 2011] Morin, G., Dersch, J., Eck, M., Comparison of Linear Fresnel and Parabolic Trough Collector power plants, Solar Energy

[Moser 2009] Moser, M., Concept of a sustainable seawater desalination plant, Diploma Thesis, University of Karlsruhe and University of Trento, April 2009

[Moser 2013] Moser, M., Trieb, F., Fichter, T., Potential of Concentrating Solar Power Plants for the Combined Production of Water and Electricity in MENA Countries, JSDEWES Journal of Sustainable Development of Energy, Water and Environment Systems, 1 (2013), Issue 2, pp 122-140

[Moser 2013 b] Moser, M., Trieb, F., Fichter, T., Maier, H., Schicktanz, P., Techno-economic analysis of enhanced dry cooling for CSP, paper presented at the SolarPACES Conference 2012, Las Vegas, Sept. 2013

[Müller-Holst 1999] Müller-Holst, H., Engelhardt, M., Schölkopf, W., Small-scale thermal seawater desalination simulation and optimization of system design, Desalination 122 (1999) 255-262

[Nafey 2010] Nafey, A.S., Sharaf, M.A., Garcia-Rodriguez, L., A new visual library for design and simulation of solar desalination systems (SDS), Desalination 259 (2010) 197–207

[Niepelt 2007] Niepelt, A., Development of interfaces for the coupling of hydrodynamic models for brine discharges from desalination plants, Diploma Thesis, University of Karlsruhe

[NOAA] National Oceanographic Atmospherical Administration (NOAA) - National Oceanographic Data Center (NODC): Online [Apr. 2014]: http://www.nodc.noaa.gov/OC5/SELECT/woaselect/woaselect.html

[Novatec Solar 2013] Novatec Solar, Online [Jun. 2013]: www.novatecsolar.com

[O´Hagan 2003] O'Hagan, J., Zammit, K., Buckard, D., Spray cooling enhancement of air cooled condensers, PIER and EPRI Consultant report, 2003, Online [Nov. 2014]: http://www.energy.ca.gov/reports/2004-03-09_500-03-109.PDF

[Pacheco 2002] Pacheco, J.E., Final Test and Evaluation Results from the Solar Two Project, Sandia National Laboratories

[Palenzuela 2011] Palenzuela, P., Alarcon, D., Blanco, J., Guillen, E., Ibarra, M., Zaragoza, G., Modeling of the heat transfer of a solar multi-effect distillation plant at the Plataforma Solar de Almería, Desalination and Water Treatment, 31 (2011), 257-268

[Patnode 2006] Patnode, A., Simulation and Performance Evaluation of Parabolic Trough Solar Power Plants, Master Thesis University of Wisconsin- Madison, 2006

[Pawellek 2011] Pawellek, R. und Löw, T. und Hirsch, T. und Giuliano, S. und Schwarzbözl, P., Solar Tower Simulation with Ebsilon Professional. In: Proceedings of the SolarPACES 2011 conference. Sept. 2011, Spain

[Peters 2008] Peters, T., Pinto, D., Seawater intake and pre-treatment/brine discharge - environmental issues, Desalination 221 (2008) 576–584

[Pregger 2009] Pregger, T., Graf, D., Krewitt, W., Sattler, C., Roeb, M., Möller, S., Prospects of solar thermal hydrogen production processes, International Journal of Hydrogen Energy 34 (2009), 4256-4267

[Price 2002] Price, H., Lüpfert, E., Kearney, D., Zarza, E., Cohen, G., Gee, R., Mahoney, R., Advances in Parabolic Trough Solar Power Technology, Journal of Solar Energy Engineering (124), 2002, 109-125.

[PRODES 2010] PRODES Report: Commercial Desalination Products powered by Renewable Energy, 2010, Online [Nov. 2014]: http://www.prodes-project.org/fileadmin/Files/ProDes_D_4_2_Commercial_Products.pdf

[Prognos 2013] Prognos AG, Peter, F., Krampe, L., Ziegenhagen, I., Entwicklung von Stromproduktionskosten – Die Rolle von Freiflächen-Solarkraftwerken in der Energiewende, October 2013, Berlin

[PV WATTS 2013] NREL, A Performance Calculator for Grid-Connected PV Systems, Online [Nov. 2014]: http://rredc.nrel.gov/solar/calculators/pvwatts/system.html

[Quaschning 2007] Quaschning, V., Regenerative Energiesysteme – Technologie, Berechnung, Simulation, Hanser Verlag, 2007

[Raade 2010] Raade, J.W., Padowitz, D., Development of molten salt heat transfer fluid with low melting point and high thermal stability, paper presented at the Solar PACES Conference 2010, Perpignan

[Rheinländer 2010] Rheinländer, J., Erbes, M.R., Bergmann, S., Simulation of Solar Field Start-up in a PTC-CSP Plant, paper presented at the SolarPACES Conference 2010, Perpignan

[Riffelmann 2009] Riffelmann, K.-J., , Kötter, J., Nava, P., Meuser, F., Weinrebe, G., Schiel, W., Kuhlmann, G., Wohlfahrt, A., Nady, A., Dracker, R., Heliotrough- A new collector generation for parabolic trough power plants, paper presented at the SolarPACES conference 2009, Berlin, Online [Nov. 2014]: http://www.heliotrough.com/doc/SolarPaces2009_Heliotrough.pdf

[Riffelmann 2012] Riffelmann, K.-J., Lüpfert, E., Richtert, T., Nava, P., Performance of the Ultimate Trough® Collector with molten Salts as Heat Transfer Fluid, paper presented at the SolarPACES Conference 2012, Marrakesh

[ROSA] Reverse Osmosis System Analysis, Dow Water & Process Solutions, Online [Apr. 2014]: http://www.dowwaterandprocess.com/en/resources/rosa_system_design_software

[Ruegamer 2013] Ruegamer, T., Kamp, H., Kuckelkorn, T., Schiel, W., Weinrebe, G., Nava, P., Riffelmann, K., Richter, T., Molten Salt for Parabolic Trough Applications: System Simulation and Scale Effects, paper presented at the SolarPACES 2013, Las Vegas, Sept. 2013

[SAM] NREL, System Advisor Model, Online [Apr. 2014]: https://sam.nrel.gov/

[Sader 2012] Sader, H., personal communication, 2012

[Schenk 2012] Schenk, H., Hirsch, T., Feldhoff, J.F., Energetic comparison of Linear Fresnel and Parabolic Trough Collector Systems, ASME 2012 6th Int. Conference on Energy Sustainability, San Diego, CA, USA

[Schenk 2012 b] Schenk, H., private communication, 2012

[Schmidt 1981] Schmidt, F.W., Willmott, A.J., Thermal Energy Storage and Regeneration, Hemisphere Publishing Corporation, McGraw-Hill Book Company, 1981

[Schmidt 1996] Schmidt, H., Sauer, D.U., Wechselrichter-Wirkungsgrade - Praxisgerechte Modellierung und Abschätzung, Sonnenenergie 4 (1996), 43-47

[Scholz 2012] Scholz, Y., Renewable energy based electricity supply at low costs: development of the REMix model and application for Europe, PhD thesis, University Stuttgart

[Schüller 1999] Schüller, K.H., Repetitorium Wärmetechnik, Grundlagen, Auslegungen, Berechnungen, Energie & Management Verlagsgesellschaft, München, 1999

[Schwarzbözl 2006] Schwarzbözl, P., Buck, R., Sugarmen, C., Ring, A., Crespo, J.M., Altwegg, P., and Enrile, J., Solar gas turbine systems: Design, cost and perspectives, Solar Energy 80 (2006), 1231–1240

[Schwarzbözl 2009] Schwarzbözl, P., Schmitz, M., Pitz-Paal, R., Visual HFLCAL – A software for layout and optimization of heliostat fields, paper presented at the SolarPACES Conference 2009

[SIDEM 2010] Laborie, J., SIDEM, private communication, 2010

[Sigloch 1993] Sigloch, H., Strömungsmaschinen – Grundlagen und Anwendungen – 2. Auflage, Hanser Verlag München Wien, 1993

[Singer 2013] Singer, C., Doctoral Thesis: Solarturmreceiver für überkritische Dampfprozesse und ihre technische und ökonomische Bewertung, Springer Fachmedien, Wiesbaden 2013

[Sioshansi 2010] Sioshansi, R., Denholm, P., The Value of Concentrating Solar Power and Thermal Energy Storage, Technical Report NREL-TP-6A2-45833, February 2010

[Sokrates 2004] Trieb, F., Kronshage, S., Quaschning, V., Dersch, J., Lerchenmüller, H., Morin, G., Häberle, A., Solarthermische Kraftwerkstechnologie für den Schutz des Erdklimas - Technologiedatenbank und –modelle, 2004

[SOLEMI] Hoyer-Klick, C., Schillings, C., SOLEMI - Solar Energy Mining, DLR Institute of Technical Thermodynamics, Online [Nov. 2014]: http://www.dlr.de/tt/desktopdefault.aspx/tabid-2885/4422_read-6581

[Sommariva 2010] Sommariva, C., Desalination and Advanced Water Treatment – Economics and Financing, Book, Balaban Desalination Publications, 2010

[Steinmann 2005] Steinmann, W.-D., Buschle, J., Analysis of thermal storage systems using Modelica, Proceedings of the 4th International Modelica Conference, March 2005, Hamburg

[Steinmann 2006] Steinmann, W.-D., Eck, M., Buffer Storage for Direct Steam Generation, Solar Energy 80 (2006) 1277-1282

[Steinmann 2010] Steinmann, W.-D., Laing, D., Tamme, R., Latent Heat Storage Systems for Solar Thermal Power Plants and Process Heat Applications, Journal of Solar Energy Engineering 132(2), Apr 2010, doi:10.1115/1.4001405

[Steinmann 2011] Steinmann, W.-D., Laing, D., Odenthal, C., Development of the CellFlux storage concept for sensible heat; 17th SolarPACES Conference, 20-23 Sept. 2011, Granada, Spain

[Stine 2001] Stine, W., Geyer, M,. Online [Jun. 2009]: www.powerfromthesun.net, chapter 10, Central Receiver Systems

[Strauß 2007] Strauß, K., Kraftwerkstechnik: zur Nutzung fossiler, nuklearer und regenerativer Energiequellen (VDI-Buch), Springer Verlag, 2007

[Taprogge 2014] Taprogge, Online [Jan. 2014]: www.taprogge.de/products-and-services/in-ta-ctR/intake-systems/single-stage-system-tapisR/index.htm

[Tegen 2013] Tegen, S., Lantz, E., Hand, M., Maples, B., Smith, A., Schwabe, P., 2011 Cost of Wind Energy Review, NREL Technical Report, NREL/TP-5000-56266, March 2013

[Therminol] 2011: Online [Apr. 2011]: http://www.therminol.com/pages/products/vp-1.asp

[Thermoflow] Thermoflow Inc., Online [Apr. 2014]: http://www.thermoflow.com/index.html

[Trieb 2009] Trieb, F., Schillings C., O´Sullivan M., Pregger, T., Hoyer-Click, C., Global Potential of Concentrating Solar Power, presented at the SolarPACES Conference 2009, Berlin, 2009

[Trieb 2009 b] Trieb F., O'Sullivan M., Pregger T, Schillings C, Krewitt W. 2009 (DLR-ITT Stuttgart): Characterization of Solar Electricity Import Corridors from MENA to Europe – REACCESS, Online [Nov. 2014]: http://elib.dlr.de/59448/

[Trieb 2012] Trieb, F., Fichter, T., Moser, M., The Role of Concentrated Solar Power in the Future Energy Mix, submitted for review to Journal of Energy Policy, Stuttgart, April 2012

[TRNSYS] TRNSYS, University of Wisconsin, Madison, Online [Apr. 2014]: http://sel.me.wisc.edu/trnsys/

[TroughNet 2013] TroughNet, Online [Apr. 2013]: http://www.nrel.gov/csp/troughnet/power_plant_data.html

[Turchi 2010] Turchi, C., Parabolic Trough Reference Plant for Cost Modeling with the Solar Advisor Model (SAM), Technical NREL Report, NREL/TP-550-47605, July 2010

[Turchi 2013] Turchi, C., Heath, G., Molten Salt Power Tower Cost Model for the System Advisor Model (SAM), Technical NREL Report, NREL/TP-5500-57625, February 2013

[UTCE 2009] Union for the Co-ordination of Transmission of Electricity (UTCE), Policy 1: Load-Frequency Control and Performance, 2009

[Valenzuela 2005] Valenzuela, L., Zarza, E., Berenguel, M., Camacho, E.F., Control Concepts for Direct Steam Generation in Parabolic Troughs, Solar Energy 78 (2005), 301-311

[VDI 2010] Verband deutscher Ingenieure e.V. (VDI): Heat Atlas, VDI-Verlag, Düsseldorf, 2.Aufl. 2010

[Vestas 2012] Vestas, Online [Jul. 2012]: www.vestas.com

[Voutchkov 2010] Voutchkov, N., Seawater Pretreatment, Water Treatment Academy - TechnoBiz Communications Co., Ltd., 2010

[Voutchkov 2010 b] Voutchkov, N., Considerations for Selection of Seawater Filtration Pretreatment System, Desalination 261 (2010), 354-364

[Wade 1999] Wade, N.M., Energy and cost allocation in dual-purpose power and desalination plants, Desalination 123 (1999) 115-125

[Wagner 1998] Wagner, W., Overhoff, U., Extended IAPWS-IF97 Steam Tables: Interactive Software for the calculation of thermodynamic and transport properties of water and steam - DLL for user specific programs, Springer 1998

[Wagner 2011] Wagner, M., J., Gilman, P., Technical Manual for the SAM Physical Trough Model, NREL Report: NREL/TP-5500-51825, June 2011

[Wagner 2012] Wagner, P., Thermodynamic simulation of solar thermal power stations with liquid salt as heat transfer fluid, Diploma Thesis, Technical University Munich, 2012

[waterworld 2013] Online [Jan. 2014]: http://www.waterworld.com/articles/2013/10/global-desalination-capacity-tops-80-million-cubic-meters-per-day.html

[Weinrebe 2013] Weinrebe, G., von Reeken, F., Wöhrbach, M., Plaz, T., Göcke, V., Balz, M., Towards Holistic Power Tower System Optimization, paper presented at the SolarPACES 2013, Las Vegas, Sept. 2013

[WHO 2014] World Health Organization, Online [Apr. 2014]: www.who.int/water_sanitation_health/dwq/en/

[Wilf 2007] Wilf, M., Awerbuch, L., Bartels, C., Mickley, M., Pearce, G., Voutchkov, N., 2007, The Guidebook to Membrane Desalination Technology: Reverse Osmosis, Nanofiltration and Hybrid Systems Process, Design, Applications and Economics, L'Aquila

[Wittmann 2009], Wittmann, M., private communication, 2009

[Wittmann 2012], Wittmann, M., private communication, 2012

[Wu 2011] Wu, W., Gobereit, B., Singer, C., Amsbeck, L., Pitz-Paal, R., Direct Absorption receiver for high temperatures, presentation at the SolarPACES Conference 2011, Granada

[Zarza 2002] Zarza, E., Valenzuela, L., Leon, J., Weyers, H.-D., Eickhoff, M., Eck, M., Hennecke, K., The DISS Project: Direct Steam Generation in Parabolic Trough Systems. Operation and Maintenance Experience and Update on Project Status, Journal of Solar Energy Engineering 124 (2), 126-133

[Zarza 2012] Zarza, E., Basic principles of solar radiation and STE plants, Presentation at the SFERA Summer School 2012, June 28, 2012, Almeria, Spain

[Zavoico 2001] Zavoico, A., Solar Power Tower – Design Basis Document, Sandia National Laboratories, San Francisco, California, July 2001

Eidesstattliche Erklärung

Hiermit erkläre ich, diese Arbeit selbständig angefertigt, alle benutzten Hilfsmittel vollständig und genau angegeben sowie alles kenntlich gemacht zu haben, was aus Arbeiten anderer unverändert oder mit Abänderungen entnommen wurde.

Ort Datum Unterschrift